FACULTEIT
WETENSCHAPPEN

Short-range correlations and meson-exchange currents in neutrino-nucleus scattering

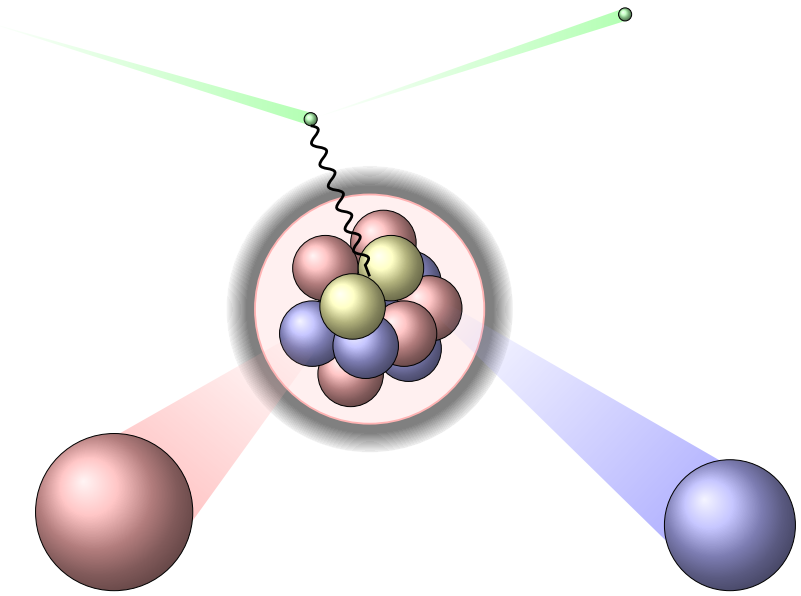

UNIVERSITEIT
GENT

Tom Van Cuyck

FACULTEIT
WETENSCHAPPEN

Short-range correlations and meson-exchange currents in neutrino-nucleus scattering

Promotor: Prof. Dr. Natalie Jachowicz

Proefschrift ingediend tot het behalen van de academische graad van
Doctor in de Wetenschappen: Fysica

Universiteit Gent
Faculteit Wetenschappen
Vakgroep Fysica en Sterrenkunde
Academiejaar 2016-2017

UNIVERSITEIT
GENT

Tom Van Cuyck

Dankwoord

In de eerste plaats wil ik Natalie bedanken, om me de kans te geven om een doctoraat in de Fysica te behalen. Het was een fijne samenwerking, bedankt voor het vertrouwen, advies en begeleiding. Ook Jan wil ik bedanken, voor het erven van de code en nota's, en voor de vele informatieve discussies.

Camille en Benjamin, het was aangenaam vanaf ons ontbijt op de eerste werkdag, tot aan het bittere einde. Maarten, Wim, Nils, Bart, Jannes en Sam, jullie waren toffe collega's. Vanaf nu val ik jullie niet meer lastig als ik loop te ijsberen door de gang. Vishvas, Marco and Raúl (I will stop inventing new ways to misspell your name now), it was fun collaborating with you guys.

Bedankt aan alle andere collega's en lunchpauze- en koffiepauzegenoten en pingpong tegenstanders: Sander (zonder hem zou het INW niet functioneren: ☎ 6555) , Celine, Ianthe, Ward, Matthias, Sam en al de rest, het was een leuke tijd op het INW.

Als laatste: bedankt aan mijn ouders om me de kans te geven te studeren, en aan Lore om er te zijn voor mij!

Tom Van Cuyck

Table of contents

I Main material

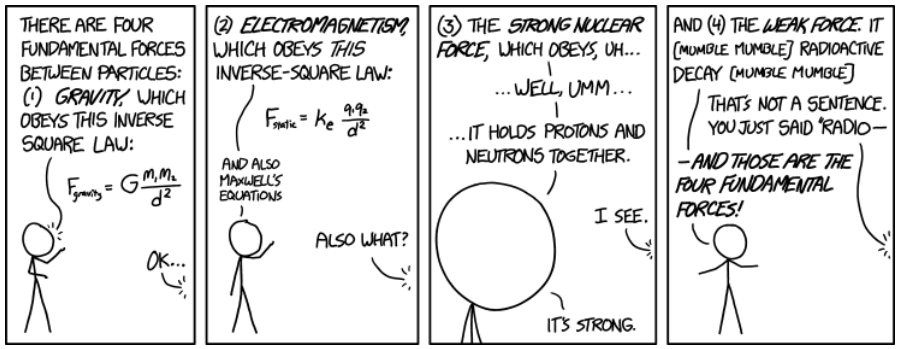

"Of these four forces, there's one we don't really understand." "Is it the weak force or the strong–" "It's gravity."

Chapter 1

Introduction

The onset of neutrino history dates back to the beginning of the 20th century. In 1914, it was demonstrated that the nuclear beta decay spectrum was continuous, in contrast to the spectra of alpha and gamma decays. This seemed to imply that energy and momentum were not conserved in beta decay. Some physicists were ready to accept the fact that the conservation laws could be violated in this process. Niels Bohr, for example, proposed a statistical version of the conservation laws to explain the observed continuous spectrum. One of the scientists who didn't accept this explanation was Wolfgang Pauli. In 1930, he postulated that a neutral particle must be emitted from the nucleus, together with the beta particle or electron. He didn't dare publish this idea, but sent a letter to a conference about radioactive decay instead, where they could scrutinize and judge his newly invented particle [1]. This particle, that was not yet observed, was the carrier of the missing energy and momentum. He used the name neutron for the hypothetical particle. To avoid confusion with the particle we know today as the neutron, which was discovered two years later, Enrico Fermi, in his theory of beta decay [2], called this particle a *neutrino*. This term was coined by Edoardo Amaldi, one of the young members of Fermi's group, and means little neutron.

More than twenty years later, in 1956, the neutrino was discovered experimentally by Clyde Cowan and Frederick Reines [4]. The predicted neutrino was detected via inverse beta decay. In the actual experiment, an antineutrino interacted with a proton, producing a neutron and a positron

$$\overline{\nu}_e + \mathrm{p} \rightarrow e^+ + \mathrm{n}. \tag{1.1}$$

The produced positron quickly annihilates with an electron in the detector emitting two gamma rays which are easily detectable. The existence of the neutrino associated with this reaction is associated with the electron, hence it was named the electron neutrino (ν_e).

Later, neutrinos associated with the other two charged leptons were discovered: the muon neutrino (ν_μ) in 1975 at the Stanford Linear Accelerator Center [5], and the tau neutrino (ν_τ) in 2000 at Fermilab [6]. The three types of neutrinos are also called neutrino flavors. With the discovery of the tau neutrino, the symmetry in the lepton sector of the standard model of physics was restored: it now contains six leptons of which three are charged and three neutral.

For several years, however, the *solar neutrino problem* kept puzzling the physics community. The sun, a nuclear fusion reactor powered by the proton-proton chain, showers the earth with trillions of electron neutrinos each second. The proton-proton cycle converts four protons into a helium nucleus in various steps, whereby positrons, gamma radiation and electron neutrinos with an energy up to 18 MeV are produced. In the late 1960s, the Homestake experiment, lead by Raymond Davis and John Bahcall, was built to 'count' the neutrinos emitted by the nuclear fusion process in the sun. The detector, designed by Davis [7], was the first to successfully detect neutrinos originating from the sun. The Homestake experiment detected electron neutrinos via neutrino capture on ^{37}Cl, producing the radioactive isotope ^{37}Ar and an electron. The decay products of the radioactive argon isotope allowed them to count the number of neutrino interactions that occurred in the detector.

The counting rate, however, was inconsistent with the theoretical predictions by Bahcall, only one third of the expected number of neutrinos was observed [8]. Modifications to the solar model were proposed as a solution, but these were ruled out as the standard solar model was confirmed and corroborated by several other observations. This discrepancy between the so-called standard solar model and experiments persisted for several decades and became known as the solar neutrino problem. Subsequent experiments such as the Super-Kamiokande detector and the Sudbury Neutrino Observatory (SNO), used a different detection mechanism. They relied on the Cherenkov radiation of the particles produced by a neutrino interaction to detect neutrinos. They were also unable to measure the expected electron neutrino flux emitted by the sun, however, together they helped unveil the physics behind the solar neutrino problem.

Neutrino oscillations

One explanation for the solar neutrino problem was the possibility of *neutrino oscillations*. In 1957, Bruno Pontecorvo suggested, that the electron neutrinos produced in the sun can change into another neutrino flavor when they propagate: they oscillate [9,10]. These flavor

Figure 1.1: An artistic impression of an oscillating neutrino, figure taken from [3].

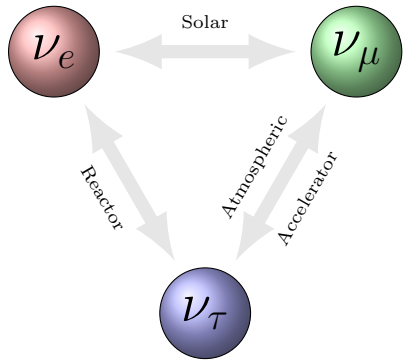

Figure 1.2: The different neutrino oscillation regimes.

changes, or oscillations, are only possible if the flavor and mass eigenstates of the neutrino do not coincide, and the mass eigenstates have different masses. In a simplified model, with only two neutrino flavors, the probability of the oscillation of a neutrino with flavor α into flavor β is

$$P(\nu_\alpha \to \nu_\beta) = \sin^2 2\theta_{12} \left(\frac{\Delta m^2_{12} L}{4\epsilon_\nu} \right),$$

with $\Delta m^2_{12} = m^2_1 - m^2_2$ the squared mass differences and θ_{12} the mixing angle of the mass eigenstates. L is the distance between the production and the detection site and ϵ_ν is the energy of the neutrino. Situations with different values for the ratio L/ϵ_ν allow one to probe different oscillation regimes, as shown schematically in Fig. 1.2. As the solar neutrinos are produced with similar energies, and the distance between the sun and the earth remains roughly equal, solar neutrinos turn out to be useful for the study of $\nu_e \leftrightarrow \nu_\mu$. Alternatively, atmospheric neutrinos are used mainly to study the $\nu_\mu \leftrightarrow \nu_\tau$ transition.

Around the turn of the millennium, two collaborations came with evidence for these neutrino oscillations. The Super-Kamiokande collaboration was looking at neutrinos from cosmic radiation, see Fig. 1.3. When highly energetic cosmic particles collide with the Earth's atmosphere, muon neutrinos are created. The flux of these atmospheric neutrinos is considerably lower than the solar neutrino flux, but the neutrinos are more energetic, which increases their detection probability. In 1998, the collaboration reported a deficit in muons produced by atmospheric muon neutrinos [11]. More important, this deficit seemed to depend on the direction from which the neutrinos were coming. More neutrinos were coming straight from the atmosphere compared to the neutrinos which had to travel through the earth, while the earth is not a considerable obstacle for these neutrinos. This suggested that neutrinos that traveled further had the opportunity to undergo a flavor change, and was explained by the oscillation of muon neutrinos in tau neutrinos, with $\Delta m^2_{atm} \approx 2.6 \times 10^{-3}$ eV^2 and $\sin 2\theta_{atm} \approx 1$. These tau neutrinos, however, could not be observed with the Super-Kamiokande detector.

A couple of years later, the SNO collaboration reported on the first evidence for solar neutrino oscillations [12,13]. The electron neutrinos produced in the sun did not disappear on their way to the detector, yet they arrived with a different flavor. The heavy water in the detector allowed for the detection of all three neutrino flavors through neutral current interactions, Fig. 1.4, and by counting all three types of neutrinos, the expected solar neutrino flux was obtained.

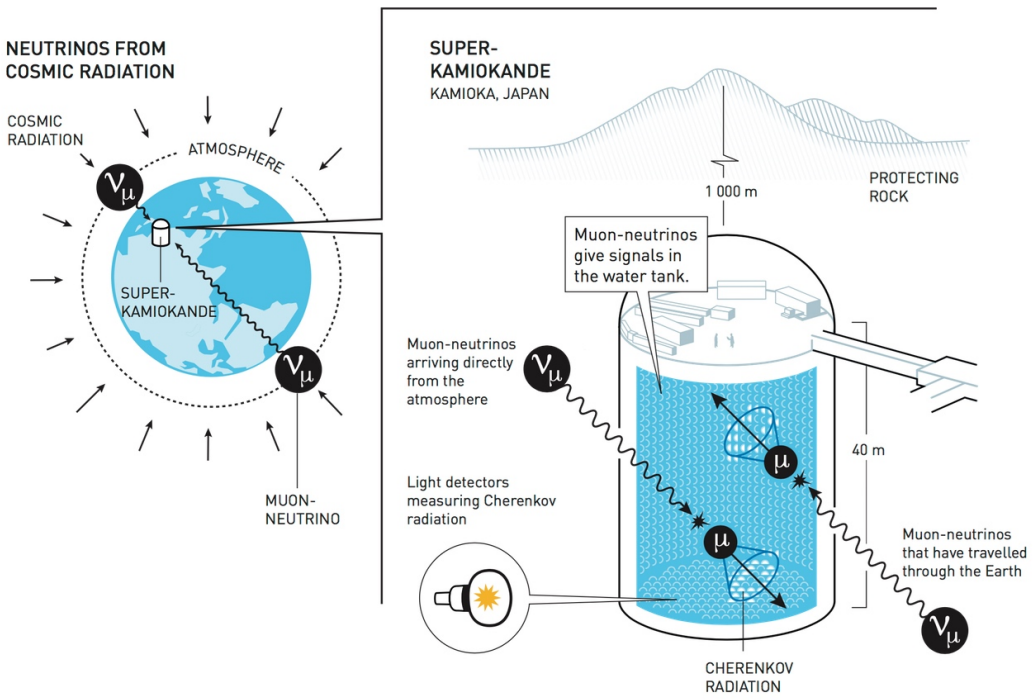

Figure 1.3: Schematic overview of the Super-Kamiokande experiment, figure taken from [3].

These discoveries led to the Nobel Prize in physics 2015 being awarded to Takaaki Kajita (Super-Kamiokande Collaboration) and Arthur B. McDonald (Sudbury Neutrino Observatory) *for the discovery of neutrino oscillations, which shows that neutrinos have mass.* The solar neutrino puzzle, which had troubled physicists for decades, was solved and it had far-reaching implications. In the standard model of physics, which had resisted experimental challenges for decades, neutrinos are massless. The discovery that they have a mass, however small, shows that the standard model is incomplete.

Neutrino experiments

The discovery of neutrino oscillations initiated a new generation of neutrino experiments. These experiments aim at the precise determination of the oscillation parameters e.g. θ_{ij}, Δm^2_{ij}. The Super-Kamiokande and SNO experiments for example, were looking at atmospheric and solar neutrinos, hence the ratio L/ϵ_ν was fixed by nature. A new generation of accelerator-based experiments produces neutrinos in such a way that the energy ϵ_ν and distance L are optimized for maximizing the oscillation probability. Further, the high flux of neutrinos implies better statistics. In general, the production of neutrinos occurs as shown in Fig. 1.5. A beam of high-energy protons collides with a carbon target. These high energy collisions primarily produce pions, which can be separated based on their charge.

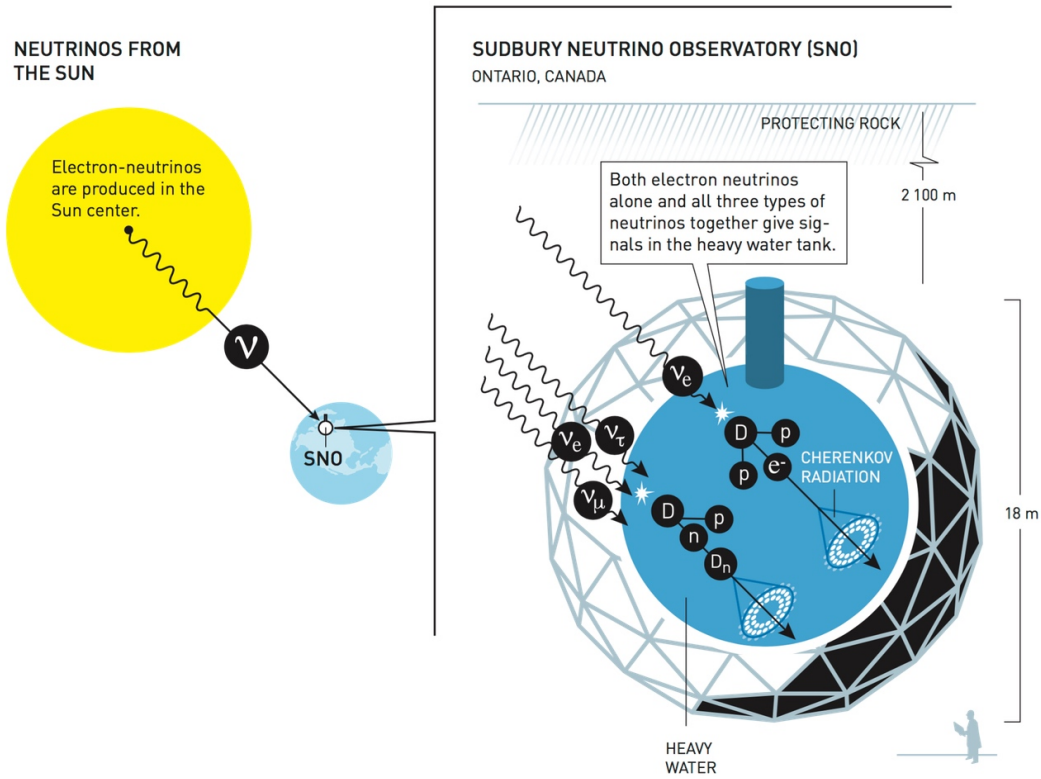

Figure 1.4: Schematic overview of the Sudbury Neutrino Observatory experiment, figure taken from [3].

The charged pions are then sent into a decay pipe where they decay into muons and muon neutrinos. This beam of neutrinos is then directed through the earth to a detector a couple of hundred kilometers away, as shown in Fig. 1.6. While traveling through the earth, the neutrinos can undergo oscillations. When counting the number of muon neutrinos at the production site (near detector) and after they traveled 100s of kilometers (far detector), it becomes possible to extract the neutrino oscillation parameters.

Several types of detectors exist. The first type are Cherenkov detectors, used in experiments such as MiniBooNE [14] and T2K [15] (far detector). In a simplified way, these detectors work as follows: a huge tank is filled with detector liquid (e.g. CH_2, C_8H_8 or H_2O) and the sides of the tank are covered with photomultiplier tubes. When a muon neutrino interacts with a neutron in the detector liquid via a charged current interaction, a muon is produced

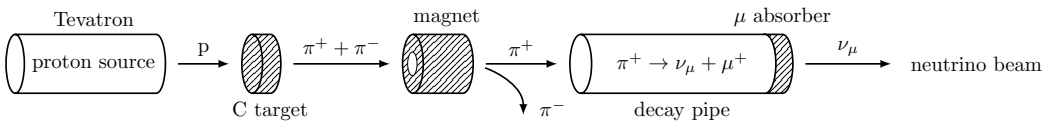

Figure 1.5: Neutrino production mechanism in an accelerator-based experiment.

next to the recoiling proton. The muons can be identified via their Cherenkov light, while the recoiling proton energy is often below the detection threshold. Similarly, an electron created by the interaction of an electron neutrino can be detected by its Cherenkov signal, which is slightly different from the signature of a muon. Interactions in which a pion is produced can be separated from interactions without, as the decay products of the pion can be identified in the detector.

The second type of detectors are different in their ability to detect nucleons in the final state. The MINERvA [16] and T2K near detector (ND280) consist of many layers of parallel scintillator strips. The end of each strip is connected to a photomultiplier tube. A different orientation of subsequent layers makes it possible to make a 3D reconstruction of the tracks of the outgoing charged particles produced in the interaction, thus including protons. The NOvA [17] detector uses a very similar design, however the scintillator strips are highly transparent PVC containers filled with a liquid scintillator.

ArgoNeuT [18] and MicroBooNE [19] on the other hand, use the liquid argon time projection chamber (LArTPC) technology to detect neutrinos. The chamber is filled with inert liquid argon and when a neutrino interacts with an argon nucleus, charged particles are created. An electric field in the detector causes these particles to drift towards a set of wires at the boundary of the detector. The charged particles induce a current in these wires, which, together with timing information, is sufficient for a 3D reconstruction of the event, including all charged particles that are produced. The future DUNE experiment [20] will also use LArTPC detectors.

Neutrino-nucleus cross sections

Since neutrinos are confirmed to oscillate into other flavors in many experiments, the next step is to determine the oscillation parameters more precisely. In order to do this, one must be able to accurately register the number of neutrinos passing through a detector, and for this, one needs to know the probability that a neutrino will interact with a target nucleus in the detector: the neutrino-nucleus cross section.

In Fig. 1.7, the total neutrino and antineutrino cross sections per nucleon (divided by energy) are shown as a function of the incoming neutrino energy ϵ_ν. Three different reaction channels are shown and their relative strength depends strongly on the energy of the neutrino.

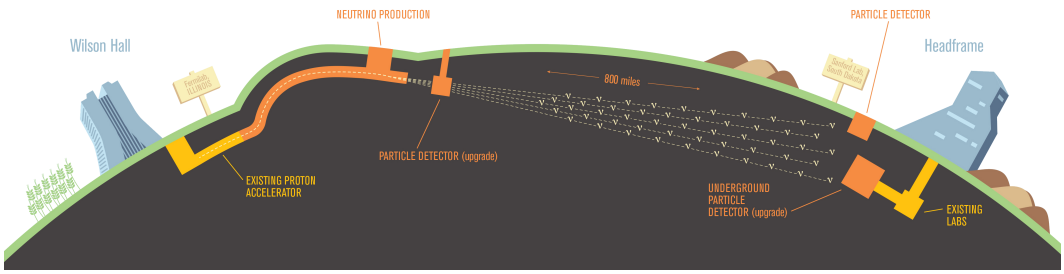

Figure 1.6: Accelerator-based neutrino experiment (DUNE).

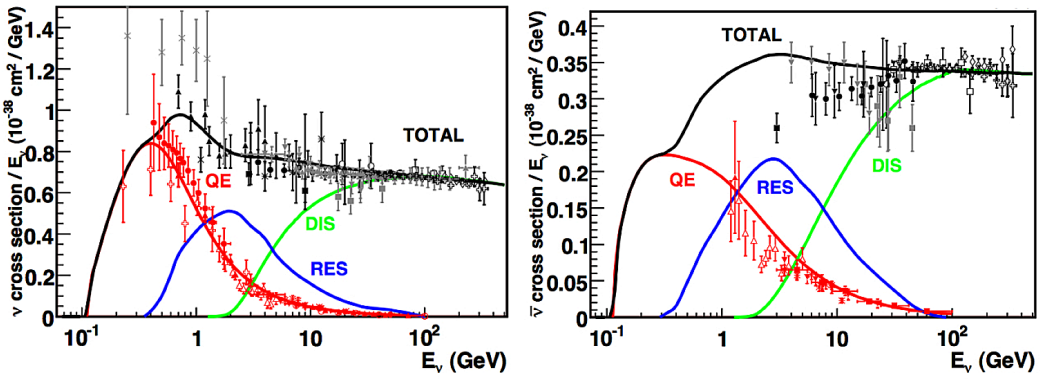

Figure 1.7: Neutrino (left) and antineutrino (right) cross sections per nucleon (divided by the neutrino energy, E_ν in the figure). The figure is taken from Ref. [21].

- QE - Quasielastic scattering: the neutrino interacts with a single bound nucleon. For a charged-current (CC) interaction, the nucleon undergoes a charge change and is emitted from the nucleus. The neutrino changes into its corresponding lepton, e.g.

$$\nu_\mu + \mathrm{n} \rightarrow \mu^- + \mathrm{p},$$
$$\nu_e + \mathrm{n} \rightarrow e^- + \mathrm{p}.$$

- RES - Resonance production: if the energy transfer of the neutrino to the bound nucleon is sufficiently high, it can excite the nucleon into one of its resonances (Δ or N^*), which subsequently decays producing e.g. nucleon and a pion

$$\nu_\mu + \mathrm{n} \rightarrow \mu^- + \Delta^+$$
$$\hookrightarrow \mathrm{p} + \pi^0 \text{ (or } \mathrm{n}' + \pi^+).$$

- DIS - Deep inelastic scattering: the neutrino energy is high enough to break up the target nucleon, producing a range of particles in the final state, e.g.

$$\nu_\mu + \mathrm{n} \rightarrow \mu^- + X.$$

The examples mentioned above are CC events, i.e. the boson exchanged between the neutrino and the nucleon is the charged boson W^+. For CCQE interactions, only neutrons are subject to interaction with the W^+ boson. For antineutrino scattering interactions, the negatively charged boson W^- is exchanged, and only the protons in the nucleus are subject to the reaction. For a CCQE antineutrino event the reaction is

$$\overline{\nu}_\mu + \mathrm{p} \rightarrow \mu^+ + \mathrm{n}.$$

A second type of neutrino reactions are weak neutral-current (WNC or NC) interactions. This implies that a neutral boson is exchanged, the Z^0. In this case the flavor of the nucleon remains unchanged and protons and neutrons both are subject to the interaction,

$$\nu_\mu + \mathrm{p} \rightarrow \nu'_\mu + \mathrm{p}',$$

$$\nu_\mu + \mathrm{n} \rightarrow \nu'_\mu + \mathrm{n}'.$$

Throughout this thesis, we will only consider CC interactions, but the formalism can in principle easily be extended to WNC interactions. Further, we will always consider muon neutrinos as incoming neutrinos, mainly because the neutrino flux of the accelerator-based experiments primarily consists of this type of neutrinos.

Finally, because of the similarities between the uncharged leptons (neutrinos) and the charged leptons, we will often compare with electron scattering interactions. Therefore we introduce the notation l which refers to the incoming lepton and l' for the lepton in the final state. The interacting nucleon is denoted by N and the nucleon in the final state by N'. Using this notation, a general electromagnetic (em) or weak interaction with a single nucleon is written as

$$l + N \rightarrow l' + N'.$$

An unspecified boson, which can either be a γ for electromagnetic interactions, or a $W^\pm$ for weak interactions, will be denoted by X throughout this work.

The cross section displayed in Fig. 1.7 is given as a function of ϵ_ν. However, from a theoretical point of view, the neutrino energy is not the most interesting quantity. The important variables are the energy (ω) and momentum transfer ($\boldsymbol{q}$) from the neutrino to the nuclear system. Throughout this work we focus our attention to energy transfers ranging from 10s of MeV to roughly 1 GeV.

The red curve in Fig. 1.8 sketches the response of a nucleon to a leptonic probe. For lepton scattering on a nucleon, the elastic peak occurs when the Bjorken variable $x_B = Q^2/(2m_N\,\omega) = 1$, with m_N the mass of the nucleon. The next peak, corresponding with the Δ resonance lies around 300 MeV to the right, which is the energy necessary for the creation of a Δ resonance. The subsequent peak is produced by a heavier nucleon resonance.

In most detectors, the target material consists of nuclei such as ^{12}C, ^{16}O, ^{40}Ar or ^{56}Fe, or molecules such as CH_2 and C_8H_8, and not of hydrogen nuclei. This implies that the nucleon which interacts with the neutrino, is bound inside the nucleus and nuclear effects will play a major role in the calculation of neutrino-nucleus cross sections. The response of the nucleus to a leptonic interaction is displayed by the blue curve in Fig. 1.8. When a lepton scatters off the nucleus as a whole, via a NC interaction, it gives rise to the coherent elastic scattering peak, and this peak is located at $Q^2/(2M_A\,\omega)$, with M_A the mass of the nucleus.

If the lepton scatters off a single nucleon, bound inside the nucleus, this nucleon can be emitted from the nucleus, leaving the residual nucleus in a one-particle one-hole ($1p1h$) state. This is a genuine QE event. We write this one-nucleon ($1N$) knockout interaction as

$$l + A \rightarrow l' + (A-1)^* + N,$$

where the target nucleus and the residual nuclear system are represented by their mass numbers A and $A-1$. If the nucleon emitted from the nucleus A is detected in coincidence with the final state lepton, this is called an exclusive $1N$ knockout cross section, denoted by $A(l, l'N)$. When only the lepton in the final state is detected, this is an inclusive cross section $A(l, l')$. For bound nucleons, the QE peak is shifted slightly to the right of $x_B = 1$, the size of the shift is related to the binding energy of the nucleons. The broadening of the

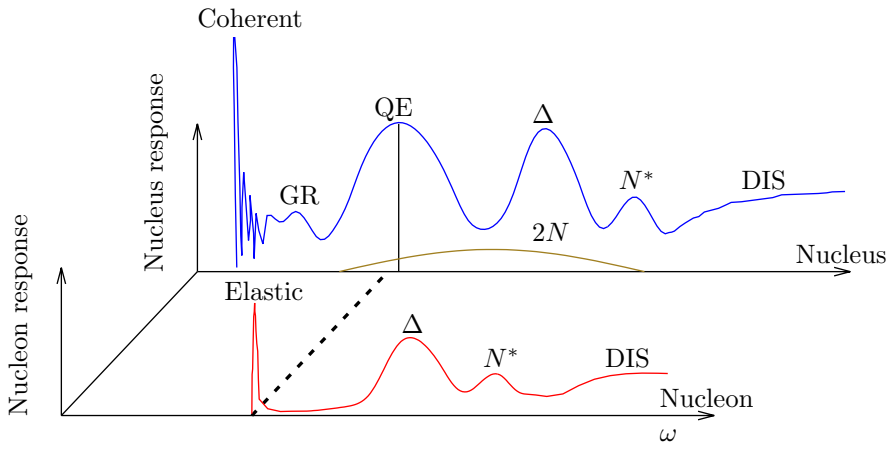

Figure 1.8: Schematic nucleon and nucleus responses to a leptonic probe.

QE peak for nuclei compared to the elastic peak for lepton-nucleon scattering is due to the Fermi motion of the nucleons.

Between the coherent and the QE peak lies the giant resonance (GR) region. These excitations occur when the neutrino interacts with a single nucleon, but due to long-range nuclear correlations, the energy transfer is shared among the nuclear constituents and the nucleus undergoes a collective excitation.

A second type of multinucleon effect arises when the neutrino interacts with a pair of correlated nucleons in the target, causing both of them to be knocked out of the nucleus, resulting in a two-particle two-hole ($2p2h$) final state. These two-nucleon ($2N$) knockout interactions are one of the main topics of this work. Adopting the same conventions as before, we denote the $2N$ knockout reactions by

$$l + A \to l' + (A-2)^* + N_a + N_b,$$

where N_a and N_b are the two emitted nucleons. When both emitted nucleons are detected together with the lepton in the final state, the process is called an exclusive $2N$ knockout cross section, denoted as $A(l, l' N_a N_b)$. If only one of the two of the emitted nucleons is detected, we call this a semi-exclusive $2N$ knockout event $A(l, l' N_a)$. The case when only the final state lepton is detected is an inclusive $2N$ knockout cross section. Throughout this work, we discuss two effects which cause nucleons to appear in pairs: short-range correlations and meson-exchange currents. We stress that these two-body effects can influence the $1N$ knockout cross section as well.

Experiments often analyze CC neutrino interaction data by only considering the lepton in the final state, meaning that inclusive cross sections are studied. The MiniBooNE experiment, for example, used a Cherenkov-type detector, and they only used the final state muon for CC events.

In a situation like that, it is hard to distinguish $2N$-knockout events from genuine QE events discussed above, where a single nucleon is emitted from the nucleus. Thus, the measured cross section will consists of a sum of $1N$ and $2N$ (and eventually $3N$ etc.) knockout cross sections. This led to some confusion between the experimental and theoretical community,

as both were using a different definition for the QE cross section. Therefore, the term quasielastic-like was introduced, which includes real QE events and events that mimic the signature of a QE event in the detector, such as $2N$ knockout events. Another solution was to define the data better, e.g. the CC0π data includes neutrino scattering events where one muon and no pions were detected.

One of the tasks of this thesis is to calculate the contribution of these $2N$ knockout events to the inclusive QE-like cross section. The relative effect of these $2N$ knockout events to the QE-like cross section will be largest in the so-called dip region: lying between the QE peak and the Δ peak, as shown schematically in Fig. 1.8.

Probing the axial structure of the nucleon

For the neutrino oscillation experiments, neutrino-nucleus cross sections are a tool to measure the number of neutrinos passing through the detector. From the point of view of a nuclear physicist, neutrino-nucleus scattering processes are an interesting tool to study the weak response of nuclei and the axial structure of nucleons.

Experimentally, the majority of the information on the nuclear response was obtained with the aid of scattering processes. Hadron probes yield the largest scattering cross sections, but their internal structure, and the fact that they interact via the strong force, complicates the interpretation of the data. Distinguishing between the effects arising from the internal structure of the hadrons and from the structure of the nucleus is very difficult. Leptonic probes, on the other hand, have a smaller interaction probability, but have no internal structure, which facilitates the interpretation of lepton-nucleus scattering data. Because they are easily produced, electrons have been used extensively to study the nuclear structure. Due to the heavy mass of the exchanged bosons, the interaction probability of neutrinos is several orders of magnitude smaller than for electrons. However, the advent of high-intensity neutrino beams, at Fermilab and J-PARC for example, provides an opportunity to use neutrinos as a tool to study the nuclear response. Due to their intrinsic polarization, neutrinos provide a unique way to study the axial response of nuclei.

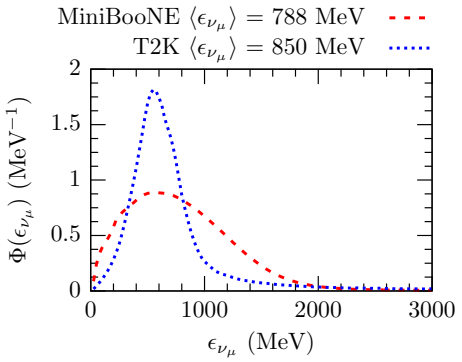

Figure 1.9: The normalized muon neutrino flux $\Phi(\epsilon_{\nu_\mu})$ for MiniBooNE and T2K.

The main disadvantage of using neutrinos as a probe, is that these high-intensity neutrino beams do not provide mono-energetic neutrinos. The mechanism described in Fig. 1.5

produces neutrinos with a broad range of energies. Understanding the neutrino flux is one of the major issues when studying neutrino-nucleus interactions.

The fluxes are predicted using simulations that consider the whole neutrino production process. Fig. 1.9 shows the predicted muon neutrino flux for MiniBooNE and for the T2K near-detector. In both cases, the peak of the flux lies around $\epsilon_{\nu_\mu} = 750$ MeV and the majority of the neutrinos have an energy $\epsilon_{\nu_\mu} < 2$ GeV. In this interval, the QE channel, the $2N$ knockout processes and the resonance productions provide the majority of the cross section strength.

A consequence of the broad neutrino energy distribution is that when an interaction with a nucleon in the detector occurs, the energy of the neutrino that interacted is unknown. One can only make an educated guess of the interaction process that happened based on the particles in the final state. This complicates the interpretation of the experimental data. To make a comparison between a theoretical model and experimental results, one has to integrate over the neutrino flux.

Modeling the nucleus

The calculation of neutrino-nucleus cross sections is an interesting but challenging problem. Knowledge of the weak and strong nuclear forces is necessary to tackle the problem at hand, but most of the difficulties are related to the description of the nuclear system. The nucleus is made out of quarks which are bound by the exchange of gluons, making the nucleus a complicated many-body system. The fundamental theory of the strong interaction, quantum chromodynamics, falls short in the description of nuclei. Fortunately, as this work focuses on relatively low energy transfers (up to ≈ 1 GeV), it is possible to describe the nucleus using effective degrees of freedom: the protons and neutrons. The finite sizes of the different particles are accounted for by using form factors, regularizing the coupling strengths at higher energy and momentum transfers.

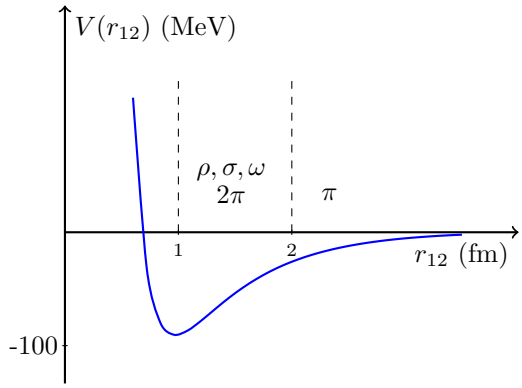

Figure 1.10: The radial dependence of the nucleon-nucleon potential $V(r_{12})$.

For the description of nuclei using these effective degrees of freedom, several approaches are possible, many of them are based on an independent-particle model (IPM) picture [22,23]. This approach is justified by the properties of the nucleon-nucleon (NN) interaction,

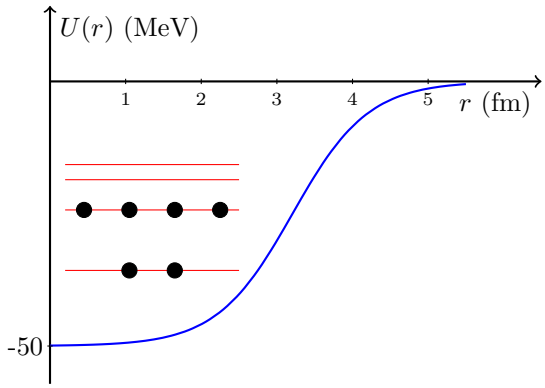

Figure 1.11: A shell model picture used to describe the nucleus. $U(r)$ is the MF-potential and the red horizontal lines are the energy levels.

Fig. 1.10. The NN interaction has a finite range: it vanishes at large internucleon distances. At medium range it is attractive and at very short distances it becomes repulsive, which is related to Pauli repulsion. This results in a large mean free path for the nucleons inside the nucleus, justifying the IPM picture.

In a global Fermi-gas model, the nucleons are considered to move freely within the nuclear volume. The protons and neutrons are described by plane waves and have a momentum smaller than the Fermi momentum p_F. In a local Fermi-gas, the Fermi momentum depends on the distance from the center of the nucleus r.

Another way of modeling the nucleus is a mean-field (MF) approach. The main idea is that the nucleons move independently in the potential well of the nucleus, generated by the nucleons themselves. The practical difficulty lies in the description of this potential. The different choices of the potential can be roughly categorized in two distinct groups. The first group relies on a parameterized or phenomenological MF-potential, the Woods-Saxon and harmonic-oscillator potentials are the most widely used. The Woods-Saxon potential is a simple parameterization of the nuclear potential that approximates the real potential for heavy nuclei. The harmonic-oscillator potential allows for analytical solutions of the single-particle wave functions.

In the second group, the determination of the MF-potential happens iteratively via a Hartree-Fock (HF) calculation, using an effective nucleon-nucleon interaction. The trouble in this method is not the determination of the nuclear potential, but the description of the NN interaction, which is not known analytically. Therefore, effective NN interactions are used which are fitted to data to reproduce experimentally measured quantities such as nuclear binding energy, etc. In these MF-potentials, the nucleons occupy single-particle energy levels, as shown in Fig. 1.11.

The IPMs also have some limitations. By definition, all nucleons move independently from each other in the nuclear potential well. This means they can approach each other infinitely close, which should be impossible due to the repulsive behavior of the NN interaction. We will correct the IPM for this pathology by introducing short-range correlations (SRCs) in an effective way.

Another missing ingredient is related to the coupling between lepton and the nucleus. In the

impulse approximation (IA), the residual interactions between the nucleons in the nucleus are ignored during the collision. The nuclear current that is used to describe the coupling of the boson with the nucleus is approximated by a sum one-body currents. As displayed in Fig. 1.10, the NN interaction is understood effectively via the exchange of virtual light mesons such as the π, ρ and ω meson. This suggests that the leptons can couple to these virtual mesons as well. Therefore, meson-exchange currents (MECs) are introduced, to describe a pair of nucleons that are correlated by the exchange of a virtual π.

To finalize the overview of nuclear models, we mention ab-initio approaches. These calculations start from the first principles of quantum mechanics. Using the same effective degrees of freedom as before: the protons and neutrons, these models in principle include all nuclear effects by treating the protons and neutrons as particles which are coupled via a realistic NN force in a multinucleon model. However, these calculations are computationally too demanding that approximations have to be made to make them feasible, e.g. one has to revert to nonrelativistic calculations and a variational Monte Carlo approach.

Theoretical neutrino-nucleus scattering calculations

Several theoretical models have been developed to study neutrino-nucleus (νA) and anti-neutrino-nucleus ($\overline{\nu} A$) cross sections and have been compared with experimental data [21,24–28]. The necessity of multinucleon effects in the description of νA cross sections was first pointed out by Martini *et al.* [29]. This drew the attention of several other groups who aimed at reproducing neutrino-scattering data. A complete theoretical model should in principle include short-range and long-range nuclear correlations, MECs and final-state interactions (FSIs). The FSIs include all interactions that nucleons undergo when they propagate out of the residual nuclear system.

The microscopic models of Martini *et al.* [29–32] and Nieves *et al.* [33–35] were the first able to reproduce neutrino inclusive QE scattering data by including the contribution of $2p2h$ excitations. Both are based on the Fermi gas, which is the simplest IPM. Nuclear finite-size effects are taken into account via a local density approximation and a semi-classical expansion of the response function, but the shell structure of the nucleus is not taken into account. Long-range correlations are taken into account in a random phase approximation (RPA) approach. In the $2p2h$ sector, both approaches consider two-body MEC contributions. The nucleon-nucleon SRCs are included by considering an additional two-body current, the correlation current. With the introduction of the correlation contributions, the interference between correlations and MECs naturally appears.

In the superscaling approach (SuSA), an analysis of electron scattering results is used to predict νA cross sections [36,37]. The effects of long and short-range correlations and MECs in the $1p1h$ sector are effectively included via the phenomenological superscaling function. In [38,39], the SuSA model is combined with MECs in the $2p2h$ sector, by using a parameterization of the relativistic microscopic calculations by De Pace *et al.* [40] and Ruiz-Simo *et al.* [41]. The nuclear correlations and correlation-MEC interference terms are absent in the $2p2h$ channel.

A relativistic Fermi gas (RFG)-based model that accounts for MECs, correlations and interference in the $1p1h$ and $2p2h$ sector for electron-nucleus (eA) scattering has been developed by Amaro *et al.* [42,43], which was recently extended towards νA scattering [41].

In the ab-initio calculations on ^{12}C by Lovato *et al.* [44,45], nuclear correlations and MEC contributions are inherently taken into account. The authors conclude that the presence of two-body currents significantly influences the nuclear responses and sum rules, even at QE kinematics.

Recent work on electron scattering by Benhar *et al.* [46] and Rocco *et al.* [47] have generalized the formalism based on a factorization ansatz and nuclear spectral functions to treat transition matrix elements involving two-body currents.

The semi-phenomenological GiBUU model [48] considers bound nucleons in a density-dependent MF potential, and multinucleon effects are fitted to data. FSIs are accounted for by using a hadron transport model for the propagation of the nucleons in the nucleus, which accounts for elastic and inelastic collisions with other nucleons.

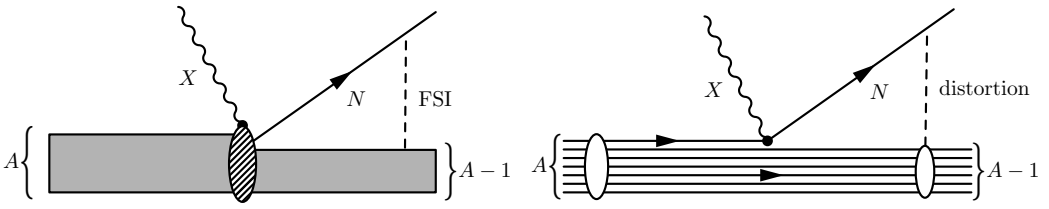

(a) Full model **(b)** Spectator approach in an IPM within the IA

Figure 1.12: Graphical representation of the $1N$ knockout model.

The model described in this thesis has been developed in Ghent and has a long history in the description of eA and νA cross sections. An IPM picture is used for the description of the nuclei, where it is assumed that the protons and neutrons move in a MF potential. An effective Skyrme-type NN force is used [49] for the determination of the MF potential, using a HF calculation. The used effective interaction was fitted to accurately describe the ground-state and low-lying excitations of nuclei. The particles in the continuum are calculated using the same potential, guaranteeing that the initial and final nuclear states are orthogonal. These HF nuclear wave functions are used to calculate one-nucleon emission processes.

How this is modeled is displayed graphically in Fig. 1.12. The left panel shows the total picture, where a single nucleon is emitted from an A-body system, leaving an $A-1$ system behind. The right panel gives a simplified picture of how this is calculated throughout this work. The nucleus is described using an IPM, the MF potential is depicted by the white oval and each horizontal line depicts a nucleon in the MF potential. The nucleon subject to the electromagnetic or weak interaction is the one that becomes asymptotically free, but it is still under the influence of the MF potential of the $A-1$ system (dashed line). This is the so-called spectator approach (SA).

In the $1N$ knockout calculations, long-range correlations in the nucleus were accounted for in a continuum random phase approximation (CRPA). Photo-induced (γ, N) and electron-induced $(e, e'N)$ single-nucleon knockout interactions from ^{16}O were studied in [50–52]. These cross section calculations were extended to NC and CC neutrino-induced interactions at energies relevant for supernova neutrinos in Refs. [53–55]. The CC neutrino-nucleus cross

sections in the CRPA approach were integrated over the neutrino flux and compared with experimental data from MiniBooNE and T2K in [56–59].

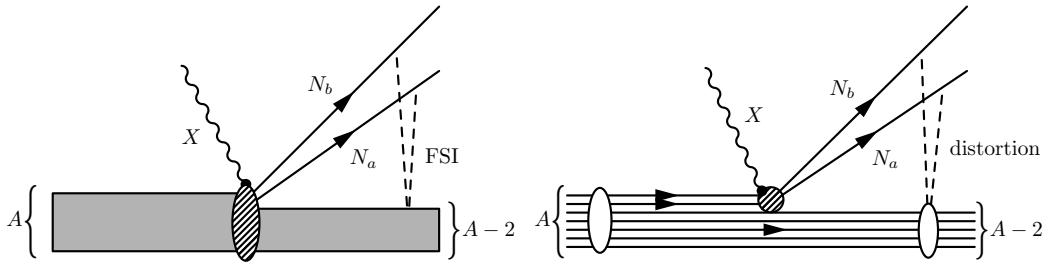

(a) Full model **(b)** An IPM extended with two-body currents

Figure 1.13: Graphical representation of the $2N$ knockout model.

The approach used for the $2N$ knockout calculations is shown schematically in Fig. 1.13. The left panel shows the complete picture where a nucleon pair is emitted from an A-body system, leaving an $A-2$ system behind. The right panel shows how this is modeled in this work. The nuclear wave functions are calculated using the same MF potential. The pair of correlated nucleons subject to the incoming lepton is described by a two-body current (dashed circle). The two-nucleon version of the spectator approach is used, which means that the pair of nucleons that interacted with the boson are the two nucleons which are emitted from the nucleus. Both nucleons are still subject to the MF potential of the $A-2$ system. In Fig. 1.14, it is shown graphically how two-body currents influence $1N$ knockout cross sections: only one nucleon of the two-body current is emitted from the nucleus.

Two-nucleon knockout cross sections were initially studied for photo-induced (γ, pn) and (γ, pp) interactions in [60], where only MECs were considered. Later central and spin-dependent correlations were introduced and electron-induced $(e, e'\mathrm{pn})$ and $(e, e'\mathrm{pp})$ interactions were considered [61,62]. The model describes exclusive $^{16}\mathrm{O}(e, e'\mathrm{pp})$ [63,64], semi-exclusive $^{16}\mathrm{O}(e, e'\mathrm{p})$ [65,66] as well as inclusive $^{12}\mathrm{C}(e, e')$ and $^{40}\mathrm{Ca}(e, e')$ [67] scattering with a satisfactory accuracy. This thesis is an extension of the model for electron-scattering interactions described above, accounting for two-body currents in neutrino-induced $1N$ and $2N$ knockout reactions.

Several groups studied these two-body effects in inclusive and exclusive eA interactions. Calculations by Alberico *et al.* included MECs, Δ-currents and correlation currents in a Fermi gas framework for inclusive [68–70], as well as exclusive [71] electron scattering interactions. Similar calculations including two-body currents were performed in a Fermi gas model by Gil *et al.* [72,73]. The calculations by Alberico and Gil lie at the basis of the inclusive neutrino scattering models by Martini and Nieves respectively. Similarly, the $2p2h$ contributions of Refs. [38,39,41,74] are based on the relativistic model of De Pace *et al.* [40].

Work by Giusti *et al.* [75,76] and Anguiano *et al.* [77,78], included MECs, Δ-currents and SRCs in a model which resembles the model presented here, for exclusive electromagnetic $2N$ knockout interactions. In both models, distortion effects of the final-state nucleons were accounted for by using an optical potential. So far, these groups have not presented results for weak interactions.

Exclusive $2N$ knockout effects for neutrino interactions have received little theoretical attention as of date. However, the collaboration around the neutrino event generator GiBUU [48]

and NuWro [79], investigated these exclusive events for neutrino interactions by simulating the outgoing nucleons. In the GiBUU model, the $2p2h$ effects are fitted to experimental data, and the nucleons are propagated through the nucleus via a hadron transport model. In the NuWro model, inclusive $2p2h$ cross section calculations are used for the strength of the effect, and the struck MEC pair is emitted from the nucleus via a nuclear cascade calculation.

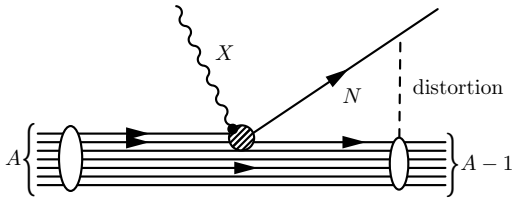

Figure 1.14: Graphical representation of the influence of two-body currents on $1N$ knockout.

Outline

The exclusive differential cross section is calculated in Chapter 2 for $1N$ and $2N$ knockout reactions and the general framework for the partial wave expansion used in the calculations is explained. The nuclear one-body currents in the IA are also described. The transition matrix elements are discussed in detail in Chapter 3 and Chapter 4, for $1p1h$ and $2p2h$ final states respectively, and it is shown how the wave functions of the emitted nucleons are expanded as a function of the continuum eigenstates.

In Chapter 3 the exclusive and inclusive $1N$ knockout cross sections are studied first. Then some numerical results for inclusive $1N$ knockout in the IA are shown for electron and neutrino interactions. In Chapter 4 we start from the exclusive $2N$ knockout cross section, and discuss some general features. This information is then used to calculate the semi-exclusive and inclusive $2N$ knockout cross sections by integrating over the phase space of one or both of the emitted nucleons.

The framework used to account for SRCs is explained in Chapter 5 and a systematic study of the influence of the correlations on the $1p1h$ and $2p2h$ calculations is presented. Further, theoretical predictions are shown for kinematic settings relevant for accelerator-based experiments. The MECs used in this work are discussed in Chapter 6, where they are compared with other numerical calculations found in literature. Numerical results for exclusive, semi-exclusive and inclusive cross sections are presented.

Finally, in Chapter 7 the results of the SRCs and MECs are combined and compared with experimental neutrino scattering data.

Supplementary material is provided in the appendices where the conventions used throughout this work are given and detailed calculations of the matrix elements are summarized.

References

[1] K. Winter, *Neutrino physics*, Cambridge Monographs on Particle Physics, Nuclear Physics and Cosmology (2000).

[2] E. Fermi, Z. Phys. **88**, 161 (1934).

[3] `http://www.nobelprize.org/nobel_prizes/physics/laureates/2015`.

[4] C. Cowan, F. Reines, F. Harrison, *et al.* Science **124**, 103 (1956).

[5] G. Danby, J. M. Gaillard, K. A. Goulianos, *et al.* Phys. Rev. Lett. **9**, 36 (1962).

[6] DONUT collaboration, K. Kodama *et al.* Phys. Lett. **B504**, 218 (2001).

[7] R. Davis, Jr., D. S. Harmer, and K. C. Hoffman, Phys. Rev. Lett. **20**, 1205 (1968).

[8] J. N. Bahcall and R. Davis, Science **191**, 264 (1976).

[9] B. Pontecorvo, Sov. Phys. JETP **6**, 429 (1957), [Zh. Eksp. Teor. Fiz. **33**, 549 (1957)].

[10] B. Pontecorvo, Sov. Phys. JETP **26**, 984 (1968), [Zh. Eksp. Teor. Fiz. **53**, 1717 (1967)].

[11] Super-Kamiokande collaboration, Y. Fukuda *et al.* Phys. Rev. Lett. **81**, 1562 (1998).

[12] SNO collaboration, Q. Ahmad *et al.* Phys. Rev. Lett. **87**, 071301 (2001).

[13] SNO collaboration, Q. Ahmad *et al.* Phys. Rev. Lett. **89**, 011301 (2002).

[14] `http://www-boone.fnal.gov`.

[15] `http://www.t2k-experiment.org`.

[16] `http://minerva.fnal.gov`.

[17] `http://www-nova.fnal.gov`.

[18] `http://t962.fnal.gov`.

[19] `http://www-microboone.fnal.gov`.

[20] `http://www.dunescience.org`.

[21] J. Formaggio and G. Zeller, Rev. Mod. Phys. **84**, 1307 (2012).

[22] M. G. Mayer, Phys. Rev. **74**, 235 (1948).

[23] O. Haxel, J. H. D. Jensen, and H. E. Suess, Phys. Rev. **75**, 1766 (1949).

[24] H. Gallagher, G. Garvey, and G. Zeller, Ann. Rev. Nucl. Part. Sci. **61**, 355 (2011).

[25] J. Morfin, J. Nieves, and J. Sobczyk, Adv. High Energy Phys. **2012**, 934597 (2012).

[26] L. Alvarez-Ruso, Y. Hayato, and J. Nieves, New J. Phys. **16**, 075015 (2014).

[27] U. Mosel, Ann. Rev. Nucl. Part. Sci. **66**, 171 (2016).

[28] T. Katori and M. Martini, (2016), arXiv:1611.07770.

[29] M. Martini, M. Ericson, G. Chanfray, *et al.* Phys. Rev. **C80**, 065501 (2009).

[30] M. Martini, M. Ericson, G. Chanfray, *et al.* Phys. Rev. **C81**, 045502 (2010).

[31] M. Martini, M. Ericson, and G. Chanfray, Phys. Rev. **C84**, 055502 (2011).

[32] M. Martini and M. Ericson, Phys. Rev. **C87**, 065501 (2013).

[33] J. Nieves, I. Ruiz Simo, and M. Vicente Vacas, Phys. Lett. **B707**, 72 (2012).

[34] J. Nieves, I. Ruiz Simo, and M. Vicente Vacas, Phys. Rev. **C83**, 045501 (2011).

[35] J. Nieves, I. Ruiz Simo, and M. Vicente Vacas, Phys. Lett. **B721**, 90 (2013).

[36] J. Amaro, M. Barbaro, J. Caballero, *et al.* Phys. Rev. **C71**, 015501 (2005).

[37] J. Amaro, M. Barbaro, J. Caballero, *et al.* Phys. Lett. **B696**, 151 (2011).

[38] G. Megias, T. Donnelly, O. Moreno, *et al.* Phys. Rev. **D91**, 073004 (2015).

[39] G. D. Megias, J. E. Amaro, M. B. Barbaro, *et al.* Phys. Rev. **D94**, 093004 (2016).

[40] A. De Pace, M. Nardi, W. Alberico, *et al.* Nucl. Phys. **A726**, 303 (2003).

[41] I. Ruiz Simo, J. Amaro, M. Barbaro, *et al.* (2016), arXiv:1604.08426.

[42] J. Amaro, M. Barbaro, J. Caballero, *et al.* Phys. Rept. **368**, 317 (2002).

[43] J. Amaro, C. Maieron, M. Barbaro, *et al.* Phys. Rev. **C82**, 044601 (2010).

[44] A. Lovato, S. Gandolfi, J. Carlson, *et al.* Phys. Rev. Lett. **112**, 182502 (2014).

[45] A. Lovato, S. Gandolfi, J. Carlson, *et al.* Phys. Rev. **C91**, 062501 (2015).

[46] O. Benhar, A. Lovato, and N. Rocco, Phys. Rev. **C92**, 024602 (2015).

[47] N. Rocco, A. Lovato, and O. Benhar, Phys. Rev. Lett. **116**, 192501 (2016).

[48] O. Lalakulich, K. Gallmeister, and U. Mosel, Phys. Rev. **C86**, 014614 (2012).

[49] M. Waroquier, J. Ryckebusch, J. Moreau, *et al.* Phys. Rept. **148**, 249 (1987).

[50] J. Ryckebusch, *Photon and electron-induced one-nucleon emission within a selfconsistent* HF-RPA *model*, PhD thesis (Ghent University, 1988).

[51] J. Ryckebusch, M. Waroquier, K. Heyde, *et al.* Nucl. Phys. **A476**, 237 (1988).

[52] J. Ryckebusch, K. Heyde, D. Van Neck, *et al.* Nucl. Phys. **A503**, 694 (1989).

[53] N. Jachowicz, *Many-body description of neutrino-nucleus interactions*, PhD thesis (Ghent University, 2000).

[54] N. Jachowicz, S. Rombouts, K. Heyde, *et al.* Phys. Rev. **C59**, 3246 (1999).

[55] N. Jachowicz, K. Heyde, J. Ryckebusch, *et al.* Phys. Rev. **C65**, 025501 (2002).

[56] V. Pandey, *Quasielastic electroweak scattering cross sections in kinematics relevant for accelerator-based neutrino-oscillation experiments*, PhD thesis (Ghent University, 2016).

[57] V. Pandey, N. Jachowicz, J. Ryckebusch, *et al.* Phys. Rev. **C89**, 024601 (2014).

[58] V. Pandey, N. Jachowicz, T. Van Cuyck, *et al.* Phys. Rev. **C92**, 024606 (2015).

[59] V. Pandey, N. Jachowicz, M. Martini, *et al.* Phys. Rev. **C94**, 054609 (2016).

[60] J. Ryckebusch, M. Vanderhaeghen, L. Machenil, *et al.* Nucl. Phys. **A568**, 828 (1994).

[61] J. Ryckebusch, V. Van der Sluys, K. Heyde, *et al.* Nucl. Phys. **A624**, 581 (1997).

[62] S. Janssen, J. Ryckebusch, W. Van Nespen, *et al.* Nucl. Phys. **A672**, 285 (2000).

[63] R. Starink *et al.* Phys. Lett. **B474**, 33 (2000).

[64] J. Ryckebusch and W. Van Nespen, Eur. Phys. J. **A20**, 435 (2004).

[65] Jefferson Lab Hall A collaboration, K. Fissum *et al.* Phys. Rev. **C70**, 034606 (2004).

[66] M. Iodice, E. Cisbani, R. De Leo, *et al.* Phys. Lett. **B653**, 392 (2007).

[67] V. Van der Sluys, J. Ryckebusch, and M. Waroquier, Phys. Rev. **C49**, 2695 (1994).

[68] W. Alberico, M. Ericson, and A. Molinari, Nucl. Phys. **A379**, 429 (1982).

[69] W. Alberico, M. Ericson, and A. Molinari, Ann. Phys. **154**, 356 (1984).

[70] W. Alberico, T. Donnelly, and A. Molinari, Nucl. Phys. **A512**, 541 (1990).

[71] W. Alberico, G. Chanfray, J. Delorme, *et al.* Nucl. Phys. **A634**, 233 (1998).

[72] A. Gil, J. Nieves, and E. Oset, Nucl. Phys. **A627**, 543 (1997).

[73] A. Gil, J. Nieves, and E. Oset, Nucl. Phys. **A627**, 599 (1997).
[74] I. Ruiz Simo, J. Amaro, M. Barbaro, *et al.* Phys. Lett. **B762**, 124 (2016).
[75] C. Giusti, F. Pacati, K. Allaart, *et al.* Phys. Rev. **C57**, 1691 (1998).
[76] C. Giusti, H. Muther, F. Pacati, *et al.* Phys. Rev. **C60**, 054608 (1999).
[77] M. Anguiano, G. Co', A. Lallena, *et al.* Ann. Phys. **296**, 235 (2002).
[78] M. Anguiano, G. Co', and A. M. Lallena, J. Phys. **G29**, 1119 (2003).
[79] J. Sobczyk, Phys. Rev. **C86**, 015504 (2012).

Chapter 2

Differential cross sections

A cross section, usually denoted by σ, quantifies the probability that an incident probe interacts with a target particle. This quantity depends strongly on the nature of the particles and physical quantities such as the energy of the incident particle. The differential cross section, e.g. $\mathrm{d}\sigma/\mathrm{d}\Omega$, is the probability for an interaction for which the scattered particle is emitted in a certain direction, denoted by its solid angle Ω. In this chapter, we calculate the exclusive differential cross sections for electron-induced and muon-neutrino induced one-nucleon ($1N$) and two-nucleon ($2N$) knockout interactions. We will develop a cross section formula for interactions where the residual nuclear system is left in the ground state or a low-lying excited state.

In the derivation of the differential cross section, we follow the approach used by a.o. Donnelly and Raskin [1–3] for polarized electron scattering and neutrino scattering. The expressions for the differential cross sections obtained in this chapter can be compared with e.g. [4] and [5], where similar expressions for the differential cross section can be found.

2.1 Differential $1N$ knockout cross section

In exclusive $1N$ knockout interactions, an incoming lepton l scatters off a target nucleus, knocking out a single nucleon N. The final state lepton l' is observed in coincidence with the emitted nucleon. In this section, we develop the differential cross section for exclusive electron-induced and charged-current (CC) muon-neutrino induced $1N$ knockout reactions $A(l, l'N)$

$$e + A \to e' + (A-1)^* + N, \tag{2.1}$$

$$\nu_\mu + A \to \mu^- + (A-1)^* + \mathrm{p}, \tag{2.2}$$

$$\overline{\nu}_\mu + A \to \mu^+ + (A-1)^* + \mathrm{n}. \tag{2.3}$$

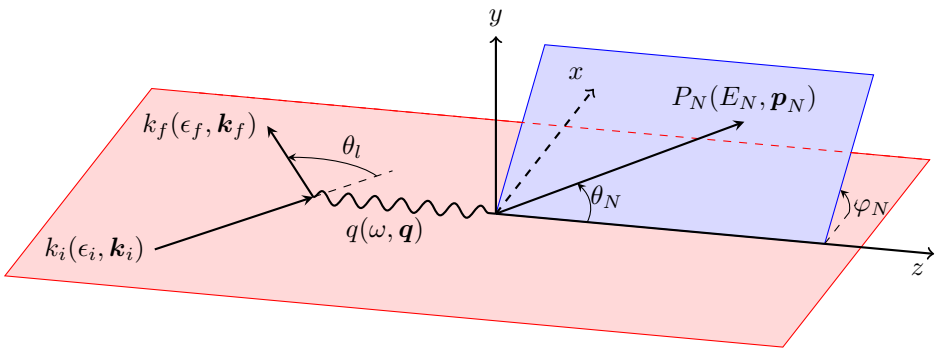

Figure 2.1: The definition of the angular variables used in the $1N$ knockout calculations.

The target nucleus is represented by its mass number A. The residual system with $A-1$ nucleons is left in a one-hole state, its excitation energy doesn't exceed a few 10s of MeV. In the derivation of the cross section, we adopt the following conventions: the incoming lepton is denoted by $k_i = (\epsilon_i, \boldsymbol{k}_i)$ and the corresponding lepton mass is given by m_i, the final state lepton is denoted by $k_f = (\epsilon_f, \boldsymbol{k}_f)$ and has mass m_f. The initial nucleus is represented by $P_A = (E_A, \boldsymbol{p}_A)$ and the residual $A-1$ system by $P_{A-1} = (E_{A-1}, \boldsymbol{p}_{A-1})$. The outgoing nucleon is denoted as $P_N = (E_N, \boldsymbol{p}_N)$ and has mass m_N. Working in the lab frame, the four-vector of the initial nucleus can be written as $P_A = (M_A, 0)$. The four-momentum transfer $q^\mu = (\omega, \boldsymbol{q})$ is defined as

$$\omega = \epsilon_i - \epsilon_f, \qquad \boldsymbol{q} = \boldsymbol{k}_i - \boldsymbol{k}_f, \tag{2.4}$$

with $Q^2 = \boldsymbol{q}^2 - \omega^2$. The boson exchanged between the lepton and hadron current can be either a γ^* or a $W^\pm$, and is denoted as X unless otherwise specified. We adopt the convention that $\boldsymbol{q}$ is aligned along the z-axis and the scattering plane coincides with the xz plane. The scattering angle of the lepton is θ_l. Fig. 2.1 clarifies the adopted conventions. Although CC ν_μ and $\overline{\nu}_\mu$ scattering are mentioned specifically, the derivations in this chapter are also valid for CC ν_e and ν_τ scattering, when the masses of the final state leptons e and τ are considered correctly.

To derive the expression for the differential cross section, we start with the general formula in the Bjorken and Drell convention [6]

$$\begin{aligned} \mathrm{d}\sigma = & \frac{m_i}{\epsilon_i}\frac{m_f}{\epsilon_f}\frac{\mathrm{d}\boldsymbol{k}_f}{(2\pi)^3}\frac{\mathrm{d}\boldsymbol{p}_N}{(2\pi)^3}\frac{\mathrm{d}\boldsymbol{p}_{A-1}}{(2\pi)^3} \\ & \times (2\pi)^4\delta^{(4)}\left(k_i + P_A - k_f - P_N - P_{A-1}\right)\overline{\sum_{if}}|\mathcal{M}_{fi}|^2, \end{aligned} \tag{2.5}$$

$$= \frac{m_i}{\epsilon_i}\frac{m_f}{\epsilon_f}\frac{1}{(2\pi)^5}\,\mathrm{d}\boldsymbol{k}_f\,\mathrm{d}\boldsymbol{p}_N\,\delta\left(\epsilon_i + M_A - \epsilon_f - E_N - E_{A-1}\right)\overline{\sum_{if}}|\mathcal{M}_{fi}|^2, \tag{2.6}$$

where we used four-momentum conservation to integrate over the phase space of the residual nucleus. The summation stands for a correct averaging and summation over initial and final states. The matrix element $\mathcal{M}_{fi}$ is a Lorentz scalar containing all the dynamics of the interaction, while the delta function ensures four-momentum conservation. The definition of the differential cross section in Bjorken and Drell, given in Eq. (A.45), is valid for scattering

of on-shell, massive, Dirac particles. In our model, the initial and final state leptons are considered as on-shell particles, however, the nucleons are bound states, described with MF wave functions.

The remaining delta function can now be exploited to integrate over the magnitude of the momentum of the outgoing nucleon p_N. We write the delta function as

$$\delta\left(\epsilon_i + M_A - \epsilon_f - \sqrt{p_N^2 + m_N^2} - \sqrt{\left(\boldsymbol{q} - \boldsymbol{p}_N\right)^2 + (M_{A-1}^*)^2}\right), \tag{2.7}$$

where we accounted for the excitation energy of the residual nucleus via $M_{A-1}^* = M_{A-1} + E^{exc}$. Now we can use the following property of the delta function

$$\int \mathrm{d}x\, \delta(a - f(x)) g(x) = \left[\frac{g(x)}{\left|\frac{\partial f}{\partial x}\right|}\right]_{f(x)=a}, \tag{2.8}$$

to integrate over p_N. This results in

$$\mathrm{d}\sigma = \frac{m_i}{\epsilon_i}\frac{m_f}{\epsilon_f}\frac{p_N E_N}{(2\pi)^5}\, f_{rec}^{-1}\, \mathrm{d}\boldsymbol{k}_f\, \mathrm{d}\Omega_N \overline{\sum_{if}} |\mathcal{M}_{fi}|^2, \tag{2.9}$$

where the recoil factor is defined as

$$f_{rec} = \left|1 + \frac{E_N}{E_{A-1}}\left(1 - \frac{\boldsymbol{p}_N \cdot \boldsymbol{q}}{p_N^2}\right)\right|. \tag{2.10}$$

In the ideal case where all the momentum is transferred to the outgoing nucleon, this factor tends to one.

The invariant matrix element $\mathcal{M}_{fi}$ can be calculated using the Feynman rules in momentum space. The diagrams corresponding with eA and CC νA scattering are given in Fig. 2.2, and the relevant coupling constants are shown. In this figure, the final nuclear system is represented by B and it can be either an $A-1$ system with a single outgoing nucleon, or an $A-2$ residual nucleus with two outgoing nucleons, etc. The propagator of a virtual photon is given by

$$P_{\mu\nu}^{\gamma} = \frac{i g_{\mu\nu}}{Q^2}, \tag{2.11}$$

and for the propagator of the massive $W^{\pm}$ bosons, the following approximation has been used

$$P_{\mu\nu}^{W} \approx \frac{i g_{\mu\nu}}{M_W^2}, \tag{2.12}$$

with M_W the mass of the bosons. These are valid approximations at the energy transfers studied in this work, corresponding with the QE peak and the dip region ($\omega \lesssim 1.5$ GeV), since the bosons have a mass of $M_W = 80$ GeV. Applying the Feynman rules, the expressions for the invariant matrix elements are

$$\mathcal{M}_{fi}^{\gamma} = -i\frac{e^2}{Q^2}\mathcal{J}_{\nu}^{\mathrm{lep}}(q)\mathcal{J}_{\mathrm{nuc}}^{\nu}(q), \tag{2.13}$$

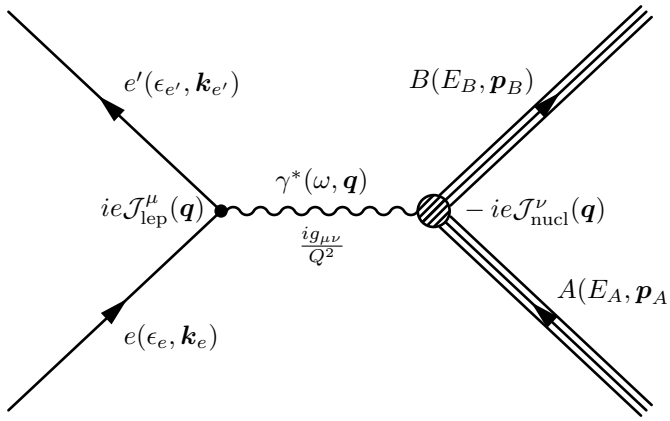

(a) eA scattering.

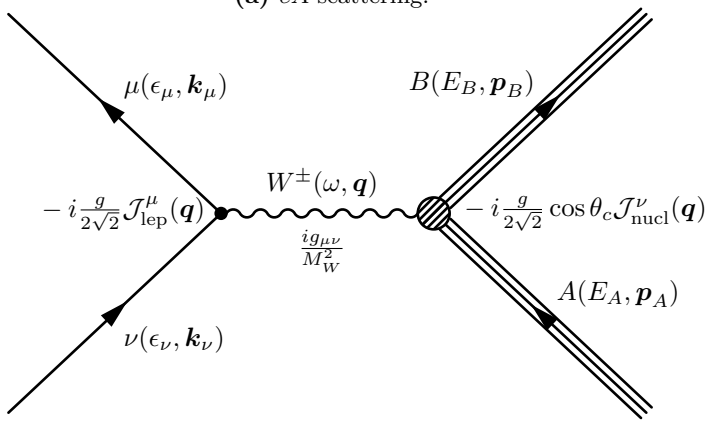

(b) CC νA scattering.

Figure 2.2: Feynman diagrams for lepton-nucleon scattering processes.

$$\mathcal{M}^W_{fi} = -i\frac{G_F}{\sqrt{2}}\cos\theta_c\,\mathcal{J}^{\text{lep}}_{\nu}(q)\mathcal{J}^{\nu}_{\text{nuc}}(q), \tag{2.14}$$

where θ_c is the Cabibbo angle. The relations between the electric charge e, the weak coupling constant g, M_W, the Weinberg angle θ_W, and the Fermi constant G_F are

$$\sin\theta_W = \frac{e}{g}, \qquad\qquad \frac{G_F}{\sqrt{2}} = \frac{g^2}{8M_W^2}. \tag{2.15}$$

The lepton and hadron currents are defined as

$$\mathcal{J}^{\text{lep}}_{\mu}(q) \equiv \overline{u}(k_f, s_f)\,\widehat{J}^{\text{lep}}_{\mu}\,u(k_i, s_i) = \overline{u}(k_f, s_f)\,\gamma_\mu(1 + h\gamma^5)\,u(k_i, s_i), \tag{2.16}$$

$$\mathcal{J}^{\text{nuc}}_{\mu}(q) \equiv \langle\,\Psi_f\,|\,\widehat{J}^{\text{nuc}}_{\mu}(\boldsymbol{q})\,|\,\Psi_i\,\rangle, \tag{2.17}$$

where we introduced the Dirac spinors $u(k_i, s_i)$ and $\overline{u}(k_f, s_f)$ for the incoming and scattered lepton. The $|\,\Psi_i\,\rangle$ and $|\,\Psi_f\,\rangle$ refer to the initial and final nuclear states and the operators $\widehat{J}^{\text{lep}}_{\mu}$ and $\widehat{J}^{\text{nuc}}_{\mu}(\boldsymbol{q})$ are the lepton and nuclear current operators in momentum space. The structure of the nuclear current operator will be discussed throughout this work.

The lepton current operator is known exactly from field theory. In the lepton current, $h = 0$ for (unpolarized) electron scattering and h equals $-(+)$ for neutrino (antineutrino) interactions, reflecting the $V - A$ structure of the weak interaction. By convention, the factor $1/2$ of the spin-projection operator $(1 + h\gamma^5)/2$ is absorbed in the weak coupling constant.

For the nuclear current, we rely on the rules corresponding to the Feynman rules but for nuclear physics [7–9]. These nuclear current matrix elements are the building blocks of the nuclear responses and will be at the center of our modeling efforts. They contain all the dynamical information of the electromagnetic or electroweak interaction.

Squaring the matrix elements $\mathcal{M}_{fi}$, we obtain the following expressions

$$\overline{\sum_{if}}|\mathcal{M}^{\gamma}_{fi}|^2 = \frac{e^4}{4Q^4} L_{\mu\nu} W^{\mu\nu}, \tag{2.18}$$

$$\overline{\sum_{if}}|\mathcal{M}^{W}_{fi}|^2 = \frac{G_F^2}{2} \cos^2\theta_c \, L_{\mu\nu} W^{\mu\nu}, \tag{2.19}$$

where the lepton and hadron tensors, $L_{\mu\nu}$ and $W^{\mu\nu}$, are introduced, defined as bilinear products of the currents. The calculation of the lepton tensor can easily be found in literature, e.g. in [1–3],

$$L_{\mu\nu} = \overline{\sum_{if}} \left[\mathcal{J}^{\text{lep}}_{\mu}(q)\right]^{\dagger} \mathcal{J}^{\text{lep}}_{\nu}(q), \tag{2.20}$$

$$= \frac{2}{m_i m_f} \left(k_{i,\mu} k_{f,\nu} + k_{f,\nu} k_{i,\mu} - g_{\mu\nu} k_i \cdot k_f + g_{\mu\nu} m_i m_f - ih\epsilon_{\mu\nu\alpha\beta} k_i^{\alpha} k_f^{\beta} \right). \tag{2.21}$$

As this work only considers electrons and neutrinos as initial leptons, we will put $m_i \approx 0$, thus dropping the fourth term in $L_{\mu\nu}$.

For the hadron tensor, the averaging and summation over initial and final states is written as

$$W^{\mu\nu} = \frac{1}{2J_i + 1} \sum_{M_i} \sum_{J_R, M_R} \sum_{m_{s_N}} \left[\mathcal{J}^{\mu}_{\text{nuc}}(q)\right]^{\dagger} \mathcal{J}^{\nu}_{\text{nuc}}(q), \tag{2.22}$$

with (J_i, M_i) the quantum numbers of the initial nucleus and (J_R, M_R) those of the residual nucleus, m_{s_N} is the spin projection of the outgoing nucleon. Throughout this work, we only consider target nuclei with $J_i = 0$, so the first factor equals one and the sum over M_i is discarded. The structure of nuclear current is more complicated compared to the lepton current as it involves the evaluation of many-body operators between the initial and final nuclear state. We defer its calculation to later chapters, for the time being Eq. (2.22) is sufficient.

Now we consider the contraction of the lepton and hadron tensors, we drop the subscript 'nuc' from the nuclear current for simplicity. Choosing the reference frame as in Fig. 2.1, this results in [1,5]

$$L_{\mu\nu} W^{\mu\nu} = \frac{2\epsilon_i \epsilon_f}{m_i m_f} \big[v_{CC} W_{CC} + v_{CL} W_{CL} + v_{LL} W_{LL} + v_T W_T + v_{TT} W_{TT} + v_{TC} W_{TC} \\ + v_{TL} W_{TL} + h(v_{T'} W_{T'} + v_{TC'} W_{TC'} + v_{TL'} W_{TL'}) \big], \tag{2.23}$$

with

$$v_{CC} = 1 + \zeta \cos\theta, \tag{2.24}$$

$$v_{CL} = -\left(\frac{\omega}{q}\left(1 + \zeta\cos\theta\right) + \frac{m_f^2}{\epsilon_f q}\right), \tag{2.25}$$

$$v_{LL} = 1 + \zeta\cos\theta - \frac{2\epsilon_i\epsilon_f}{q^2}\zeta^2\sin^2\theta, \tag{2.26}$$

$$v_T = 1 - \zeta\cos\theta + \frac{\epsilon_i\epsilon_f}{q^2}\zeta^2\sin^2\theta, \tag{2.27}$$

$$v_{TT} = -\frac{\epsilon_i\epsilon_f}{q^2}\zeta^2\sin^2\theta, \tag{2.28}$$

$$v_{TC} = -\frac{\sin\theta}{\sqrt{2}q}\zeta\left(\epsilon_i + \epsilon_f\right), \tag{2.29}$$

$$v_{TL} = \frac{\sin\theta}{\sqrt{2}q^2}\zeta\left(\epsilon_i^2 - \epsilon_f^2 + m_f^2\right), \tag{2.30}$$

$$v_{T'} = \frac{\epsilon_i + \epsilon_f}{q}\left(1 - \zeta\cos\theta\right) - \frac{m_f^2}{\epsilon_f q}, \tag{2.31}$$

$$v_{TC'} = -\frac{\sin\theta}{\sqrt{2}}\zeta, \tag{2.32}$$

$$v_{TL'} = \frac{\omega}{q}\frac{\sin\theta}{\sqrt{2}}\zeta, \tag{2.33}$$

and

$$W_{CC} = \left|\mathcal{J}_0\right|^2, \tag{2.34}$$

$$W_{CL} = 2\,\mathrm{Re}\left(\mathcal{J}_0\mathcal{J}_3^\dagger\right), \tag{2.35}$$

$$W_{LL} = \left|\mathcal{J}_3\right|^2, \tag{2.36}$$

$$W_T = \left|\mathcal{J}_{+1}\right|^2 + \left|\mathcal{J}_{-1}\right|^2, \tag{2.37}$$

$$W_{TT} = 2\,\mathrm{Re}\left(\mathcal{J}_{+1}\mathcal{J}_{-1}^\dagger\right), \tag{2.38}$$

$$W_{TC} = 2\,\mathrm{Re}\left(\mathcal{J}_0\left(\mathcal{J}_{+1}^\dagger - \mathcal{J}_{-1}^\dagger\right)\right), \tag{2.39}$$

$$W_{TL} = 2\,\mathrm{Re}\left(\mathcal{J}_3\left(\mathcal{J}_{+1}^\dagger - \mathcal{J}_{-1}^\dagger\right)\right), \tag{2.40}$$

$$W_{T'} = \left|\mathcal{J}_{+1}\right|^2 - \left|\mathcal{J}_{-1}\right|^2, \tag{2.41}$$

$$W_{TC'} = 2\,\mathrm{Re}\left(\mathcal{J}_0\left(\mathcal{J}_{+1}^\dagger + \mathcal{J}_{-1}^\dagger\right)\right), \tag{2.42}$$

$$W_{TL'} = 2\,\mathrm{Re}\left(\mathcal{J}_3\left(\mathcal{J}_{+1}^\dagger + \mathcal{J}_{-1}^\dagger\right)\right). \tag{2.43}$$

$\mathcal{J}_{+1}$ and $\mathcal{J}_{-1}$ are the spherical components of the nuclear current

$$\mathcal{J}_{\pm1} = \mp\frac{1}{\sqrt{2}}\left(\mathcal{J}_x \pm i\mathcal{J}_y\right), \tag{2.44}$$

and ζ is defined as

$$\zeta = \frac{k_f}{\epsilon_f} = \sqrt{1 - \frac{m_f^2}{\epsilon_f^2}}. \tag{2.45}$$

The azimuthal information of the emitted nucleon is contained in the response functions $\{TT, TC, TL, TC', TL'\}$ while all responses contain polar angle information. We have defined all response functions with a positive sign and absorbed the minus signs in the corresponding kinematic factors[1]. In this work, the response W_{CC} is referred to as the Coulomb response, but it is often called the longitudinal response in literature. We reserve the name longitudinal response for W_{LL}. The reason for this is that for electron scattering there is a one-to-one relation between both responses, and the expressions can be simplified, as shown below. This relation is not valid for neutrino scattering. The response W_T is called the transverse response in this work and all other responses are referred to by their corresponding symbol. Combining the results obtained so far, the differential cross section for $A(l, l'N)$ can be written as [4],

$$\begin{aligned}\frac{\mathrm{d}\sigma^X}{\mathrm{d}\epsilon_f \mathrm{d}\Omega_f \mathrm{d}\Omega_N} = \frac{p_N E_N}{(2\pi)^3} f_{rec}^{-1} \sigma^X \zeta \\ \times \big[v_{CC} W_{CC} + v_{CL} W_{CL} + v_{LL} W_{LL} + v_T W_T + v_{TT} W_{TT} + v_{TC} W_{TC} \\ + v_{TL} W_{TL} + h(v_{T'} W_{T'} + v_{TC'} W_{TC'} + v_{TL'} W_{TL'}) \big]. \end{aligned} \tag{2.46}$$

A Mott-like prefactor has been introduced to differentiate between eA and νA interactions

$$\sigma^\gamma = \frac{1}{2} \left(\frac{e^2 \epsilon_f}{2\pi Q^2} \right)^2, \tag{2.47}$$

$$\sigma^W = \left(\frac{G_F \cos\theta_c \, \epsilon_f}{2\pi} \right)^2, \tag{2.48}$$

and the factor $p_N E_N / (2\pi)^3$ is related to the normalization of the nuclear wave functions. In this expression for the differential cross section, the functions v_i contain all the lepton kinematic information and the response functions, or structure functions, W_i include the nuclear dynamics.

For $A(e, e'N)$ interactions, this expression can be simplified using the conserved vector current (CVC) relation [13]. In momentum space, this hypothesis states that

$$q_\mu \mathcal{J}^\mu(q) = 0, \tag{2.49}$$

or, as $\boldsymbol{q}$ is aligned with the z-axis,

$$\mathcal{J}_3(q) = \frac{\omega}{q} \mathcal{J}_0(q). \tag{2.50}$$

Further, the scattered e has a negligible mass $m_e \approx 0$, so that $\zeta \approx 1$. Using this information, we extract a prefactor from the v_i functions

$$1 + \cos\theta_l = 2\cos^2(\theta_l/2), \tag{2.51}$$

which is absorbed in the Mott cross section. Combining this, the differential cross section for electron scattering can be written as [14–16]

$$\frac{\mathrm{d}\sigma^\gamma}{\mathrm{d}\epsilon_f \mathrm{d}\Omega_f \mathrm{d}\Omega_N} = \frac{p_N E_N}{(2\pi)^3} f_{rec}^{-1} \sigma^{\mathrm{Mott}} \big[v_L^e W_{CC} + v_T^e W_T + v_{TT}^e W_{TT} + v_{TL}^e W_{TC} \big], \tag{2.52}$$

[1] Note that the responses W_{TC} and W_{TL} have been defined with an opposite sign compared to [10–12]

with

$$\sigma^{\text{Mott}} = \left(\frac{\alpha \cos(\theta_l/2)}{2\epsilon_i \sin^2(\theta_l/2)} \right)^2, \tag{2.53}$$

where $\alpha = e^2/4\pi$ is the fine structure constant. The kinematic factors for eA scattering are given by

$$v_L^e = \frac{Q^4}{q^4}, \tag{2.54}$$

$$v_T^e = \frac{Q^2}{2q^2} + \tan^2 \frac{\theta_l}{2}, \tag{2.55}$$

$$v_{TT}^e = -\frac{Q^2}{2q^2}, \tag{2.56}$$

$$v_{TL}^e = -\frac{Q^2}{\sqrt{2}q^3} (\epsilon_i + \epsilon_f) \tan^2 \frac{\theta_l}{2}, \tag{2.57}$$

and the response functions W_i identical as those defined above.

2.2 Differential $2N$ knockout cross section

In this section, we develop a differential cross section for exclusive electron-induced and CC muon-neutrino induced $2N$ knockout interactions $A(l, l' N_a N_b)$

$$e + A \to e' + (A-2)^* + N_a + N_b, \tag{2.58}$$

$$\nu_\mu + A \to \mu^- + (A-2)^* + N_a + N_b, \tag{2.59}$$

$$\overline{\nu}_\mu + A \to \mu^+ + (A-2)^* + N_a + N_b, \tag{2.60}$$

where the $A-2$ system is left in a low-lying excited state. For exclusive $2N$ knockout cross sections, both emitted nucleons are detected in coincidence with the scattered lepton. We follow the same approach as for the $1N$ knockout cross section and use the same conventions as before. The outgoing nucleons are denoted by a and b with four-vectors $P_a = (E_a, \boldsymbol{p}_a)$ and $P_b = (E_b, \boldsymbol{p}_b)$, Fig. 2.3 clarifies the angular conventions.

The general differential cross section, using the same conventions as earlier, is written as

$$\begin{aligned} \mathrm{d}\sigma = & \frac{m_i}{\epsilon_i} \frac{m_f}{\epsilon_f} \frac{\mathrm{d}\boldsymbol{k}_f}{(2\pi)^3} \frac{\mathrm{d}\boldsymbol{p}_a}{(2\pi)^3} \frac{\mathrm{d}\boldsymbol{p}_b}{(2\pi)^3} \frac{\mathrm{d}\boldsymbol{p}_{A-2}}{(2\pi)^3} \\ & \times (2\pi)^4 \delta^{(4)} \left(k_i + P_A - k_f - P_a - P_b - P_{A-2} \right) \overline{\sum_{fi}} |\mathcal{M}_{fi}|^2, \end{aligned} \tag{2.61}$$

$$= \frac{m_i}{\epsilon_i} \frac{m_f}{\epsilon_f} \frac{1}{(2\pi)^8} \mathrm{d}\boldsymbol{k}_f \, \mathrm{d}\boldsymbol{p}_a \, \mathrm{d}\boldsymbol{p}_b \, \delta \left(\epsilon_i + M_A - \epsilon_f - E_a - E_b - E_{A-1} \right) \overline{\sum_{fi}} |\mathcal{M}_{fi}|^2, \tag{2.62}$$

where we exploited the delta function to integrate over the momentum of the residual $A-2$ nuclear system. The delta function ensures four-momentum conservation, while the matrix

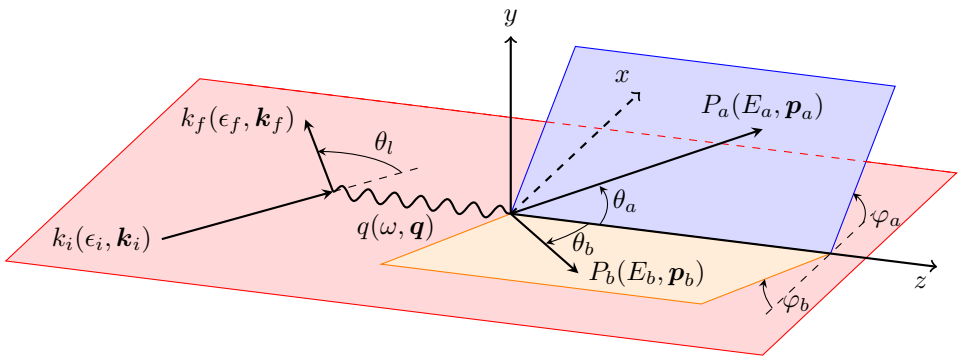

Figure 2.3: The definition of the angular variables used in the $2N$ knockout calculations

element $\mathcal{M}_{fi}$ contains all the dynamic information of the interaction. Writing the delta function as

$$\delta\left(\epsilon_i + M_A - \epsilon_f - E_a - \sqrt{p_b^2 + m_N^2} - \sqrt{\left(\boldsymbol{q} - \boldsymbol{p_a} - \boldsymbol{p_b}\right)^2 + (M^*_{A-2})^2}\right), \tag{2.63}$$

we can use the property of the delta function, Eq. (2.8), to integrate over p_b. This yields

$$\mathrm{d}\sigma = \frac{m_i}{\epsilon_i}\frac{m_f}{\epsilon_f}\frac{p_b E_b}{(2\pi)^8}\, g_{rec}^{-1}\, \mathrm{d}\boldsymbol{k}_f\, \mathrm{d}\boldsymbol{p}_a\, \mathrm{d}\Omega_b \overline{\sum_{fi}} |\mathcal{M}_{fi}|^2, \tag{2.64}$$

where the recoil factor for $2N$ knockout is defined as

$$g_{rec} = \left|1 + \frac{E_b}{E_{A-2}}\left(1 - \frac{\boldsymbol{p}_b \cdot (\boldsymbol{q} - \boldsymbol{p}_a)}{p_b^2}\right)\right|. \tag{2.65}$$

In the ideal case where all the momentum is divided over both outgoing nucleons, and the $A-2$ system has no recoil, this factor tends to one. For the calculation of the squared matrix element $|\mathcal{M}_{fi}|^2$, we refer to Section 2.1, as the calculation was done for a general nuclear final state B. The expression for the contraction of the lepton and hadron tensors for $2N$ knockout is identical as for $1N$ knockout calculations. As a result, the functions v_i containing the lepton information and the expressions for the response functions W_i are identical for $1N$ and $2N$ knockout. The only differences are the nuclear current operators $\widehat{J}^{\mathrm{nuc}}_{\mu}(\boldsymbol{q})$ in the definition of the nuclear currents, which are necessary for the calculation of the response functions, and the summation over the final state nucleons

$$W^{\mu\nu} = \sum_{J_R, M_R} \sum_{m_{s_a}, m_{s_b}} \left[\mathcal{J}^{\mu}_{\mathrm{nuc}}(q)\right]^{\dagger} \mathcal{J}^{\nu}_{\mathrm{nuc}}(q). \tag{2.66}$$

Substituting the squared matrix element in Eq. (2.64), the exclusive $2N$ knockout cross section for CC muon-neutrino scattering $A(\nu_\mu, \mu^- N_a N_b)$ interactions can be written as (T_a refers to the kinetic energy of nucleon a)

$$\begin{aligned}\frac{\mathrm{d}\sigma^W}{\mathrm{d}\epsilon_f \mathrm{d}\Omega_f \mathrm{d}T_a \mathrm{d}\Omega_a \mathrm{d}\Omega_b} = \frac{p_a p_b E_a E_b}{(2\pi)^6} g_{rec}^{-1}\, \sigma^W\, \zeta \\ \times \big[v_{CC} W_{CC} + v_{CL} W_{CL} + v_{LL} W_{LL} + v_T W_T + v_{TT} W_{TT} + v_{TC} W_{TC}\end{aligned}$$

$$+v_{TL}W_{TL} + h(v_{T'}W_{T'} + v_{TC'}W_{TC'} + v_{TL'}W_{TL'})\big]. \tag{2.67}$$

For $2N$ knockout, the azimuthal information of the emitted nucleons is contained in the responses $\{TT, TC, TL, TC', TL'\}$ while all responses depend on θ_a and θ_b, as will be explicitly shown in Chapter 4. As for the $1N$ knockout cross section, the expression for $A(e, e'N_aN_b)$ can be simplified by using CVC to relate the Coulomb and longitudinal currents. The result is given by [4,11]

$$\frac{\mathrm{d}\sigma^{\gamma}}{\mathrm{d}\epsilon_f \mathrm{d}\Omega_f \mathrm{d}T_a \mathrm{d}\Omega_a \mathrm{d}\Omega_b} = \frac{p_a p_b E_a E_b}{(2\pi)^6}\, g_{rec}^{-1}\, \sigma^{\mathrm{Mott}} \times \big[v_L^e W_{CC} + v_T^e W_T + v_{TT}^e W_{TT} + v_{TL}^e W_{TC}\big]. \tag{2.68}$$

This expression for the $2N$ knockout differential cross section was used in earlier work to study exclusive $(e, e'\mathrm{pp})$ scattering on ^{12}C and ^{16}O to discrete final states [11,17]. Furthermore, it was used when looking for evidence for SRCs in ^{12}C at Mainz [18], and in ^{3}He and ^{16}O at NIKHEF [19–21].

From a neutrino point of view, these exclusive $2N$ knockout cross sections provide an interesting tool for experiments which have information on the nucleons in the final states, for example the so-called 'hammer events' seen by the ArgoNeuT collaboration [22].

2.3 Partial wave expansion

The ten response functions, Eqs. (2.34)-(2.43), are defined as bilinear products of the time-like and spherical components of the nuclear transition matrix elements,

$$\mathcal{J}_{\mu}^{\mathrm{nuc}}(q) \equiv \langle\, \Psi_f \,|\, \widehat{J}_{\mu}^{\mathrm{nuc}}(\boldsymbol{q}) \,|\, \Psi_i \,\rangle, \tag{2.69}$$

and their complex conjugates. In the following two chapters, the nuclear final state $|\,\Psi_f\,\rangle$ for $1N$ and $2N$ knockout interactions will be constructed using a partial wave expansion for the emitted nucleons in terms of the continuum eigenstates of the MF potential. Therefore, it is convenient to introduce a partial wave expansion for the nuclear current operator as well.

The nuclear current operator in momentum space is defined as a Fourier transform

$$\widehat{J}_{\mu}^{\mathrm{nuc}}(\boldsymbol{q}) = \int \mathrm{d}\boldsymbol{r}\, e^{i\boldsymbol{r}\cdot\boldsymbol{q}} \widehat{J}_{\mu}^{\mathrm{nuc}}(\boldsymbol{r}). \tag{2.70}$$

Using the Rayleigh formula, Eq. (A.13), the four spherical components of the nuclear current in momentum space can be expressed in terms of the well-known Coulomb ($\widehat{M}_{JM}^{\mathrm{Coul}}$), longitudinal ($\widehat{L}_{JM}^{\mathrm{long}}$), electric ($\widehat{T}_{JM}^{\mathrm{elec}}$) and magnetic ($\widehat{T}_{JM}^{\mathrm{magn}}$) multipole operators, see e.g. [8,9], ($\widehat{J} \equiv \sqrt{2J+1}$)

$$\widehat{\rho}^{\mathrm{nuc}}(\boldsymbol{q}) = +\sqrt{4\pi} \sum_{J\geq 0} i^J \widehat{J} \widehat{M}_{J0}^{\mathrm{Coul}}(q), \tag{2.71}$$

$$\widehat{J}_3^{\mathrm{nuc}}(\boldsymbol{q}) = -\sqrt{4\pi} \sum_{J\geq 0} i^J \widehat{J} \widehat{L}_{J0}^{\mathrm{long}}(q), \tag{2.72}$$

$$\widehat{J}^{\rm nuc}_{\pm1}(\boldsymbol{q}) = -\sqrt{2\pi}\sum_{J\geq1} i^J \widehat{J}\left[\widehat{T}^{\rm elec}_{J\pm1}(q) \pm \widehat{T}^{\rm magn}_{J\pm1}(q)\right]. \tag{2.73}$$

The multipole operators are defined by

$$\widehat{M}^{\rm Coul}_{JM}(q) = \int {\rm d}\boldsymbol{r}\,[j_J(qr)Y_{JM}(\Omega_r)]\,\widehat{\rho}^{\rm nuc}(\boldsymbol{r}), \tag{2.74}$$

$$\widehat{L}^{\rm long}_{JM}(q) = \frac{i}{q}\int {\rm d}\boldsymbol{r}\,[\boldsymbol{\nabla}\,(j_J(qr)Y_{JM}(\Omega_r))]\cdot\widehat{\boldsymbol{J}}^{\rm nuc}(\boldsymbol{r}), \tag{2.75}$$

$$\widehat{T}^{\rm elec}_{JM}(q) = \frac{1}{q}\int {\rm d}\boldsymbol{r}\left[\boldsymbol{\nabla}\times\left(j_J(qr)\boldsymbol{\mathcal{Y}}^M_{J(J,1)}(\Omega_r)\right)\right]\cdot\widehat{\boldsymbol{J}}^{\rm nuc}(\boldsymbol{r}), \tag{2.76}$$

$$\widehat{T}^{\rm magn}_{JM}(q) = \int {\rm d}\boldsymbol{r}\left[j_J(qr)\boldsymbol{\mathcal{Y}}^M_{J(J,1)}(\Omega_r)\right]\cdot\widehat{\boldsymbol{J}}^{\rm nuc}(\boldsymbol{r}), \tag{2.77}$$

with $\widehat{\rho}^{\rm nuc}(\boldsymbol{r})$ and $\widehat{\boldsymbol{J}}^{\rm nuc}(\boldsymbol{r})$ the time and space component of the nuclear current operator in coordinate space, $Y_{JM}(\Omega)$ the spherical harmonics and $\boldsymbol{\mathcal{Y}}^M_{J(L,1)}(\Omega)$ the vector spherical harmonics, defined in Eq. (A.10). Introducing the operator

$$\widehat{O}^{\kappa}_{JM}(q) = \int {\rm d}\boldsymbol{r}\left[j_{J+\kappa}(qr)\boldsymbol{\mathcal{Y}}^M_{J(J+\kappa,1)}(\Omega_r)\right]\cdot\widehat{\boldsymbol{J}}^{\rm nuc}(\boldsymbol{r}), \tag{2.78}$$

the longitudinal, electric and magnetic operators can be written as

$$\widehat{L}^{\rm long}_{JM}(q) = i\sum_{\kappa=\pm1}\left(\frac{J+\delta_{\kappa,+1}}{2J+1}\right)^{1/2}\widehat{O}^{\kappa}_{JM}(q), \tag{2.79}$$

$$\widehat{T}^{\rm elec}_{JM}(q) = i\sum_{\kappa=\pm1}(-1)^{\delta_{\kappa,+1}}\left(\frac{J+\delta_{\kappa,-1}}{2J+1}\right)^{1/2}\widehat{O}^{\kappa}_{JM}(q), \tag{2.80}$$

$$\widehat{T}^{\rm magn}_{JM}(q) = \widehat{O}^{\kappa=0}_{JM}(q). \tag{2.81}$$

Accordingly, the calculation of the matrix elements of two operators $\widehat{M}$ and $\widehat{O}$ suffice to determine the four components of the nuclear transition matrix elements and thus the ten response functions as well.

The advantage of the partial wave expansion is that the multidimensional integral in Eq. (2.70) can be reduced to a one-dimensional integral, the angular integration can be performed analytically using properties of the spherical harmonics. Yet, this comes at a high analytical cost. Although these multipole expansions contain an infinite sum of terms, we will show that it can be truncated at a finite number of multipole contributions. In Fig. 3.7, the convergence of the multipole contributions to the cross section is shown explicitly, which demonstrates that the infinite sum can be truncated at low order.

2.4 Nuclear currents in the IA

The expressions for the differential cross section and the partial wave expansion given above are general, in the sense that no model dependencies have been introduced. For the description of the nuclear current operator, however, we have to revert to approximations or model dependencies. In the present section, we will describe the impulse approximation, with

which one can describe the general features of lepton-nucleus cross sections. It is the simplest and most widely used method to model the nuclear current: the residual interactions between the nucleons are ignored at the moment of the interaction. In Chapter 6, we will explicitly include these residual interactions in the nuclear current by including two-body MEC operators in the nuclear current.

In the IA, the nuclear many-body current operator is approximated by a sum of one-body current operators $\widehat{J}^{[1]}_\mu$, each of which yields the same contribution to the nuclear current

$$\widehat{J}^{\rm nuc}_\mu(\boldsymbol{r}) \approx \widehat{J}^{\rm IA}_\mu(\boldsymbol{r}) = \sum_{i=1}^{A} \widehat{J}^{[1]}_\mu(\boldsymbol{r}_i)\delta^{(3)}(\boldsymbol{r}-\boldsymbol{r}_i). \tag{2.82}$$

For electron scattering interactions, the nuclear current operators in coordinate space are constructed by using the nuclear charge density and the standard expressions of the nuclear current that has a convection and a magnetization part [9]

$$\widehat{\rho}^{\rm nuc}_V(\boldsymbol{r}) = \sum_{i=1}^{A} G_D(Q^2)\,\delta^{(3)}(\boldsymbol{r}-\boldsymbol{r}_i)\,e(i), \tag{2.83}$$

$$\widehat{\boldsymbol{J}}^{\rm nuc}_V(\boldsymbol{r}) = \widehat{\boldsymbol{J}}^{\rm nuc}_{\rm con}(\boldsymbol{r}) + \widehat{\boldsymbol{J}}^{\rm nuc}_{\rm mag}(\boldsymbol{r}) \tag{2.84}$$

$$= \sum_{i=1}^{A} \frac{G_D(Q^2)}{2m_N i}\left[\delta^{(3)}(\boldsymbol{r}-\boldsymbol{r}_i)\overrightarrow{\boldsymbol{\nabla}}_i - \overleftarrow{\boldsymbol{\nabla}}_i\,\delta^{(3)}(\boldsymbol{r}-\boldsymbol{r}_i)\right]e(i)$$

$$+ \sum_{i=1}^{A} \frac{G_D(Q^2)}{2m_N}\left(\overrightarrow{\boldsymbol{\nabla}}\times\boldsymbol{\sigma}_i\right)\delta^{(3)}(\boldsymbol{r}-\boldsymbol{r}_i)\,\mu(i). \tag{2.85}$$

A dipole form factor $G_D(Q^2)$ has been introduced to account for the spatial extension of the nucleons and we defined

$$e(i) = \frac{1}{2}\left[1+\tau_3(i)\right], \tag{2.86}$$

$$\mu(i) = 2.793\frac{1}{2}\left[1+\tau_3(i)\right] - 1.913\frac{1}{2}\left[1-\tau_3(i)\right], \tag{2.87}$$

with

$$\tau_3\,|\,\mathrm{p}\,\rangle = |\,\mathrm{p}\,\rangle \qquad\qquad \tau_3\,|\,\mathrm{n}\,\rangle = -\,|\,\mathrm{n}\,\rangle. \tag{2.88}$$

At zero momentum transfer ($G_D(0)=1$), the coupling strength $e(i)$, is equal to 1 for protons and 0 for neutrons[2], and the magnetic coupling strength $\mu(i)$ equals 2.793(-1.913) for protons(neutrons). Note that the value of the electric charge has been absorbed in the prefactor of the differential cross section. The small electric coupling between electrons and neutrons is neglected in these expressions.

As a natural extension to the charge and current operators for electron scattering, the expressions are generalized for CC neutrino interactions

$$\widehat{\rho}^{\rm nuc}_V(\boldsymbol{r}) = \sum_{i=1}^{A} F_1(Q^2)\delta^{(3)}(\boldsymbol{r}-\boldsymbol{r}_i)\tau_\pm(i), \tag{2.89}$$

[2]In the actual calculations, the electric coupling to the neutron is accounted for, as explained in Appendix B.

$$\widehat{\rho}_A^{\rm nuc}(\boldsymbol{r}) = \sum_{i=1}^{A} \frac{G_A(Q^2)}{2m_N i} \boldsymbol{\sigma}_i \cdot \left[\delta^{(3)}(\boldsymbol{r}-\boldsymbol{r}_i) \overrightarrow{\boldsymbol{\nabla}}_i - \overleftarrow{\boldsymbol{\nabla}}_i \delta^{(3)}(\boldsymbol{r}-\boldsymbol{r}_i) \right] \tau_\pm(i), \tag{2.90}$$

$$\widehat{\boldsymbol{J}}_V^{\rm nuc}(\boldsymbol{r}) = \widehat{\boldsymbol{J}}_{\rm con}^{\rm nuc}(\boldsymbol{r}) + \widehat{\boldsymbol{J}}_{\rm mag}^{\rm nuc}(\boldsymbol{r}) \tag{2.91}$$

$$= \sum_{i=1}^{A} \frac{F_1(Q^2)}{2m_N i} \left[\delta^{(3)}(\boldsymbol{r}-\boldsymbol{r}_i) \overrightarrow{\boldsymbol{\nabla}}_i - \overleftarrow{\boldsymbol{\nabla}}_i \delta^{(3)}(\boldsymbol{r}-\boldsymbol{r}_i) \right] \tau_\pm(i)$$

$$+ \sum_{i=1}^{A} \frac{F_1(Q^2)+F_2(Q^2)}{2m_N} \left(\overrightarrow{\boldsymbol{\nabla}} \times \boldsymbol{\sigma}_i \right) \delta^{(3)}(\boldsymbol{r}-\boldsymbol{r}_i) \tau_\pm(i), \tag{2.92}$$

$$\widehat{\boldsymbol{J}}_A^{\rm nuc}(\boldsymbol{r}) = \sum_{i=1}^{A} G_A(Q^2) \boldsymbol{\sigma}_i \delta^{(3)}(\boldsymbol{r}-\boldsymbol{r}_i) \tau_\pm(i). \tag{2.93}$$

The Pauli, Dirac and axial form factors are introduced, which are defined and discussed in detail in Appendix B. The isospin raising and lowering operators $\tau_\pm$ are defined as

$$\tau_+ \,|\, \mathrm{n} \,\rangle = + \,|\, \mathrm{p} \,\rangle \qquad \tau_+ \,|\, \mathrm{p} \,\rangle = 0 \tag{2.94}$$

$$\tau_- \,|\, \mathrm{p} \,\rangle = - \,|\, \mathrm{n} \,\rangle \qquad \tau_- \,|\, \mathrm{n} \,\rangle = 0, \tag{2.95}$$

and the $\pm$ sign corresponds with the incoming $W^\pm$ boson. The expressions are valid for electron scattering as well, when replacing the isospin operator $\tau_\pm$ with τ_3 and using the appropriate form factors as discussed in Appendix B.

These nuclear current operators are referred to as the nuclear charge density $\widehat{\rho}_V$, the axial charge density $\widehat{\rho}_A$, the convection current $\widehat{\boldsymbol{J}}_{\rm con}$, the magnetization current, $\widehat{\boldsymbol{J}}_{\rm mag}$ and the axial current $\widehat{\boldsymbol{J}}_A$.

Substituting the nuclear current operators in the IA, Eqs. (2.89)-(2.93), in the two multipole operators, Eqs. (2.74) and (2.78), we have to calculate expectation values for the following five operators to construct the time-like and three spherical components of the nuclear current in the IA

$$\widehat{M}_{JM}^{\rm Coul}\left[\widehat{\rho}_V\right], \quad \widehat{M}_{JM}^{\rm Coul}\left[\widehat{\rho}_A\right], \quad \widehat{O}_{JM}^{\kappa}\left[\widehat{\boldsymbol{J}}_{\rm con}\right], \quad \widehat{O}_{JM}^{\kappa}\left[\widehat{\boldsymbol{J}}_{\rm mag}\right] \quad \text{and} \quad \widehat{O}_{JM}^{\kappa}\left[\widehat{\boldsymbol{J}}_A\right]. \tag{2.96}$$

References

[1] T. Donnelly, Prog. Part. Nucl. Phys. **13**, 183 (1985).

[2] T. Donnelly and A. Raskin, Ann. Phys. **169**, 247 (1986).

[3] A. Raskin and T. Donnelly, Ann. Phys. **191**, 78 (1989).

[4] Y. Umino and J. Udias, Phys. Rev. **C52**, 3399 (1995).

[5] O. Moreno, T. Donnelly, J. Van Orden, *et al.* Phys. Rev. **D90**, 013014 (2014).

[6] J. Bjorken and S. Drell, *Relativistic quantum fields* (1965).

[7] J. Ryckebusch, *Photon and electron-induced one-nucleon emission within a selfconsistent* HF-RPA *model*, PhD thesis (Ghent University, 1988).

[8] N. Jachowicz, *Many-body description of neutrino-nucleus interactions*, PhD thesis (Ghent University, 2000).

[9] J. Walecka, *Theoretical nuclear and subnuclear physics* (2004).

[10] J. Ryckebusch, M. Vanderhaeghen, L. Machenil, *et al.* Nucl. Phys. **A568**, 828 (1994).

[11] J. Ryckebusch, V. Van der Sluys, K. Heyde, *et al.* Nucl. Phys. **A624**, 581 (1997).

[12] S. Janssen, J. Ryckebusch, W. Van Nespen, *et al.* Nucl. Phys. **A672**, 285 (2000).

[13] W. Haxton and E. Henley, *Symmetries and fundamental interactions in nuclei* (1995).

[14] J. Ryckebusch, K. Heyde, D. Van Neck, *et al.* Nucl. Phys. **A503**, 694 (1989).

[15] V. Van der Sluys, *The role of electron distortion and two-body currents in the (e,e′) and (e,e′p) reaction*, PhD thesis (Ghent University, 1995).

[16] P. Lava, *Nucleon propagation induced by electroweak excitation of atomic nuclei*, PhD thesis (Ghent University, 2006).

[17] J. Ryckebusch and W. Van Nespen, Eur. Phys. J. **A20**, 435 (2004).

[18] K. Blomqvist, W. Boeglin, R. Bohm, *et al.* Phys. Lett. **B421**, 71 (1998).

[19] C. Onderwater, K. Allaart, E. Aschenauer, *et al.* Phys. Rev. Lett. **81**, 2213 (1998).

[20] D. Groep *et al.* Phys. Rev. Lett. **83**, 5443 (1999).

[21] R. Starink *et al.* Phys. Lett. **B474**, 33 (2000).

[22] ArgoNeuT collaboration, R. Acciarri *et al.* Phys. Rev. **D90**, 012008 (2014).

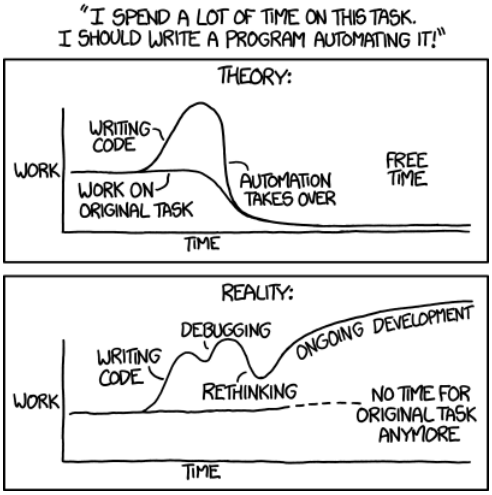

'Automating' comes from the roots 'auto-' meaning 'self-', and 'mating', meaning 'screwing'.

Chapter 3

One-nucleon knockout

In Chapter 2, the differential cross sections for electron- and neutrino-induced $1N$ and $2N$ knockout interactions were derived. The cross section was written as a function of ten response functions, which are defined as bilinear products of the time-like and spherical components of the transition matrix elements. In this chapter, we only handle single nucleon knockout interactions, resulting in a $1p1h$ final state. We discus how the response functions are calculated, irrespective of the exact structure of the nuclear current. The only information on the nuclear current that is necessary is that it consists of one- and two-body operators. The framework developed here is general and is valid for all types of electroweak scattering. In Fig. 3.1, a $1N$ knockout process from ^{16}O is shown as interpreted in a shell-model picture. The incoming boson X, which can either be a γ^* or a $W^{\pm}$ in this work, ejects a proton from the $1p_{1/2}$ shell to the continuum. E_N is the energy of the ejected nucleon.

In this chapter, we first consider the nuclear current in the IA. This means that the current consists of a sum of one-body currents. This is the simplest way to model QE lepton-nucleus scattering. Fig. 3.2a is a graphical representation of how a one-body current contributes to the $1p1h$ final state.

Next, the influence of two-body currents on the $1N$ knockout channel is studied. The nature of the two-body current is left open. For the formalism developed here, the only

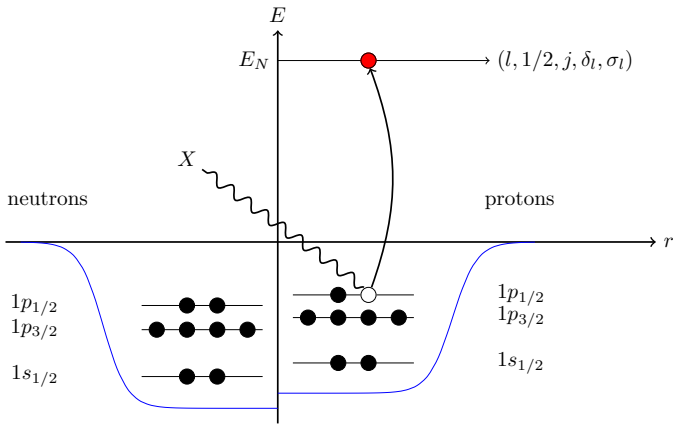

Figure 3.1: One-nucleon knockout from ^{16}O as interpreted in a shell-model picture. One nucleon is ejected to the continuum and the residual nucleus is left in a one-hole state h^{-1}.

requirement is that the current consists of two-body operators. Two types of two-body currents are studied in subsequent chapters, SRCs in Chapter 5 and MECs in Chapter 6. Fig. 3.2b shows schematically how a two-body current can result in a $1p1h$ final state.

In the first section, we discuss the exclusive $1N$ knockout cross section. Afterwards, we calculate inclusive $A(l, l')$ $1N$ knockout differential cross sections by integrating over the direction of the undetected nucleon. In the last section, numerical results for the inclusive $1N$ knockout cross sections, calculated in the IA, are presented, and for electron scattering calculations, comparison with data is shown.

3.1 Exclusive $1N$ knockout cross section

In this work, an exclusive $1N$ knockout reaction, denoted by $A(l, l'N)$, refers to an interaction where the nucleon that is emitted from the nucleus A is detected in coincidence with the final state lepton[1]. The most general expression for exclusive $A(l, l'N)$ scattering is given by Eq. (2.46)

$$\begin{aligned}\frac{\mathrm{d}\sigma^X}{\mathrm{d}\epsilon_f \mathrm{d}\Omega_f \mathrm{d}\Omega_N} = \frac{p_N E_N}{(2\pi)^3} f_{rec}^{-1}\, \sigma^X \zeta \\ \times \big[v_{CC} W_{CC} + v_{CL} W_{CL} + v_{LL} W_{LL} + v_T W_T + v_{TT} W_{TT} + v_{TC} W_{TC} \\ + v_{TL} W_{TL} + h(v_{T'} W_{T'} + v_{TC'} W_{TC'} + v_{TL'} W_{TL'}) \big]. \end{aligned} \tag{3.1}$$

The response functions W_i for $1N$ knockout are defined as bilinear products of the transition matrix elements $\mathcal{J}_\lambda$ and their complex conjugates.

$$\mathcal{J}_\lambda = \langle\, \Psi^{1p1h} \,|\, \widehat{J}_\lambda(\boldsymbol{q}) \,|\, \Psi_i \,\rangle, \tag{3.2}$$

[1] This definition is different from the conventional definition of exclusive $1N$ knockout, where the emitted nucleon, the final state lepton as well as the residual nucleus are observed.

(a) One-body current **(b)** Two-body current correction

Figure 3.2: Graphical representation of the particle-hole diagrams contributing to the $1N$ knockout reaction channel.

where $|\,\Psi_i\,\rangle$ refers to the initial correlated nuclear state and $|\,\Psi^{1p1h}\,\rangle$ describes the $1p1h$ nuclear final state, consisting of a single nucleon which is asymptotically free and a correlated residual nuclear state. $\widehat{J}_\lambda$ are the spherical components of the nuclear current operator. As a first approximation, we assume that the initial nuclear state is described by a Slater determinant of the target nucleus, neglecting the correlations in the ground state[2]: $|\,\Psi_i\,\rangle \approx |\,\Phi_{gs}\,\rangle$. In Chapter 5, we will discus how to account for the correlations in the ground state. For $^{12}\mathrm{C}(e,e'N)$ two final states are possible

$$|\,\Psi^{1p1h}\,\rangle = |\,{}^{11}\mathrm{B},\mathrm{p}\,\rangle,\, |\,{}^{11}\mathrm{C},\mathrm{n}\,\rangle, \tag{3.3}$$

while for $^{12}\mathrm{C}(\nu,l^-N)$ the final state is

$$|\,\Psi^{1p1h}\,\rangle = |\,{}^{11}\mathrm{C},\mathrm{p}\,\rangle. \tag{3.4}$$

We specifically use ^{12}C as a target nucleus, because it's common target nucleus, but the framework developed below is valid for all target nuclei with a $J^P = 0^+$ ground state. In all cases, the final states consist of a nucleon with momentum $\boldsymbol{p}_N$ and spin m_{s_N} and a residual $A-1$ nucleus with quantum numbers J_R, M_R, which can either be the ground state or a low lying excited state. The excitation energy E^{exc} is defined relative to the ground state of the residual nucleus. We use a similar approximation as for the target nucleus, and describe the residual $A-1$ system with its Slater determinant $|\,\Phi_f^{(A-1)}\,\rangle$. Combining this we can write the transition matrix elements as

$$\mathcal{J}_\lambda = \langle\,\Phi_f^{(A-1)}(E^{exc}, J_R M_R);\, \boldsymbol{p}_N m_{s_N}\,|\,\widehat{J}_\lambda(\boldsymbol{q})\,|\,\Phi_{gs}\,\rangle. \tag{3.5}$$

Further, the nuclear current $\widehat{J}_\lambda(\boldsymbol{q})$ consists of a one- and a two-body part, so the matrix elements can be written as a coherent sum of a one- and a two-body part

$$\mathcal{J}_\lambda = \mathcal{J}_\lambda^{[1]} + \mathcal{J}_\lambda^{[2]}. \tag{3.6}$$

For the hadron tensor, this yields

$$W_{\mu\nu} = W_{\mu\nu}^{[1]} + W_{\mu\nu}^{[2]} + W_{\mu\nu}^{[1,2]} \tag{3.7}$$

$$= \sum_{J_R,M_R} \sum_{m_{s_N}} \left(\left[\mathcal{J}_\mu^{[1]}\right]^\dagger \mathcal{J}_\nu^{[1]} + \left[\mathcal{J}_\mu^{[2]}\right]^\dagger \mathcal{J}_\nu^{[2]} + 2\,\mathrm{Re}\left\{ \left[\mathcal{J}_\mu^{[1]}\right]^\dagger \mathcal{J}_\nu^{[2]} \right\} \right). \tag{3.8}$$

[2]We will refer to correlated states as $|\,\Psi\,\rangle$ and to uncorrelated states as $|\,\Phi\,\rangle$.

The first two terms in this expression contain one- and two-body operators respectively, and the last term accounts for the interference between the one- and two-body operators. The first two terms are positive, while the interference term can be either positive or negative.

3.1.1 Nuclear wave functions for 1N knockout

The calculation of the nuclear wave functions, which are the building blocks of the Slater determinants and describe the emitted nucleon, is a challenging problem. The initial and residual nuclei are highly interacting many-body systems and the nucleon interacting with the boson can undergo several final-state interactions (FSIs) before it leaves the nucleus. It can scatter elastically off another nucleon inside the nucleus, changing its original direction, or knock the other nucleon out of the nucleus as well. It can also undergo charge exchange or produce a pion via an inelastic scattering process.

In the model described here, we work in the so-called spectator approach (SA), where the nucleon absorbing the boson leaves the nucleus without being subject to inelastic collisions and becomes asymptotically free. But even in this direct-knockout model, the nucleon in the continuum is still under the influence of the potential of the $A-1$ system: the outgoing waves are no plane waves. This distortion effect of the residual nuclear system on the continuum nucleon is accounted for by computing the continuum and bound-state wave functions using the same potential. This approach ensures orthogonality between initial and final states. The single-particle wave functions are calculated by assuming that the protons and neutrons move in a MF potential.

These approximations are represented schematically in Fig. 3.3. The A-body wave function is replaced by A single-particle wave functions. The dashed oval represents all correlations in the nuclear system and the empty oval represents the MF potential in which the single-particle wave functions are calculated. The MF potential has a distortive effect on the continuum wave function.

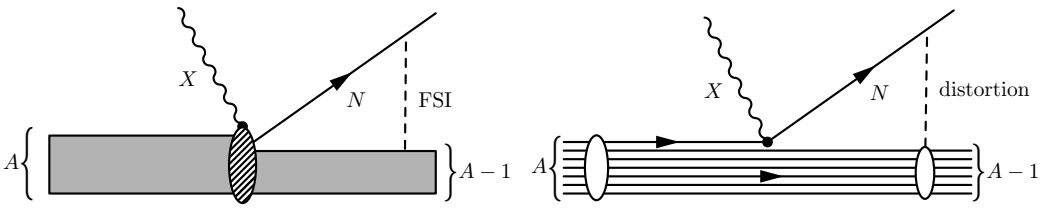

(a) Full model **(b)** Spectator approach in an IPM within the IA

Figure 3.3: Graphical representation of the 1N knockout reaction channel. Same as Fig. 1.12.

An effective Skyrme (SkE2) nucleon-nucleon interaction [1] is used to construct the MF potential. In a rotationally invariant potential, the single-particle wave functions can be written as

$$\psi_\alpha(\boldsymbol{r},\boldsymbol{\sigma}) = \varphi_{alj}(r,E)\,\mathcal{Y}^m_{j(l,1/2)}(\Omega_r), \tag{3.9}$$

where α denotes the whole set of quantum numbers $(E, l, 1/2, j, m)$ that are necessary to determine the orbit completely. Further, $\mathcal{Y}$ is the spin spherical harmonic, defined in Eq. (A.11), and the radial wave function φ is a solution of the radial Schrödinger equation

$$\widehat{H}_\alpha(r)\varphi_{alj}(r,E) = E\,\varphi_{alj}(r,E). \tag{3.10}$$

These wave functions are then used to construct the Slater determinants of the target and residual nuclei.

The solution of this equation is discussed in detail in many textbooks, they are found by imposing physical boundary conditions. At the origin, the radial wave functions which are regular, are solutions for which

$$\varphi_{alj}(r,E) \xrightarrow{r\to 0} r^l. \tag{3.11}$$

For $r \gg r_A$, with r_A the nuclear radius, the asymptotic values of the continuum wave functions tend to the solutions of the Coulomb equation[3]. The positive energy solutions have a damped oscillating character, while the bound states are exponentially tending to 0

$$\varphi_{alj}(r,E) \xrightarrow{r\gg r_A} \sim \frac{\sin\left(pr - \eta\ln(2pr) - \pi l/2 + \delta_l + \sigma_l\right)}{r} \qquad (E>0), \tag{3.12}$$

$$\varphi_{alj}(r,E) \xrightarrow{r\gg r_A} \sim 0 \qquad (E<0). \tag{3.13}$$

The wave number p is related to the energy eigenvalue E by

$$E = \frac{p^2}{2\mu_N}, \qquad \mu_N = \frac{A}{A-1}m_N, \tag{3.14}$$

with μ_N the reduced mass. The δ_l and σ_l are the central and Coulomb phase shifts of the ejectiles and the factor η accounts for the Coulomb part of the single-nucleon potential

$$\eta = (Z-1)\frac{e^2\mu_N}{p}. \tag{3.15}$$

For neutrons one has $\sigma_l = \eta = 0$. Applying proper normalization, the asymptotic behavior $(r \gg r_A)$ for the radial wave function of the outgoing nucleons is given by [2–4]

$$\varphi_{alj}(r,E) \xrightarrow{r\gg r_A} \sqrt{\frac{2m_N}{\pi p}}\,\frac{\sin\left(pr - \eta\ln(2pr) - \pi l/2 + \delta_l + \sigma_l\right)}{r}. \tag{3.16}$$

The radial wave functions over the whole range of r are then obtained by solving the Schrödinger equation, constrained by this asymptotic behavior.

Applying a partial wave expansion for the emitted nucleon with momentum $\boldsymbol{p}_N$ and spin m_{s_N} in terms of the continuum eigenstates of the MF potential $p_N(E_N l j m_j)$ $(E_N \equiv p_N^2/2m_N)$, and writing this in second quantization, we obtain

$$\begin{aligned} |\,\boldsymbol{p}_N m_{s_N}\,\rangle = \sum_{lm_l}\sum_{jm_j}(4\pi)\frac{\sqrt{\pi}}{\sqrt{2m_N p_N}} i^l e^{i(\delta_l+\sigma_l)} Y^*_{lm_l}(\Omega_N) \\ \times \langle l\ m_l\ 1/2\ m_{s_N}\,|\,j\ m_j\rangle\,\widehat{c}^\dagger_{ljm_j}\,|\,\Phi_{gs}\,\rangle. \end{aligned} \tag{3.17}$$

[3]The radial Schrödinger equation in a Coulomb potential, for $r \to \infty$, equals the Coulomb equation. The solutions with $E > 0$ are the Coulomb functions, see e.g. `http://dlmf.nist.gov/33`.

For the $A-1$ system, we change the notation from a residual nucleus with quantum numbers J_R, M_R to a hole state with quantum numbers j_h, m_h ($J_R = j_h, M_R = m_h$). In second quantization this is written as

$$| \Phi_f^{(A-1)}(E^{exc}, J_R M_R) \rangle = | h^{-1}(E^{exc}, j_h m_h) \rangle \tag{3.18}$$

$$= (-1)^{j_h+m_h} \widehat{c}_{j_h,-m_h} | \Phi_{gs} \rangle. \tag{3.19}$$

This expression shows that the removal of a particle from the single-particle level with quantum numbers $j_h, -m_h$ leaves the residual nucleus in a state with quantum numbers j_h, m_h.

Combining the expressions for the emitted nucleon and the residual nucleus, the full nuclear final state can be written as

$$| \Phi^{1p1h} \rangle = | \Phi_f^{(A-1)}(E^{exc}, J_R M_R);\, \boldsymbol{p}_N m_{s_N} \rangle_{as} \tag{3.20}$$

$$= \sum_{lm_l} \sum_{jm_j} (4\pi) \frac{\sqrt{\pi}}{\sqrt{2m_N p_N}} i^l e^{i(\delta_l+\sigma_l)} Y^*_{lm_l}(\Omega_N)(-1)^{j_h+m_h}$$

$$\times \langle l \;\; m_l \;\; 1/2 \;\; m_{s_N} \,|\, j \;\; m_j \rangle \widehat{c}^\dagger_{ljm_j} \widehat{c}_{j_h,-m_h} | \Phi_{gs} \rangle. \tag{3.21}$$

The subscript 'as' in the first line stands for the antisymmetrization of the $A-1$ nucleons in the residual nucleus. As the expression is written in second quantization in Eq. (3.21), this antisymmetry condition is automatically satisfied.

3.1.2 Exclusive one-body matrix elements for $1N$ knockout

With the nuclear final state written in second quantization, we have all the necessary elements to calculate the transition matrix elements of Eq. (3.5). In this subsection, we discuss the case where the nuclear current operator consists purely of one-body operators. This corresponds to the IA. The expressions for the nuclear current in the IA are given in Chapter 2.

As discussed in Chapter 2, the time-like and three spherical components of the nuclear current can be expressed as a function of the two multipole operators $\widehat{M}$ and $\widehat{O}$, Eqs. (2.74) and (2.78), and it is sufficient to calculate the matrix elements of these two operators to obtain the expectation values of the four components of the nuclear current. They are just linear combinations of the two matrix elements.

First we show how to calculate matrix elements of the type $\langle \Phi^{1p1h} | \widehat{\mathcal{O}}^{[1]}_{JM}(q) | \Phi_{gs} \rangle$, where $\widehat{\mathcal{O}}^{[1]}_{JM}(q)$ can be any of the multipole operators, Eqs. (2.74-2.78). The superscript '[1]' indicates that we are working with a one-body operator. As a starting point, we write down the one-body operator in second quantization, this is where the difference between the one-body and two-body operators originates,

$$\widehat{\mathcal{O}}^{[1]}_{JM}(q) = \sum_{\alpha\beta} \langle \alpha | \widehat{\mathcal{O}}^{[1]}_{JM}(q) | \beta \rangle \widehat{c}^\dagger_\alpha \widehat{c}_\beta. \tag{3.22}$$

Using this, and substituting the expression for the $1p1h$ final state, Eq. (3.21), we can write the transition matrix element as

$$\langle \Phi^{1p1h} | \widehat{\mathcal{O}}^{[1]}_{JM}(q) | \Phi_{gs} \rangle = \sum_{lm_l} \sum_{jm_j} (4\pi) \frac{\sqrt{\pi}}{\sqrt{2m_N p_N}} (-i)^l e^{-i(\delta_l+\sigma_l)} Y_{lm_l}(\Omega_N)(-1)^{j_h+m_h}$$

$$\times \langle\, l\ \ m_l\ \ 1/2\ \ m_{s_N} \,|\, j\ \ m_j \rangle \sum_{\alpha\beta} \langle\, \alpha \,|\, \widehat{\mathcal{O}}^{[1]}_{JM}(q) \,|\, \beta \,\rangle \langle\, \Phi_{gs} \,|\, \widehat{c}^{\dagger}_h \widehat{c}_p \widehat{c}^{\dagger}_\alpha \widehat{c}_\beta \,|\, \Phi_{gs} \,\rangle, \tag{3.23}$$

where we have abbreviated the notation of the particle and hole creation operators. The $\widehat{c}^{\dagger}_p$ creates a particle with quantum numbers l, j, m_j and $\widehat{c}_h$ removes a particle with quantum numbers $j_h, -m_h$ from the nucleus $|\, \Phi_{gs} \,\rangle$. The operator expansion in the second line can be written as

$$\sum_{\alpha\beta} \langle\, \alpha \,|\, \widehat{\mathcal{O}}^{[1]}_{JM}(q) \,|\, \beta \,\rangle \langle\, \Phi_{gs} \,|\, \widehat{c}^{\dagger}_h \widehat{c}_p \widehat{c}^{\dagger}_\alpha \widehat{c}_\beta \,|\, \Phi_{gs} \,\rangle = -\langle\, p \,|\, \widehat{\mathcal{O}}^{[1]}_{JM}(q) \,|\, h \,\rangle, \tag{3.24}$$

which is used to write the transition matrix element as

$$\begin{aligned}
\langle\, \Phi^{1p1h} \,|\, \widehat{\mathcal{O}}^{[1]}_{JM}(q) \,|\, \Phi_{gs} \,\rangle &= \sum_{lm_l} \sum_{jm_j} (4\pi) \frac{\sqrt{\pi}}{\sqrt{2m_N p_N}} (-i)^l e^{-i(\delta_l + \sigma_l)} Y_{lm_l}(\Omega_N) (-1)^{j_h + m_h + 1} \\
&\quad \times \langle\, l\ \ m_l\ \ 1/2\ \ m_{s_N} \,|\, j\ \ m_j \rangle \langle\, p \,|\, \widehat{\mathcal{O}}^{[1]}_{JM}(q) \,|\, h \,\rangle \qquad (3.25) \\
&= \sum_{lm_l} \sum_{jm_j} (4\pi) \frac{\sqrt{\pi}}{\sqrt{2m_N p_N}} (-i)^l e^{-i(\delta_l + \sigma_l)} Y_{lm_l}(\Omega_N) (-1)^{j_h + m_h + 1} \\
&\quad \times \langle\, l\ \ m_l\ \ 1/2\ \ m_{s_N} \,|\, j\ \ m_j \rangle (-1)^{j - m_j} \begin{pmatrix} j & J & j_h \\ -m_j & M & m_h \end{pmatrix} \langle\, p \parallel \widehat{\mathcal{O}}^{[1]}_J(q) \parallel h \,\rangle. \qquad (3.26)
\end{aligned}$$

In the second line, we relied on the fact that the multipole operators are spherical tensor operators and used the Wigner-Eckart theorem to write the $1p1h$ matrix element as a reduced matrix element, multiplied by a 3j symbol and a phase factor. The derived expression is valid for each spherical tensor one-body operator. Using the partial wave expressions for the nuclear current in momentum space, Eqs. (2.71)-(2.73), the time-like and spherical components of the transition matrix elements which are needed for the calculation of the responses are given by

$$\begin{aligned}
\mathcal{J}^{[1]}_0 &= +\sqrt{4\pi} \sum_{J \geq 0} i^J \widehat{J} \sum_{lm_l} \sum_{jm_j} (4\pi) \frac{\sqrt{\pi}}{\sqrt{2m_N p_N}} (-i)^l e^{-i(\delta_l + \sigma_l)} Y_{lm_l}(\Omega_N) (-1)^{j_h + m_h + 1} \\
&\quad \times \langle\, l\ \ m_l\ \ 1/2\ \ m_{s_N} \,|\, j\ \ m_j \rangle (-1)^{j - m_j} \begin{pmatrix} j & J & j_h \\ -m_j & 0 & m_h \end{pmatrix} \langle\, p \parallel \widehat{M}^{\mathrm{Coul},[1]}_J(q) \parallel h \,\rangle, \qquad (3.27) \\
\mathcal{J}^{[1]}_3 &= -\sqrt{4\pi} \sum_{J \geq 0} i^J \widehat{J} \sum_{lm_l} \sum_{jm_j} (4\pi) \frac{\sqrt{\pi}}{\sqrt{2m_N p_N}} (-i)^l e^{-i(\delta_l + \sigma_l)} Y_{lm_l}(\Omega_N) (-1)^{j_h + m_h + 1} \\
&\quad \times \langle\, l\ \ m_l\ \ 1/2\ \ m_{s_N} \,|\, j\ \ m_j \rangle (-1)^{j - m_j} \begin{pmatrix} j & J & j_h \\ -m_j & 0 & m_h \end{pmatrix} \langle\, p \parallel \widehat{L}^{\mathrm{long},[1]}_J(q) \parallel h \,\rangle, \qquad (3.28) \\
\mathcal{J}^{[1]}_{\pm 1} &= -\sqrt{2\pi} \sum_{J \geq 1} i^J \widehat{J} \sum_{lm_l} \sum_{jm_j} (4\pi) \frac{\sqrt{\pi}}{\sqrt{2m_N p_N}} (-i)^l e^{-i(\delta_l + \sigma_l)} Y_{lm_l}(\Omega_N) (-1)^{j_h + m_h + 1} \\
&\quad \times \langle\, l\ \ m_l\ \ 1/2\ \ m_{s_N} \,|\, j\ \ m_j \rangle (-1)^{j - m_j} \begin{pmatrix} j & J & j_h \\ -m_j & \pm 1 & m_h \end{pmatrix} \\
&\quad \times \left[\langle\, p \parallel \widehat{T}^{\mathrm{elec},[1]}_J(q) \parallel h \,\rangle \pm \langle\, p \parallel \widehat{T}^{\mathrm{magn},[1]}_J(q) \parallel h \,\rangle \right]. \qquad (3.29)
\end{aligned}$$

The nuclear current matrix elements are expressed as a function of four different $1p1h$ reduced matrix elements $\langle\, p \parallel \widehat{\mathcal{O}}^{[1]}_{JM}(q) \parallel h \,\rangle$. In Appendix E, the results for these reduced

matrix elements, with the nuclear current operator in the low-energy limit, are summarized. We explicitly calculate the response function W_{CC}, this is done by multiplying the expression for $\mathcal{J}_0^{[1]}$ by its complex conjugate and summing over the final states. It results in

$$\begin{aligned} W_{CC}^{[1]} = & \sum_{j_h m_h} 4\pi \sum_{J,J'\geq 0} i^{J-J'} \widehat{J}\widehat{J'} \sum_{lm_l} \sum_{l'm'_l} \sum_{jm_j} \sum_{j',m'_j} \frac{(2\pi)^3}{m_N p_N} (-i)^{l-l'} \\ & \times e^{-i(\delta_l+\sigma_l-\delta_{l'}-\sigma_{l'})} Y_{lm_l}(\Omega_N) Y^*_{l'm_{l'}}(\Omega_N) (-1)^{j-m_j+j'-m_{j'}} \\ & \times \langle l \;\; m_l \;\; 1/2 \;\; m_{s_N} \,|\, j \;\; m_j \rangle \langle l' \;\; m_{l'} \;\; 1/2 \;\; m_{s_N} \,|\, j' \;\; m_{j'} \rangle \\ & \times \begin{pmatrix} j & J & j_h \\ -m_j & 0 & m_h \end{pmatrix} \begin{pmatrix} j' & J' & j_h \\ -m_{j'} & 0 & m_h \end{pmatrix} \\ & \times \langle\, p \parallel \widehat{M}_J^{\mathrm{Coul},[1]}(q) \parallel h \,\rangle \left(\langle\, p' \parallel \widehat{M}_{J'}^{\mathrm{Coul},[1]}(q) \parallel h \,\rangle \right)^* . \end{aligned} \tag{3.30}$$

We did not explicitly write the sum over m_{s_N} as its value is fixed by $m_l + m_{s_N} = m_j$. The expressions for the other nine response functions can be obtained easily.

3.1.3 Exclusive two-body and interference matrix elements for $1N$ knockout

Above exclusive $1N$ knockout responses for processes with pure one-body currents were presented. This section deals with interactions where the boson interacts with a two-body current, but only a single nucleon is emitted from the nucleus. This reaction is displayed in Fig. 3.4, where the shaded circle represents the two-body current.

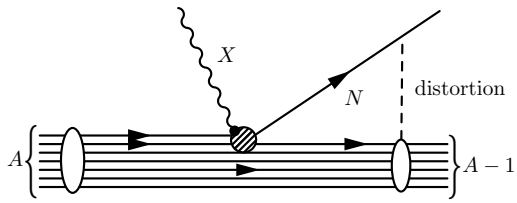

Figure 3.4: Graphical representation of the influence of two-body currents on $1N$ knockout. Same as Fig. 1.14.

To calculate the expectation values of a two-body operator for $1N$ knockout interactions, we follow the same steps as for the one-body operator. The superscript '[2]' is introduced to indicate that we are working with a two-body operator. A general two-body operator $\widehat{\mathcal{O}}_{JM}^{[2]}(q)$ is written in second quantization as

$$\widehat{\mathcal{O}}_{JM}^{[2]}(q) = \frac{1}{2} \sum_{\alpha\beta\gamma\delta} \langle\, \alpha\beta \,|\, \widehat{\mathcal{O}}_{JM}^{[2]}(q) \,|\, \gamma\delta \,\rangle \widehat{c}_\alpha^\dagger \widehat{c}_\beta^\dagger \widehat{c}_\delta \widehat{c}_\gamma . \tag{3.31}$$

Using Eq. (3.21), the transition matrix element can be written as

$$\langle\, \Phi^{1p1h} \,|\, \widehat{\mathcal{O}}_{JM}^{[2]}(q) \,|\, \Phi_{gs} \,\rangle = \sum_{lm_l} \sum_{jm_j} (4\pi) \frac{\sqrt{\pi}}{\sqrt{2m_N p_N}} (-i)^l e^{-i(\delta_l+\sigma_l)} Y_{lm_l}(\Omega_N) (-1)^{j_h+m_h}$$

$$\times \langle l\ \ m_l\ \ 1/2\ \ m_{s_N} \,|\, j\ \ m_j\rangle \frac{1}{2} \sum_{\alpha\beta\gamma\delta} \langle\, \alpha\beta \,|\, \widehat{\mathcal{O}}^{[2]}_{JM}(q) \,|\, \gamma\delta \,\rangle \langle\, \Phi_{gs} \,|\, \widehat{c}^\dagger_h \widehat{c}_p \widehat{c}^\dagger_\alpha \widehat{c}^\dagger_\beta \widehat{c}_\delta \widehat{c}_\gamma \,|\, \Phi_{gs} \,\rangle, \tag{3.32}$$

using the same shorthand notation for the particle and hole states as in Section 3.1.2. The second quantization expression in the last line results in

$$\frac{1}{2} \sum_{\alpha\beta\gamma\delta} \langle\, \alpha\beta \,|\, \widehat{\mathcal{O}}^{[2]}_{JM}(q) \,|\, \gamma\delta \,\rangle \langle\, \Phi_{gs} \,|\, \widehat{c}^\dagger_h \widehat{c}_p \widehat{c}^\dagger_\alpha \widehat{c}^\dagger_\beta \widehat{c}_\delta \widehat{c}_\gamma \,|\, \Phi_{gs} \,\rangle = -\sum_{h'} \langle\, ph' \,|\, \widehat{\mathcal{O}}^{[2]}_{JM}(q) \,|\, hh' \,\rangle_{as}, \tag{3.33}$$

the sum extends over all occupied single-particle states of the target nucleus. This is the sum that was shown schematically in Fig. 3.2b. In the next step, we couple the $|\, ph' \,\rangle$ and $|\, hh' \,\rangle$ states to a total quantum number J_1 and J_2

$$\sum_{h'} \langle\, ph' \,|\, \widehat{\mathcal{O}}^{[2]}_{JM}(q) \,|\, hh' \,\rangle_{as} = \sum_{l'_h} \sum_{j'_h m_{j'_h}} \langle\, j m_j; j'_h m_{j'_h} \,|\, \widehat{\mathcal{O}}^{[2]}_{JM}(q) \,|\, j_h m_h; j'_h m_{j'_h} \,\rangle_{as} \tag{3.34}$$

$$= \sum_{l'_h} \sum_{j'_h m_{j'_h}} \sum_{J_1 M_1} \sum_{J_2 M_2} \langle j\ \ m_j\ \ j'_h\ \ m_{j'_h} \,|\, J_1\ \ M_1\rangle \langle j_h\ \ m_h\ \ j'_h\ \ m_{j'_h} \,|\, J_2\ \ M_2\rangle$$

$$\times \langle\, ph'; J_1 M_1 \,|\, \widehat{\mathcal{O}}^{[2]}_{JM}(q) \,|\, hh'; J_2 M_2 \,\rangle_{as} \tag{3.35}$$

$$= \sum_{l'_h} \sum_{j'_h m_{j'_h}} \sum_{J_1 M_1} \sum_{J_2 M_2} \langle j\ \ m_j\ \ j'_h\ \ m_{j'_h} \,|\, J_1\ \ M_1\rangle \langle j_h\ \ m_h\ \ j'_h\ \ m_{j'_h} \,|\, J_2\ \ M_2\rangle$$

$$\times (-1)^{J_1 - M_1} \begin{pmatrix} J_1 & J & J_2 \\ -M_1 & M & M_2 \end{pmatrix} \langle\, ph'; J_1 \,\|\, \widehat{\mathcal{O}}^{[2]}_{J}(q) \,\|\, hh'; J_2 \,\rangle_{as}. \tag{3.36}$$

Substituting this expression in Eq. (3.32), the transition matrix element can be written as

$$\langle\, \Phi^{1p1h} \,|\, \widehat{\mathcal{O}}^{[2]}_{JM}(q) \,|\, \Phi_{gs} \,\rangle = \sum_{l m_l} \sum_{j m_j} \sum_{l'_h} \sum_{j'_h m_{j'_h}} \sum_{J_1 M_1} \sum_{J_2 M_2} (4\pi) \frac{\sqrt{\pi}}{\sqrt{2 m_N p_N}} (-i)^l e^{-i(\delta_l + \sigma_l)} Y_{l m_l}(\Omega_N)$$

$$\times \langle l\ \ m_l\ \ 1/2\ \ m_{s_N} \,|\, j\ \ m_j\rangle \langle j\ \ m_j\ \ j'_h\ \ m_{j'_h} \,|\, J_1\ \ M_1\rangle \langle j_h\ \ m_h\ \ j'_h\ \ m_{j'_h} \,|\, J_2\ \ M_2\rangle$$

$$\times (-1)^{j_h + m_h + J_1 - M_1 + 1} \begin{pmatrix} J_1 & J & J_2 \\ -M_1 & M & M_2 \end{pmatrix} \langle\, ph'; J_1 \,\|\, \widehat{\mathcal{O}}^{[2]}_{J}(q) \,\|\, hh'; J_2 \,\rangle_{as}, \tag{3.37}$$

$$= \sum_{l m_l} \sum_{j m_j} \sum_{l'_h j'_h} \sum_{J_1} \sum_{J_2} (4\pi) \frac{\sqrt{\pi}}{\sqrt{2 m_N p_N}} (-i)^l e^{-i(\delta_l + \sigma_l)} Y_{l m_l}(\Omega_N)$$

$$\times \langle l\ \ m_l\ \ 1/2\ \ m_{s_N} \,|\, j\ \ m_j\rangle \begin{pmatrix} j & J & j_h \\ m_j & -M & -m_h \end{pmatrix} \begin{Bmatrix} j & J & j_h \\ J_2 & j'_h & J_1 \end{Bmatrix}$$

$$\times \widehat{J_1} \widehat{J_2} (-1)^{-j + j'_h - J_2 - M + 1} \langle\, ph'; J_1 \,\|\, \widehat{\mathcal{O}}^{[2]}_{J}(q) \,\|\, hh'; J_2 \,\rangle_{as}. \tag{3.38}$$

We used a Racah-algebra to relate three three-j symbols with one three-j symbol and one six-j symbol in the last step. Using this expression to calculate $\mathcal{J}_0$, the expectation value of Coulomb current operator Eq. (2.71), we obtain

$$\mathcal{J}^{[2]}_0 = \sqrt{4\pi} \sum_{J \geq 0} i^J \widehat{J} \sum_{l m_l} \sum_{j m_j} \sum_{l'_h j'_h} \sum_{J_1} \sum_{J_2} (4\pi) \frac{\sqrt{\pi}}{\sqrt{2 m_N p_N}} (-i)^l e^{-i(\delta_l + \sigma_l)} Y_{l m_l}(\Omega_N)$$

$$\times \langle l\ \ m_l\ \ 1/2\ \ m_{s_N} \,|\, j\ \ m_j\rangle \begin{pmatrix} j & J & j_h \\ m_j & 0 & -m_h \end{pmatrix} \begin{Bmatrix} j & J & j_h \\ J_2 & j'_h & J_1 \end{Bmatrix}$$

$$\times \widehat{J_1}\widehat{J_2}(-1)^{-j+j'_h-J_2+1}\mathcal{M}^{\mathrm{Coul},[2]}_{ph';hh'}(J_1,J,J_2), \tag{3.39}$$

the matrix elements $\mathcal{M}$ are defined as

$$\begin{aligned}\mathcal{M}^{\mathrm{Coul},[2]}_{ph';hh'}(J_1,J,J_2) =& \langle\, p_N(E_N lj)h';J_1 \parallel \widehat{M}^{\mathrm{Coul},[2]}_J(q) \parallel hh';J_2\,\rangle \\ &-(-1)^{j_h+j'_h+J_2}\langle\, p_N(E_N lj)h';J_1 \parallel \widehat{M}^{\mathrm{Coul},[2]}_J(q) \parallel h'h;J_2\,\rangle.\end{aligned} \tag{3.40}$$

The operator $\widehat{M}^{\mathrm{Coul},[2]}$ is the same operator as the one in Eq. (3.27), defined in Eq. (2.74), but the nuclear current in the expression has been replaced with a two-body operator. Similar expressions for the expectation values of the longitudinal and transverse currents can be obtained. Multiplying this expression with its complex conjugate, the contribution of the two-body currents to the $1N$ knockout response function W_{CC} is calculated

$$\begin{aligned}W^{[2]}_{CC} =& \sum_{j_h m_h} 4\pi \sum_{JJ'\geq 0} i^{J-J'}\widehat{J}\widehat{J'}\sum_{lm_l}\sum_{jm_j}\sum_{l'm'_l}\sum_{j'm'_j}\sum_{l_{h_1}j_{h_1}}\sum_{l_{h_2}j_{h_2}}\sum_{J_1J'_1}\sum_{J_2J'_2}\frac{(2\pi)^3}{m_N p_N}(-i)^{l-l'} \\ &\times e^{-i(\delta_l+\sigma_l-\delta_{l'}-\sigma_{l'})}Y_{lm_l}(\Omega_N)Y^*_{l'm'_l}(\Omega_N)\widehat{J_1}\widehat{J_2}\widehat{J'_1}\widehat{J'_2}(-1)^{-j-j'+j_{h_1}+j_{h_2}-J_2-J'_2} \\ &\times \langle l\ m_l\ 1/2\ m_{s_N}\,|\,j\ m_j\rangle \begin{pmatrix} j & J & j_h \\ m_j & 0 & -m_h\end{pmatrix}\begin{Bmatrix} j & J & j_h \\ J_2 & j_{h_1} & J_1\end{Bmatrix} \\ &\times \langle l'\ m'_l\ 1/2\ m_{s_N}\,|\,j'\ m'_j\rangle \begin{pmatrix} j' & J' & j_h \\ m'_j & 0 & -m_h\end{pmatrix}\begin{Bmatrix} j' & J' & j_h \\ J'_2 & j_{h_2} & J'_1\end{Bmatrix} \\ &\times \mathcal{M}^{\mathrm{Coul},[2]}_{ph_1;hh_1}(J_1,J,J_2)\Big(\mathcal{M}^{\mathrm{Coul},[2]}_{p'h_2;hh_2}(J'_1,J',J'_2)\Big)^*.\end{aligned} \tag{3.41}$$

The third term contributing to the $1N$ knockout response functions is the interference term between the one- and two-body currents. For the response W_{CC}, this term is calculated by combining Eqs. (3.27) and (3.39)

$$W^{[1,2]}_{CC} = \sum_{j_h m_h} 2\,\mathrm{Re}\left[\mathcal{J}^{[1]}_0\left(\mathcal{J}^{[2]}_0\right)^*\right] \tag{3.42}$$

$$\begin{aligned}=& \sum_{j_h m_h} 2\,\mathrm{Re}\Bigg[4\pi \sum_{JJ'\geq 0} i^{J-J'}\widehat{J}\widehat{J'}\sum_{lm_l}\sum_{jm_j}\sum_{l'm'_l}\sum_{'jm'_j}\sum_{l'_h j'_h}\sum_{J_1}\sum_{J_2}\frac{(2\pi)^3}{m_N p_N}(-i)^{l-l'} \\ &\times e^{-i(\delta_l+\sigma_l-\delta_{l'}-\sigma_{l'})}Y_{lm_l}(\Omega_N)Y^*_{l'm'_l}(\Omega_N)(-1)^{j_h+m_h+1}\widehat{J_1}\widehat{J_2}(-1)^{-j'+j'_h-J_2+1}(-1)^{j-m_j} \\ &\times \langle l\ m_l\ 1/2\ m_{s_N}\,|\,j\ m_j\rangle \begin{pmatrix} j & J & j_h \\ -m_j & 0 & m_h\end{pmatrix} \\ &\times \langle l'\ m'_l\ 1/2\ m_{s_N}\,|\,j'\ m'_j\rangle \begin{pmatrix} j' & J' & j_h \\ m'_j & 0 & -m_h\end{pmatrix}\begin{Bmatrix} j' & J' & j_h \\ J_2 & j'_h & J_1\end{Bmatrix} \\ &\times \langle\, p \parallel \widehat{M}^{\mathrm{Coul},[1]}_J(q) \parallel h\,\rangle\left(\mathcal{M}^{\mathrm{Coul},[2]}_{ph';hh'}(J_1,J',J_2)\right)^*\Bigg].\end{aligned} \tag{3.43}$$

The total $1N$ knockout Coulomb response is given by the sum of the three contributions

$$W_{CC} = W^{[1]}_{CC} + W^{[2]}_{CC} + W^{[1,2]}_{CC}. \tag{3.44}$$

The other nine $1p1h$ response functions with two-body currents and interference terms are obtained following the same steps.

3.2 Exclusive $1N$ knockout studies

Exclusive $(e, e'\mathrm{p})$ reactions in QE kinematics have long been used to study nuclear electromagnetic responses [5,6]. Electron scattering experiments that detect the final state electron, the emitted nucleon and the final state nucleus can select events where the nucleon is emitted from the nucleus without being subject to inelastic collisions or charge-exchange type reactions[4]. The exclusive $1N$ knockout responses derived above can then be used to study these exclusive $1N$ knockout interactions.

Knockout of $1p_{1/2}$ and $1p_{3/2}$-shell protons in $^{16}\mathrm{O}(e, e'\mathrm{p})$ was studied at Saclay [7], NIKHEF [8,9] and MAMI (Mainz) [10] at $Q^2 < 0.4$ $(\mathrm{GeV/c})^2$ as a function of missing momentum ($p_m = |\boldsymbol{q} - \boldsymbol{p}_N|$). The IA does a fair job in describing the shape of these exclusive cross section results, as most of the data were taken at QE kinematics. However, when moving away from the QE region, multinucleon mechanisms should be taken into account. For very low energy transfers, long-range correlations should be taken into account [11]. For high missing momenta, the model should account for MECs and SRCs [12–14].

More recent studies by Fissum *et al.* [15] and Iodice *et al.* [16] investigated these reactions at higher missing energies, corresponding with the dip region. Discrepancies between exclusive $(e, e'\mathrm{p})$ data and $1N$ knockout calculations at high missing energy indicate that reactions where two nucleons are emitted play a role in the description of the process.

From a neutrino point of view, these very exclusive $1N$ knockout interactions have been less interesting as most available neutrino data is very inclusive. The interest is growing however, as the new generations of neutrino detectors are able to detect the nucleons in the final state, and more exclusive data is becoming available. Remark that for the current generation of neutrino experiments, the energy of the incoming neutrino is not known, it is distributed over a range of energies, hence the exact energy and momentum transfer is unknown.

3.3 Inclusive $1N$ knockout cross section

The $1N$ knockout differential cross section derived in the previous chapter, Eq. (2.46), is valid for exclusive $A(l, l'N)$ interactions, where the final state nucleon is observed in coincidence with the final state lepton. For inclusive $1N$ knockout reactions $A(l, l')$, only the final state lepton is detected, so we need to integrate over the angle Ω_N of the undetected nucleon

$$\frac{\mathrm{d}\sigma^X}{\mathrm{d}\epsilon_f \mathrm{d}\Omega_f}(l, l') = \int \mathrm{d}\Omega_N \frac{\mathrm{d}\sigma^X}{\mathrm{d}\epsilon_f \mathrm{d}\Omega_f \mathrm{d}\Omega_N}(l, l'N). \tag{3.45}$$

We will work in the ideal case, where all the momentum is transferred to the outgoing nucleon ($f_{rec} = 1$). As the kinematic factors v_i and the Mott-like prefactors σ^X are independent of Ω_N, we need to integrate the ten responses. In the following sections we will show that the inclusive cross section for neutrino interactions can be written as function of five response

[4] This is the conventional way to define an exclusive $1N$ knockout event in the electron scattering community.

functions. For electron scattering, using CVC only two responses are necessary

$$\frac{\mathrm{d}\sigma^W}{\mathrm{d}\epsilon_f \mathrm{d}\Omega_f} = 4\pi \, \frac{E_N}{m_N} \, \sigma^W \zeta \big[v_{CC} W_{CC} + v_{CL} W_{CL} + v_{LL} W_{LL} + v_T W_T + h v_{T'} W_{T'} \big], \tag{3.46}$$

$$\frac{\mathrm{d}\sigma^\gamma}{\mathrm{d}\epsilon_f \mathrm{d}\Omega_f} = 4\pi \, \frac{E_N}{m_N} \, \sigma^{\mathrm{Mott}} \big[v_L^e W_{CC} + v_T^e W_T \big]. \tag{3.47}$$

The five response functions $\{TC, TL, TT, TC', TL'\}$ in Eq. (2.46) canceled after the integration, because they are odd functions of Ω_N.

3.3.1 Inclusive one-body matrix elements for $1N$ knockout

Similar as for exclusive $1N$ knockout cross sections, we start with the responses of the one-body part of the nuclear current operator, before we continue with the two-body and interference responses. For the Coulomb response $W_{CC}^{[1]}$ we integrate Eq. (3.30) over the outgoing nucleon angle Ω_N

$$\begin{aligned}
\int \mathrm{d}\Omega_N W_{CC}^{[1]} = \int \mathrm{d}\Omega_N \sum_{j_h m_h} 4\pi \sum_{J,J' \geq 0} i^{J-J'} \widehat{J}\widehat{J'} \sum_{l m_l} \sum_{l', m_l'} \sum_{j m_j} \sum_{j', m_j'} \frac{(2\pi)^3}{m_N p_N} (-i)^{l-l'} \\
\times e^{-i(\delta_l + \sigma_l - \delta_{l'} - \sigma_{l'})} Y_{l m_l}(\Omega_N) Y^*_{l' m_{l'}}(\Omega_N) (-1)^{j - m_j + j' - m_{j'}} \\
\times \langle l \;\; m_l \;\; 1/2 \;\; m_{s_N} \,|\, j \;\; m_j \rangle \langle l' \;\; m_{l'} \;\; 1/2 \;\; m_{s_N} \,|\, j' \;\; m_{j'} \rangle \\
\times \begin{pmatrix} j & J & j_h \\ -m_j & 0 & m_h \end{pmatrix} \begin{pmatrix} j' & J' & j_h \\ -m_{j'} & 0 & m_h \end{pmatrix} \\
\times \langle p \parallel \widehat{M}_J^{\mathrm{Coul},[1]}(q) \parallel h \rangle \Big(\langle p \parallel \widehat{M}_{J'}^{\mathrm{Coul},[1]}(q) \parallel h \rangle \Big)^* .
\end{aligned} \tag{3.48}$$

This integral is easily calculated when using the orthogonality relation of the spherical harmonics in the first step, and using the orthogonality of the Clebsch-Gordan coefficients and Wigner three-j symbols in the subsequent steps. This results in

$$\int \mathrm{d}\Omega_N W_{CC}^{[1]} = 4\pi \frac{(2\pi)^3}{m_N p_N} \sum_{j_h} \sum_{J \geq 0} \sum_{lj} \Big| \langle p \parallel \widehat{M}_J^{\mathrm{Coul},[1]}(q) \parallel h \rangle \Big|^2 . \tag{3.49}$$

The results for $W_{CL}^{[1]}$ and $W_{LL}^{[1]}$ are found following the same steps.

$$\begin{aligned}
\int \mathrm{d}\Omega_N W_{CL}^{[1]} = -4\pi \frac{(2\pi)^3}{m_N p_N} \sum_{j_h} \sum_{J \geq 0} \sum_{lj} \\
\times 2 \, \mathrm{Re} \Big[\langle p \parallel \widehat{M}_J^{\mathrm{Coul},[1]}(q) \parallel h \rangle \Big(\langle p \parallel \widehat{M}_L^{\mathrm{long},[1]}(q) \parallel h \rangle \Big)^* \Big],
\end{aligned} \tag{3.50}$$

$$\int \mathrm{d}\Omega_N W_{LL}^{[1]} = 4\pi \frac{(2\pi)^3}{m_N p_N} \sum_{j_h} \sum_{J \geq 0} \sum_{lj} \Big| \langle p \parallel \widehat{L}_J^{\mathrm{long},[1]}(q) \parallel h \rangle \Big|^2 . \tag{3.51}$$

Calculating the integral of the other seven response functions, the following step is encountered

$$\sum_{m_j} \sum_{m_h} \begin{pmatrix} j & J & j_h \\ -m_j & \lambda & m_h \end{pmatrix} \begin{pmatrix} j & J' & j_h \\ -m_j & \lambda' & m_h \end{pmatrix} = \frac{1}{2J+1} \delta_{JJ'} \delta_{\lambda\lambda'}, \tag{3.52}$$

where the $\lambda = 0$ for the Coulomb and longitudinal components and $+1$ or -1 for the transverse components. This shows that the responses $\{TC, TL, TT, TC', TL'\}$ will drop out, because they only contain terms with e.g. $\lambda = 0$ and $\lambda' = \pm 1$, and thus $\delta_{\lambda\lambda'} = 0$. Calculating the integral for the transverse response W_T, we obtain

$$\begin{aligned}
&\int \mathrm{d}\Omega_N W_T^{[1]} \\
&\quad = 2\pi \frac{(2\pi)^3}{m_N p_N} \sum_{j_h} \sum_{J\geq 1} \sum_{lj} \sum_{\lambda=\pm 1} \left| \langle p \parallel \widehat{T}_J^{\mathrm{elec},[1]}(q) \parallel h \rangle + \lambda \langle p \parallel \widehat{T}_J^{\mathrm{magn},[1]}(q) \parallel h \rangle \right|^2 \\
&\quad = 4\pi \frac{(2\pi)^3}{m_N p_N} \sum_{j_h} \sum_{J\geq 1} \sum_{lj} \left| \langle p \parallel \widehat{T}_J^{\mathrm{elec},[1]}(q) \parallel h \rangle \right|^2 + \left| \langle p \parallel \widehat{T}_J^{\mathrm{magn},[1]}(q) \parallel h \rangle \right|^2 . \qquad (3.53)
\end{aligned}$$

For $W_{T'}$ only the interference terms remain

$$\begin{aligned}
&\int \mathrm{d}\Omega_N W_{T'}^{[1]} \\
&\quad = 2\pi \frac{(2\pi)^3}{m_N p_N} \sum_{j_h} \sum_{J\geq 1} \sum_{lj} \sum_{\lambda=\pm 1} \lambda \left| \langle p \parallel \widehat{T}_J^{\mathrm{elec},[1]}(q) \parallel h \rangle + \lambda \langle p \parallel \widehat{T}_J^{\mathrm{magn},[1]}(q) \parallel h \rangle \right|^2 \\
&\quad = 4\pi \frac{(2\pi)^3}{m_N p_N} \sum_{j_h} \sum_{J\geq 1} \sum_{lj} 2\,\mathrm{Re} \left[\langle p \parallel \widehat{T}_J^{\mathrm{elec},[1]}(q) \parallel h \rangle \left(\langle p \parallel \widehat{T}_J^{\mathrm{magn},[1]}(q) \parallel h \rangle \right)^* \right] . \qquad (3.54)
\end{aligned}$$

The structure of the T' response shows why it is often called the interference response in literature. We will not use this term as we have more than one response function that contains interference contributions, the CL response for example for inclusive scattering and more for exclusive scattering.

The factor $4\pi(2\pi)^3/(m_N p_N)$ appearing in all the expressions is absorbed in the prefactor of the differential cross section. Combining these results, the expressions Eqs. (3.46) and (3.47) given at the beginning of this section are obtained.

As explained in Chapter 2, the longitudinal, electric and magnetic multipole operators are calculated using the operator $\widehat{O}$, Eq. (2.78). Substituting the expressions for the nuclear current operator in the IA, Eqs. (2.89)-(2.93), in the multipole operators, the inclusive $1p1h$ response functions in the IA can be calculated. The expressions for the reduced matrix elements are given in Appendix E. In Section 3.4, results of these inclusive $1N$ knockout calculations in the IA are shown for electron-induced and muon-neutrino induced interactions and the electron calculations are compared with (e, e') data.

3.3.2 Inclusive two-body and interference matrix elements for $1N$ knockout

For the inclusive responses with the two-body part of the nuclear current, we integrate Eq. (3.41) over the direction of the outgoing nucleon Ω_N

$$\int \mathrm{d}\Omega_N W_{CC}^{[2]} = \int \mathrm{d}\Omega_N \sum_{j_h m_h} 4\pi \sum_{JJ'\geq 0} i^{J-J'} \widehat{J}\widehat{J'} \sum_{lm_l} \sum_{jm_j} \sum_{l'm'_l} \sum_{j'm'_j} \sum_{l_{h_1} j_{h_1}} \sum_{l_{h_2} j_{h_2}} \sum_{J_1 J'_1} \sum_{J_2 J'_2}$$

$$\times \frac{(2\pi)^3}{m_N p_N}(-i)^{l-l'}e^{-i(\delta_l+\sigma_l-\delta_{l'}-\sigma_{l'})}Y_{lm_l}(\Omega_N)Y^*_{l'm'_l}(\Omega_N)\widehat{J_1}\widehat{J_2}\widehat{J'_1}\widehat{J'_2}(-1)^{-j-j'+j_{h_1}+j_{h_2}-J_2-J'_2}$$
$$\times \langle l\ m_l\ 1/2\ m_{s_N}\,|\,j\ m_j\rangle \begin{pmatrix} j & J & j_h \\ m_j & 0 & -m_h \end{pmatrix} \begin{Bmatrix} j & J & j_h \\ J_2 & j_{h_1} & J_1 \end{Bmatrix}$$
$$\times \langle l'\ m'_l\ 1/2\ m_{s_N}\,|\,j'\ m'_j\rangle \begin{pmatrix} j' & J' & j_h \\ m'_j & 0 & -m_h \end{pmatrix} \begin{Bmatrix} j' & J' & j_h \\ J'_2 & j_{h_2} & J'_1 \end{Bmatrix}$$
$$\times \mathcal{M}^{\mathrm{Coul},[2]}_{ph_1;hh_1}(J_1,J,J_2)\Big(\mathcal{M}^{\mathrm{Coul},[2]}_{p'h_2;hh_2}(J'_1,J',J'_2)\Big)^*. \tag{3.55}$$

To calculate this integral, the orthogonality between the spherical harmonics is used in the first step. Orthogonality relations between Clebsch-Gordan coefficients and three-j symbols are used in the following steps. It results in

$$\int \mathrm{d}\Omega_N W^{[2]}_{CC} = 4\pi\frac{(2\pi)^3}{m_N p_N}\sum_{j_h}\sum_{J\geq 0}\sum_{lj}\sum_{l_{h_1}j_{h_1}}\sum_{l_{h_2}j_{h_2}}\sum_{J_1J'_1}\sum_{J_2J'_2}$$
$$\times \widehat{J_1}\widehat{J_2}\widehat{J'_1}\widehat{J'_2}(-1)^{j_{h_1}+j_{h_2}-J_2-J'_2}\begin{Bmatrix} j & J & j_h \\ J_2 & j_{h_1} & J_1 \end{Bmatrix}\begin{Bmatrix} j & J & j_h \\ J'_2 & j_{h_2} & J'_1 \end{Bmatrix}$$
$$\times \mathcal{M}^{\mathrm{Coul},[2]}_{ph_1;hh_1}(J_1,J,J_2)\Big(\mathcal{M}^{\mathrm{Coul},[2]}_{ph_2;hh_2}(J'_1,J,J'_2)\Big)^*. \tag{3.56}$$

This can be written in a different way, to make it easier to implement numerically

$$\int \mathrm{d}\Omega_N W^{[2]}_{CC} = 4\pi\frac{(2\pi)^3}{m_N p_N}\sum_{j_h}\sum_{J\geq 0}\sum_{lj}$$
$$\times \left|\sum_{l_{h_1}j_{h_1}}\sum_{J_1J_2}\widehat{J_1}\widehat{J_2}(-1)^{j_{h_1}-J_2}\begin{Bmatrix} j & J & j_h \\ J_2 & j_{h_1} & J_1 \end{Bmatrix}\mathcal{M}^{\mathrm{Coul},[2]}_{ph_1;hh_1}(J_1,J,J_2)\right|^2. \tag{3.57}$$

The integration over Ω_N for the interference contribution, Eq. (3.43), results in

$$\int \mathrm{d}\Omega_N W^{[1,2]}_{CC} = 4\pi\frac{(2\pi)^3}{m_N p_N}\sum_{j_h}\sum_{J\geq 0}\sum_{lj} 2\,\mathrm{Re}\Bigg[\langle\, p \parallel \widehat{M}^{\mathrm{Coul}[1]}_J(q) \parallel h\,\rangle$$
$$\times\left(\sum_{l'_hj'_h}\sum_{J_1J_2}\widehat{J_1}\widehat{J_2}(-1)^{j_h+j'_h-J_2}\begin{Bmatrix} j & J & j_h \\ J_2 & j'_h & J_1 \end{Bmatrix}\mathcal{M}^{\mathrm{Coul},[2]}_{ph';hh'}(J_1,J,J_2)\right)^*\Bigg]. \tag{3.58}$$

The same kinematic factor as for inclusive one-body responses, $4\pi(2\pi)^3/(m_N p_N)$, is absorbed in the prefactor. The other four responses $\{CL, LL, T, T'\}$ can be calculated analogously and the five remaining responses will cancel, for the same reason as in the case of the one-body responses.

With the combination of the one-body, two-body and interference contributions to the inclusive $1N$ knockout responses, the influence of the two-body currents to the $1N$ knockout cross section can be studied. We will defer discussing these effects to the chapters where the two-body currents are discussed.

3.4 Inclusive $1N$ knockout results in the IA

The nuclear current in the IA was described in Section 2.4 and it was mentioned that it can describe the general features of lepton scattering cross sections. In the previous section, the inclusive double differential cross section for electron and neutrino interactions was derived. This means all ingredients are present to test the validity and accuracy of the model in the IA. Below, results for electron scattering are compared with (e, e') data and results are shown for muon-neutrino induced interactions on ^{12}C.

Our description of the single-particle wave functions is based on a nonrelativistic framework, Eq. (3.10). The SkE2 parameterization of the Skyrme potential, used for the calculation of the outgoing nucleons, was fitted to describe the ground state properties of the nucleus and low-lying excited states.

When describing interactions with higher energy and momentum transfers, $q \gtrsim 500$ MeV/c, the momentum of the outgoing nucleon becomes comparable with its rest mass and relativistic effects should be taken into account. In our model, these relativistic corrections are implemented in an effective fashion as explained in Refs. [17–19]. It is achieved by the following substitution for ω in the computation of the outgoing nucleon wave functions

$$\omega \to \omega \left(1 + \frac{\omega}{2m_N}\right). \tag{3.59}$$

This substitution effectively changes the position of the QE peak from its nonrelativistic value to the relativistic position

$$\omega = \frac{q^2}{2m_N} \to \omega = \frac{Q^2}{2m_N}. \tag{3.60}$$

The overall effect of this correction is a shift of the QE peak towards smaller ω and a reduction of the width of the one-body responses.

Due to the wealth of information in electron scattering data, our model is first validated against electron scattering data, before it is confronted with neutrino scattering. The $1p1h$ responses for ^{12}C(e, e') scattering, calculated in the IA, are shown in Fig. 3.5 and compared with data. The form factors used in the electron scattering calculations are the standard dipole form factors and a Galster parameterization for the neutron electric form factor [28]. The predictions are compared with Rosenbluth separated cross section data for a fixed momentum transfer. The IA calculations overestimate the longitudinal responses, while the transverse responses are slightly underestimated for ω-values beyond the QE peak. These results are in-line with other predictions using similar approaches [21,29]. The discrepancy between the results and data can partly be attributed to long-range correlations [30]. In general, the inclusion of long-range correlations decreases both responses. Except at small ω, corresponding with the GR region, it increases the cross sections.

Another effect that influences $1N$ knockout processes is that of two-body currents. The interference effect between one- and two-body currents in the $1N$ knockout channel can either increase or decrease the responses. Furthermore, as the data sets in Fig. 3.5 are inclusive, $2N$ knockout contributions should be considered as well. The influence of these two-body currents will be studied in subsequent chapters.

In Fig. 3.6, we compare the theoretical prediction for the $1p1h$ differential cross section, calculated in the IA, with data for three different target nuclei ^{12}C, ^{16}O and ^{40}Ca for a wide

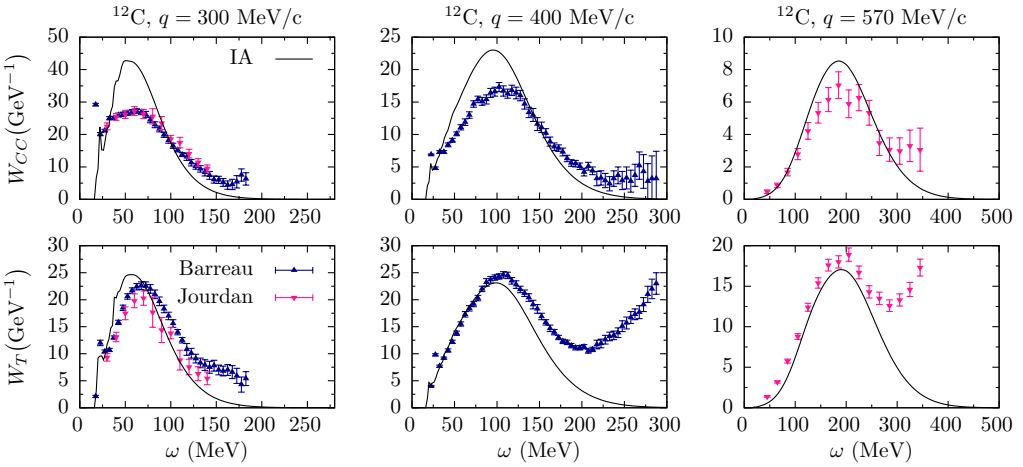

Figure 3.5: The Coulomb and transverse responses for ^{12}C(e, e') for different values of the momentum transfer q in a HF approach. The results are compared with data taken from Refs. [20,21].

range of kinematics. Overall these results provide a reasonable agreement with the QE peak in the data. We stress that the second peak that is visible in some of the data sets is caused by the Δ excitation, which is not described in our model. For small ω, e.g. the top left panel, the IA is not sufficient for a correct description of the data, long-range correlations should be taken into account to describe the low energy excitations [30].

The agreement between the predictions and the two data sets of Baran *et al.* is less good than the other data sets. These two data sets were taken at a forward scattering angle $\theta_{e'} = 11.95°$, which means the cross sections are dominated by the Coulomb channel. As shown above, the description of the W_{CC} response is less satisfactory than the description of the transverse response, which explains the lesser agreement for these two data sets.

In Fig. 3.7, we show the convergence of the different multipole contributions to the inclusive ^{12}C(e, e') cross sections. For a scattering angle $\theta_e = 15°$, four multipoles were sufficient to calculate the cross section. At $\theta_e = 30°$, eight multipoles were necessary and for $\theta_e = 60°$, 14 multipoles were needed before the calculation converged. We do not expect this multipole convergence to be different between electron and neutrino interactions. Unless stated otherwise, all $1N$ knockout calculations in this work are calculated with 14 multipoles.

The double differential cross section for ^{12}C(ν_μ, μ^-) scattering in the IA is shown in Fig. 3.8. For neutrino interactions, the BBBA05 parameterization for the Q^2 dependence of the vector form factors is used [31]. For the axial form factor G_A, the standard dipole form with $m_A = 1.03$ GeV is used. We have chosen an incoming neutrino energy of 750 MeV, which roughly corresponds to the peak of the MiniBooNE and T2K fluxes. The numerical results are shown for three values of the lepton scattering angle. The contribution of the transverse part of the cross section $T - T'$ is shown separately, which demonstrates that the neutrino cross sections are dominated by the transverse currents, especially at large scattering angles.

Similar as for electron scattering, the two-body currents will influence the $1N$ knockout results and the $2N$ knockout interactions will provide a contribution as well. In the following chapters, we will investigate how the SRCs and MECs affect these results.

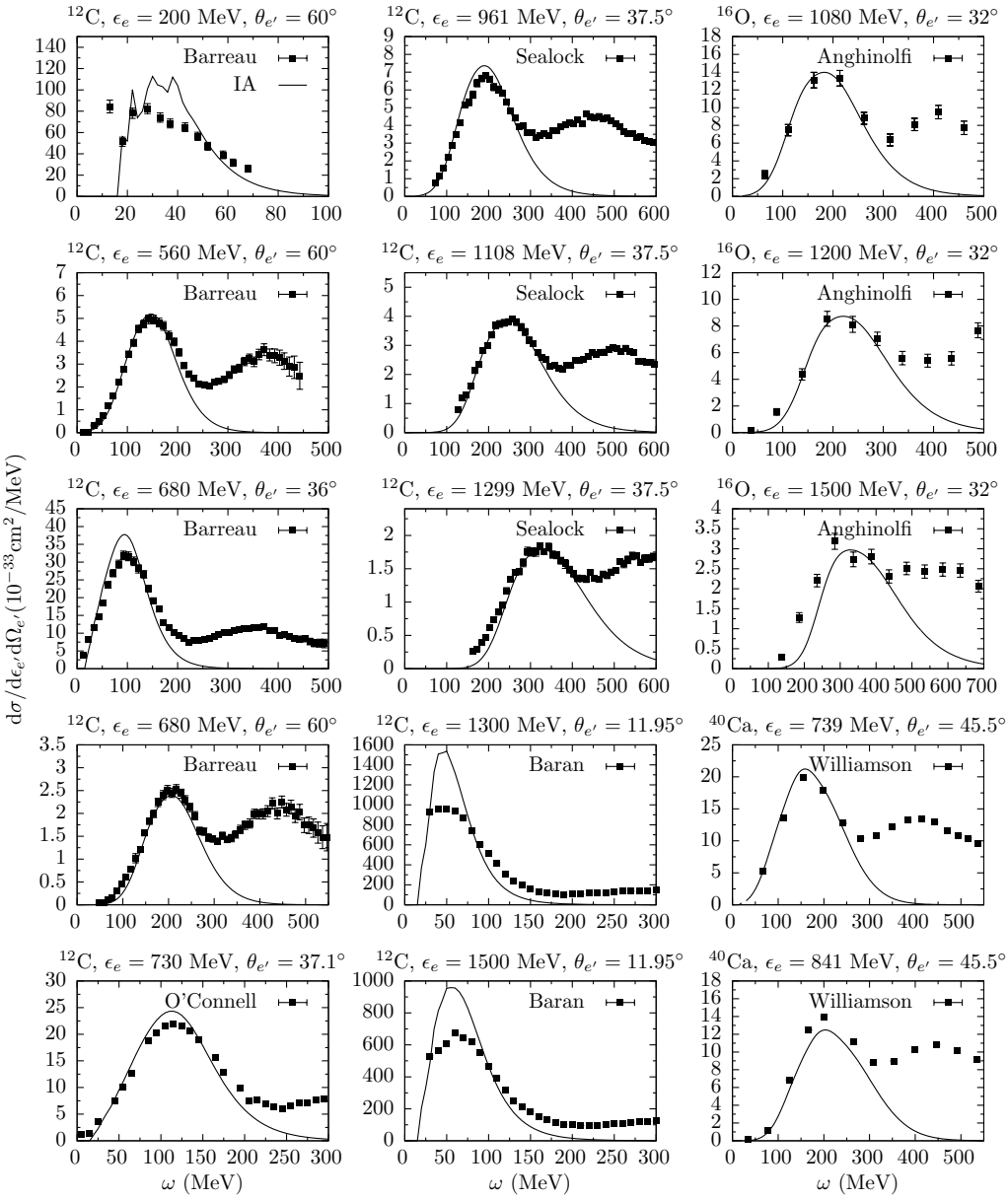

Figure 3.6: The double differential cross section for $A(e, e')$ for different kinematics in an IA approach. The results are compared with data taken from Refs. [20,22–27].

The five $1p1h$ responses in the IA for $^{12}\mathrm{C}(\nu_\mu, \mu^-)$ scattering are shown in Fig. 3.9, for the same kinematics as the responses for electron scattering in Fig. 3.5. Unfortunately, because neutrinos have a very small interaction probability, and because mono-energetic neutrino beams do not exist in this kinematic regime, these results cannot be compared to data. We rely on the electron scattering data to test our model. To make the comparison with the

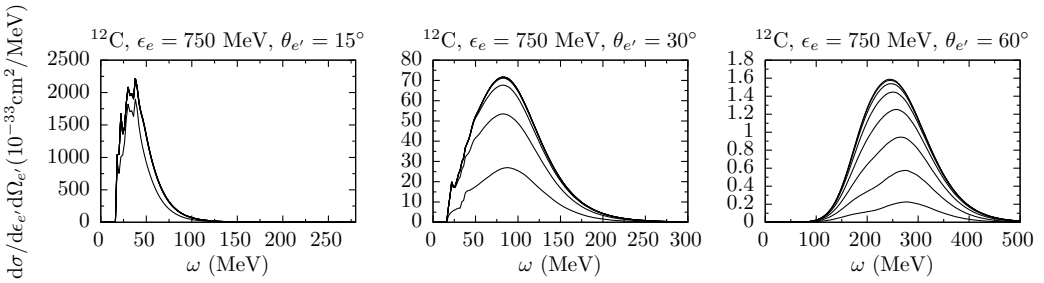

Figure 3.7: Cumulative contribution of the multipoles to the double differential cross section for $^{12}\mathrm{C}(e, e')$ at $\epsilon_e = 750$ MeV for three different values of the lepton scattering angle θ_e in an IA approach. The contributions from the first 2, 4, ... 16 multipoles are shown atop each other.

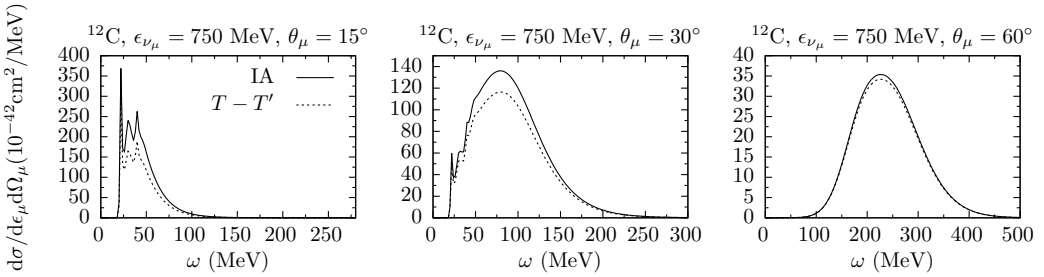

Figure 3.8: The double differential cross section for $^{12}\mathrm{C}(\nu_\mu, \mu^-)$ for $\epsilon_{\nu_\mu} = 750$ MeV for three different values of the lepton scattering angle θ_μ in an IA approach. The dashed line shows the contribution of the transverse part of the differential cross section.

results for electron scattering easier, the contribution of the vector part of the current is shown separately in Fig. 3.9. The results for W_{CC} for electron and neutrino scattering are similar in shape and magnitude. This is because the Coulomb response is dominated by the vector part of the current, especially for the smallest momentum transfer $q = 300$ MeV/c. The W_T response on the other hand is much bigger than its electron counterpart, as a big contribution comes axial part of the current. The contribution of the vector part to the longitudinal response is negligible.

We conclude by stating that the IA does a fair job at describing the QE peak for inclusive (e, e') responses and cross sections and we expect the same to be true for inclusive (ν_μ, μ^-) interactions. However, two-body effects should be taken into account for a better description of the data in the dip region, where the data is underpredicted.

References

[1] M. Waroquier, J. Ryckebusch, J. Moreau, *et al.* Phys. Rept. **148**, 249 (1987).

[2] J. Ryckebusch, *Photon and electron-induced one-nucleon emission within a selfconsistent* HF-RPA *model*, PhD thesis (Ghent University, 1988).

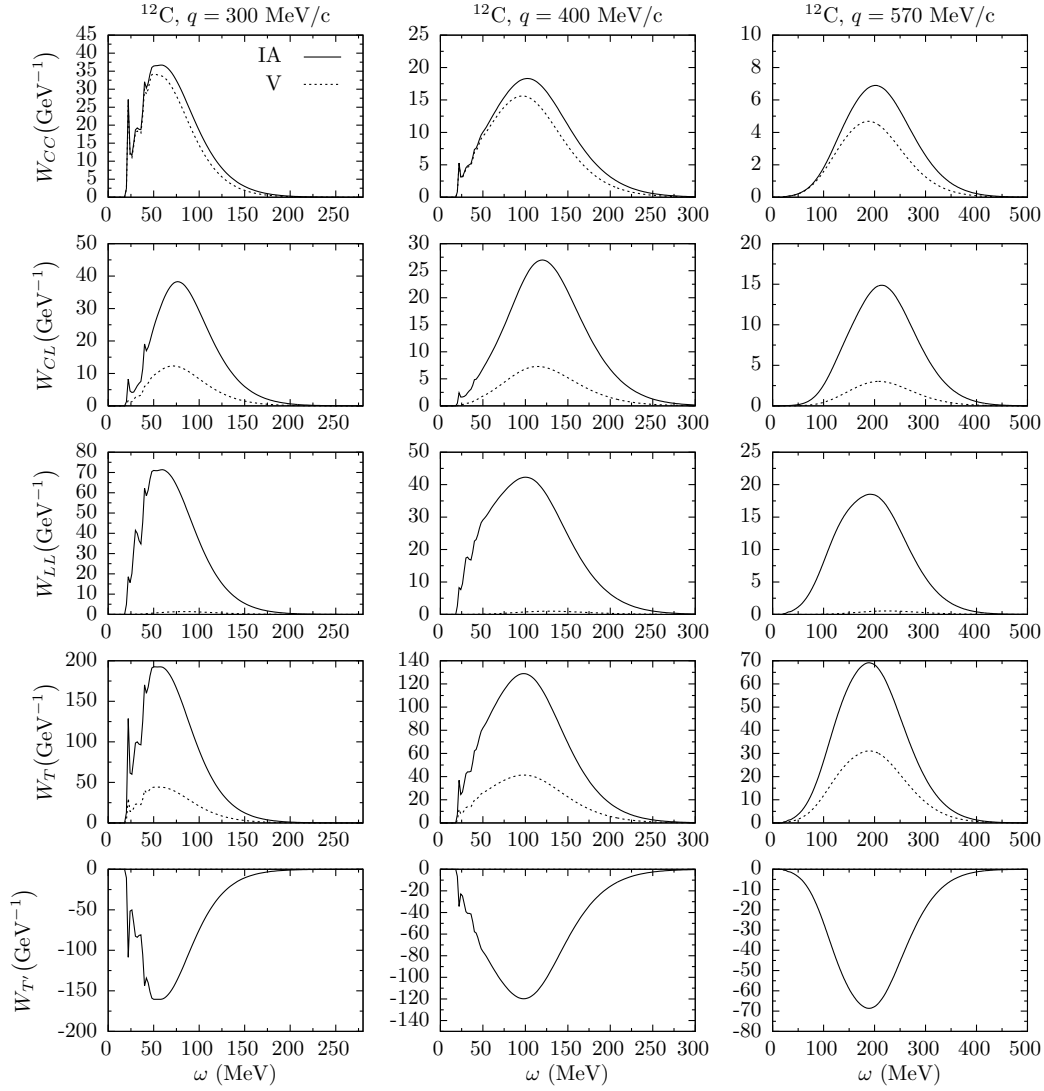

Figure 3.9: The five responses for $^{12}\mathrm{C}(\nu_\mu, \mu^-)$ for different values of q in an IA approach. The contribution of the vector part of the current is shown separately (V).

[3] J. Ryckebusch, L. Machenil, M. Vanderhaeghen, *et al.* Phys. Rev. **C49**, 2704 (1994).

[4] J. Ryckebusch, M. Vanderhaeghen, L. Machenil, *et al.* Nucl. Phys. **A568**, 828 (1994).

[5] J. J. Kelly, Adv. Nucl. Phys. **23**, 75 (1996).

[6] J. J. Kelly, Phys. Rev. **C56**, 2672 (1997).

[7] L. Chinitz *et al.* Phys. Rev. Lett. **67**, 568 (1991).

[8] C. Spaltro, H. Blok, E. Jans, *et al.* Phys. Rev. **C48**, 2385 (1993).

[9] M. Leuschner *et al.* Phys. Rev. **C49**, 955 (1994).

[10] K. Blomqvist *et al.* Phys. Lett. **B344**, 85 (1995).
[11] J. Ryckebusch, K. Heyde, D. Van Neck, *et al.* Nucl. Phys. **A503**, 694 (1989).
[12] V. Van der Sluys, J. Ryckebusch, and M. Waroquier, Phys. Rev. **C49**, 2695 (1994).
[13] J. Ryckebusch, D. Debruyne, W. Van Nespen, *et al.* Phys. Rev. **C60**, 034604 (1999).
[14] J. Ryckebusch, Phys. Rev. **C64**, 044606 (2001).
[15] Jefferson Lab Hall A collaboration, K. Fissum *et al.* Phys. Rev. **C70**, 034606 (2004).
[16] M. Iodice, E. Cisbani, R. De Leo, *et al.* Phys. Lett. **B653**, 392 (2007).
[17] J. Amaro, J. Caballero, T. Donnelly, *et al.* Nucl. Phys. **A602**, 263 (1996).
[18] S. Jeschonnek and T. Donnelly, Phys. Rev. **C57**, 2438 (1998).
[19] J. Amaro, M. Barbaro, J. Caballero, *et al.* Phys. Rev. **C71**, 065501 (2005).
[20] P. Barreau, M. Bernheim, J. Duclos, *et al.* Nucl. Phys. **A402**, 515 (1983).
[21] J. Jourdan, Nucl. Phys. **A603**, 117 (1996).
[22] J. O'Connell, W. Dodge, J. Lightbody, *et al.* Phys. Rev. Lett. **53**, 1627 (1984).
[23] R. Sealock, K. Giovanetti, S. Thornton, *et al.* Phys. Rev. Lett. **62**, 1350 (1989).
[24] D. Baran, B. Filippone, D. Geesaman, *et al.* Phys. Rev. Lett. **61**, 400 (1988).
[25] M. Anghinolfi, M. Ripani, M. Battaglieri, *et al.* Nucl. Phys. **A602**, 405 (1996).
[26] C. Williamson, T. Yates, W. Schmitt, *et al.* Phys. Rev. **C56**, 3152 (1997).
[27] D. Day, J. McCarthy, Z. Meziani, *et al.* Phys. Rev. **C48**, 1849 (1993).
[28] S. Galster, H. Klein, J. Moritz, *et al.* Nucl. Phys. **B32**, 221 (1971).
[29] J. Amaro, G. Co, and A. Lallena, (1999), arXiv:nucl-th/9902072.
[30] V. Pandey, N. Jachowicz, T. Van Cuyck, *et al.* Phys. Rev. **C92**, 024606 (2015).
[31] R. Bradford, A. Bodek, H. Budd, *et al.* Nucl. Phys. Proc. Suppl. **159**, 127 (2006).

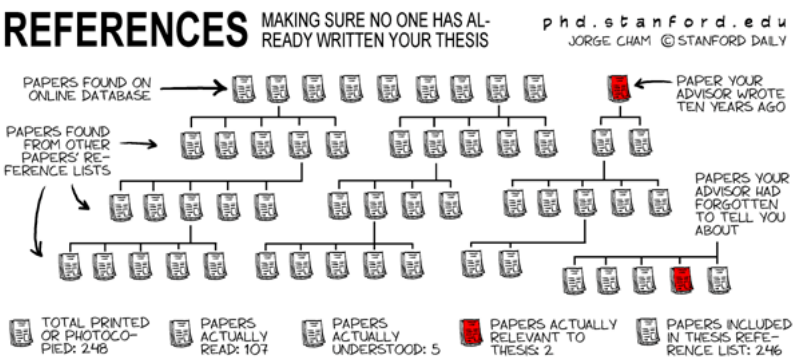

© Jorge Cham

Chapter 4

Two-nucleon knockout

In the previous chapter, the response functions for exclusive $A(l,l'N)$ and inclusive $A(l,l')$ $1N$ knockout interactions were presented. They were used to show the numerical results of the inclusive differential cross section in the IA, thereby testing the validity of the IA. This chapter deals with exclusive $A(l,l'N_aN_b)$, semi-exclusive $A(l,l'N_a)$ and inclusive $A(l,l')$ $2N$ knockout processes. The $2N$ knockout transition matrix elements will be calculated, with a final nuclear state that has two nucleons in the continuum, and a residual nucleus which is left in a low-lying excited state. Only the two-body part of the nuclear current operator should be considered as only this can contribute to the $2N$ knockout processes. From these matrix elements, the ten exclusive $2N$ knockout responses W_i can be constructed which are used in the calculation of the exclusive $2N$ knockout cross section, Eq. (2.67). Subsequently, the semi-exclusive and inclusive responses are obtained by integrating the exclusive responses over the phase space of one or both of the emitted nucleons respectively.

In Fig. 4.1, a $2N$ knockout process from ^{16}O is illustrated as interpreted in a shell-model picture. The incoming boson X ejects a pair of correlated protons to the continuum. Fig. 4.2 shows the diagrams resulting in a $2p2h$ final state, represented as a particle-hole diagram or as a current diagram. Both ways of representing the process are equivalent. The nature of the two-body current is left open throughout this chapter, the only requirement is that the current is built out of two-body operators.

Again, the framework developed in this chapter is general and valid for all types of electroweak interactions. The formalism described below was originally developed for (γ,pp) and (γ,pn) [1,2] and $(e,e'\mathrm{pp})$ and $(e,e'\mathrm{pn})$ [3,4] interactions, where the effects of MECs and SRCs were studied. In the following chapters, we will investigate how neutrino interactions are affected by these two-body mechanisms. The SRCs are studied in Chapter 5 and the MECs in Chapter 6.

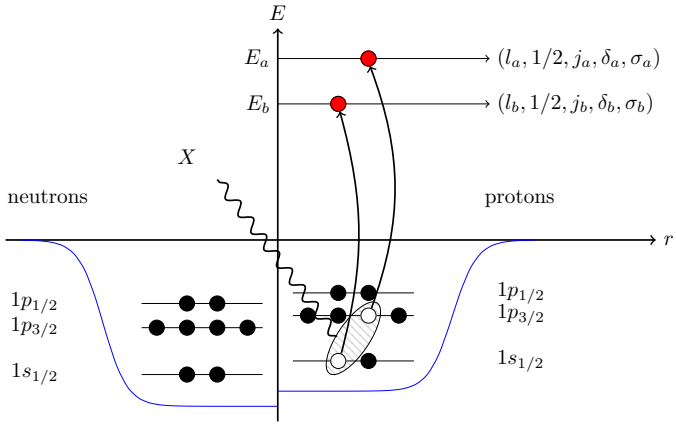

Figure 4.1: Two-nucleon knockout from ^{16}O as interpreted in a shell-model picture. Two nucleons are ejected to the continuum and the residual nucleus is left in a two-hole state $(hh')^{-1}$.

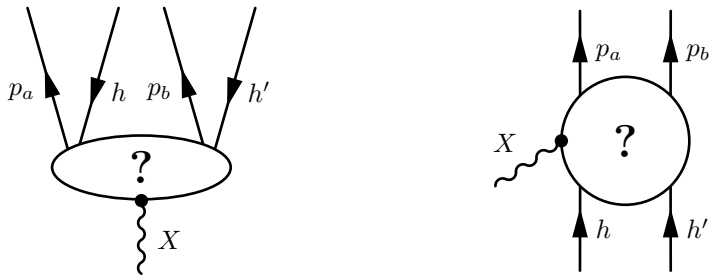

(a) Particle-hole diagram **(b)** Current diagram

Figure 4.2: Two different representations of a $2N$ knockout diagram.

4.1 Exclusive $2N$ knockout cross section

The exclusive $A(l, l' N_a N_b)$ differential cross section was derived in Chapter 2. It is given by Eq. (2.67)

$$\frac{\mathrm{d}\sigma^X}{\mathrm{d}E_f \mathrm{d}\Omega_f \mathrm{d}T_b \mathrm{d}\Omega_b \mathrm{d}\Omega_a} = \frac{p_a p_b E_a E_b}{(2\pi)^6} g_{rec}^{-1} \sigma^X \zeta \times \big[v_{CC} W_{CC} + v_{CL} W_{CL} + v_{LL} W_{LL} + v_T W_T + v_{TT} W_{TT} + v_{TC} W_{TC} + v_{TL} W_{TL} + h(v_{T'} W_{T'} + v_{TC'} W_{TC'} + v_{TL'} W_{TL'}) \big], \tag{4.1}$$

where the response functions W_i are defined as bilinear products of the transition matrix elements,

$$\mathcal{J}_\lambda = \langle\, \Psi^{2p2h} \,|\, \widehat{J}_\lambda(\boldsymbol{q}) \,|\, \Psi_i \,\rangle, \tag{4.2}$$

and their complex conjugates $\mathcal{J}_\lambda^\dagger$. The states $|\, \Psi_i \,\rangle$ and $|\, \Psi^{2p2h} \,\rangle$ refer to the initial correlated nuclear state and the final correlated $2p2h$ state. $\widehat{J}_\lambda$ are the time-like and spherical components of the nuclear current. As mentioned before, only the two-body part of the

nuclear current $\widehat{J}^{[2]}_{\lambda}$ should be considered in the calculation of the $2N$ knockout matrix elements. We will describe the initial nuclear state by its ground state Slater determinant, ignoring correlations in the ground state: $|\,\Psi_i\,\rangle \approx |\,\Phi_{gs}\,\rangle$. This is the same approximation as was done for $1N$ knockout interactions. In Chapter 5, we will take correlations in the target and residual nucleus into account. Only target nuclei with a $J^P = 0^+$ ground state are considered. For electron scattering interactions with ^{12}C as a target, the following $2p2h$ final states are accessible

$$|\,\Psi^{2p2h}\,\rangle = |\,{}^{10}\mathrm{Be}, \mathrm{pp}\,\rangle, |\,{}^{10}\mathrm{B}, \mathrm{pn}\,\rangle, |\,{}^{10}\mathrm{C}, \mathrm{nn}\,\rangle, \tag{4.3}$$

while $^{12}\mathrm{C}(\nu_\mu, \mu^- N_a N_b)$ interactions only have two possible final states

$$|\,\Psi^{2p2h}\,\rangle = |\,{}^{10}\mathrm{B}, \mathrm{pp}\,\rangle, |\,{}^{10}\mathrm{C}, \mathrm{pn}\,\rangle. \tag{4.4}$$

We stress that the final states mentioned here do not account for the isospin operators in the specific two-body operators. E.g. when calculating $2N$ knockout of MEC pairs from electron scatting interactions, only final states with an emitted pn pair are possible. However, all these final states consist of a residual nucleus with quantum numbers $|\,J_R, M_R\,\rangle$ and excitation energy E^{exc} and two escaping nucleons with momenta $\boldsymbol{p}_a$ and $\boldsymbol{p}_b$ and spins m_{s_a} and m_{s_b}. The excitation energy is defined relative to the ground state of the residual nucleus. Describing the residual $A-2$ nuclear system by its Slater determinant $|\,\Phi^{(A-2)}_f\,\rangle$, the matrix elements are written as

$$\mathcal{J}_\lambda = \langle\,\Phi^{(A-2)}_f(E^{exc}, J_R M_R);\, \boldsymbol{p}_a m_{s_a};\, \boldsymbol{p}_b m_{s_b}\,|\,\widehat{J}^{[2]}_{\lambda}(\boldsymbol{q})\,|\,\Phi_{gs}\,\rangle. \tag{4.5}$$

4.1.1 Nuclear wave functions for $2N$ knockout

For $2N$ knockout from finite nuclei, the same approach as for the $1N$ knockout calculations is followed. We adopt the SA and neglect the mutual interaction between the outgoing particles, as shown in Fig. 4.3. The nucleon pair, represented by the shaded circle, that interacts with the incoming boson, is emitted from the nucleus. The emitted nucleons are still under the influence of the distortion effect of the MF potential. In a shell-model picture, the emission of two nucleons from the nucleus will leave the residual nucleus in a two-hole state relative to the target nucleus.

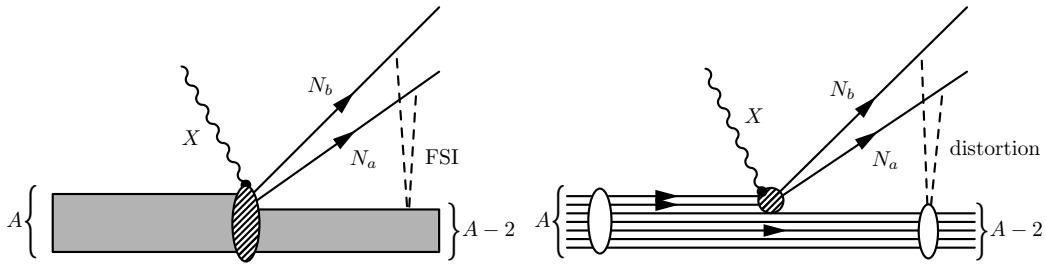

(a) Full model **(b)** An IPM extended with two-body currents

Figure 4.3: Graphical representation of the $2N$ knockout reaction channel. Same as Fig. 1.13.

As a natural extension of the $1p1h$ final state, Eq. (3.21), the outgoing nucleon wave functions in the $2p2h$ final state are expanded in terms of the continuum eigenstates of the MF

potential $p_N(E_N lkm_j)$. The $A-2$ system with quantum numbers J_R, M_R is written as a two-hole state

$$|\,\Phi_f^{(A-2)}(E^{exc}, J_R M_R)\,\rangle = |\,(hh')^{-1}(E^{exc}, J_R M_R)\,\rangle \tag{4.6}$$

$$= \sum_{m_h m'_h} \langle j_h \;\; m_h \;\; j'_h \;\; m'_h \,|\, J_R \;\; M_R\rangle (-1)^{j_h+m_h+j'_h+m'_h} \widehat{c}_{j_h,-m_h} \widehat{c}_{j'_h,-m'_h} \,|\,\Phi_{gs}\,\rangle. \tag{4.7}$$

Combining the expressions for the emitted nucleons and the residual nucleus, the $2p2h$ final nuclear state is written as

$$|\,\Phi^{2p2h}\,\rangle = |\,\Phi_f^{(A-2)}(E^{exc}, J_R M_R);\, \boldsymbol{p}_a m_{s_a};\, \boldsymbol{p}_b m_{s_b}\,\rangle_{as} \tag{4.8}$$

$$\begin{aligned} &= \sum_{l_a m_{l_a}} \sum_{j_a m_{j_a}} \sum_{l_b m_{l_b}} \sum_{j_b m_{j_b}} \sum_{m_h m'_h} (4\pi)^2 \frac{\pi}{2m_N\sqrt{p_a p_b}} \\ &\times i^{l_a+l_b} e^{i(\delta_{l_a}+\sigma_{l_a}+\delta_{l_b}+\sigma_{l_b})} Y^*_{l_a m_{l_a}}(\Omega_a) Y^*_{l_b m_{l_b}}(\Omega_b) \\ &\times \langle l_a \;\; m_{l_a} \;\; 1/2 \;\; m_{s_a} \,|\, j_a \;\; m_{j_a}\rangle \langle l_b \;\; m_{l_b} \;\; 1/2 \;\; m_{s_b} \,|\, j_b \;\; m_{j_b}\rangle \\ &\times \langle j_h \;\; m_h \;\; j'_h \;\; m'_h \,|\, J_R \;\; M_R\rangle (-1)^{j_h+m_h+j'_h+m'_h} \\ &\times \widehat{c}^{\,\dagger}_{l_a j_a m_{j_a}} \widehat{c}^{\,\dagger}_{l_b j_b m_{j_b}} \widehat{c}_{j_h,-m_h} \widehat{c}_{j'_h,-m'_h} \,|\,\Phi_{gs}\,\rangle. \end{aligned} \tag{4.9}$$

The subscript '*as*' refers to the mutual antisymmetrization of the wave functions of the outgoing nucleons with respect to each other and with respect to the residual $A-2$ system. Since the final expression is written in second quantization, it obeys the antisymmetrization requirements. The particles that are knocked out, p_a and p_b, can be any pair (pp, pn or nn), depending on the interaction process, the two-body current and the target nucleus.

4.1.2 Two-body matrix elements for $2N$

All the elements necessary to calculate the two-body matrix elements are now present: the ground state Slater determinant of the target nucleus $|\,\Phi_{gs}\,\rangle$ and the $2p2h$, final state written in second quantization. We first calculate the expectation value of a general spherical two-body operator $\widehat{\mathcal{O}}^{[2]}_{JM}(q)$. When the expectation value of this operator is known, the expectation values of the four components of the nuclear current operator follow easily after a simple substitution. First, the operator $\widehat{\mathcal{O}}^{[2]}_{JM}(q)$ is written in second quantization, in an analogous way as was done in Chapter 3,

$$\widehat{\mathcal{O}}^{[2]}_{JM}(q) = \frac{1}{2} \sum_{\alpha\beta\gamma\delta} \langle\,\alpha\beta\,|\,\widehat{\mathcal{O}}^{[2]}_{JM}(q)\,|\,\gamma\delta\,\rangle \widehat{c}^{\,\dagger}_\alpha \widehat{c}^{\,\dagger}_\beta \widehat{c}_\delta \widehat{c}_\gamma. \tag{4.10}$$

Using this, and substituting the expression for the $2p2h$ final state, Eq. (4.9), we can write the transition matrix element as

$$\begin{aligned} \langle\,\Phi^{2p2h}\,|\,\widehat{\mathcal{O}}^{[2]}_{JM}(q)\,|\,\Phi_{gs}\,\rangle = &\sum_{l_a m_{l_a}} \sum_{j_a m_{j_a}} \sum_{l_b m_{l_b}} \sum_{j_b m_{j_b}} \sum_{m_h m'_h} (4\pi)^2 \frac{\pi}{2m_N\sqrt{p_a p_b}} \\ &\times (-i)^{l_a+l_b} e^{-i(\delta_{l_a}+\sigma_{l_a}+\delta_{l_b}+\sigma_{l_b})} Y_{l_a m_{l_a}}(\Omega_a) Y_{l_b m_{l_b}}(\Omega_b) \\ &\times \langle l_a \;\; m_{l_a} \;\; 1/2 \;\; m_{s_a} \,|\, j_a \;\; m_{j_a}\rangle \langle l_b \;\; m_{l_b} \;\; 1/2 \;\; m_{s_b} \,|\, j_b \;\; m_{j_b}\rangle \\ &\times \langle j_h \;\; m_h \;\; j'_h \;\; m'_h \,|\, J_R \;\; M_R\rangle (-1)^{j_h+m_h+j'_h+m'_h} \end{aligned}$$

$$\times \frac{1}{2}\sum_{\alpha\beta\gamma\delta}\langle\,\alpha\beta\,|\,\widehat{\mathcal{O}}^{[2]}_{JM}(q)\,|\,\gamma\delta\,\rangle\langle\,\Phi_{gs}\,|\,\widehat{c}^{\dagger}_{h'}\widehat{c}^{\dagger}_{h}\widehat{c}_{p_b}\widehat{c}_{p_a}\widehat{c}^{\dagger}_{\alpha}\widehat{c}^{\dagger}_{\beta}\widehat{c}_{\delta}\widehat{c}_{\gamma}\,|\,\Phi_{gs}\,\rangle, \tag{4.11}$$

where the notation of the creation and annihilation operators was abbreviated as before, p_a refers to $l_a j_a m_{j_a}$ and h to $j_h, -m_h$ etc. Using the orthogonality relations of the creation and annihilation operators, we obtain

$$\begin{aligned}\frac{1}{2}\sum_{\alpha\beta\gamma\delta}\langle\,\alpha\beta\,|\,\widehat{\mathcal{O}}^{[2]}_{JM}(q)\,|\,\gamma\delta\,\rangle\langle\,\Phi_{gs}\,|\,\widehat{c}^{\dagger}_{h'}\widehat{c}^{\dagger}_{h}\widehat{c}_{p_b}\widehat{c}_{p_a}\widehat{c}^{\dagger}_{\alpha}\widehat{c}^{\dagger}_{\beta}\widehat{c}_{\delta}\widehat{c}_{\gamma}\,|\,\Phi_{gs}\,\rangle &= \langle\,p_a p_b\,|\,\widehat{\mathcal{O}}^{[2]}_{JM}(q)\,|\,h'h - hh'\,\rangle \\ &= -\langle\,p_a p_b\,|\,\widehat{\mathcal{O}}^{[2]}_{JM}(q)\,|\,hh'\,\rangle_{as},\end{aligned} \tag{4.12}$$

the antisymmetric state is defined as $|\,hh'\,\rangle_{as} \equiv |\,hh' - h'h\,\rangle$. The first and second terms in this antisymmetric expression will be referred to as the direct and exchange matrix elements. Subsequently, we couple the particle and hole states to a combined quantum state

$$-\langle\,p_a p_b\,|\,\widehat{\mathcal{O}}^{[2]}_{JM}(q)\,|\,hh'\,\rangle_{as} = -\langle\,j_a m_{j_a},\,j_b m_{j_b}\,|\,\widehat{\mathcal{O}}^{[2]}_{JM}(q)\,|\,j_h - m_h,\,j'_h - m'_h\,\rangle \tag{4.13}$$

$$\begin{aligned}&= \sum_{J_1 M_1}\sum_{J_3 M_3}(-1)^{j_h + j'_h + J_3 + 1}\langle j_h\;\; m_h\;\; j'_h\;\; m'_h\,|\,J_3\;\; -M_3\rangle \\ &\times \langle j_a\;\; m_{j_a}\;\; j_b\;\; m_{j_b}\,|\,J_1\;\; M_1\rangle\langle\,p_a p_b, J_1 M_1\,|\,\widehat{\mathcal{O}}^{[2]}_{JM}(q)\,|\,hh', J_3 M_3\,\rangle_{as}\end{aligned} \tag{4.14}$$

$$\begin{aligned}&= \sum_{J_1 M_1}\sum_{J_3 M_3}\frac{1}{\widehat{J_1}}(-1)^{j_h + j'_h + J_3 + 1}\langle j_h\;\; m_h\;\; j'_h\;\; m'_h\,|\,J_3\;\; -M_3\rangle \\ &\times \langle j_a\;\; m_{j_a}\;\; j_b\;\; m_{j_b}\,|\,J_1\;\; M_1\rangle\langle J_3\;\; M_3\;\; J\;\; M\,|\,J_1\;\; M_1\rangle \\ &\times \langle\,p_a p_b; J_1\,\|\,\widehat{\mathcal{O}}^{[2]}_{JM}(q)\,\|\,hh'; J_3\,\rangle_{as}.\end{aligned} \tag{4.15}$$

The Wigner-Eckart theorem was used to transform the matrix element into a reduced matrix element in the last step. The resulting transition matrix element can now be cast in the form

$$\begin{aligned}\langle\,\Phi^{2p2h}\,|\,\widehat{\mathcal{O}}^{[2]}_{JM}(q)\,|\,\Phi_{gs}\,\rangle &= \sum_{l_a m_{l_a}}\sum_{j_a m_{j_a}}\sum_{l_b m_{l_b}}\sum_{j_b m_{j_b}}\sum_{J_1 M_1}(4\pi)^2\frac{\pi}{2m_N\sqrt{p_a p_b}} \\ &\times (-i)^{l_a + l_b}e^{-i(\delta_{l_a}+\sigma_{l_a}+\delta_{l_b}+\sigma_{l_b})}Y_{l_a m_{l_a}}(\Omega_a)Y_{l_b m_{l_b}}(\Omega_b)\frac{(-1)^{J_R + M_R + 1}}{\widehat{J_1}} \\ &\times \langle l_a\;\; m_{l_a}\;\; 1/2\;\; m_{s_a}\,|\,j_a\;\; m_{j_a}\rangle\langle l_b\;\; m_{l_b}\;\; 1/2\;\; m_{s_b}\,|\,j_b\;\; m_{j_b}\rangle \\ &\times \langle j_a\;\; m_{j_a}\;\; j_b\;\; m_{j_b}\,|\,J_1\;\; M_1\rangle\langle J_R\;\; -M_R\;\; J\;\; M\,|\,J_1\;\; M_1\rangle \\ &\times \langle\,p_a p_b; J_1\,\|\,\widehat{\mathcal{O}}^{[2]}_{JM}(q)\,\|\,hh'; J_R\,\rangle_{as}.\end{aligned} \tag{4.16}$$

The expression was simplified using orthogonality relations of the Clebsch-Gordan coefficients. The expressions for the transition matrix elements of the Coulomb, longitudinal and transverse components of the nuclear current in momentum space can now be expressed as a function of the four multipole operators, Eqs. (2.71)-(2.73),

$$\mathcal{J}_0 = +\sqrt{4\pi}\sum_{J\geq 0} i^J \widehat{J}\sum_{l_a m_{l_a}}\sum_{j_a m_{j_a}}\sum_{l_b m_{l_b}}\sum_{j_b m_{j_b}}\sum_{J_1 M_1}(4\pi)^2\frac{\pi}{2m_N\sqrt{p_a p_b}}$$

$$\times (-i)^{l_a+l_b} e^{-i(\delta_{l_a}+\sigma_{l_a}+\delta_{l_b}+\sigma_{l_b})} Y_{l_a m_{l_a}}(\Omega_a) Y_{l_b m_{l_b}}(\Omega_b) \frac{(-1)^{J_R+M_R+1}}{\widehat{J_1}}$$
$$\times \langle l_a \;\; m_{l_a} \;\; 1/2 \;\; m_{s_a} \,|\, j_a \;\; m_{j_a} \rangle \langle l_b \;\; m_{l_b} \;\; 1/2 \;\; m_{s_b} \,|\, j_b \;\; m_{j_b} \rangle$$
$$\times \langle j_a \;\; m_{j_a} \;\; j_b \;\; m_{j_b} \,|\, J_1 \;\; M_1 \rangle \langle J_R \;\; -M_R \;\; J \;\; 0 \,|\, J_1 \;\; M_1 \rangle \mathcal{M}^{\mathrm{Coul},[2]}_{p_a p_b; hh'}(J_1, J, J_R), \tag{4.17}$$

$$\mathcal{J}_3 = -\sqrt{4\pi} \sum_{J \geq 0} i^J \widehat{J} \sum_{l_a m_{l_a}} \sum_{j_a m_{j_a}} \sum_{l_b m_{l_b}} \sum_{j_b m_{j_b}} \sum_{J_1 M_1} (4\pi)^2 \frac{\pi}{2 m_N \sqrt{p_a p_b}}$$
$$\times (-i)^{l_a+l_b} e^{-i(\delta_{l_a}+\sigma_{l_a}+\delta_{l_b}+\sigma_{l_b})} Y_{l_a m_{l_a}}(\Omega_a) Y_{l_b m_{l_b}}(\Omega_b) \frac{(-1)^{J_R+M_R+1}}{\widehat{J_1}}$$
$$\times \langle l_a \;\; m_{l_a} \;\; 1/2 \;\; m_{s_a} \,|\, j_a \;\; m_{j_a} \rangle \langle l_b \;\; m_{l_b} \;\; 1/2 \;\; m_{s_b} \,|\, j_b \;\; m_{j_b} \rangle$$
$$\times \langle j_a \;\; m_{j_a} \;\; j_b \;\; m_{j_b} \,|\, J_1 \;\; M_1 \rangle \langle J_R \;\; -M_R \;\; J \;\; 0 \,|\, J_1 \;\; M_1 \rangle \mathcal{M}^{\mathrm{long},[2]}_{p_a p_b; hh'}(J_1, J, J_R), \tag{4.18}$$

$$\mathcal{J}_{\pm 1} = -\sqrt{2\pi} \sum_{J \geq 1} i^J \widehat{J} \sum_{l_a m_{l_a}} \sum_{j_a m_{j_a}} \sum_{l_b m_{l_b}} \sum_{j_b m_{j_b}} \sum_{J_1 M_1} (4\pi)^2 \frac{\pi}{2 m_N \sqrt{p_a p_b}}$$
$$\times (-i)^{l_a+l_b} e^{-i(\delta_{l_a}+\sigma_{l_a}+\delta_{l_b}+\sigma_{l_b})} Y_{l_a m_{l_a}}(\Omega_a) Y_{l_b m_{l_b}}(\Omega_b) \frac{(-1)^{J_R+M_R+1}}{\widehat{J_1}}$$
$$\times \langle l_a \;\; m_{l_a} \;\; 1/2 \;\; m_{s_a} \,|\, j_a \;\; m_{j_a} \rangle \langle l_b \;\; m_{l_b} \;\; 1/2 \;\; m_{s_b} \,|\, j_b \;\; m_{j_b} \rangle$$
$$\times \langle j_a \;\; m_{j_a} \;\; j_b \;\; m_{j_b} \,|\, J_1 \;\; M_1 \rangle \langle J_R \;\; -M_R \;\; J \;\; \pm 1 \,|\, J_1 \;\; M_1 \rangle$$
$$\times \left[\mathcal{M}^{\mathrm{elec},[2]}_{p_a p_b; hh'}(J_1, J, J_R) \pm \mathcal{M}^{\mathrm{magn},[2]}_{p_a p_b; hh'}(J_1, J, J_R) \right]. \tag{4.19}$$

The antisymmetric matrix elements $\mathcal{M}$ in these expressions have been defined according to

$$\mathcal{M}^{\mathrm{Coul},[2]}_{p_a p_b; hh'}(J_1, J, J_R) = \langle\, p_a(E_a l_a j_a) p_b(E_b l_b j_b); J_1 \parallel \widehat{M}^{\mathrm{Coul},[2]}_J(q) \parallel hh'; J_R \,\rangle$$
$$-(-1)^{j_h + j'_h + J_R} \langle\, p_a(E_a l_a j_a) p_b(E_b l_b j_b); J_1 \parallel \widehat{M}^{\mathrm{Coul},[2]}_J(q) \parallel h'h; J_R \,\rangle, \tag{4.20}$$

and identical for the other three matrix elements $\mathcal{M}^{\mathrm{long},[2]}$, $\mathcal{M}^{\mathrm{elec},[2]}$ and $\mathcal{M}^{\mathrm{magn},[2]}$. The superscript '[2]' marks that the multipole operators are constructed with a two-body current. For the actual calculation of these matrix elements, we refer to the following chapters where the framework is presented for the SRC and MEC two-body operators, the results can be found in Appendix F and Appendix G respectively. The ten $2N$ knockout responses, W_i, are then calculated by taking bilinear combinations of the $\mathcal{J}_\lambda$ and their complex conjugates summing over the nuclear final states. The Coulomb response e.g. is calculated via

$$W_{CC} = \sum_{J_R M_R} \sum_{m_{s_a} m_{s_b}} |\mathcal{J}_0|^2 . \tag{4.21}$$

If a specific final state of the residual nucleus is studied, the sum over J_R has to be left out. Examining the four expectation values, Eqs. (4.17)-(4.19), a common prefactors shows up

$$(4\pi)^2 \frac{\pi}{2 m_N \sqrt{p_a p_b}} = \frac{(2\pi)^3}{m_N \sqrt{p_a p_b}}, \tag{4.22}$$

which is squared in the response functions. This factor can be extracted from the responses and added to the prefactor of the differential cross section, this results in

$$\frac{\mathrm{d}\sigma^X}{\mathrm{d}\epsilon_f \mathrm{d}\Omega_f \mathrm{d}T_a \mathrm{d}\Omega_a \mathrm{d}\Omega_b} = \frac{E_a E_b}{m_N^2} g_{rec}^{-1} \sigma^X \zeta$$

$$\times\big[v_{CC}W_{CC} + v_{CL}W_{CL} + v_{LL}W_{LL} + v_T W_T + v_{TT}W_{TT} + v_{TC}W_{TC} + v_{TL}W_{TL} + h(v_{T'}W_{T'} + v_{TC'}W_{TC'} + v_{TL'}W_{TL'})\big]. \tag{4.23}$$

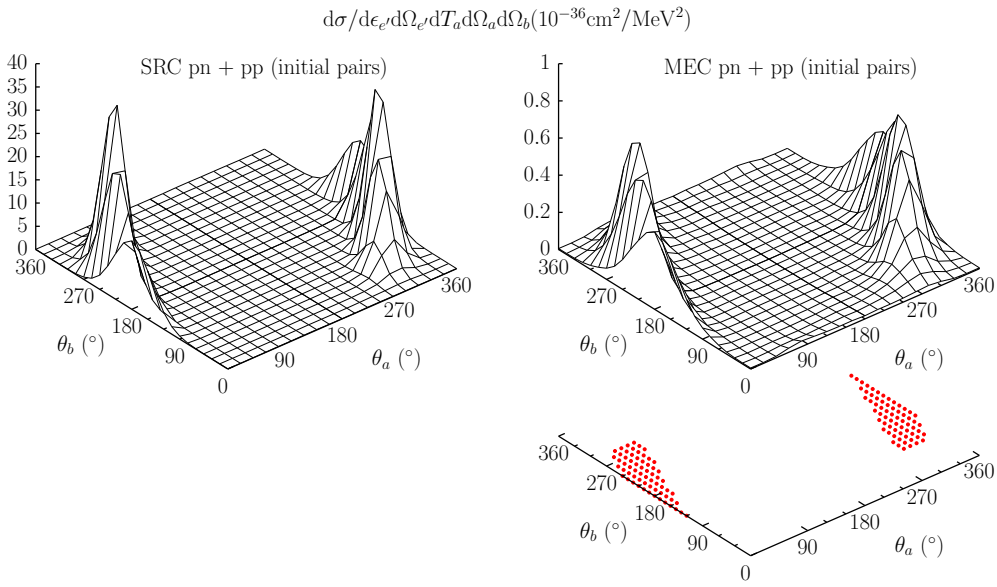

Figure 4.4: The ^{12}C$(e, e'N_aN_b)$ cross section (N_a = p, N_b = p′, n) at ϵ_e = 1200 MeV, $\epsilon_{e'}$ = 900 MeV, $\theta_{e'} = 16^\circ$ and T_p = 50 MeV for in-plane kinematics. Left with SRCs, right with MECs, the bottom plot shows the (θ_a, θ_b) regions with $P_{12} < 300$ MeV/c.

In Figs. 4.4 and 4.5 the results of an exclusive ^{12}C$(e, e'N_aN_b)$ and ^{12}C$(\nu_\mu, \mu^-N_aN_b)$ cross section calculation with SRCs and MECs are shown (N_a = p, N_b = p′, n). We refer to the following chapters for the details of these results. We considered in-plane kinematics, with both nucleons emitted in the lepton scattering plane ($\varphi_{a,b} = 0^\circ$, $\varphi_{a,b} = 180^\circ$). A striking feature of the cross section is the dominance of back-to-back nucleon knockout, reminiscent of the 'hammer events' seen by the ArgoNeuT collaboration [5]. This feature appears to be independent of the interacting lepton and the type of two-body currents, whether they be SRCs or MECs [2,3,6] and will be exploited in the next section.

For $2N$ knockout reactions, the following momentum conservation relation is fulfilled

$$\boldsymbol{P}_{12} + \boldsymbol{q} = \boldsymbol{p}_a + \boldsymbol{p}_b, \tag{4.24}$$

with $\boldsymbol{P}_{12}$ the initial center-of-mass (c.o.m.) momentum of the pair. Referring to the bottom plots of Figs. 4.4 and 4.5, it is clear that most strength is residing in a region with $P_{12} < 300$ MeV/c.

In Fig. 4.6, numerical results from [7] for the two-nucleon c.o.m. momentum distributions $P^{[2]}(P_{12})$ for pp and pn pairs in ^{12}C are shown. Both distributions look very Gaussian. The quantity $P^{[2]}(P_{12})P_{12}^2\mathrm{d}P_{12}$ is the probability of finding a nucleon pair with P_{12} in the interval $[P_{12}, P_{12} + \mathrm{d}P_{12}]$ and is normalized to one. The figure demonstrates that the probability of finding a nucleon pair with $P_{12} > 300$ MeV/c in the nucleus is relatively small. Consequently, the contribution from those pairs to the cross sections is small. It also

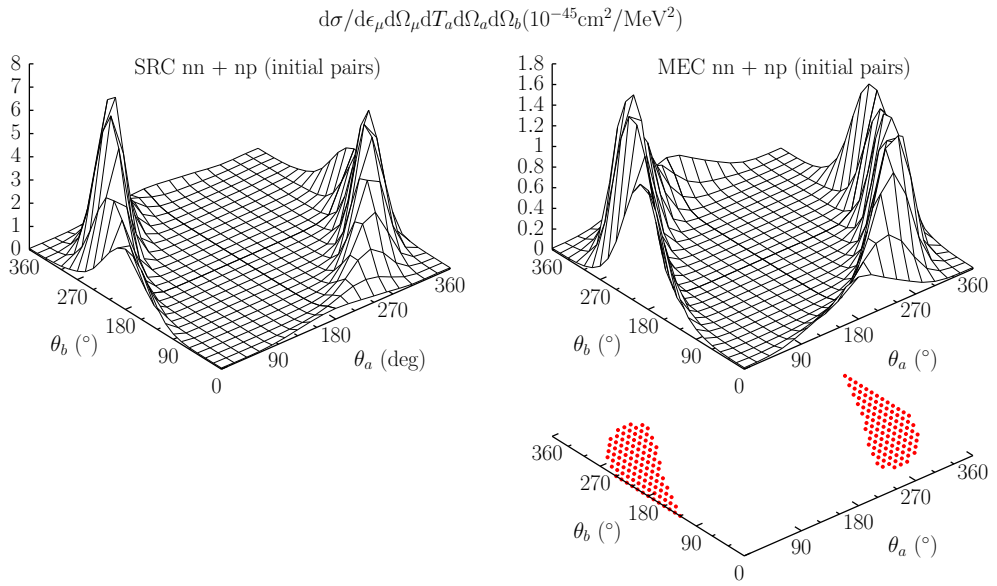

Figure 4.5: The ^{12}C$(\nu_\mu, \mu^- N_a N_b)$ cross section (N_a = p, N_b = p′, n) at $\epsilon_{\nu_\mu} = 750$ MeV, $\epsilon_\mu = 550$ MeV, $\theta_\mu = 15^\circ$ and $T_{\rm p} = 50$ MeV for in-plane kinematics. Left with SRCs, right with MECs, the bottom plot shows the (θ_a, θ_b) regions with $P_{12} < 300$ MeV/c.

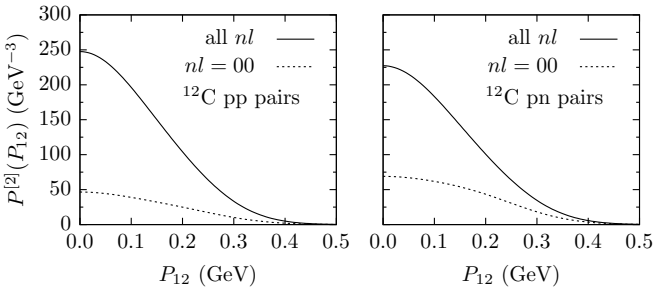

Figure 4.6: The two-nucleon c.o.m. momentum distribution $P^{[2]}(P_{12})$ for pp and pn pairs in ^{12}C (full line). Figure taken from [7].

shows that confinement in phase space of the $2N$ knockout cross sections of Figs. 4.4 and 4.5, is a property of the nucleus rather than a property of the two-body currents.

4.2 Semi-exclusive $2N$ knockout cross section

For neutrino interactions, it is interesting to study the contribution of the exclusive $2N$ knockout $A(\nu_\mu, \mu^- N_a N_b)$ cross section to the inclusive $A(\nu_\mu, \mu^-)$ cross section, as there is very little data on exclusive cross sections. As of now, the only available neutrino-induced exclusive $2N$ knockout data we are aware of, are the 'hammer events' reported by the ArgoNeuT collaboration [5].

Exclusive $1N$ knockout cross sections detect the final state lepton and the emitted nucleon in coincidence. However, processes where two nucleons are emitted from the nucleus, but only one of them is detected also contribute to the experimental signal. The second nucleon can have an energy below the detection threshold, it can be absorbed before it can reach the detector, or it can be emitted in a direction where no detector is present. The semi-exclusive $A(l, l'N_a)$ cross section calculates this contribution to the exclusive $1N$ knockout $A(l, l'N)$ cross section.

This means that for neutrino experiments which have the ability to detect nucleons in the final state, but have a relatively high detection threshold, these semi-exclusive cross sections will be a very interesting tool. For electron scattering interactions, these semi-exclusive $2N$ knockout processes were an important contribution in the study of exclusive $1N$ knockout cross sections. Semi-exclusive cross sections calculated within the model outlined in this work, partially explained the discrepancy between the $(e, e'\mathrm{p})$ data and the exclusive $1N$ knockout calculations at high missing momenta [3,6,8,9].

The calculation of the semi-exclusive cross section involves an integration over the phase space of the undetected ejected nucleons. In the case where the detected particle is a proton ($N_a = \mathrm{p}$), the total semi-exclusive cross section is a incoherent sum of the semi-exclusive pp and pn pair knockout cross sections ($N_b = \mathrm{p}'$ or n),

$$\frac{\mathrm{d}\sigma}{\mathrm{d}\epsilon_f \mathrm{d}\Omega_f \mathrm{d}T_\mathrm{p} \mathrm{d}\Omega_\mathrm{p}}(l, l'\mathrm{p}) = \int \mathrm{d}\Omega_{\mathrm{p}'} \frac{\mathrm{d}\sigma}{\mathrm{d}\epsilon_f \mathrm{d}\Omega_f \mathrm{d}T_\mathrm{p} \mathrm{d}\Omega_\mathrm{p} \mathrm{d}\Omega_{\mathrm{p}'}}(l, l'\mathrm{pp}') + \int \mathrm{d}\Omega_\mathrm{n} \frac{\mathrm{d}\sigma}{\mathrm{d}\epsilon_f \mathrm{d}\Omega_f \mathrm{d}T_\mathrm{p} \mathrm{d}\Omega_\mathrm{p} \mathrm{d}\Omega_\mathrm{n}}(l, l'\mathrm{pn}). \tag{4.25}$$

One could calculate the exclusive cross section over the full phase space of the undetected nucleons and perform a numerical integration. We use the method outlined in [3] and exploit the fact that the exclusive $2N$ knockout strength resides in a well-defined part of phase space. Since the original work of Gottfried [10] it has been clear that most of the $2N$ knockout reactions occur in back-to-back situations. This means that for each particular semi-exclusive kinematic setting ($\mathrm{d}T_\mathrm{p}\mathrm{d}\Omega_\mathrm{p}$) the exclusive $(l, l'\mathrm{p}N_b)$ cross section is restricted to a small part of the phase space of the undetected particle ($\mathrm{d}\Omega_b$), see e.g. Figs. 4.4 and 4.5. In this limited part of the phase space, the momentum of the undetected particle $\boldsymbol{p}_b$ varies very little, which allows one to set $\boldsymbol{p}_b \approx \boldsymbol{p}_b^{ave}$. The average momentum ($\boldsymbol{p}_b^{ave}$) is determined by imposing quasi-deuteron kinematics

$$\boldsymbol{p}_b^{ave} = \boldsymbol{q} - \boldsymbol{p}_\mathrm{p}, \tag{4.26}$$

with $\boldsymbol{p}_\mathrm{p}$ the momentum of the detected proton. As seen from Eq. (4.24), this average momentum is equivalent to the case where the c.o.m. momentum of the initial pair is zero, or equivalently, where the residual nucleus has zero recoil momentum ($g_{rec} = 1$). After the introduction of the average momentum, the integration over $\mathrm{d}\Omega_{\mathrm{p}'}$ and $\mathrm{d}\Omega_\mathrm{n}$ in Eq. (4.25) can be performed analytically [3].

We note that the prefactors (σ^X, ζ) and kinematic factors (v_i) of the exclusive $2N$ knockout cross section, Eq. (2.67), are independent of the nucleon angular variables. This means the integration in Eq. (4.25) only involves an integration over the response functions, e.g.

$$\int \mathrm{d}\Omega_b W_{CC} = \int \mathrm{d}\Omega_b \sum_{J_R M_R} \sum_{m_{s_a} m_{s_b}} |\mathcal{J}_0|^2. \tag{4.27}$$

Below, the calculation is summarized for W_{CC} and the results are given for the other nine responses[1]. First, we write the complete expression for the W_{CC} response by multiplying Eq. (4.17) by its complex conjugate and introducing the sum over the nuclear final states. The result can be written as

$$\begin{aligned}
W_{CC} = &\sum_{J_R}\sum_{JJ'\geq 0}\sum_{l_a j_a}\sum_{l_b j_b}\sum_{l'_a j'_a}\sum_{l'_b j'_b}\sum_{J_1 J'_1}\sum_{J_2 M_2}\sum_{J'_2 J_3}\\
&\times i^{J-J'}(-i)^{l_a+l_b-l'_a-l'_b} e^{-i(\delta_{l_a}+\sigma_{l_a}+\delta_{l_b}+\sigma_{l_b}-\delta_{l'_a}-\sigma_{l'_a}-\delta_{l'_b}-\sigma_{l'_b})} Y^*_{J_2 M_2}(\Omega_b) Y^*_{J'_2 - M_2}(\Omega_a)\\
&\times \widehat{j_a}\widehat{j_b}\widehat{j'_a}\widehat{j'_b}\widehat{J}\widehat{J'}\widehat{J_1}\widehat{J'_1}\widehat{J_2}\widehat{J'_2}(2J_3+1)(-1)^{1+j'_b-j'_a+J_1+J_R}\\
&\times \begin{pmatrix} j_a & j'_a & J_2 \\ 1/2 & -1/2 & 0 \end{pmatrix} \frac{1}{2}\left(1+(-1)^{l_a+l'_a+J_2}\right)\\
&\times \begin{pmatrix} j_b & j'_b & J'_2 \\ 1/2 & -1/2 & 0 \end{pmatrix} \frac{1}{2}\left(1+(-1)^{l_b+l'_b+J'_2}\right)\\
&\times \begin{pmatrix} J & J' & J_3 \\ 0 & 0 & 0 \end{pmatrix} \begin{Bmatrix} J'_1 & J' & J_R \\ J & J_1 & J_3 \end{Bmatrix} \begin{pmatrix} J_2 & J'_2 & J_3 \\ -M_2 & M_2 & 0 \end{pmatrix} \begin{Bmatrix} j_a & j_b & J_1 \\ j'_a & j'_b & J'_1 \\ J_2 & J'_2 & J_3 \end{Bmatrix}\\
&\times \mathcal{M}^{\mathrm{Coul},[2]}_{p_a p_b;hh'}(J_1,J,J_R)\left(\mathcal{M}^{\mathrm{Coul},[2]}_{p'_a p'_b;hh'}(J'_1,J',J_R)\right)^*,
\end{aligned} \tag{4.28}$$

where we left out the common prefactor as discussed earlier. Now the only factor which depends on Ω_b is a spherical harmonic, which produces two Kronecker deltas when the integration is performed

$$\int \mathrm{d}\Omega_b Y^*_{J_2 M_2}(\Omega_b) = \sqrt{4\pi}\delta_{J_2,0}\delta_{M_2,0}. \tag{4.29}$$

Using these delta functions, the following parts of the expression can be simplified, producing more Kronecker deltas

$$\frac{1}{2}\left(1+(-1)^{l_a+l'_a+J_2}\right) \to \frac{1}{2}\left(1+(-1)^{l_a+l'_a}\right) = \delta_{l_a,l'_a}, \tag{4.30}$$

$$\begin{pmatrix} J_2 & J'_2 & J_3 \\ -M_2 & M_2 & 0 \end{pmatrix} \to \begin{pmatrix} 0 & J'_2 & J_3 \\ 0 & 0 & 0 \end{pmatrix} = \delta_{J'_2,J_3}\frac{(-1)^{J_3}}{\widehat{J_3}}, \tag{4.31}$$

$$\begin{pmatrix} j_a & j'_a & J_2 \\ 1/2 & -1/2 & 0 \end{pmatrix} \to \begin{pmatrix} j_a & j'_a & 0 \\ 1/2 & -1/2 & 0 \end{pmatrix} = \delta_{j_a,j'_a}\frac{(-1)^{j_a-1/2}}{\widehat{j_a}}. \tag{4.32}$$

The first replacement is not trivial as it relies on information which is not visible anymore after all the simplifications that preceded expression (4.28). Using the definition of the spherical harmonic, it can be replaced by a Legendre polynomial

$$Y^*_{J'_2 - M_2}(\Omega_a) \to Y_{J_3 0}(\Omega_a) = \frac{\widehat{J_3}}{\sqrt{4\pi}} P_{J_3}(\cos\theta_a). \tag{4.33}$$

Combining all the above information and simplifying the expression further, we obtain

$$\int \mathrm{d}\Omega_a W_{CC} = \sum_{J_R}\sum_{JJ'\geq 0}\sum_{l_a j_a}\sum_{l_b j_b}\sum_{l'_b j'_b}\sum_{J_1 J'_1}\sum_{J_3}$$

[1] We stress that the response function W_{CC} goes under the name W_L in [3].

$$
\begin{aligned}
&\times (-1)^{1+j'_b+J_1+J_R-1/2} P_{J_3}(\cos\theta_b)\langle J'\ \ 0\ \ J\ \ 0\,|\,J_3\ \ 0\rangle \\
&\times \mathcal{B}\left[p_a(E_a l_a j_a), p_b(E_b l_b j_b) p'_b(E_b l'_b j'_b), h, h', J_1, J, J'_1, J', J_R, J_3\right] \\
&\times \mathcal{M}^{\mathrm{Coul},[2]}_{p_a p_b; hh'}(J_1, J, J_R) \left(\mathcal{M}^{\mathrm{Coul},[2]}_{p_a p'_b; hh'}(J'_1, J', J_R)\right)^* ,
\end{aligned}
\tag{4.34}
$$

where we defined $\mathcal{B}$ as

$$
\begin{aligned}
&\mathcal{B}\left[p_a(E_a l_a j_a), p_b(E_b l_b j_b) p'_b(E_b l'_b j'_b), h, h', J_1, J, J'_1, J', J_R, J_3\right] \\
&\quad = i^{J-J'-l_b+l'_b} e^{-i(\delta_{l_b}+\sigma_{l_b}-\delta_{l'_b}-\sigma_{l'_b})} \widehat{j_b}\widehat{j'_b}\widehat{J}\widehat{J'}\widehat{J_1}\widehat{J'_1}\frac{1}{2}\left(1+(-1)^{l_b+l'_b+J_3}\right) \\
&\quad \times \langle j_b\ \ 1/2\ \ j'_b\ \ -1/2\,|\,J_3\ \ 0\rangle \begin{Bmatrix} J'_1 & J' & J_R \\ J & J_1 & J_3 \end{Bmatrix} \begin{Bmatrix} j_b & J_1 & j_a \\ J'_1 & j'_b & J_3 \end{Bmatrix}.
\end{aligned}
\tag{4.35}
$$

The derivations for W_{CL} and W_{LL} are analogous. From expressions (4.17) and (4.18), it follows that one can simply replace the matrix elements $\mathcal{M}^{\mathrm{Coul},[2]}$ by $\mathcal{M}^{\mathrm{long},[2]}$ in the expression for W_{CC}. Note that these currents have an opposite sign, which results in a minus sign in front of the interference response W_{CL}.

$$
\begin{aligned}
\int \mathrm{d}\Omega_a \begin{Bmatrix} W_{CC} \\ W_{CL} \\ W_{LL} \end{Bmatrix} &= \sum_{J_R} \sum_{J J' \geq 0} \sum_{l_a j_a} \sum_{l_b j_b} \sum_{l'_b j'_b} \sum_{J_1 J'_1} \sum_{J_3} \\
&\times (-1)^{1+j'_b+J_1+J_R-1/2} P_{J_3}(\cos\theta_a)\langle J'\ \ 0\ \ J\ \ 0\,|\,J_3\ \ 0\rangle \\
&\times \mathcal{B}\left[p_a(E_a l_a j_a), p_b(E_b l_b j_b) p'_b(E_b l'_b j'_b), h, h', J_1, J, J'_1, J', J_R, J_3\right] \\
&\times \begin{Bmatrix} +\mathcal{M}^{\mathrm{Coul},[2]}_{p_a p_b; hh'}(J_1, J, J_R) \left(\mathcal{M}^{\mathrm{Coul},[2]}_{p_a p'_b; hh'}(J'_1, J', J_R)\right)^* \\ -2\,\mathrm{Re}\left\{\mathcal{M}^{\mathrm{Coul},[2]}_{p_a p_b; hh'}(J_1, J, J_R) \left(\mathcal{M}^{\mathrm{long},[2]}_{p_a p'_b; hh'}(J'_1, J', J_R)\right)^*\right\} \\ +\mathcal{M}^{\mathrm{long},[2]}_{p_a p_b; hh'}(J_1, J, J_R) \left(\mathcal{M}^{\mathrm{long},[2]}_{p_a p'_b; hh'}(J'_1, J', J_R)\right)^* . \end{Bmatrix}
\end{aligned}
\tag{4.36}
$$

The same strategy can be used to calculate the other seven integrated responses. First the responses are calculated and afterwards they can be integrated over Ω_b. By efficiently using the symmetries in the definitions of the response functions and the similarities between the Coulomb and longitudinal current, only three other types of responses have to be calculated. Some simple bookkeeping can then be used to obtain the expressions for the remaining four responses. The first type consists of W_T and $W_{T'}$

$$
\begin{aligned}
\int \mathrm{d}\Omega_b W_{T/T'} &= \sum_{J_R} \sum_{J J' \geq 1} \sum_{l_a j_a} \sum_{l_b j_b} \sum_{l'_b j'_b} \sum_{J_1 J'_1} \sum_{J_3} \\
&\times (-1)^{j_a-1/2+J_R+j_b-j'_b+J+J'} P_{J_3}(\cos\theta_a)\langle J'\ \ -1\ \ J\ \ 1\,|\,J_3\ \ 0\rangle \\
&\times \mathcal{B}\left[p_a(E_a l_a j_a), p_b(E_b l_b j_b) p'_b(E_b l'_b j'_b), h, h', J_1, J, J'_1, J', J_R, J_3\right] \\
&\times \left\{ \frac{1}{2}\left(1 \overset{+}{/} -(-1)^{J+J'+J_2}\right) \left[\mathcal{M}^{\mathrm{elec},[2]}_{p_a p_b; hh'}(J_1, J, J_R) \left(\mathcal{M}^{\mathrm{elec},[2]}_{p_a p'_b; hh'}(J'_1, J', J_R)\right)^* \right.\right. \\
&\qquad \left.\left. + \mathcal{M}^{\mathrm{magn},[2]}_{p_a p_b; hh'}(J_1, J, J_R) \left(\mathcal{M}^{\mathrm{magn},[2]}_{p_a p'_b; hh'}(J'_1, J', J_R)\right)^* \right] \right. \\
&\quad + \frac{1}{2}\left(1 \overset{-}{/} +(-1)^{J+J'+J_2}\right) \left[\mathcal{M}^{\mathrm{elec},[2]}_{p_a p_b; hh'}(J_1, J, J_R) \left(\mathcal{M}^{\mathrm{magn},[2]}_{p_a p'_b; hh'}(J'_1, J', J_R)\right)^* \right.
\end{aligned}
$$

$$+\mathcal{M}^{\mathrm{magn},[2]}_{p_a p_b;hh'}(J_1,J,J_R)\left(\mathcal{M}^{\mathrm{elec},[2]}_{p_a p'_b;hh'}(J'_1,J',J_R)\right)^*\Bigg]\Bigg\}. \quad (4.37)$$

The red (first) sign should be used in the calculation for W_T and the blue (second) in the calculation of $W_{T'}$. The second type of response is W_{TT}, and has no analogue

$$\begin{aligned}\int \mathrm{d}\Omega_b W_{TT} = &\sum_{J_R}\sum_{J'\geq 1}\sum_{l_a j_a}\sum_{l_b j_b}\sum_{l'_b j'_b}\sum_{J_1 J'_1}\sum_{J_3\geq 2}\\
&\times(-1)^{j_a-1/2+J_R+j_b-j'_b+J_2}P^2_{J_3}(\cos\theta_a)\frac{\langle J'\ 1\ J\ 1\,|\,J_3\ 2\rangle}{\sqrt{(J_2-1)J_2(J_2+1)(J_2+2)}}\\
&\times\mathcal{B}\left[p_a(E_a l_a j_a),p_b(E_b l_b j_b)p'_b(E_b l'_b j'_b),h,h',J_1,J,J'_1,J',J_R,J_3\right]\\
&\times\Bigg\{\frac{1}{2}\left(e^{-2i\varphi_a}+(-1)^{J+J'+J_2}e^{2i\varphi_a}\right)\Bigg[\mathcal{M}^{\mathrm{elec},[2]}_{p_a p_b;hh'}(J_1,J,J_R)\left(\mathcal{M}^{\mathrm{elec},[2]}_{p_a p'_b;hh'}(J'_1,J',J_R)\right)^*\\
&\qquad-\mathcal{M}^{\mathrm{magn},[2]}_{p_a p_b;hh'}(J_1,J,J_R)\left(\mathcal{M}^{\mathrm{magn},[2]}_{p_a p'_b;hh'}(J'_1,J',J_R)\right)^*\Bigg]\\
&-\frac{1}{2}\left(e^{-2i\varphi_a}-(-1)^{J+J'+J_2}e^{2i\varphi_a}\right)\Bigg[\mathcal{M}^{\mathrm{magn},[2]}_{p_a p_b;hh'}(J_1,J,J_R)\left(\mathcal{M}^{\mathrm{elec},[2]}_{p_a p'_b;hh'}(J'_1,J',J_R)\right)^*\\
&\qquad-\mathcal{M}^{\mathrm{elec},[2]}_{p_a p_b;hh'}(J_1,J,J_R)\left(\mathcal{M}^{\mathrm{magn},[2]}_{p_a p'_b;hh'}(J'_1,J',J_R)\right)^*\Bigg]\Bigg\}.\end{aligned} \quad (4.38)$$

The third type of response contains W_{TC}, $W_{TC'}$, W_{TL} and $W_{TL'}$

$$\begin{aligned}\int \mathrm{d}\Omega_b W_{TC/TC'} = &\sum_{J_R}\sum_{J\geq 1 J'\geq 0}\sum_{l_a j_a}\sum_{l_b j_b}\sum_{l'_b j'_b}\sum_{J_1 J'_1}\sum_{J_3\geq 1}\\
&\times(-1)^{j_a-1/2+J_R+j_b-j'_b+J_2}P^1_{J_3}(\cos\theta_a)\langle J\ 1\ J'\ 0\,|\,J_3\ 1\rangle\frac{\sqrt{2}}{\sqrt{J_2(J_2+1)}}\\
&\times\mathcal{B}\left[p_a(E_a l_a j_a),p_b(E_b l_b j_b)p'_b(E_b l'_b j'_b),h,h',J_1,J,J'_1,J',J_R,J_3\right]\\
\times\mathrm{Re}\Bigg\{&\frac{1}{2}\left(e^{-i\varphi_a}+/-(-1)^{J+J'+J_2}e^{i\varphi_a}\right)\mathcal{M}^{\mathrm{elec},[2]}_{p_a p_b;hh'}(J_1,J,J_R)\left(\mathcal{M}^{\mathrm{Coul},[2]}_{p_a p'_b;hh'}(J'_1,J',J_R)\right)^*\\
&-\frac{1}{2}\left(e^{-i\varphi_a}-/+(-1)^{J+J'+J_2}e^{i\varphi_a}\right)\mathcal{M}^{\mathrm{magn},[2]}_{p_a p_b;hh'}(J_1,J,J_R)\left(\mathcal{M}^{\mathrm{Coul},[2]}_{p_a p'_b;hh'}(J'_1,J',J_R)\right)^*\Bigg\}.\end{aligned} \quad (4.39)$$

The interference responses with the longitudinal current are then obtained by replacing the Coulomb operator with the longitudinal operator and introducing an overall minus sign

$$\begin{aligned}\int \mathrm{d}\Omega_b W_{TL/TL'} = -&\sum_{J_R}\sum_{J\geq 1 J'\geq 0}\sum_{l_a j_a}\sum_{l_b j_b}\sum_{l'_b j'_b}\sum_{J_1 J'_1}\sum_{J_3\geq 1}\\
&\times(-1)^{j_a-1/2+J_R+j_b-j'_b+J_2}P^1_{J_3}(\cos\theta_a)\langle J\ 1\ J'\ 0\,|\,J_3\ 1\rangle\frac{\sqrt{2}}{\sqrt{J_2(J_2+1)}}\\
&\times\mathcal{B}\left[p_a(E_a l_a j_a),p_b(E_b l_b j_b)p'_b(E_b l'_b j'_b),h,h',J_1,J,J'_1,J',J_R,J_3\right]\end{aligned}$$

$$\times \mathrm{Re}\Bigg\{ \frac{1}{2}\left(e^{-i\varphi_a} + / - (-1)^{J+J'+J_2} e^{i\varphi_a}\right) \mathcal{M}^{\mathrm{elec},[2]}_{p_a p_b;hh'}(J_1,J,J_R) \left(\mathcal{M}^{\mathrm{long},[2]}_{p_a p'_b;hh'}(J'_1,J',J_R)\right)^* - \frac{1}{2}\left(e^{-i\varphi_a} - / + (-1)^{J+J'+J_2} e^{i\varphi_a}\right) \mathcal{M}^{\mathrm{magn},[2]}_{p_a p_b;hh'}(J_1,J,J_R) \left(\mathcal{M}^{\mathrm{long},[2]}_{p_a p'_b;hh'}(J'_1,J',J_R)\right)^* \Bigg\}. \tag{4.40}$$

These expressions can be compared with the expressions for electron scattering in [2]. The responses $\{CC, CL, LL, T, T'\}$ are written as a linear combination of the standard Legendre polynomials, while the responses $\{TC, TC', TL, TL'\}$ and TT are linear combinations of the first and second order associated Legendre polynomials respectively. This will be exploited in the next section for the integration over Ω_a.

4.3 Inclusive $2N$ knockout cross section

As a last step, the $2N$ knockout contribution to the inclusive $A(l,l')$ cross section can be calculated following the same approach. An integration over the phase space $\mathrm{d}T_a \mathrm{d}\Omega_a$ of the second particle is performed. For Eq. (4.25), where the detected particle is a proton ($N_a = \mathrm{p}$), this results in

$$\frac{\mathrm{d}\sigma}{\mathrm{d}\epsilon_f \mathrm{d}\Omega_f}(l,l') = \int \mathrm{d}T_\mathrm{p} \mathrm{d}\Omega_\mathrm{p} \frac{\mathrm{d}\sigma}{\mathrm{d}\epsilon_f \mathrm{d}\Omega_f \mathrm{d}T_\mathrm{p} \mathrm{d}\Omega_\mathrm{p}}(l,l'\mathrm{p}). \tag{4.41}$$

Integration of the responses $\{CC, CL, LL, T, T'\}$ is trivial since they are written as a linear combinations of the Legendre polynomials $P_{J_3}(\cos\theta_a)$. All the Legendre polynomials except $P_0(\cos\theta_a)$ are odd functions of $\cos\theta_a$. Integration over Ω_a thus implies that only the $J_3 = 0$ term remains in the sum and an overall factor 4π shows up. The other five responses $\{TT, TC, TL, TC', TL'\}$ cancel because they are odd functions of φ_a. The integration over kinetic energy of the outgoing nucleon T_a is performed numerically.

This inclusive $2N$ knockout contribution was examined using the same approach in [11] to study the difference between theory and experiment in the Coulomb and longitudinal responses for (e,e') scattering on ^{12}C and ^{40}Ca. The $2N$ knockout channel was found to provide a large fraction of the missing strength in the dip region.

References

[1] J. Ryckebusch, L. Machenil, M. Vanderhaeghen, *et al.* Phys. Rev. **C49**, 2704 (1994).

[2] J. Ryckebusch, M. Vanderhaeghen, L. Machenil, *et al.* Nucl. Phys. **A568**, 828 (1994).

[3] J. Ryckebusch, V. Van der Sluys, K. Heyde, *et al.* Nucl. Phys. **A624**, 581 (1997).

[4] J. Ryckebusch and W. Van Nespen, Eur. Phys. J. **A20**, 435 (2004).

[5] ArgoNeuT collaboration, R. Acciarri *et al.* Phys. Rev. **D90**, 012008 (2014).

[6] S. Janssen, J. Ryckebusch, W. Van Nespen, *et al.* Nucl. Phys. **A672**, 285 (2000).

[7] C. Colle, W. Cosyn, J. Ryckebusch, *et al.* Phys. Rev. **C89**, 024603 (2014).

[8] J. Ryckebusch, M. Vanderhaeghen, K. Heyde, *et al.* Phys. Lett. **B350**, 1 (1995).

[9] J. Ryckebusch, S. Janssen, W. Van Nespen, *et al.* Phys. Rev. **C61**, 021603 (2000).

[10] K. Gottfried, Nucl. Phys. **5**, 557 (1958).

[11] V. Van der Sluys, J. Ryckebusch, and M. Waroquier, Phys. Rev. **C51**, 2664 (1995).

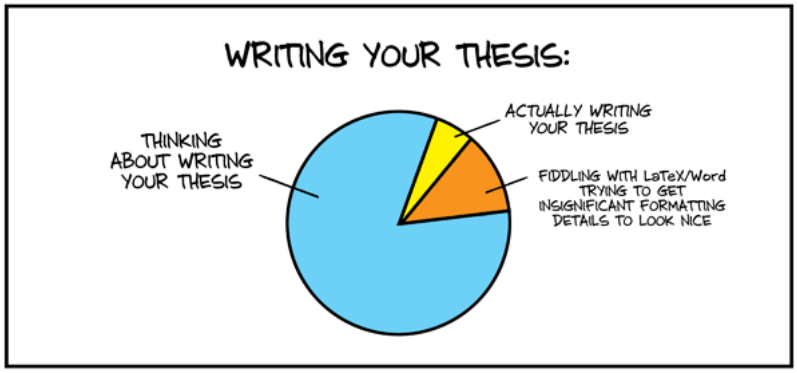

Chapter 5

Short-range correlations

The nucleons inside the nucleus are bound via the nuclear force, which is repulsive at short distances, attractive at intermediate distances, and vanishes when the distance between the nucleons becomes too large. The short-range repulsive character of this force, which correlates with the Pauli exclusion principle, results in a large mean free path of the nucleons with respect to the size of the nucleus. This allows for a treatment of the nucleus as a collection of nucleons moving independently in a MF potential well: an IPM. Essentially the nuclear A-body problem is replaced with a sum of A single-body problems.

This simple IPM provides an explanation for several nuclear properties: the nuclear binding energies and the extra stability of closed-shell systems for example, but it also has its limitations. When describing the nucleons as moving independently in a MF potential, a lot of the internucleon correlations (long and short) are not accounted for. Long-range correlations are correlations over the whole size of the nucleus and they can redistribute the incoming energy transfers to the nucleus over all the nuclear constituents. They manifest themselves in collective excitations such as giant resonances. SRCs occur when two nucleons have strongly overlapping wave functions for short periods of time. The short-range repulsive part of the nucleon-nucleon force and intermediate-range tensor component lead to strong deviations from IPM properties.

A first implication of SRCs is a high-energy and high-momentum component in the nuclear wave functions which is missing in IPM wave functions. Another consequence is the reduced occupation probability of the valence shells in nuclei compared to the IPM result: the spectroscopic strength [1]. These are usually explained as excitations of the nucleus where two nucleons are excited to a state with larger momentum. Note that these excitations are relative to the theoretical IPM and form a genuine part of the nuclear ground state.

Correlations between the constituents of an IPM can be introduced as follows. The two-

body density function is defined as the probability of finding a particle at $\boldsymbol{r}_1$ if another particle is present at $\boldsymbol{r}_2$. In an IPM with one-body density $\rho^{[1]}(\boldsymbol{r})$, the two-body density is the product of two independent one-body density functions, which signifies that the nucleons move independently from each other. Correlations can be introduced on top of the IPM by defining the two-body density as

$$\rho^{[2]}(\boldsymbol{r}_1, \boldsymbol{r}_2) = \rho^{[1]}(\boldsymbol{r}_1)\rho^{[1]}(\boldsymbol{r}_2)g(r_{12}), \tag{5.1}$$

with $r_{12} = |\boldsymbol{r}_1 - \boldsymbol{r}_2|$ and $g(r_{12})$ the correlation function. In the case $g(r_{12}) = 1$, the IPM result is obtained. For an atomic ^{4}He liquid, this correlation function has been measured experimentally, e.g. in Refs. [2,3], and its features are shown schematically in Fig. 5.1. For small internucleon distances it has a hard repulsive core, $g(r_{12}) \to 0$, representing the repulsive character of the inter-atomic potential at small distances. For larger r_{12} it rises above 1 before it reaches its asymptotic value of 1. The asymptotic value of 1 represents the fact that the atoms are not correlated beyond the range of the inter-atomic force. Since the range of the correlations is confined to $\lesssim 2$ fm, it can be considered as a universal nuclear property. Its range is shorter than the radius of most nuclei, e.g. ^{12}C has $r \approx 2.86$ fm, so only nucleons in the direct vicinity will be affected.

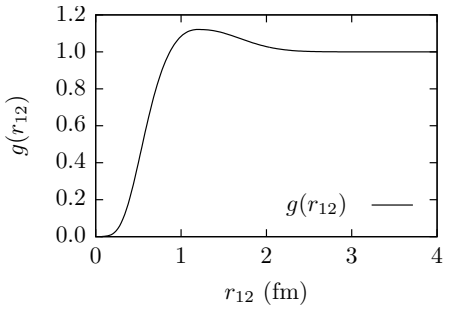

Figure 5.1: The schematic features of the correlation function $g(r_{12})$ for an atomic ^{4}He liquid.

SRCs and their influence on electromagnetic scattering cross sections have been studied intensively. The basic idea for the study of the interaction of real and virtual photons with an SRC pair in a nucleus has been proposed by Gottfried in 1958 [4]. However, it took several years and the advent of high intensity photon and electron beams to study these SRCs and how they influence cross sections [5]. Co *et al.* systematically studied the effect of central correlations on the inclusive $1N$ and $2N$ knockout responses, using an approach similar to the model presented below [6–8]. In Refs. [9,10] this approach was used to study exclusive $1N$ and $2N$ knockout interactions. In studies by Giusti *et al.* [11,12], central and tensor SRCs were included for exclusive photoinduced and electroinduced $2N$ knockout reactions. Recent work on electron scattering by Benhar *et al.* [13,14] has generalized the formalism based on a factorization ansatz and nuclear spectral functions to treat transition matrix elements involving SRCs.

To the best of our knowledge, the studies mentioned above studying SRCs have not been extended to neutrino scattering interactions at the time of writing. For neutrino scattering calculations, with the aim of comparison with experimental data, Martini *et al.* and Nieves *et al.* take nucleon-nucleon correlations in account in a Fermi gas model, by considering an additional two-body current, the correlation current[1] Martini *et al.* consider pionic correla-

[1]These correlation currents are shown in diagrams (h-k) of Fig. 6.1.

tion currents with a Landau-Midgal interaction accounting for short-range repulsion [15,16]. Nieves *et al.* consider pion and rho meson correlation currents [17].

In the SuSA approach, a superscaling analysis of electron scattering results is used to predict νA cross sections [18]. The effects of SRCs in the $1p1h$ sector are effectively included via the phenomenological superscaling function. In ab-initio calculations on ^{12}C [19,20], nuclear correlations are inherently taken into account.

The formalism presented in this chapter is an extension of the model by Ryckebusch *et al.* where central and spin-dependent correlations were introduced in $(e, e'\mathrm{pn})$ and $(e, e'\mathrm{pp})$ interactions [21,22]. In Refs. [23,24], this model was compared with $^{16}\mathrm{O}(e, e'\mathrm{pp})^{12}\mathrm{C}$ data to look for evidence of SRCs in two proton knockout reactions. The results show that this reaction is dominated by knockout of proton pairs with a small c.o.m. momentum, residing in a relative S state. In Refs. [25–27] a similar approach is used to study the effect of SRCs on nuclear properties such as the nuclear momentum distributions and the mass dependence of the SRC pairs in nuclei.

The general formalism used to include SRCs in our model is presented below as well as some general implications of the SRCs on the nuclear properties. The introduction of central correlations suppresses the probability of finding two nucleons close to each other. Tensor and spin-isospin correlations will induce a correlation between the spatial distance between nucleons and the orientation of their spins and isospin. Results are presented for $1N$ and $2N$ knockout calculations. For detailed calculations of the SRC matrix elements we refer to Appendix F.

5.1 Formalism

Different techniques to correct IPM wave functions for correlations have been developed over the years. We follow the approach outlined in Refs. [21,22,25,26,28]. Upon calculating transition matrix elements in an IPM, the nuclear wave functions are written as Slater determinants $|\Phi\rangle$. Correlated wave functions $|\Psi\rangle$ are constructed by applying a many-body correlation operator $\widehat{\mathcal{G}}$ to the uncorrelated wave function $|\Phi\rangle$,

$$|\Psi\rangle = \frac{1}{\sqrt{\mathcal{N}}}\widehat{\mathcal{G}}|\Phi\rangle, \tag{5.2}$$

with $\mathcal{N} = \langle\Phi|\widehat{\mathcal{G}}^\dagger\widehat{\mathcal{G}}|\Phi\rangle$ the normalization constant. In the derivation of the correlation operator $\widehat{\mathcal{G}}$, one is guided by the basic features of the nucleon-nucleon force. A parameterization of the nucleon-nucleon force usually contains many terms. Its short-range part is dominated by the central and tensor component. To a good approximation, the correlation operator can be written as

$$\widehat{\mathcal{G}} \approx \widehat{\mathcal{S}}\left(\prod_{i<j}^{A}\left[1 + \widehat{l}(i,j)\right]\right), \tag{5.3}$$

with $\widehat{\mathcal{S}}$ the symmetrization operator and

$$\widehat{l}(i,j) = -\widehat{g}(i,j) + \widehat{s}(i,j) + \widehat{t}(i,j)$$

$$= -f_c(r_{ij}) + f_{\sigma\tau}(r_{ij})\,(\boldsymbol{\sigma}_i \cdot \boldsymbol{\sigma}_j)\,(\boldsymbol{\tau}_i \cdot \boldsymbol{\tau}_j) + f_{t\tau}(r_{ij})\widehat{S}_{ij}\,(\boldsymbol{\tau}_i \cdot \boldsymbol{\tau}_j)\,, \tag{5.4}$$

with $r_{ij} = |\boldsymbol{r}_i - \boldsymbol{r}_j|$ and $\widehat{S}_{ij}$ is the tensor operator

$$\widehat{S}_{ij} = \frac{3}{r_{ij}^2}(\boldsymbol{\sigma}_i \cdot \boldsymbol{r}_{ij})(\boldsymbol{\sigma}_j \cdot \boldsymbol{r}_{ij}) - (\boldsymbol{\sigma}_i \cdot \boldsymbol{\sigma}_j). \tag{5.5}$$

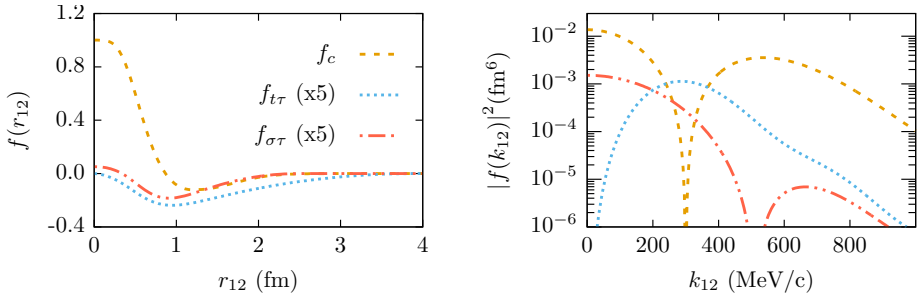

Figure 5.2: The correlation functions used in the presented calculations. For the coordinate space representation, the tensor and spin-isospin correlation functions are multiplied by a factor five.

This work uses the central correlation function $f_c(r_{ij})$ by Gearhart and Dickhoff (GD) [29]. This correlation function goes to zero for $r_{ij} \gtrsim 2$ fm and has a hard core at short distances, which guarantees that nucleons repel each other when they come too close. The same function was used successfully for the description of semi-exclusive ^{16}O$(e,e'$p$)$ [22] and exclusive ^{12}C$(e,e'$pp$')$ [30] and ^{16}O$(e,e'$pp$')$ [31,32] reactions. The central correlation function can be related to $g(r)$ in Eq. (5.1) via

$$g(r_{ij}) = 1 - f_c(r_{ij}). \tag{5.6}$$

For the tensor $f_{t\tau}(r_{ij})$ and spin-isospin correlation functions $f_{\sigma\tau}(r_{ij})$, the results by Pieper *et al.* are used [33]. Ref. [25] provides arguments and evidence to support our claim that these correlation functions can be considered realistic. Fig. 5.2 shows the correlation functions in coordinate and momentum space. For small internucleon distances, $f_{t\tau}$ and $f_{\sigma\tau}$ are considerably weaker than f_c. At medium inter-nucleon distances ($r_{ij} \gtrsim 3$ fm), $\widehat{l}(r_{ij}) \to 0$. In momentum space, $f_{t\tau}$ dominates for relative momenta $200 - 400$ MeV/c. Based on this behavior one can expect important contributions coming from the tensor correlations at intermediate missing (or, relative) momenta.

The matrix elements of an operator $\widehat{\Omega}$ between correlated states can then be written as a matrix element between uncorrelated states where the effect of the correlations are implemented by means of an effective transition operator $\widehat{\Omega}^{\,\mathrm{eff}}$

$$\langle \Psi_f | \widehat{\Omega} | \Psi_i \rangle = \frac{1}{\sqrt{\mathcal{N}_i \mathcal{N}_f}} \langle \Phi_f | \widehat{\Omega}^{\,\mathrm{eff}} | \Phi_i \rangle, \tag{5.7}$$

with

$$\widehat{\Omega}^{\,\mathrm{eff}} = \widehat{\mathcal{G}}^\dagger \widehat{\Omega} \widehat{\mathcal{G}} = \left(\prod_{i<j}^{A} \left[1 + \widehat{l}(i,j) \right] \right)^\dagger \widehat{\mathcal{S}}^\dagger \, \widehat{\Omega} \, \widehat{\mathcal{S}} \left(\prod_{k<l}^{A} \left[1 + \widehat{l}(k,l) \right] \right). \tag{5.8}$$

In the calculation of lepton-nucleus cross sections, we need to calculate transition matrix elements of the form

$$\langle \Psi_f | \widehat{J}_\mu^{\rm nuc} | \Psi_i \rangle = \frac{1}{\sqrt{\mathcal{N}_{\rm i}\mathcal{N}_{\rm f}}} \langle \Phi_f | \widehat{J}_\mu^{\rm eff} | \Phi_i \rangle, \tag{5.9}$$

where $\widehat{J}_\mu^{\rm nuc}$ is the many-body nuclear current and $\widehat{J}_\mu^{\rm eff}$ the effective nuclear current which accounts for correlations. In the IA, the many-body nuclear current can be written as a sum of one-body operators

$$\widehat{J}_\mu^{\rm nuc} \approx \widehat{J}_\mu^{\rm IA} = \sum_{i=1}^{A} \widehat{J}_\mu^{[1]}(i). \tag{5.10}$$

In principle, the effective nuclear current is now a sum of different operators, ranging from one-body operators to A-body operators. In Fig. 5.3, the first few terms of this current are shown diagrammatically. The shaded circle represents the i-th single-nucleon current $\widehat{J}_\mu^{[1]}(i)$ and the empty circle represents any other nucleon in the nucleus. The dashed lines represent a correlation between two particles. Diagrams (d) and (e) for example represent a term in the expansion where particles j and k are correlated, but have no correlation with the *active* particle i. This is a disconnected diagram and has no effect on the cross section calculations in the spectator approach.

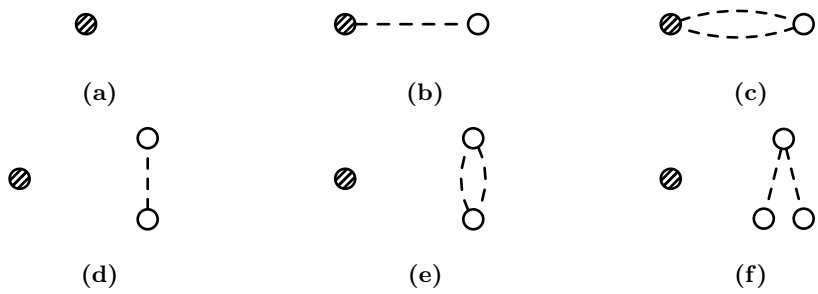

Figure 5.3: Graphical representation of the expansion of the effective operator for a one-body current.

The universal properties of the SRCs over the nuclear mass range, see e.g. Ref. [34], hint at a local property, which naturally truncates the A-body correlation operator. Given that the correlations have a short range, only terms that are linear in the correlation operator are retained in the expansion of the effective operator. Higher order terms are expected to produce little contributions to the inclusive cross section. Additionally, the probability of finding three or more correlated nucleons, at normal nuclear densities, is generally conceived to be very small[2]. Under these assumptions, the effective nuclear current, which accounts for SRCs, is written as

$$\widehat{J}_\mu^{\rm eff} \approx \sum_{i=1}^{A} \widehat{J}_\mu^{[1]}(i) + \sum_{i<j}^{A} \widehat{J}_\mu^{[1],{\rm in}}(i,j) + \left[\sum_{i<j}^{A} \widehat{J}_\mu^{[1],{\rm in}}(i,j) \right]^\dagger, \tag{5.11}$$

[2]Under these conditions, it can be argued that the terms quadratic in the correlation functions, diagram (c), should be included as well. They are not included due to analytical complexity.

with

$$\widehat{J}_{\mu}^{[1],\mathrm{in}}(i,j) = \left[\widehat{J}_{\mu}^{[1]}(i) + \widehat{J}_{\mu}^{[1]}(j)\right]\widehat{l}(i,j). \tag{5.12}$$

The effective operator consists of one- and two-body terms. The superscript 'in' refers to initial-state correlations. The first term in Eq. (5.11) corresponds to diagram (a) of Fig. 5.3 while the second and third terms correspond to diagram (b). In the absence of correlations only the first term of Eq. (5.11) does not vanish. At medium inter-nucleon distances ($r_{ij} \geqslant 3$ fm) one has $\widehat{l}(r_{ij}) \to 0$ and the effective operator $\widehat{J}^{\mathrm{eff}}$ approaches the uncorrelated operator $\widehat{J}^{\mathrm{IA}}$. Due to the local character of the SRCs, the multipole expansion of these operators can be truncated at low order.

In Chapter 6, MECs will be discussed. When MECs are included in the nuclear current, genuine two body-currents are added to the nuclear current in the IA

$$\widehat{J}_{\mu}^{\mathrm{nuc}} = \sum_{i=1}^{A} \widehat{J}_{\mu}^{[1]}(i) + \sum_{i<j}^{A} \widehat{J}_{\mu}^{[2],\mathrm{MEC}}(i,j). \tag{5.13}$$

The same steps can then be followed to construct an effective operator. The first few terms in the expansion of the effective current are shown graphically in Fig. 5.4. Diagram (a) represents a MEC between particles i and j and in diagram (b), these two particles happen to be part of an SRC pair as well, etc. In diagram (g), the particles i and j are part of a MEC pair, while particles k and l are part of a correlated pair, these kind of disconnected diagrams have no influence on the cross sections in the spectator approach. Again, only the

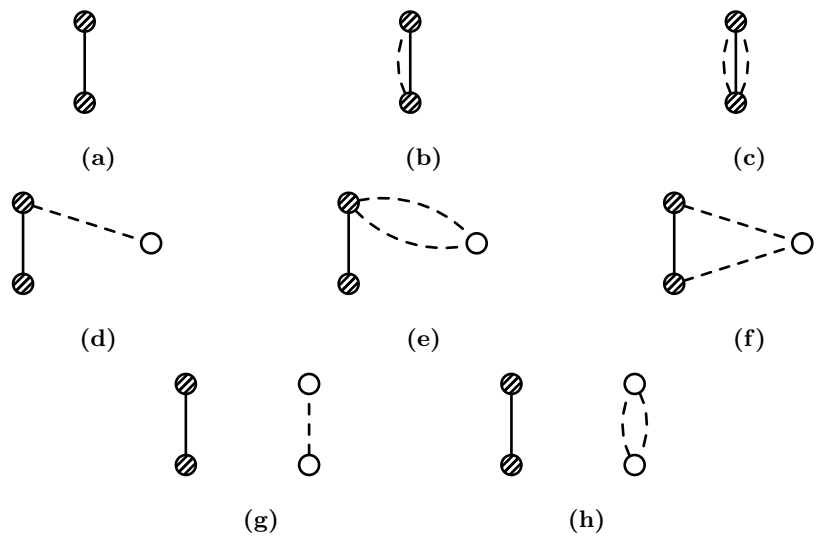

Figure 5.4: Graphical representation of the expansion of the effective operator for a two-body current.

terms linear in the correlation operator are retained. Furthermore diagrams (d-f) in which three nucleons are correlated will not be considered. This means only diagrams of type (a), the genuine two-body currents, and type (b), the MEC-SRC interference diagrams, will be retained. The effective nuclear current that accounts for SRCs and MECs can then be

written as

$$\widehat{J}_\mu^{\text{eff}} \approx \sum_{i=1}^{A} \widehat{J}_\mu^{[1]}(i) + \sum_{i<j}^{A} \widehat{J}_\mu^{[1],\text{in}}(i,j) + \left[\sum_{i<j}^{A} \widehat{J}_\mu^{[1],\text{in}}(i,j)\right]^\dagger + \sum_{i<j}^{A} \widehat{J}_\mu^{[2],\text{MEC}}(i,j) + \sum_{i<j}^{A} \widehat{J}_\mu^{[2],\text{int}}(i,j) + \left[\sum_{i<j}^{A} \widehat{J}_\mu^{[2],\text{int}}(i,j)\right]^\dagger, \tag{5.14}$$

where the MEC-SRC interference terms, 'int', are defined as

$$\widehat{J}_\mu^{[2],\text{int}}(i,j) = \widehat{J}_\mu^{[2],\text{MEC}}(i,j)\widehat{l}(i,j). \tag{5.15}$$

The Feynman diagram contributing to the $1N$ knockout channel is shown in Fig. 5.5a and those feeding the $2N$ knockout channels in Fig. 5.5b. The exchange diagrams, which follow from the antisymmetrization of the matrix element in second quantization, are not shown.

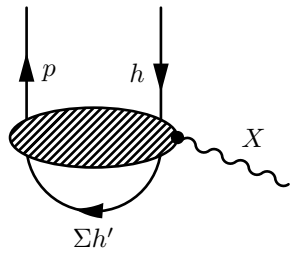

(a) $1p1h$ diagram

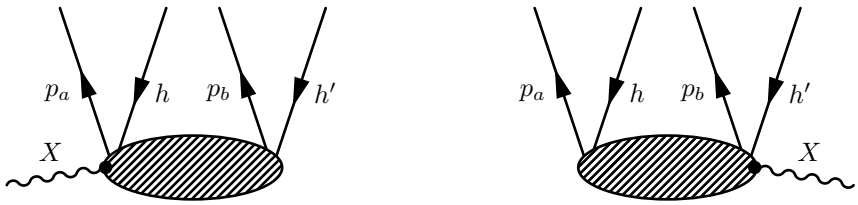

(b) $2p2h$ diagrams

Figure 5.5: Representation of the SRC currents in the $1N$ and $2N$ knockout channels, represented as particle-hole diagrams. The oval represents the correlations between two nucleons.

In Fig. 5.6, we show how the SRCs affect the mean-field properties of nuclei. Both figures are taken or adapted from [35] where a similar method to the one outlined above was used, to study nuclear momentum distributions of nuclei. The single-nucleon $n^{[1]}(p)$ and two-nucleon momentum distributions $n^{[2]}(k_{12})$ are shown for a range of nuclei. The quantity $n^{[1]}(p)p^2\mathrm{d}p$ gives the probability of finding a nucleon with momentum p in the interval $[p, p+dp]$ and $n^{[2]}(k_{12})k_{12}^2\mathrm{d}k_{12}$ is the probability to find a pair of nucleons with relative momentum $k_{12} = |\boldsymbol{p}_1 - \boldsymbol{p}_2|/\sqrt{2}$ in the interval $[k_{12}, k_{12} + \mathrm{d}k_{12}]$.

The low-order correlation operator approximation (LCA) used in [35] differs slightly from the one outlined above as more diagrams are considered. For the calculation of the single-

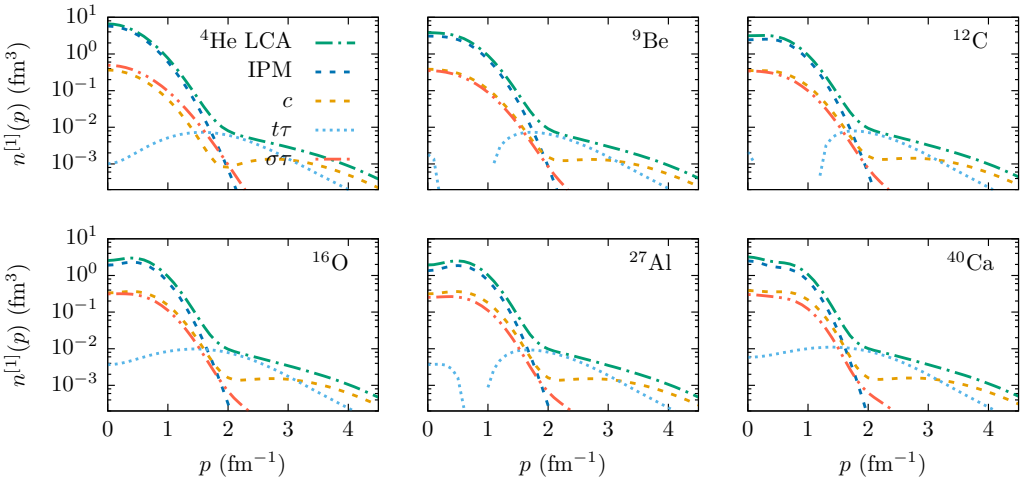

(a) Single-nucleon momentum distribution $n^{[1]}(p)$. Figure adapted from [26].

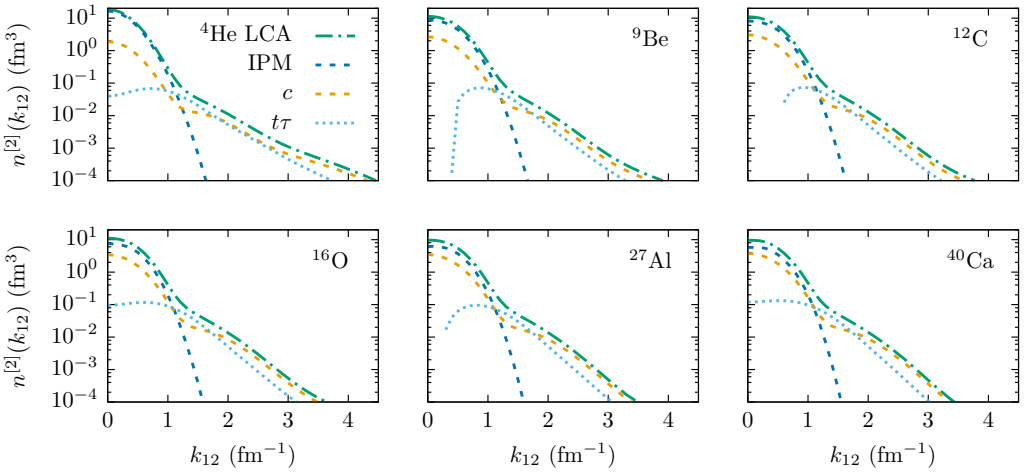

(b) Two-nucleon relative momentum distribution $n^{[2]}(k_{12})$. Figure taken from [35].

Figure 5.6: The single-nucleon momentum distribution $n^{[1]}(p)$ and two-nucleon momentum distribution $n^{[2]}(k_{12})$ for six nuclei. The LCA result is the full calculation. Also shown are the results of a calculation in an IPM and one that only includes the central (c), tensor ($t\tau$) or spin-isospin ($\sigma\tau$) correlations.

nucleon momentum distribution, the diagram quadratic in the correlation function is included: diagram (c) in Fig. 5.3. For the two-nucleon momentum distribution, diagrams (c), (d) and (e) of Fig. 5.4 are included.

The single-nucleon momentum distribution is shown in Fig. 5.6a. Some features emerge which are valid for all nuclei. The distribution is dominated by the IPM contribution for $p \lesssim 1.5$ fm^{-1} and the high momentum tail is induced by the SRCs. The tensor correlations are most important for $1.5 \lesssim p \lesssim 3$ fm^{-1} and for higher p values, the majority of the strength is coming from the central correlations. This indicates that nucleons with a momentum

below the Fermi momentumm, $p \lesssim p_F$ MeV/c, move independently in a MF potential, while nucleons with $p \gtrsim p_F$ belong to short-range correlated pairs.

The two-nucleon momentum distribution in Fig. 5.6b shows similar features. It is dominated by the IPM contributions for relative momenta $k_{12} \lesssim 1.1$ fm^{-1} and a high momentum tail is induced by the SRCs, although less pronounced than for the one-nucleon momentum distribution. Again one can distinguish two regions: for $1 \lesssim k_{12} \lesssim 1.75$ fm^{-1} the tensor correlations provide the most important contribution and for higher k_{12}, central correlations dominate.

These two figure demonstrated how the SRCs affect the MF properties of the nucleons in a nucleus. In the remainder of this chapter we will investigate how SRCs influence $1N$ and $2N$ knockout cross sections. First, the effect of SRCs on inclusive $1N$ knockout cross sections is studied. Results for ^{12}C(e,e') and ^{12}C(ν_μ,μ^-) cross sections are presented and the electron scattering calculations are compared with data.

Afterwards, exclusive, semi-exclusive and inclusive $2N$ knockout cross sections are studied systematically. The separate contributions of the three components of the SRCs: the central, tensor and spin-isospin part will be compared as well. Some general characteristics of these $2N$ knockout cross sections will be explained using simple kinematic considerations and the properties of the correlation functions in momentum space. The exclusive $2N$ knockout strength will be related to the c.o.m. momentum of the pair P_{12} in the target nucleus. The relative strength of the tensor and the central correlation functions is explained with the initial relative momentum of the pair k_{12}.

At the end of the chapter, the knockout ratio of SRC pairs from ^{16}O to ^{12}C will be shown and compared with a scaling relation derived in [36].

5.2 Influence of SRCs on inclusive $1N$ knockout

In Fig. 5.7, the numerical results for the inclusive $1p1h$ responses W_{CC} and W_T are shown for ^{12}C(e,e') interactions and compared with Rosenbluth separated cross section data at a fixed momentum transfer. The responses are denoted using the conventions of Chapter 3, where the superscripts in the responses indicate whether one- and/or two-body currents are used in the calculation of the responses

$$W_i^{\mathrm{IA}} = W_i^{[1]} \tag{5.16}$$

$$W_i^{\mathrm{IA+SRC}} = W_i^{[1]} + W_i^{[2]} + W_i^{[1,2]}. \tag{5.17}$$

The top plot, Fig. 5.7a, compares the calculations in the IA with the calculations where the SRCs were taken into account (IA+SRC). The corrections from the SRCs in the $1p1h$ channel result in a small increase of the Coulomb responses and a marginal increase of the transverse response. The increase is most sizeable for small q.

In the bottom plot, Fig. 5.7b, the two-body corrections,

$$\Delta W_i = W_i^{\mathrm{IA+SRC}} - W_i^{\mathrm{IA}} = W_i^{[2]} + W_i^{[1,2]}, \tag{5.18}$$

for the three components of the SRCs are shown separately. The central correlation has the largest influence on the $1p1h$ responses. The tensor and spin-isospin correlations have

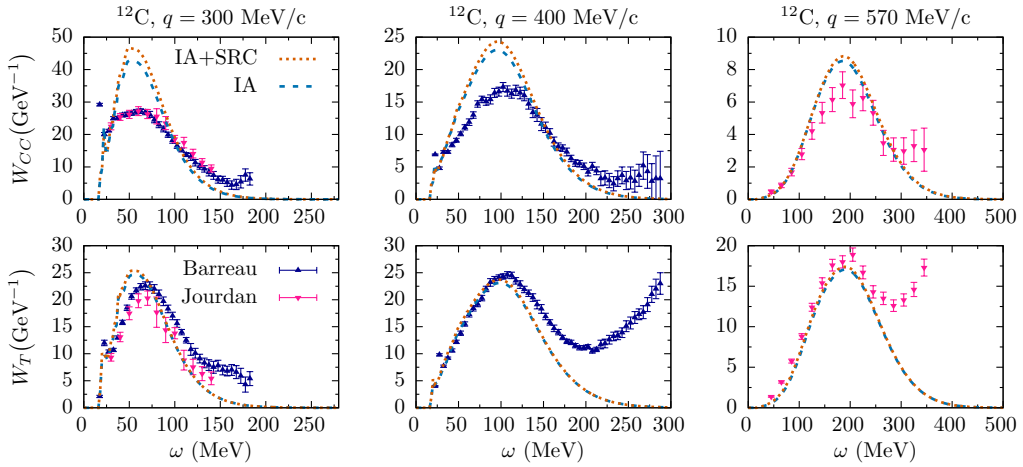

(a) The $1p1h$ responses.

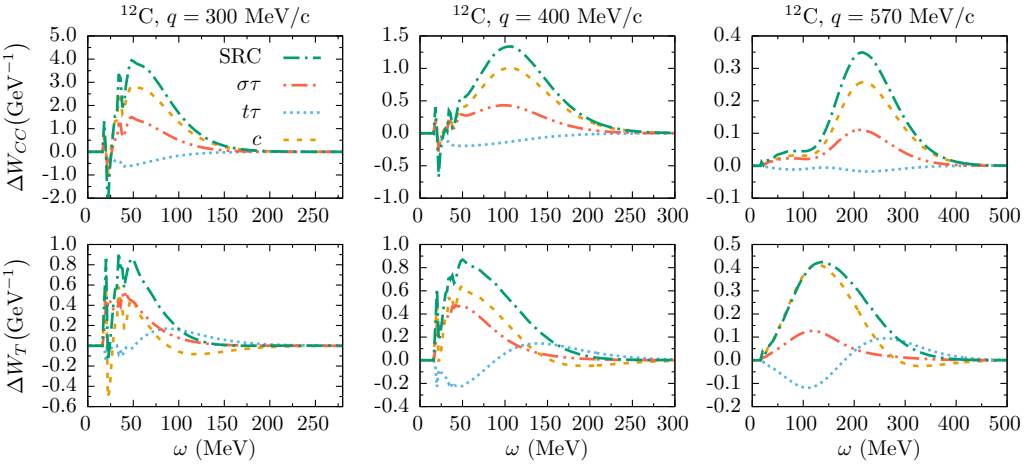

(b) The correction of the SRCs to the $1p1h$ responses.

Figure 5.7: The computed ω dependence of the ^{12}C(e, e') responses W_{CC} and W_T for three different momentum transfers. The data is from Refs. [37,38].

a smaller impact on the responses. Furthermore, the effects of the tensor and spin-isospin correlations tend to cancel each other. The relative importance of the three components of the SRCs is similar in both responses.

The results shown above have been obtained using the GD central correlation function. However, these results are very sensitive to the choice of the central correlation function, similar conclusions were obtained in [8]. Correlation functions and single-particle wave functions are not independent quantities, they are fixed by minimization of the ground-state energy. The solution of this minimization problem lies beyond the scope of this work. We selected the GD central correlation function in the numerical calculations because it was used

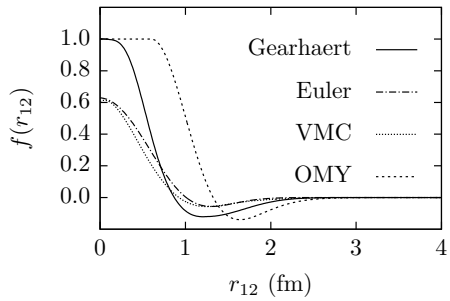

Figure 5.8: The different central correlation functions $f_c(r_{12})$.

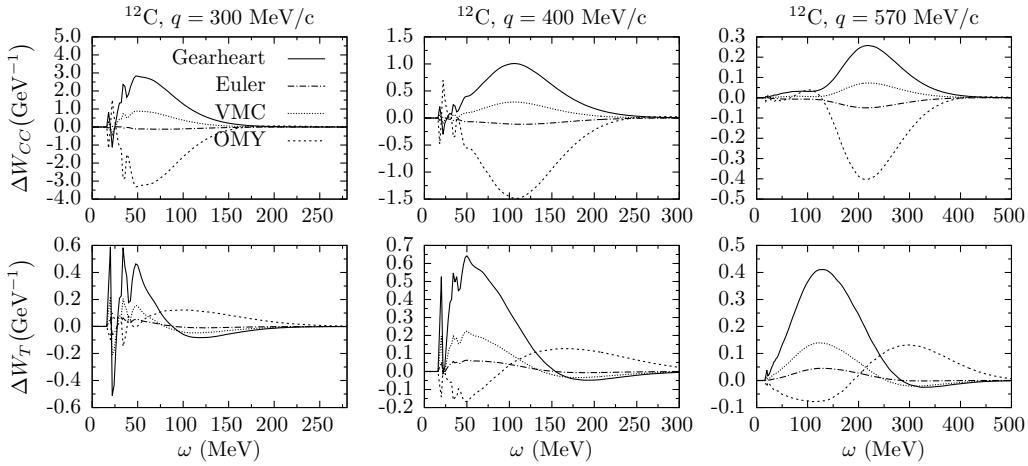

Figure 5.9: The effect of the different central correlation functions on the $1p1h$ responses for $^{12}\mathrm{C}(e,e')$ interactions.

successfully in the description of semi-exclusive $^{16}\mathrm{O}(e,e'\mathrm{p})$ [22] and exclusive $^{12}\mathrm{C}(e,e'\mathrm{pp}')$ [30] and $^{16}\mathrm{O}(e,e'\mathrm{pp}')$ [31,32] reactions.

To illustrate the sensitivity to the central correlation functions, we show the effect of four different correlation functions in Fig. 5.9. The corresponding correlation functions are shown in Fig. 5.8. The GD central correlation function [29] has a hard core guaranteeing that the nucleons repel each other strongly at short distances. It was derived using Green's function methods for nuclear matter with the Reid potential [39].

The VMC correlation function [33] follows from a variational Monte Carlo calculation using the Argonne v_{14} nucleon-nucleon potential [40] and the Urbana VII three-nucleon interaction [41]. The ground-state of ^{16}O was determined by minimizing the energy, including up to four-body terms in their cluster expansion. The Euler correlation [42] function was determined using a correlated basis function calculation for double closed shell nuclei, using only the central components of the nucleon-nucleon interaction (v_4). The VMC and Euler correlation functions have a much softer core compared to the GD correlation function. The OMY correlation function [43] resembles the GD correlation function in shape, but it

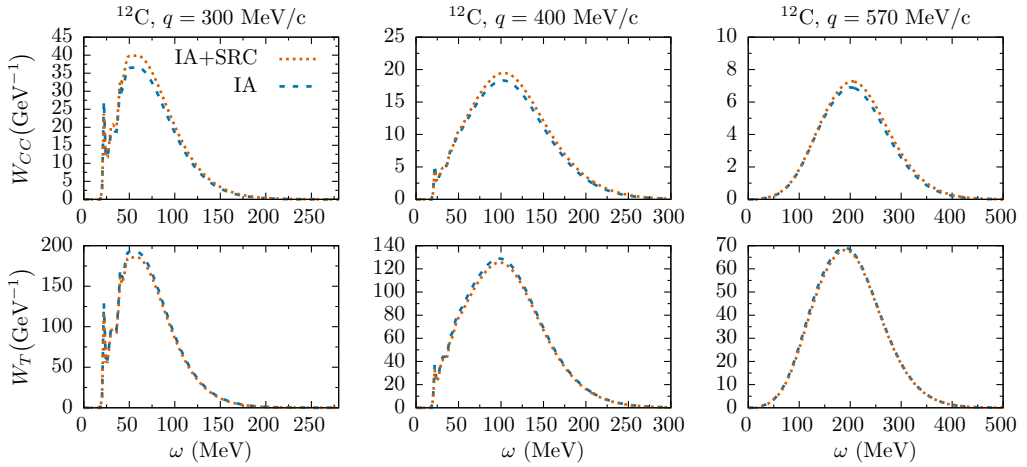

(a) The $1p1h$ responses.

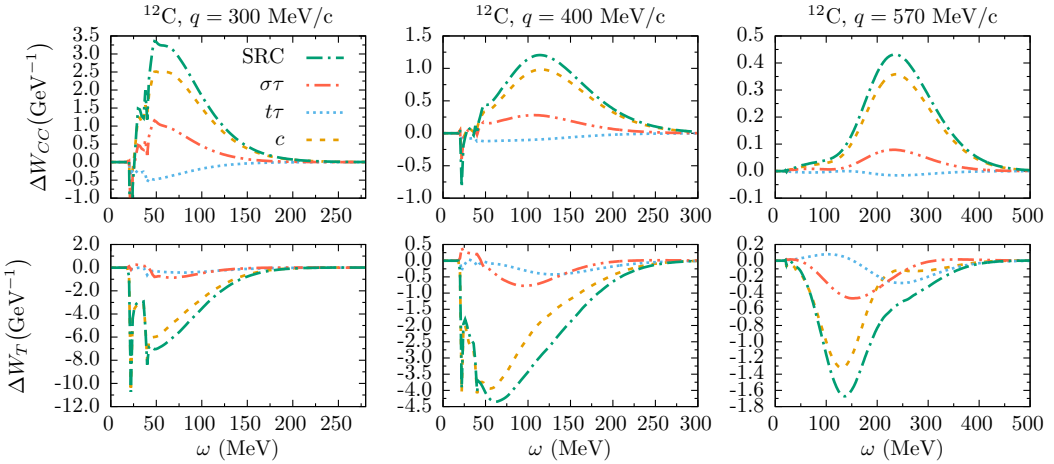

(b) The correction of the SRCs to the $1p1h$ responses.

Figure 5.10: The computed ω dependence of the ^{12}C(ν_μ, μ^-) responses W_{CC} and W_T for three different momentum transfers.

has an extended hard core. It should not be considered a realistic correlation function but maximizes the effect of the SRCs [21].

The effect of the central correlation on $1p1h$ responses is largest for correlations with a hard core, i.e. $f_c(0) = 1$. Further, the effect of the Euler and VMC correlations is very similar in the transverse channel, with the latter producing the largest effect. In the Coulomb channel, the Euler correlation function appears to have very little effect. Similar results were obtained in [8], where a systematic study of the size of the correlation at $r = 0$ and the location of the minimum, on the response functions was performed.

Now we continue with neutrino scattering interactions. All calculations discussed above were

performed with the GD central correlation function, unless mentioned otherwise. The results corresponding to Fig. 5.7, but now for neutrino scattering are given in Fig. 5.10. The IA calculations are compared with calculations that include SRC corrections in Fig. 5.10a. The inclusion of the SRCs results in a small increase of the Coulomb response. The inclusion of SRCs for neutrino interactions decreases the transverse response, in contrast to the situation observed for electron scattering interactions. The relative influence is biggest for small q.

In the bottom plot, Fig. 5.10b, the corrections of the three components of the SRCs are shown. In the Coulomb response, the results are similar to those for electron scattering. The reason for this similarity lies in the fact that the Coulomb response is dominated by the vector part of the nuclear current, as shown in Fig. 3.9. In the transverse response, the correlations and the nuclear current in the IA interfere destructively. The net negative effect of the interference is not purely a result of the axial part of the current. Even when considering only the vector part of the transverse response, the SRC correction on the transverse response for neutrino scattering resulted in a decrease of the response, while an increase of the response was seen for electron scattering. The reason of the opposite effect is related to isospin factors in the interference between the one-body and two-body matrix elements.

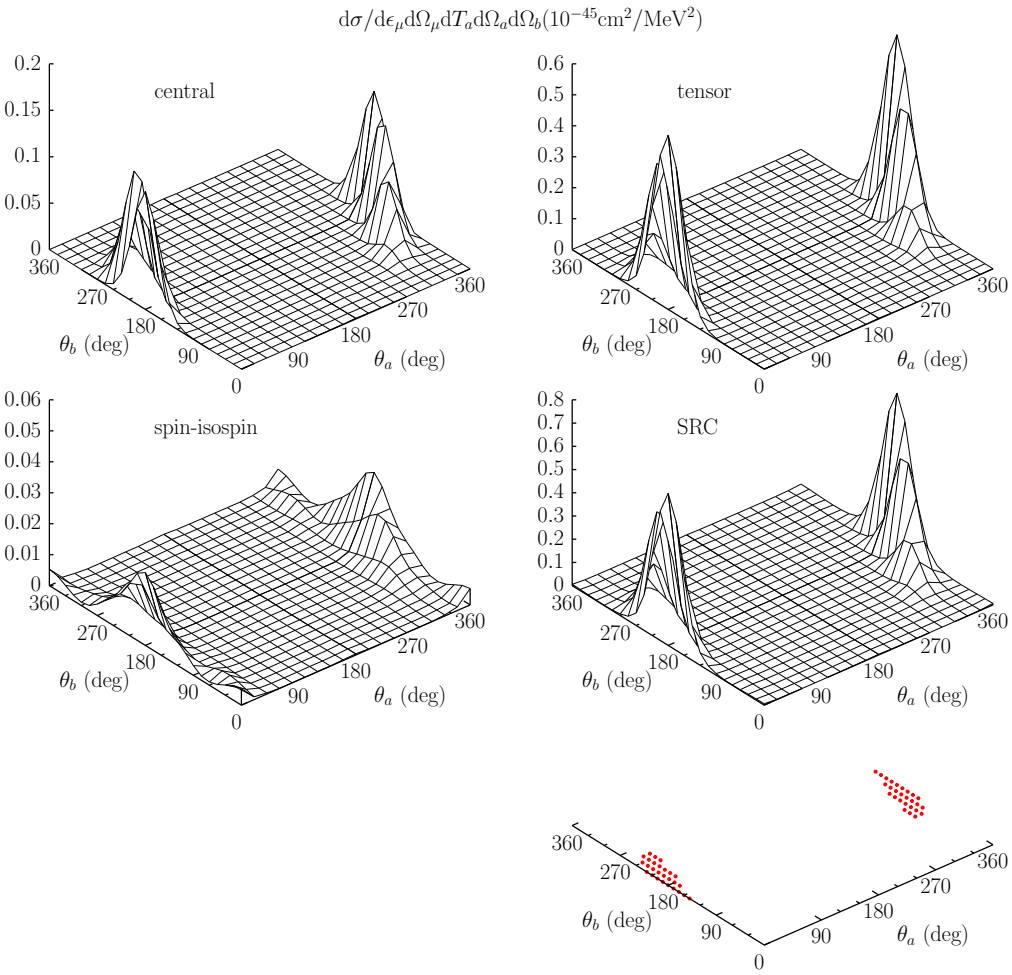

Figure 5.11: The ^{12}C$(\nu_\mu, \mu^- N_a N_b)$ cross section (N_a = p, N_b = p′, n) at ϵ_{ν_μ} = 750 MeV, ϵ_μ = 250 MeV, $\theta_\mu = 15^\circ$ and $T_{\rm p}$ = 50 MeV for in-plane kinematics (q = 534 MeV/c, $x_B = 0.04$). The three separate contributions to the SRCs are shown, and the bottom plot shows the (θ_a, θ_b) regions with initial c.o.m. momentum $P_{12} < 300$ MeV/c.

5.3 Exclusive knockout of SRC pairs

The exclusive $2N$ knockout cross section for fixed lepton kinematics depends on five independent variables $(T_a, \Omega_a, \Omega_b)$. When we consider in-plane kinematics, with both nucleons emitted in the lepton scattering plane, three independent variables remain $(T_a, \theta_a, \theta_b)$.

In Figs. 5.11-5.13 the results of an exclusive ^{12}C$(\nu_\mu, \mu^- N_a N_b)$ cross section calculation are shown (N_a = p, N_b = p′, n) for three different kinematics. The results were obtained by incoherently adding the pp and pn pair knockout contributions. The separate contributions of the three different components of the SRCs are shown as well. We have chosen kinematic situations which are of interest for the experimental community as the incoming neutrino energy corresponds to the peak of the MiniBooNE and T2K fluxes.

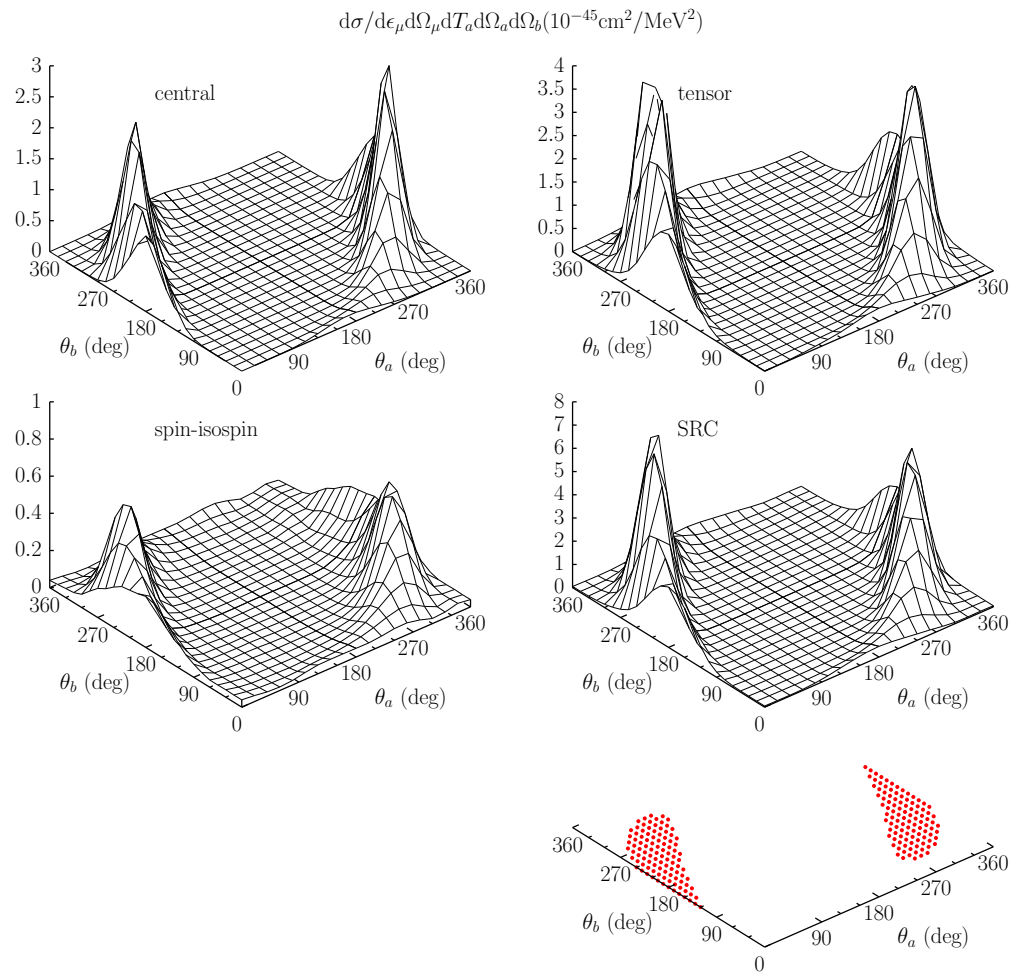

Figure 5.12: Same as Fig. 5.11, but for $\epsilon_\mu = 550$ MeV and $\theta_\mu = 15^\circ$ ($q = 268$ MeV/c, $x_B = 0.08$).

An interesting property of these exclusive cross sections, which was already mentioned in Chapter 4, is that the $2N$ knockout strength resides in a restricted part of phase space (θ_a, θ_b). Figs. 5.11-5.13 show that this feature remains when one looks at the three correlation types, central (c), tensor ($t\tau$) and spin-isospin ($\sigma\tau$), separately.

The bottom plots in Figs. 5.11-5.13 show the regions (θ_a, θ_b) for which $P_{12} < 300$ MeV/c. These regions correspond very well with the part of phase space where the $2N$ knockout strength is biggest. This behavior can be understood in a factorized model [21,27,44,45], where it is shown that the $2N$ knockout cross section of SRC pairs is proportional to the c.o.m. distribution $P^{[2]}(P_{12})$ of pairs in a relative $nl = 00$ state. Since the c.o.m. distribution $P^{[2]}(P_{12})$ of the close-proximity pairs is rapidly decreasing with increasing P_{12} (dotted line in Fig. 4.6), $2N$ knockout of SRC pairs will occur preferentially in situations where the missing momentum ($\boldsymbol{p}_m = \boldsymbol{p}_{A-2} = -\boldsymbol{P}_{12}$) is small.

Another interesting feature of the cross sections is the back-to-back nucleon emission in Figs. 5.11 and 5.12, reminiscent of the 'hammer events' seen by the ArgoNeuT collaboration

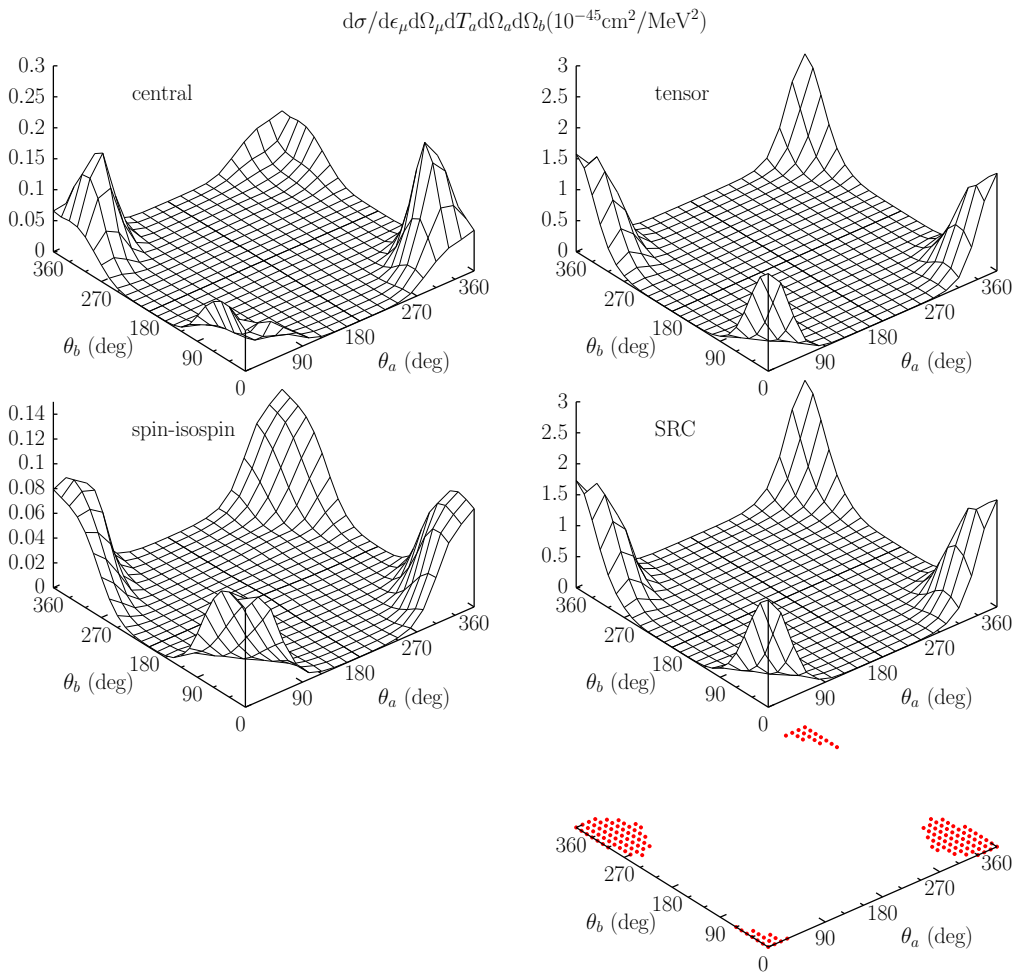

Figure 5.13: Same as Fig. 5.11, but for $\epsilon_\mu = 550$ MeV and $\theta_\mu = 60°$ ($q = 670$ MeV/c, $x_B = 1.09$).

[46]. This back-to-back emission is also visible in each of the three separate contributions. Back-to-back emission in the lab frame will be most apparent when both nucleons are emitted with roughly equal kinetic energy

$$T_a = T_b = \frac{1}{2}\left(\omega - S_{2N} - E^{exc}\right), \tag{5.19}$$

with S_{2N} the threshold energy for $2N$ emission, and when the momentum transfer to the pair is kept small.

In Fig. 5.12 these conditions are fulfilled and a clear back-to-back emission signal is visible. In Fig. 5.11, the kinetic energies of the emitted nucleons are not nearly equal, but a back-to-back emission is observed because the nucleons are emitted along the direction of q. This situation occurs when one nucleon in the pair receives the majority of the momentum transfer, and consequently is emitted along $\boldsymbol{q}$. In Fig. 5.13, the momentum transfer to the pair is too high to see a back-to-back knockout signal in the lab frame. Both nucleons are emitted in a forward direction with roughly equal kinetic energy.

In each of the three kinematic situations, the biggest contribution to the $2N$ knockout strength comes from the tensor component, the spin-isospin contribution is the smallest in all cases.

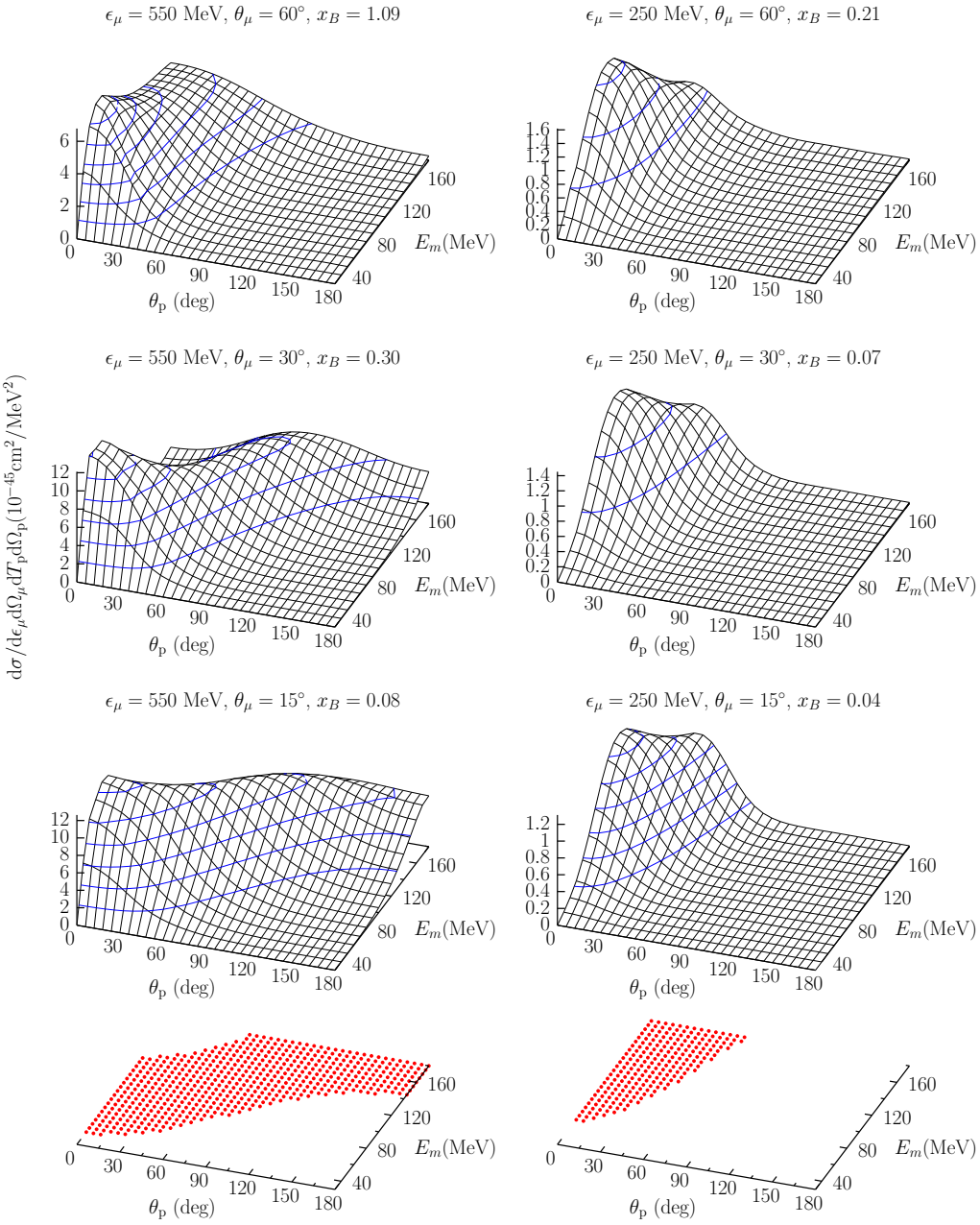

Figure 5.14: Semi-exclusive $^{12}\mathrm{C}(\nu_\mu, \mu^- \mathrm{p})$ cross section for $\epsilon_{\nu_\mu} = 750$ MeV, for six different muon kinematics and in-plane nucleon kinematics ($\varphi_\mathrm{p} = 0°$). The bottom panels shows the (θ_p, E_m) area with $P_{12} < 300$ MeV/c for the two situations with $\theta_\mu = 15°$.

5.4 Semi-exclusive knockout of SRC pairs

Integrating the exclusive $A(l, l' N_a N_b)$ cross section over the phase space of one of the emitted nucleons (Ω_b), the semi-exclusive $A(l, l' N_a)$ cross section is obtained. The way this integration is performed was explained in detail in Section 4.2. The semi-exclusive cross section, for fixed lepton kinematics, depends on three independent variables (T_a, Ω_a). In Fig. 5.14 results are shown for six different lepton kinematics relevant for ongoing experiments, with x_B ranging from 0.04 to 1.09. The differential cross section was studied versus missing energy $E_m = \omega - T_\mathrm{p}$ and proton angle θ_p for in-plane kinematics, i.e. $\varphi_\mathrm{p} = 0°$. All of the semi-exclusive $^{12}\mathrm{C}(\nu_\mu, \mu^- \mathrm{p})$ results are obtained by incoherently adding the strength from pp and pn knockout.

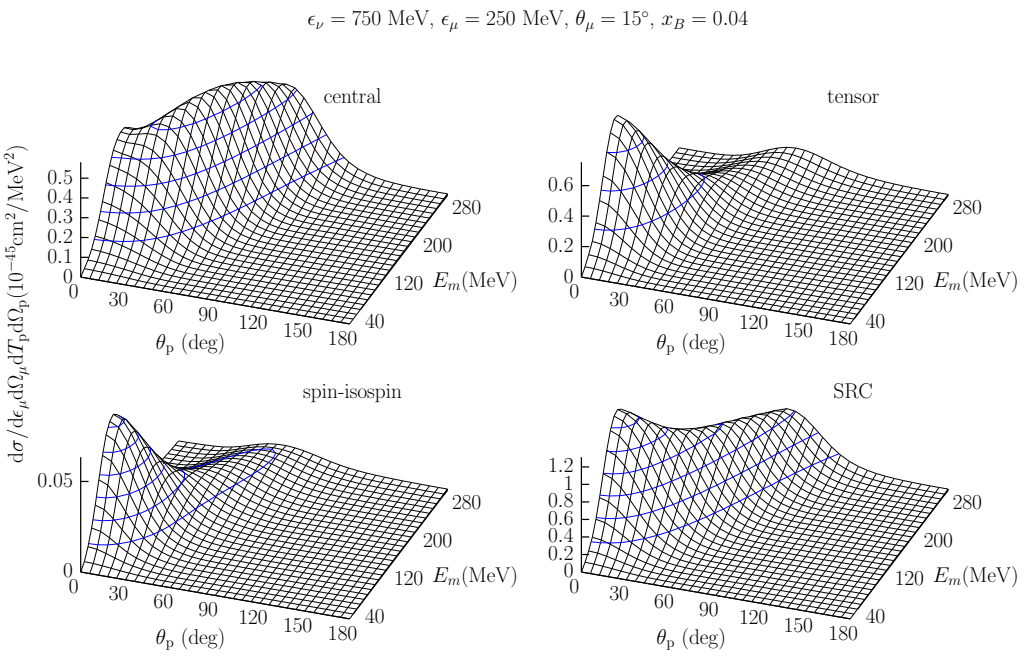

Figure 5.15: Semi-exclusive $^{12}\mathrm{C}(\nu_\mu, \mu^- \mathrm{p})$ cross section for $\epsilon_{\nu_\mu} = 750$ MeV, $\epsilon_\mu = 250$ MeV and $\theta_\mu = 15°$ for in-plane nucleon kinematics ($\varphi_\mathrm{p} = 0°$). The three contributions to the SRCs are shown separately.

We observe that the semi-exclusive strength resides in a restricted part of phase space (E_m, θ_p). A similar restriction in phase space appeared for exclusive $2N$ knockout calculations. Further, we observe that the peak of the differential cross section shifts towards higher E_m as one moves towards higher θ_p, where higher missing momenta are probed.

As for exclusive $2N$ knockout reactions, several properties of the semi-exclusive cross sections can be explained using kinematic considerations. For semi-exclusive calculations, $\boldsymbol{P}_{12}$ cannot longer be reconstructed, since the angular information of one of the particles is missing. However, a Monte Carlo (MC) simulation allows one to locate the region where $P_{12} < 300$ MeV/c is accessible. The two bottom panels of Fig. 5.14 show the result of such a calculation for $\theta_\mu = 15°$. This suggests that also semi-exclusive cross sections are dominated

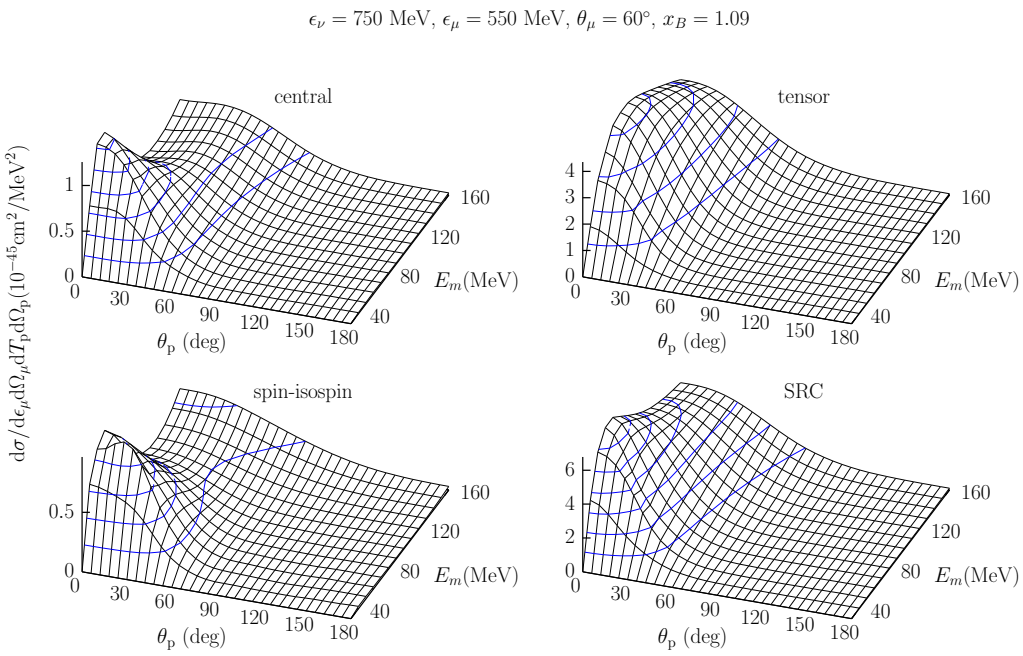

Figure 5.16: Same as Fig. 5.15 but for $\epsilon_{\nu_\mu} = 750$ MeV, $\epsilon_\mu = 550$ MeV and $\theta_\mu = 60°$.

by pairs with small initial c.o.m. momentum.

The three components of the SRCs are studied separately in Figs. 5.15 and 5.16 for two kinematic situations. The central and tensor correlations provide the largest contributions to the semi-exclusive strength, while the spin-isospin contributions are the smallest. The relative importance of the tensor correlations is biggest for large x_B values.

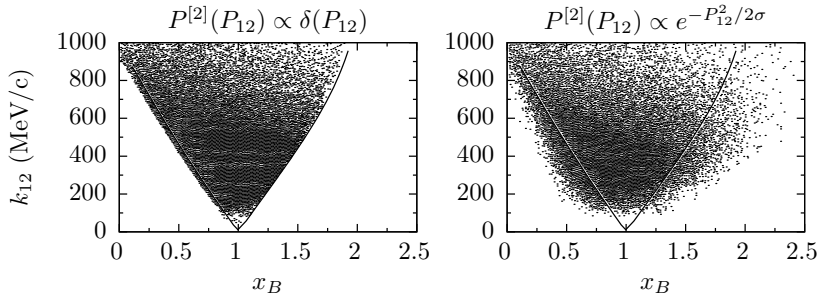

Figure 5.17: $x_B - k_{12}$ scatter plot for $^{12}\mathrm{C}(e, e'\mathrm{pn})$. Figure taken from [25].

The relative strengths of the components of the SRCs are related to the properties of the correlation functions in momentum space. Fig. 5.17 shows an $x_B - k_{12}$ scatter plot for the exclusive reaction $^{12}\mathrm{C}(e, e'\mathrm{pn})$, it was taken from [25]. The left panel was calculated with pair c.o.m. momentum distribution $P^{[2]}(P_{12}) \propto \delta(P_{12})$. This is equivalent with the quasi-deuteron approximation used to calculate the semi-exclusive cross sections analytically, Eq. (4.26).

The scatter plot shows that for $x_B = 0.04$, very high relative momenta are probed, $k_{12} \gtrsim 800$ MeV/c. For these large relative momenta, the central correlation function dominates, this explains why the strength of the central correlations is largest in Fig. 5.15. At $x_B \approx 1$, small and large relative momenta are probed, which is why the tensor correlation dominates in Fig. 5.16. The relative importance of central versus tensor correlations, for situations with intermediate x_B values, can be inferred in a similar way.

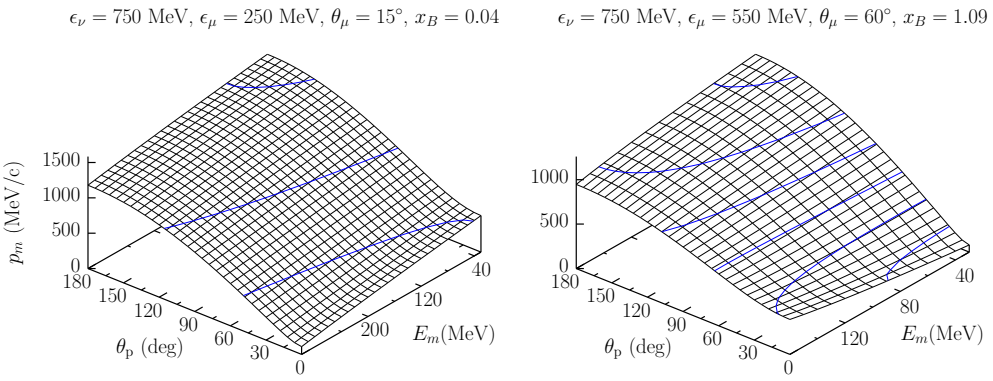

Figure 5.18: Missing momentum p_m for the kinematic situations of Figs. 5.15 and 5.16.

In general, the tensor contribution resides at small θ_p. The contribution from the central correlations spans a wider region of the proton scattering angle and missing energy. This is clearly visible in Fig. 5.15 and has been shown for semi-exclusive $A(e, e'p)$ in [22].

This can be explained with the missing momentum p_m, which is displayed as a function of E_m and θ_p in Fig. 5.18. It shows that small proton scattering angles correspond to small missing momenta and the missing momentum increases with increasing θ_p. Furthermore, in the quasi-deuteron situation, p_m is the momentum of the undetected particle, which means that it is directly related to the relative momentum of the pair k_{12}. From the properties of the correlation functions, one therefore expects that the tensor correlations will be localized in regions with intermediate p_m while central correlations span the region with higher p_m. This suggests that in general, central correlations will span a broader region in θ_p.

5.5 Influence of SRCs on inclusive cross sections

The $2N$ knockout contribution to the inclusive $A(l, l')$ cross section follows after integrating the semi-exclusive $A(l, l'N_a)$ cross section, with the $(A-1)^*$ system excited above the $2N$ knockout threshold, over the phase space $\mathrm{d}T_a \mathrm{d}\Omega_a$ of the undetected nucleon. The integration over Ω_a is performed analytically. As can be inferred from the semi-exclusive cross sections displayed above, the cross sections are smoothly varying as a function of T_a, and a straightforward numerical integration is used for the integration over T_a.

Before we study the SRC induced $2p2h$ responses for neutrino interactions, we study the influence of the four different central correlation functions in Fig. 5.19. The same four central correlations as before are used, see Fig. 5.8. The Coulomb and transverse response

functions for electron scattering interactions are shown for three values of q. Note that in the figure, the result of the OMY correlation has been divided by a factor 10. The $2p2h$ knockout strength of the three realistic central correlation functions, Gearhart, VMC and Euler, shows a very similar behavior as a function of ω. For the three values of q, the strength of the Gearhart correlation function is roughly a factor 3 larger compared to the other two. The OMY correlation function produces an unrealistically large strength to the inclusive responses, surpassing the $1p1h$ responses in strength, compare with e.g. Fig. 5.7 for the $1p1h$ strength.

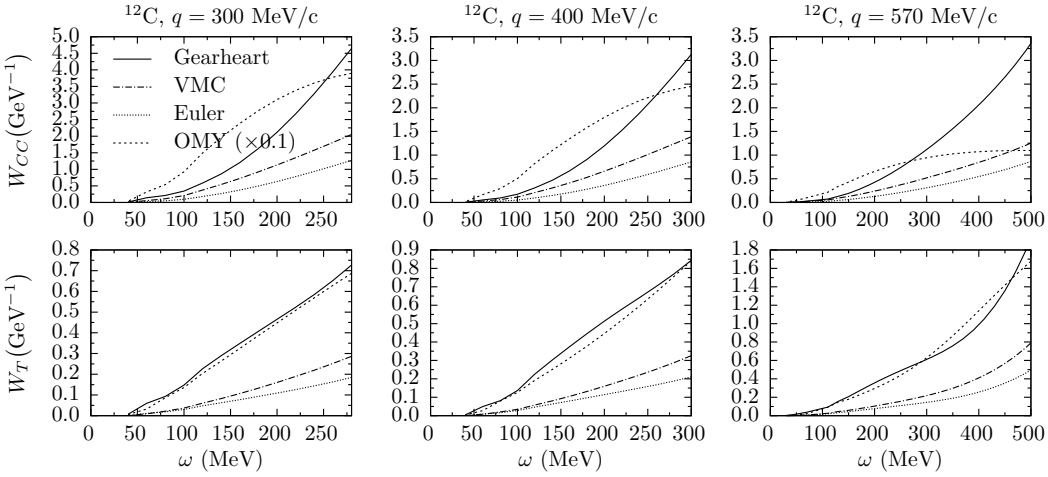

Figure 5.19: The effect of the different central correlation functions on the $2p2h$ responses for ^{12}C(e, e') interactions.

With this in mind, we present a systematic study of the SRC induced $2p2h$ responses for neutrino scattering interactions below. All results presented here, were obtained with the GD central correlation. Using one of the other two correlation functions would reduce the strength stemming from central correlations.

The SRC induced $2p2h$ responses for CC neutrino interactions at fixed momentum transfer are shown in Figs. 5.20, 5.22 and 5.23. All five responses necessary for the description of the $A(\nu_\mu, \mu^-)$ cross sections are presented. The Coulomb and transverse response functions illustrate the results for the time and space components of the nuclear current, and can be compared with the results for electron scattering. For the displayed kinematic situation with $q = 400$ MeV/c, the transverse response appears as the largest, but how these channels will contribute to the strength of the cross section depends on the kinematic functions v_i as well. For small scattering angles, the factor v_T will reduce the importance of the T channel.

In general, the ω dependence of the $2p2h$ responses does not show a distinct peak as the $1p1h$ responses do, see Fig. 3.9, but continue to grow or saturate with increasing ω. For the $1p1h$ responses, the peak is centered around $x_B = 1$ or $\omega = \frac{Q^2}{2m_N}$, and the width of the peak is generated by the spreading of the initial momentum of the interacting nucleon in the direction of the interacting neutrino, which lies within the interval $(-p_F, +p_F)$ with p_F the Fermi momentum. For $2p2h$ responses, the pairs initial momentum P_{12} is the scaling variable. Momentum conservation poses no limits on the initial momenta of the separate

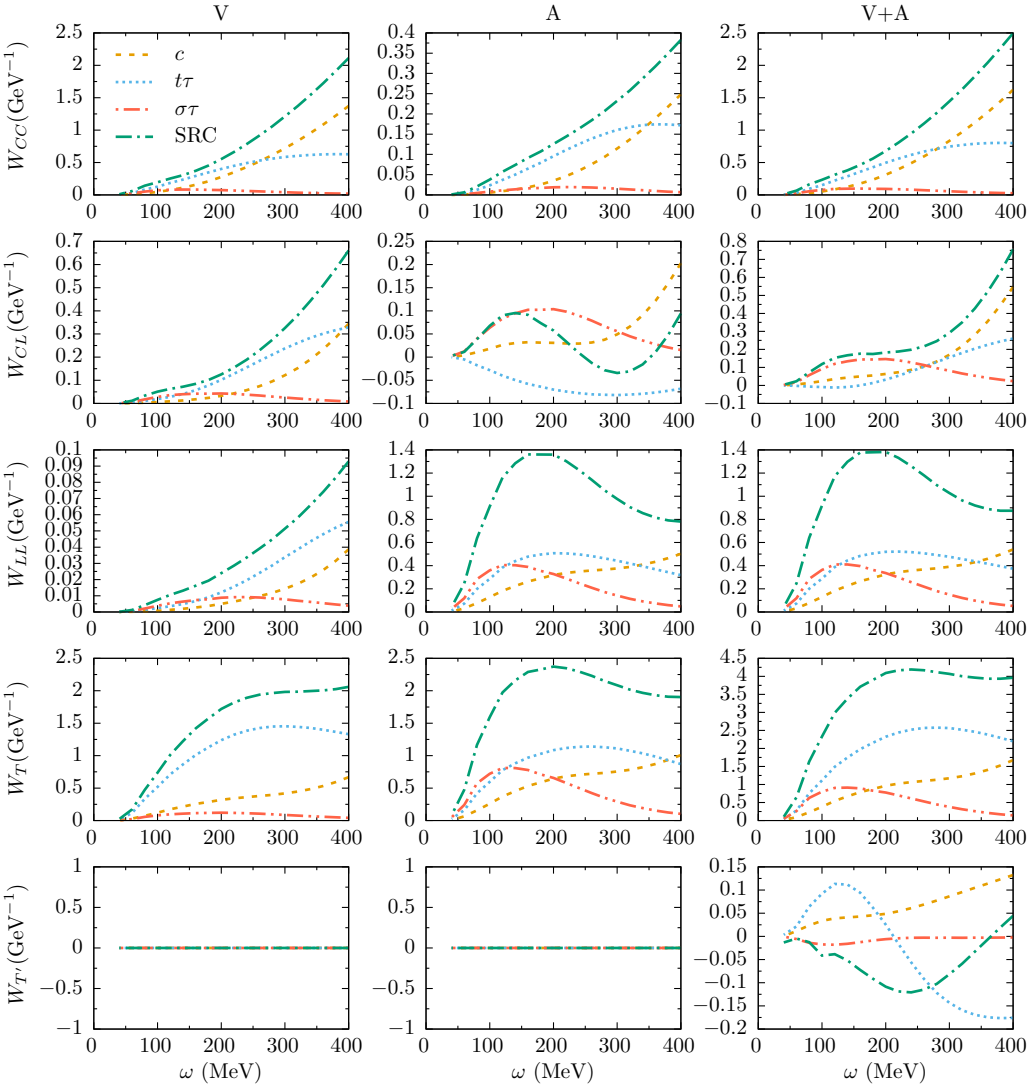

Figure 5.20: The $2p2h$ SRC response functions W_{CC} and W_T for $^{12}\mathrm{C}(\nu_\mu, \mu^-)$ at $q = 400$ MeV/c. The contributions of the three different SRC types (SRC $= c + t\tau + \sigma\tau$) are shown for the vector (V) and axial (A) parts of the nuclear current.

particles, only on the momentum of the pair. Therefore, the $2p2h$ responses of SRC pairs appear as a broad background ranging from the $2N$ knockout threshold to the maximum energy transfer, where $\omega = q$. Furthermore, the responses rise steadily with increasing ω, which is the result of the growing phase-space. This type of behavior is independent of the type of two-body current that is considered, as a similar steadily increasing behavior of the $2p2h$ responses for electron scattering is seen in Refs. [47–51], where MECs and correlations were studied.

The separate contributions of the central (c), tensor ($t\tau$) and spin-isospin ($\sigma\tau$) correlations

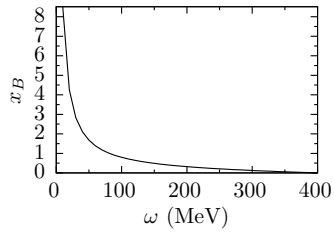

Figure 5.21: x_B for $q = 400$ MeV/c.

are shown in Fig. 5.20, for the vector and axial parts of the nuclear current. Overall, the tensor part yields the biggest contribution for small ω transfers, while the importance of the central part increases with ω. This is related to the central and tensor correlation functions in momentum space, see Fig. 5.1.

To explain this behavior, we refer to Figs. 5.17 and 5.21. Fig. 5.21 shows the Bjorken scaling variable, x_B, for $q = 400$ MeV/c. It is interesting to note that the majority of the inclusive $2N$ knockout strength occurs in situations with $x_B < 1$. Fig. 5.17 is the $x_B - k_{12}$ scatter plot for the exclusive reaction ^{12}C$(e, e'$pn$)$ taken from [25]. The left panel was calculated with pair c.o.m. momentum distribution $P^{[2]}(P_{12}) \propto \delta(P_{12})$, equivalent to the quasi-deuteron approximation. This plot shows that for $x_B \lesssim 0.5$, high relative momenta are probed, $k_{12} \gtrsim 400$ MeV/c, where the central correlation function dominates. Consequently, in the region $\omega > 200$ MeV, central correlations will grow in importance.

The right plot of Fig. 5.17 uses a more realistic pair c.o.m. momentum distribution: a Gaussian distribution, to be compared with Fig. 4.6. It can be used to get a feeling how the results would differ if we didn't rely on the quasi-deuteron approximation. The scatter plot shows that the inclusion of a realistic c.o.m. motion shifts the distribution of the events in the (x_B, k_{12}) plane to lower k_{12}, where the tensor correlation function is more important. Thus, the relative importance of the central correlations will decrease compared to the tensor correlations when including c.o.m. motion of the initial pairs.

Returning to Fig. 5.20, an interesting fact is that the spin-isospin contribution appears negligible in the vector part for all responses, while in the axial part it is of same order of magnitude as the central and tensor correlations for the CL, LL and T responses. This can be understood by looking at the operators of the spin-isospin correlation and the axial-transverse current. Both have a $\boldsymbol{\sigma} \cdot \boldsymbol{\tau}$ operator structure which strengthens the contribution. This dominance of the axial part over the vector part increases the importance of the spin-isospin correlations for neutrino compared to electron scattering. The axial LL and T responses behave very similarly, probably because they are calculated using the same multipole operator $\widehat{O}_{JM}$, Eq. (2.78). Why the vector part does not behave similarly must be related to more subtle interference effects that are at play.

The separation of Fig. 5.20 is inverted in Fig. 5.22 and the vector and axial contributions to the three SRC types are shown. The most remarkable fact is the dominance of the axial part in the longitudinal channel, and the importance of the axial part for spin-isospin correlations as stressed before.

The strength attributed to the different initial pairs is shown in Fig. 5.23. The contributions

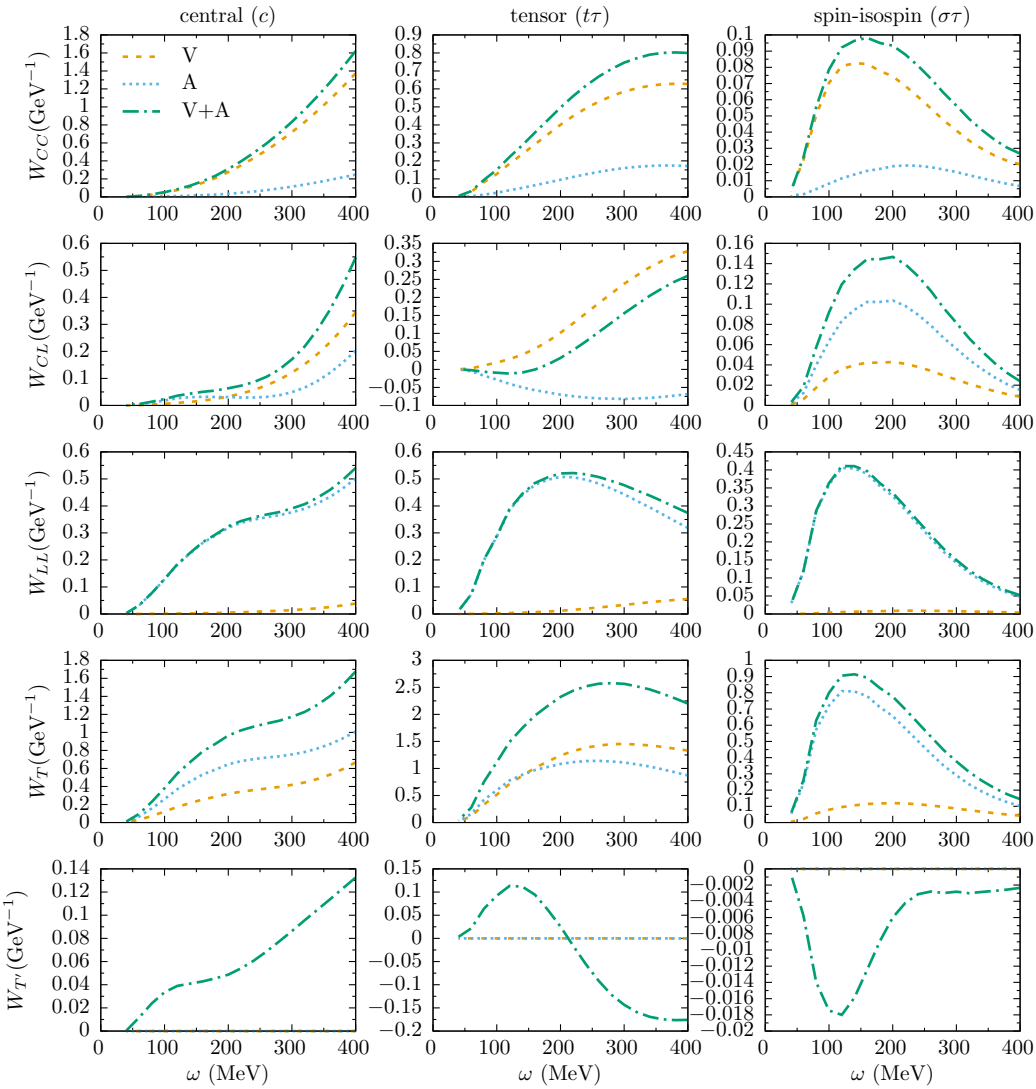

Figure 5.22: Same as Fig. 5.20, but the contributions of the vector (V) and axial (A) part are shown for the three different SRC types.

are shown for the central, tensor and spin-isospin parts of the SRCs. In the Coulomb response with central correlations, the contribution of initial nn pairs is roughly four times the contribution of the initial pn pairs. As the central correlation operator does not contain an isospin operator, it treats both protons and neutrons on an equal level. The factor four can be explained by noting that the W^+ boson only interacts with the neutrons in the initial pair, and as a consequence the nn matrix elements contain twice as many terms as the matrix elements for pn pairs. The tensor part is clearly dominated by pn pairs, as can be expected from its isospin structure. Again, the similarities between the LL and T responses are noteworthy.

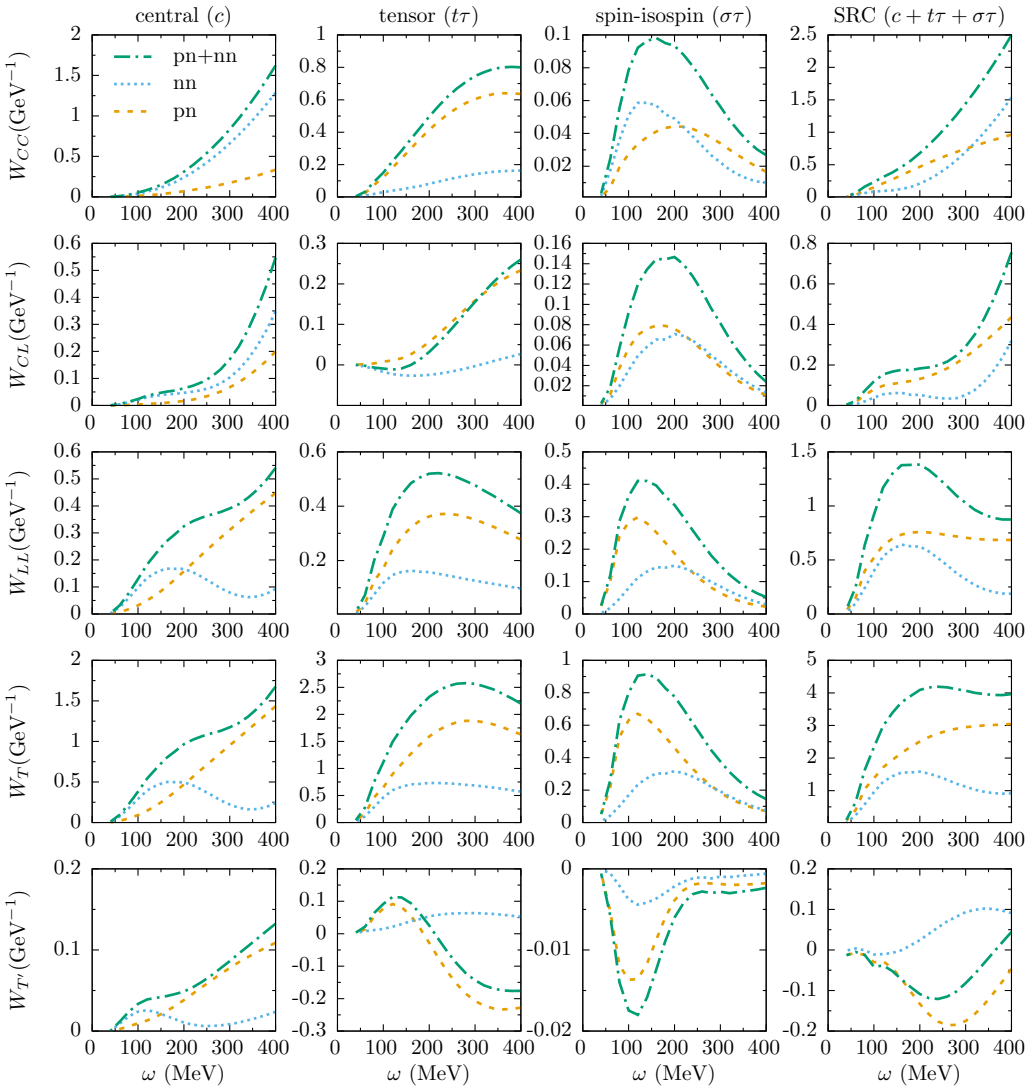

Figure 5.23: Same as Fig. 5.20, but the contributions of the initial pn and nn pairs are shown for the three different SRC types.

We show the inclusive $1p1h$ and $2p2h$ responses for electron and neutrino interactions at fixed momentum transfer in Fig. 5.24. Only the CC and T responses for neutrino scattering are shown, as only those two can be compared to the electron scattering responses. The relative size of the $2N$ knockout responses compared to the $1N$ knockout responses is very similar for electron and neutrino scattering.

In Fig. 5.25 we present the results for inclusive $^{12}\mathrm{C}(\nu_\mu, \mu^-)$ cross sections with $1N$ and $2N$ knockout as a function of ω for three different scattering angles. We have chosen an incoming neutrino energy of 750 MeV, which corresponds roughly with the peak of the MiniBooNE and T2K fluxes. The influence of SRCs on the $1p1h$ double differential cross

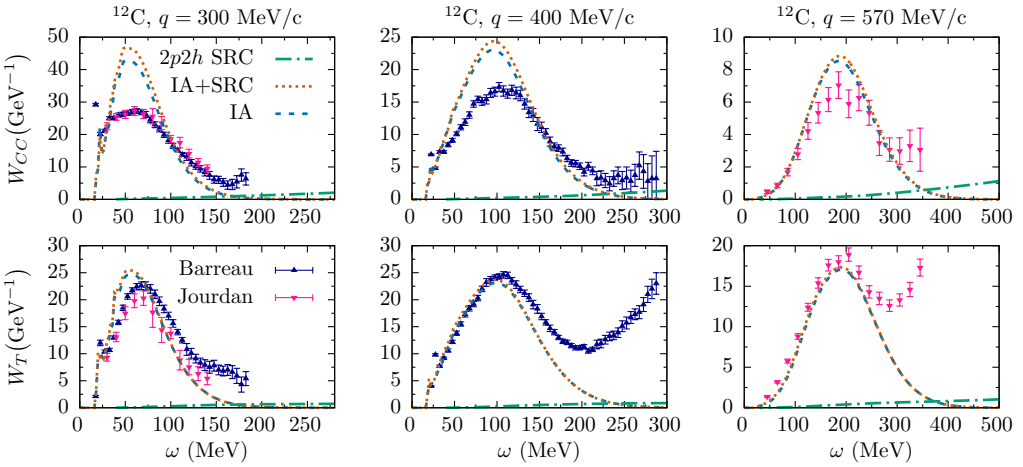

(a) ^{12}C(e, e')

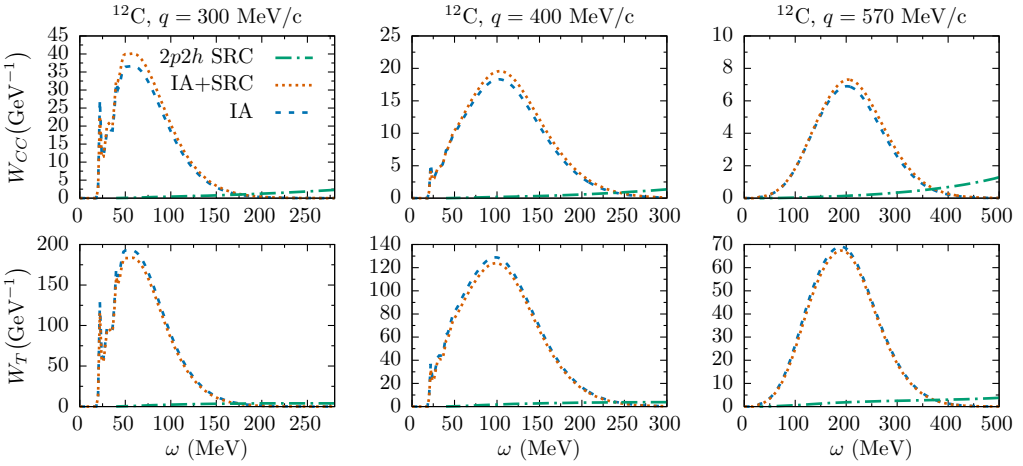

(b) ^{12}C(ν_μ, μ^-)

Figure 5.24: The computed ω dependence of the ^{12}C(l, l') responses W_{CC} and W_T for three different momentum transfers.

section results in a small reduction, instead of the increase seen for electron scattering. The reason for this opposite behavior is related to the isospin part of the matrix elements and the different strength of the electric and magnetic form factors for electrons and neutrinos. Even when considering only the vector part of the neutrino cross section, and treating the nucleons in the isospin formalism, the SRC correction for neutrinos has an opposite effect compared to electrons. The SRC correction is due to an interference between one-body and two-body matrix elements, in which the sign of the isospin matrix element can result in either an increase or a decrease.

For the 2p2h part of the cross section, the contributions of the central, tensor and spin-

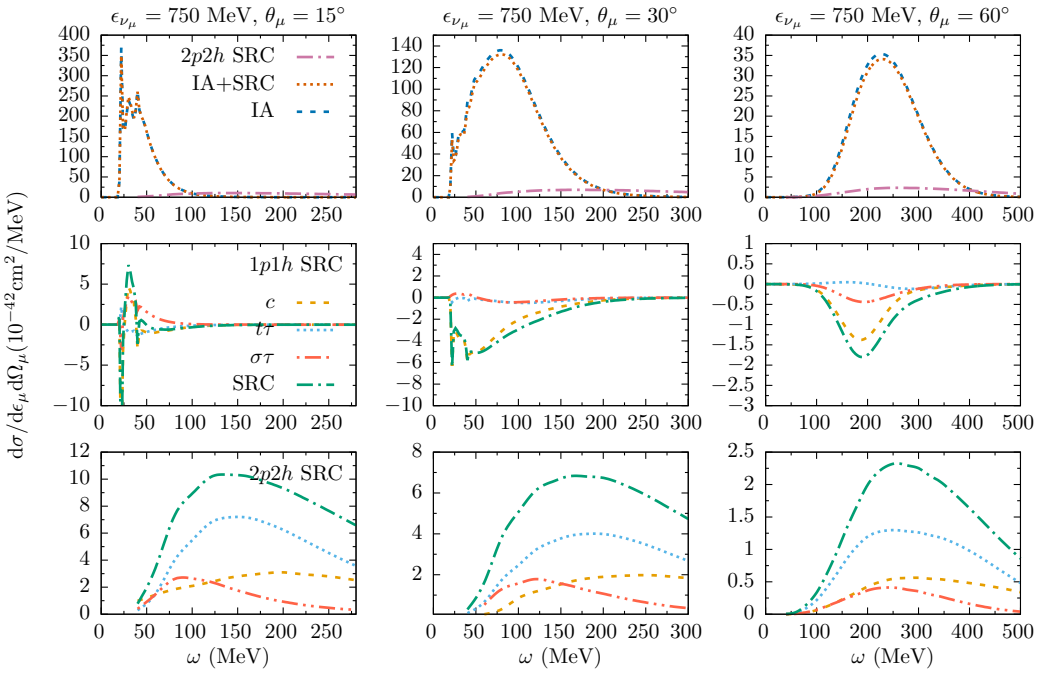

Figure 5.25: The computed ω dependence of the $^{12}C(\nu_\mu, \mu^-)$ cross section for ϵ_{ν_μ} = 750 MeV and three different values for the lepton scattering angle θ_μ. The top panels show the combined $1p1h$ and $2p2h$ cross sections. The middle panels show the correction of the SRCs to the $1p1h$ cross section and the bottom panels show the $2p2h$ SRC part of the cross section.

isospin part of the correlations are shown separately. The tensor correlation yields the biggest contribution to the differential cross section at small energy transfers, but the relative importance of the central part grows for larger ω, similar as seen in the separate responses. The contribution of the spin-isospin correlations is comparable to the central contribution and consists largely of the axial-transverse channel, as discussed earlier.

Comparing the position of the peak in the $1p1h$ and $2p2h$ channels, it is clear that the peak of the two-body channel occurs at higher ω than the QE peak for small scattering angles. The difference decreases at higher scattering angles. For $\theta_\mu = 60°$, the reduction of the $1p1h$ channel and the contribution of the $2p2h$ channel have an opposite effect of similar size. The net effect of the short-range correlations on the inclusive signal is therefore rather small.

The inclusive $1N$ and $2N$ cross sections are separated according to the response channels in Fig. 5.26, for electron interactions as well as neutrino interactions. For electron scattering, two responses are sufficient. For neutrino interactions, the combination $CC + CL + LL$, sometimes called the longitudinal response, and $T - T'$, the transverse response, are shown separately. For (e, e'), the $1p1h$ cross section in the IA is dominated by the CC channel for small scattering angles while the importance of the T channel increases for larger $\theta_{e'}$. A similar behavior for the $2p2h$ responses is visible.

For neutrino interactions, even for small scattering angles, the cross section is dominated by

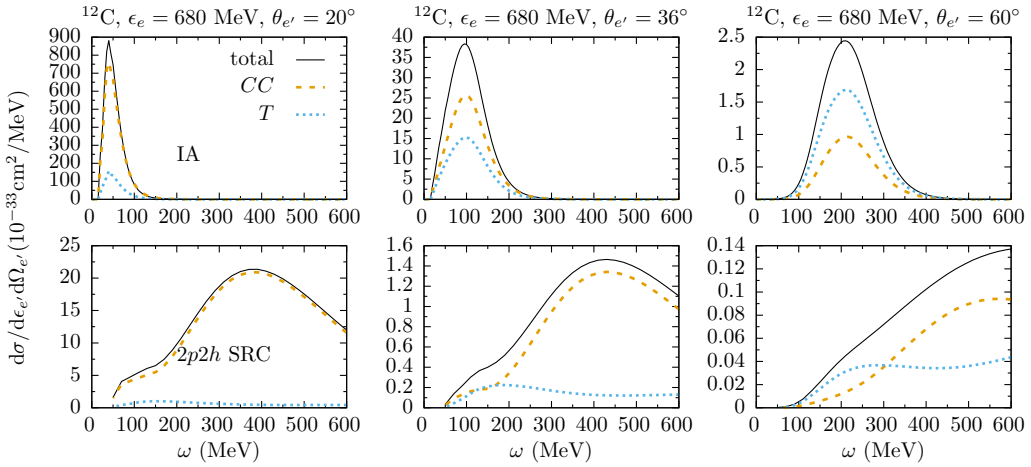

(a) $^{12}\mathrm{C}(e, e')$

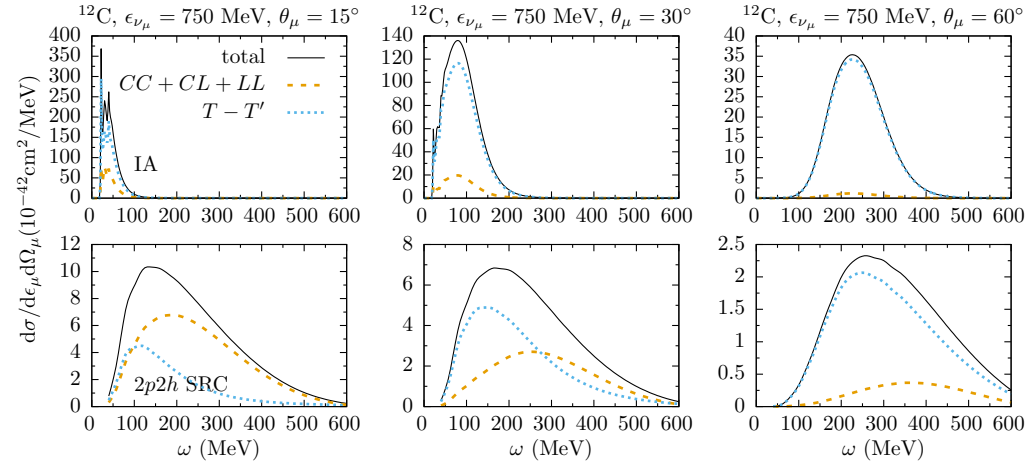

(b) $^{12}\mathrm{C}(\nu_\mu, \mu^-)$

Figure 5.26: The computed ω dependence of the $^{12}\mathrm{C}(l, l')$ cross section for $\epsilon_{\nu_\mu} = 750$ MeV and three different values for the lepton scattering angle θ_l. The top panels show the $1N$ knockout calculations in the IA. The bottom panels show the $2N$ knockout contribution of SRC pairs to the cross section.

the transverse channel, and the importance only increases for larger θ_μ. Compared to the $1p1h$ calculations, the contribution from the longitudinal channel to the $2p2h$ responses is much bigger, but this contribution also decreases in importance as one moves towards larger scattering angles. Overall, the contribution of the transverse channel is more important for neutrino scattering compared to electron interactions.

We conclude this chapter by comparing the $2N$ knockout contribution of SRC pairs from ^{16}O to ^{12}C in Fig. 5.27. The top panels show the inclusive double differential cross section for pp and pn emission. The bottom row shows the ratio of the cross sections. Also shown is

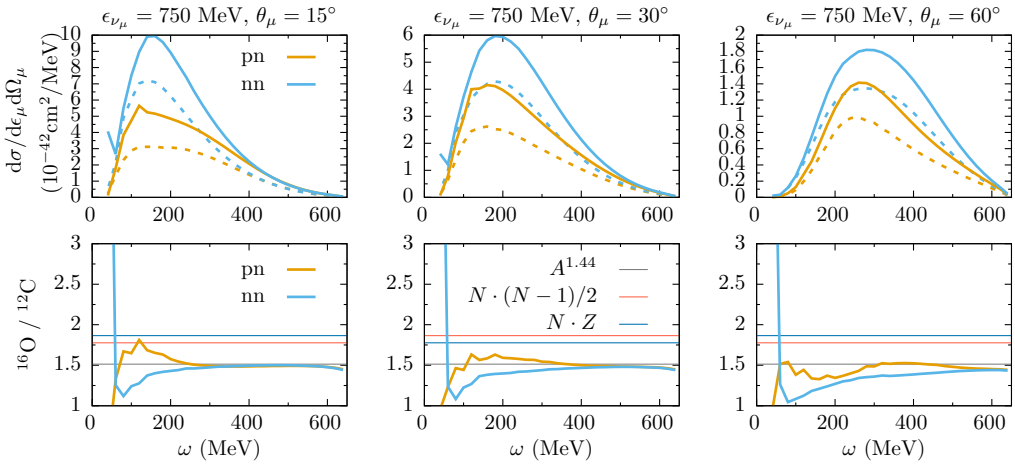

Figure 5.27: (top) The contribution of SRC pn- and nn-pair emission to the inclusive $A(\nu_\mu, \mu^-)$ cross section for ^{16}O (full line) and ^{12}C (dashed line). (bottom) The ratio of the cross sections ^{16}O/^{12}C.

the ratio of the number of nn and pn pairs in the target nucleus. The numbers of nn pairs in the target nucleus is $N(N-1)/2$ and the number of pn pairs scales like $N \cdot Z$. The number $A^{1.44}$ is a scaling relation obtained in [36], where the number of pairs in a relative $l = 0$ state were counted for several nuclei over the mass range. The results of the numeral calculations approach this scaling relation for high energy transfers. For small energy transfers, the ratio of the cross sections deviate from the scaling relation. This is partly related to the different binding energies of the nucleons in ^{16}O and ^{12}C. For $1N$ knockout processes, effects of the different energy levels are visible at small ω, see e.g. the top left panel of Fig. 5.25. For $2N$ knockout, these effects will remain visible for higher ω as the energy transfer is divided over two nucleons. We conclude that the scaling relation found in [36] is valid to a certain level of accuracy in our model and that it can be used to estimate the effect of the $2N$ knockout contribution to the inclusive cross section for an arbitrary nucleus, once the result for another nucleus is known.

5.6 Summary

In the calculation of nuclear responses, SRCs were introduced. This was done in a standard way, by applying a many-body correlation operator to the IPM wave functions. We follow the approach outlined in Refs. [21,22,25,26,28]. When calculating transition matrix elements, the effect of the correlations is shifted from the wave functions to the operator, i.e. the operator is replaced by an effective operator, accounting for SRCs. The central, tensor and isospin components of the SRCs were accounted for, using the central correlation function by Gearhart and Dickhoff and the tensor and spin-isospin correlation functions of S. Pieper *et al.*

The influence of SRCs on inclusive $1N$ knockout reactions and exclusive, semi-exclusive and

inclusive $2N$ knockout interactions was examined. Inclusive cross sections were compared for $^{12}\mathrm{C}(e,e')$ and $^{12}\mathrm{C}(\nu_\mu,\mu^-)$ interactions and the electron scattering results were compared with data.

The interference between the SRC currents and the nuclear one-body currents in the IA, yields small effects on the $1p1h$ responses. Some responses were increased by the SRCs and other responses were decreased. Differences between these interference effects, for neutrino and electron scattering, are related to isospin factors. The overall effect of the SRCs on the $1N$ knockout double differential cross section for neutrino scattering is a small decrease, which depends on the kinematics.

The $2N$ knockout contribution of SRC pairs to the inclusive double differential neutrino cross sections, shown in Fig. 5.25, yields strength ranging from the $2N$ knockout threshold into the dip region and appears as a broad background. This partly accounts for the underprediction of the data in the dip region, calculated using the IA. Furthermore, the $2N$ knockout strength seems to be following the scaling relation of SRC pairs in nuclei, proposed in [36].

Many characteristics of the $2N$ knockout cross sections could be related to the properties of the correlation functions in momentum space and kinematic considerations. The exclusive $2N$ knockout cross section, displays an interesting back-to-back behavior. This is related with the c.o.m. momentum distribution $P^{[2]}(P_{12})$ of the SRC pairs in the target nucleus. The relative strengths of the central, tensor and spin-isospin components to the cross sections, can be attributed to relative momenta k_{12} of the pairs. When mainly nucleon pairs with intermediate relative momenta are probed, the tensor strength dominates, because the tensor correlation function in momentum space is largest at intermediate momenta. When pairs with a high relative momentum are probed, e.g. at large energy transfers, the central correlations starts to prevail. Yet at these high relative momenta, the nucleon momenta are approaching the nucleon mass, and unknown relativistic effects are likely to play a role. Thus the results are subject to considerable uncertainties.

To conclude, we stress that a comparison of the results using different central correlation functions produced relatively large differences, suggesting that the choice of the central correlation function included in the framework should be studied further.

References

[1] L. Lapikas, Nucl. Phys. **A553**, 297c (1993).
[2] R. B. Hallock, Phys. Rev. A **5**, 320 (1972).
[3] E. C. Svensson, V. F. Sears, A. D. B. Woods, *et al.* Phys. Rev. B **21**, 3638 (1980).
[4] K. Gottfried, Nucl. Phys. **5**, 557 (1958).
[5] J. Arrington, D. Higinbotham, G. Rosner, *et al.* Prog. Part. Nucl. Phys. **67**, 898 (2012).
[6] G. Co' and A. Lallena, Phys. Rev. **C57**, 145 (1998).
[7] J. Amaro, A. Lallena, G. Co', *et al.* Phys. Rev. **C57**, 3473 (1998).
[8] G. Co' and A. Lallena, Annals Phys. **287**, 101 (2001).
[9] M. Anguiano, G. Co', A. Lallena, *et al.* Ann. Phys. **296**, 235 (2002).
[10] M. Anguiano, G. Co', and A. M. Lallena, J. Phys. **G29**, 1119 (2003).

[11] C. Giusti, F. Pacati, K. Allaart, *et al.* Phys. Rev. **C57**, 1691 (1998).
[12] C. Giusti, H. Muther, F. Pacati, *et al.* Phys. Rev. **C60**, 054608 (1999).
[13] O. Benhar, A. Lovato, and N. Rocco, Phys. Rev. **C92**, 024602 (2015).
[14] N. Rocco, A. Lovato, and O. Benhar, Phys. Rev. Lett. **116**, 192501 (2016).
[15] M. Martini, M. Ericson, G. Chanfray, *et al.* Phys. Rev. **C80**, 065501 (2009).
[16] M. Martini, private communication, 2017.
[17] J. Nieves, I. Ruiz Simo, and M. Vicente Vacas, Phys. Rev. **C83**, 045501 (2011).
[18] J. Amaro, M. Barbaro, J. Caballero, *et al.* Phys. Rev. **C71**, 015501 (2005).
[19] A. Lovato, S. Gandolfi, R. Butler, *et al.* Phys. Rev. Lett. **111**, 092501 (2013).
[20] A. Lovato, S. Gandolfi, J. Carlson, *et al.* Phys. Rev. **C91**, 062501 (2015).
[21] J. Ryckebusch, V. Van der Sluys, K. Heyde, *et al.* Nucl. Phys. **A624**, 581 (1997).
[22] S. Janssen, J. Ryckebusch, W. Van Nespen, *et al.* Nucl. Phys. **A672**, 285 (2000).
[23] R. Starink *et al.* Phys. Lett. **B474**, 33 (2000).
[24] J. Ryckebusch and W. Van Nespen, Eur. Phys. J. **A20**, 435 (2004).
[25] M. Vanhalst, J. Ryckebusch, and W. Cosyn, Phys. Rev. **C86**, 044619 (2012).
[26] J. Ryckebusch, W. Cosyn, and M. Vanhalst, J. Phys. **G42**, 055104 (2015).
[27] C. Colle, O. Hen, W. Cosyn, *et al.* Phys. Rev. **C92**, 024604 (2015).
[28] T. Van Cuyck, N. Jachowicz, R. González–Jiménez, *et al.* Phys. Rev. **C94**, 024611 (2016).
[29] C. Gearhart, PhD thesis (Washington University, St. Louis, MO, 1994).
[30] K. Blomqvist, W. Boeglin, R. Bohm, *et al.* Phys. Lett. **B421**, 71 (1998).
[31] J. Ryckebusch, D. Debruyne, W. Van Nespen, *et al.* Phys. Rev. **C60**, 034604 (1999).
[32] C. Onderwater, K. Allaart, E. Aschenauer, *et al.* Phys. Rev. Lett. **81**, 2213 (1998).
[33] S. Pieper, R. Wiringa, and V. Pandharipande, Phys. Rev. **C46**, 1741 (1992).
[34] O. Hen, G. A. Miller, E. Piasetzky, *et al.* (2016).
[35] M. Vanhalst, *Quantifying short-range correlations in nuclei*, PhD thesis (Ghent University, 2014).
[36] M. Vanhalst, W. Cosyn, and J. Ryckebusch, Phys. Rev. **C84**, 031302 (2011).
[37] P. Barreau, M. Bernheim, J. Duclos, *et al.* Nucl. Phys. **A402**, 515 (1983).
[38] J. Jourdan, Nucl. Phys. **A603**, 117 (1996).
[39] R. Reid, Annals Phys. **50**, 411 (1968).
[40] R. Wiringa, R. Smith, and T. Ainsworth, Phys. Rev. **C29**, 1207 (1984).
[41] R. Schiavilla, V. Pandharipande, and R. Wiringa, Nucl. Phys. **A449**, 219 (1986).
[42] F. Arias de Saavedra, G. Co', A. Fabrocini, *et al.* Nucl. Phys. **A605**, 359 (1996).
[43] T. Ohmura, M. Morita, and M. Yamada, Prog. Theor. Phys. **15**, 222 (1956).
[44] J. Ryckebusch, Phys. Lett. **B383**, 1 (1996).
[45] C. Colle, W. Cosyn, J. Ryckebusch, *et al.* Phys. Rev. **C89**, 024603 (2014).
[46] ArgoNeuT collaboration, R. Acciarri *et al.* Phys. Rev. **D90**, 012008 (2014).
[47] J. Van Orden and T. Donnelly, Ann. Phys. **131**, 451 (1981).
[48] W. Alberico, M. Ericson, and A. Molinari, Ann. Phys. **154**, 356 (1984).

[49] A. Gil, J. Nieves, and E. Oset, Nucl. Phys. **A627**, 543 (1997).

[50] M. Dekker, P. Brussaard, and J. Tjon, Phys. Rev. **C49**, 2650 (1994).

[51] A. De Pace, M. Nardi, W. Alberico, *et al.* Nucl. Phys. **A726**, 303 (2003).

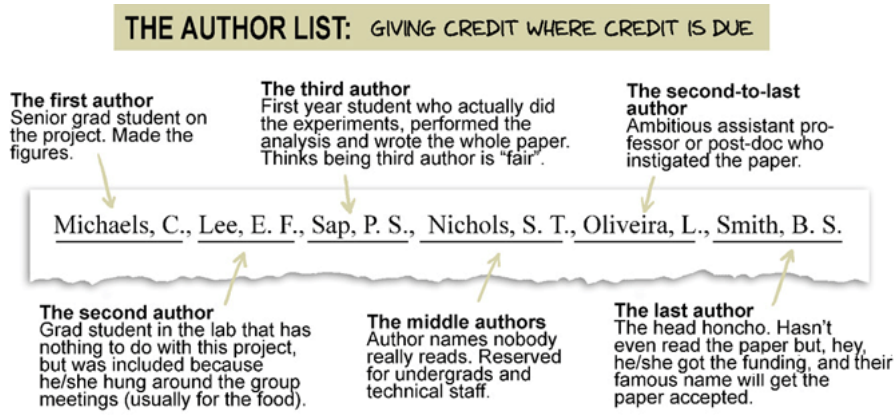

Chapter 6

Meson-exchange currents

The nucleons inside the nucleus are bound via the nuclear force. This force is understood as a residual effect of the strong force, which is the force that binding quarks together to form the nucleons. To a large extent, the nuclear force can be understood in terms of the exchange of virtual light mesons such as the π, ρ and ω meson.

When an electroweak boson interacts with a pair of nucleons which are correlated through the exchange of a meson, this will cause the knockout of one or both of the particles from the nucleus. The boson was interacting with a current consisting of two nucleons, a two-body current, called a MEC.

Several types of MECs can be constructed, depending on which meson is exchanged and to which particle or vertex the incoming boson couples. In Fig. 6.1 some of the possibilities are shown, where only the light π is considered as the exchanged meson. Diagrams (a) and (c) show the seagull current (or contact current) and (b) the pion-in-flight current (or pionic current), where the boson couples to the pion-nucleon vertex and the pion respectively.

In diagrams (d-g), the Δ-currents (or isobar currents) are displayed. In the Δ-currents, the nucleon that interacts with the boson is excited to a virtual Δ which subsequently deexcites by exchanging a meson with the second nucleon. The last four diagrams (h-k) show the correlation currents, where the nucleon propagates between the interaction vertex with the boson and the emission of the π.

The correlation currents, which are present in some lepton-nucleus scattering models based on a Fermi gas, do not have to be included in our model. In [1], it is argued that these currents are no genuine two-body currents, but a product of a one-body current and a potential. These currents are already present in a model where the one-body currents are

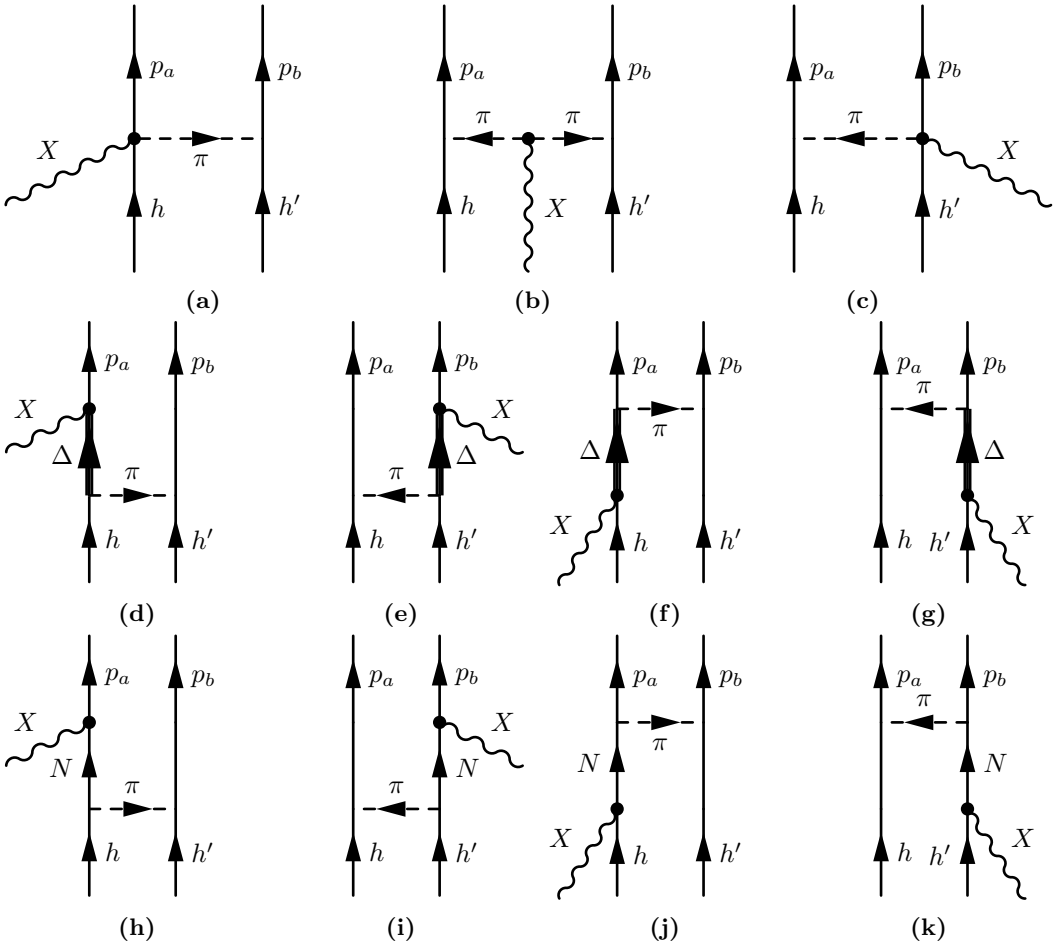

Figure 6.1: The seagull and pion-in-flight currents (top), Δ currents (middle) and correlation currents (bottom) represented as a current diagram.

evaluated with wave functions obtained using a MF potential. Thus, in order to avoid double counting with the IA, the correlation currents are not included.

Other MECs can be constructed by replacing the π (or one of the two pions in the pion-in-flight current) with a heavier meson. These heavy MECs have a much shorter range due to the heavier mass of the exchanged meson ($m_\pi \approx 135$ MeV, $m_\rho \approx 775$ MeV, $m_\omega \approx 782$ MeV) and the expectation values of the associated operators are strongly dampened by the short-range repulsion between the nucleons. Short-range effects are implemented in an effective fashion as explained in the previous chapter.

Throughout this work, only seagull and pion-in-flight currents are considered, and collectively called MECs for simplicity. The corresponding $1p1h$ and $2p2h$ diagrams are shown in Fig. 6.2. The Δ-currents, for which the basis on electron-scattering interactions is present, should be included in future calculations aiming at the comparison with νA scattering data.

Several theoretical approaches have analyzed the role of MECs in eA and νA scattering interactions. The earlier calculations, [2–8], date back some decades. The first attempt to

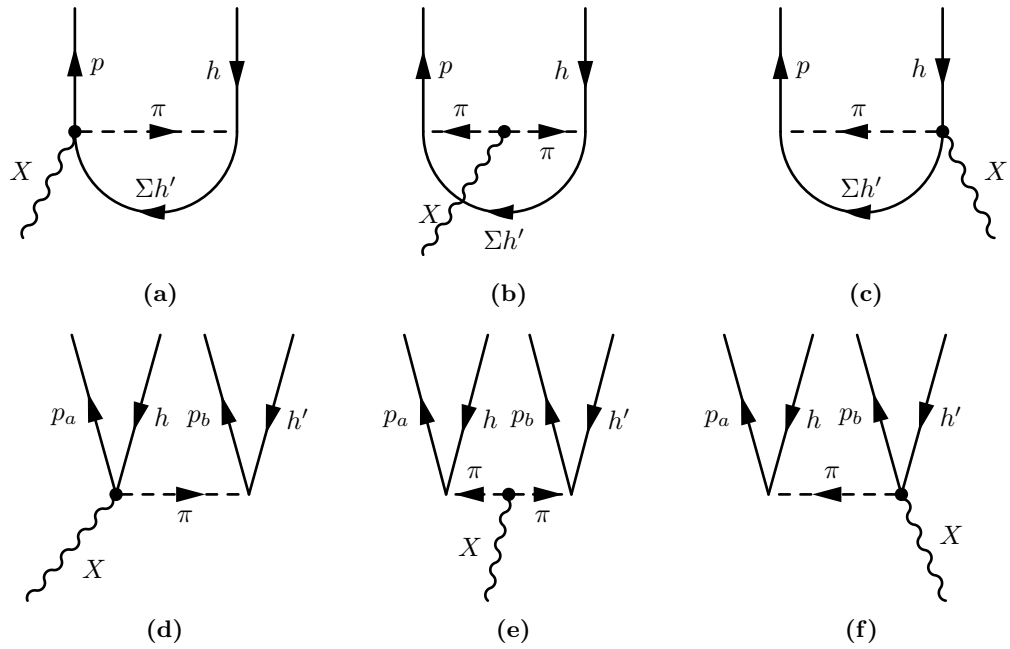

Figure 6.2: The $1p1h$ (top) and $2p2h$ (bottom) diagrams considered in the calculations in this work.

include MECs in a relativistic way in the transverse response for electron interactions were performed by Dekker *et al.* [9] and then by De Pace *et al.* [10].

Refs. [11–13], e.g, have considered SRCs and MECs for photoinduced and electroinduced exclusive $1N$ and $2N$ knockout cross sections, in a similar fashion as the model used here. Calculations on electron scattering by Benhar *et al.* [14,15] have generalized the formalism based on a factorization ansatz and nuclear spectral functions to treat transition matrix elements involving meson-exchange and Δ-currents.

For neutrino interactions, the effect of the MECs on the $1N$ knockout cross sections has been studied e.g. in [16] in nuclear matter calculations. The models by Martini *et al.* and Nieves *et al.* [17,18] take MECs, together with correlations and Δ-currents, into account in the $2p2h$ channel for a proper description of inclusive neutrino cross section data. Both approaches include the interference between MECs, Δ-currents and the correlation current in a similar way. Recently, calculations using a relativistic Fermi gas by Amaro *et al.* [19], accounting for MECs, correlations, and Δ-currents in electroinduced $2N$ emission, have been extended to (anti)neutrino interactions [20–25]. In ab-initio calculations on ^{12}C [26,27], MEC contributions are inherently taken into account.

The seagull, pion-in-flight and their axial counterparts used in this work are introduced and discussed in this chapter. Numerical results, and comparison with data and other theoretical predictions found in literature, are presented for $1N$ and $2N$ knockout calculations. In Appendix C, the CVC and PCAC relation are discussed, to help understand how the MECs can be constrained using these relations. Detailed information on the calculation of the MEC matrix elements is summarized in Appendix G. In this chapter, the SRCs and SRC-MEC interference terms discussed in Chapter 5 are not included.

6.1 Seagull and pion-in-flight currents

The vector MECs considered in this work are the seagull and pion-in-flight currents. In the seagull current, the boson couples with the MEC at the πNN vertex, while in the pion-in-flight current, the boson couples with the virtual pion. The conventional approach for the description of the seagull and pion-in-flight currents, is to consider all diagrams with a single pion exchange. In the derivation of the Feynman diagrams, the couplings are either obtained from a pion-nucleon scattering amplitude [2] or from an effective chiral Lagrangian [3]. In the low-energy limit, the vector seagull and pion-in-flight currents, for electron scattering interactions, are given by [1,28–30]

$$\widehat{\boldsymbol{J}}_V^{[2],\mathrm{sea}}(\boldsymbol{q}) = -i\left(\frac{f_{\pi NN}}{m_\pi}\right)^2 (\boldsymbol{I}_V)_3 \left(\frac{\boldsymbol{\sigma}_1\,(\boldsymbol{\sigma}_2\cdot\boldsymbol{q}_2)}{\boldsymbol{q}_2^2+m_\pi^2} - \frac{\boldsymbol{\sigma}_2\,(\boldsymbol{\sigma}_1\cdot\boldsymbol{q}_1)}{\boldsymbol{q}_1^2+m_\pi^2}\right), \tag{6.1}$$

$$\widehat{\boldsymbol{J}}_V^{[2],\mathrm{pif}}(\boldsymbol{q}) = i\left(\frac{f_{\pi NN}}{m_\pi}\right)^2 (\boldsymbol{I}_V)_3 \frac{(\boldsymbol{\sigma}_1\cdot\boldsymbol{q}_1)\,(\boldsymbol{\sigma}_2\cdot\boldsymbol{q}_2)}{(\boldsymbol{q}_1^2+m_\pi^2)\,(\boldsymbol{q}_2^2+m_\pi^2)}(\boldsymbol{q}_1-\boldsymbol{q}_2), \tag{6.2}$$

where $\boldsymbol{I}_V$ is the two-body isovector operator

$$\boldsymbol{I}_V = \left(\overrightarrow{\boldsymbol{\tau}}_1 \times \overrightarrow{\boldsymbol{\tau}}_2\right). \tag{6.3}$$

These currents are purely spacelike. The relativistic versions also contain a small timelike component. The currents for a CC neutrino interaction can be obtained via an isospin rotation, which follows from conservation of the vector current (CVC). This implies replacing the third component of the isovector operator with the $\pm$ components [1]

$$(\boldsymbol{I}_V)_3 \rightarrow (\boldsymbol{I}_V)_\pm = \frac{1}{2}\left((\boldsymbol{I}_V)_x \pm i(\boldsymbol{I}_V)_y\right). \tag{6.4}$$

The momenta $\boldsymbol{q}_1$ and $\boldsymbol{q}_2$ are defined as the momentum increase in the nuclear system

$$\boldsymbol{q}_1 = \boldsymbol{p}_a - \boldsymbol{h} \tag{6.5}$$

$$\boldsymbol{q}_2 = \boldsymbol{p}_b - \boldsymbol{h}'. \tag{6.6}$$

The momenta $\boldsymbol{p}$ and $\boldsymbol{h}$ are clarified in Figs. 6.1 and 6.2, with $\boldsymbol{q} = \boldsymbol{q}_1 + \boldsymbol{q}_2$ the momentum carried by the incoming boson X. The value of the πNN coupling constant is determined via $f_{\pi NN}^2/4\pi = 0.075$, and m_π is the mass of the pion. For the ease of notation, we denote the $\boldsymbol{q}$ dependence of the currents by $\widehat{\boldsymbol{J}}(\boldsymbol{q})$ instead of $\widehat{\boldsymbol{J}}(\boldsymbol{q},\boldsymbol{q}_1,\boldsymbol{q}_2)$, and we implicitly assume that the total MEC consists of a sum over all particle pairs

$$\widehat{\boldsymbol{J}}_V^{[2],\mathrm{MEC}}(\boldsymbol{q}) = \sum_{i<j}^{A} \widehat{\boldsymbol{J}}_V^{[2],\mathrm{MEC}}(\boldsymbol{q},\boldsymbol{q}_i,\boldsymbol{q}_j). \tag{6.7}$$

The seagull and pion-in-flight currents, Eqs. (6.1) and (6.2), fulfill the two-body CVC relation, this is shown explicitly in Appendix C.

To account for the internal structure of the hadrons, form factors have to be introduced. This is done as follows

$$\widehat{\boldsymbol{J}}_V^{[2],\mathrm{sea}}(\boldsymbol{q}) = -i\left(\frac{f_{\pi NN}}{m_\pi}\right)^2 (\boldsymbol{I}_V)_3\, F_1^V(Q^2) \left(\Gamma_\pi^2(\boldsymbol{q}_2^2)\frac{\boldsymbol{\sigma}_1\,(\boldsymbol{\sigma}_2\cdot\boldsymbol{q}_2)}{\boldsymbol{q}_2^2+m_\pi^2} - \Gamma_\pi^2(\boldsymbol{q}_1^2)\frac{\boldsymbol{\sigma}_2\,(\boldsymbol{\sigma}_1\cdot\boldsymbol{q}_1)}{\boldsymbol{q}_1^2+m_\pi^2}\right), \tag{6.8}$$

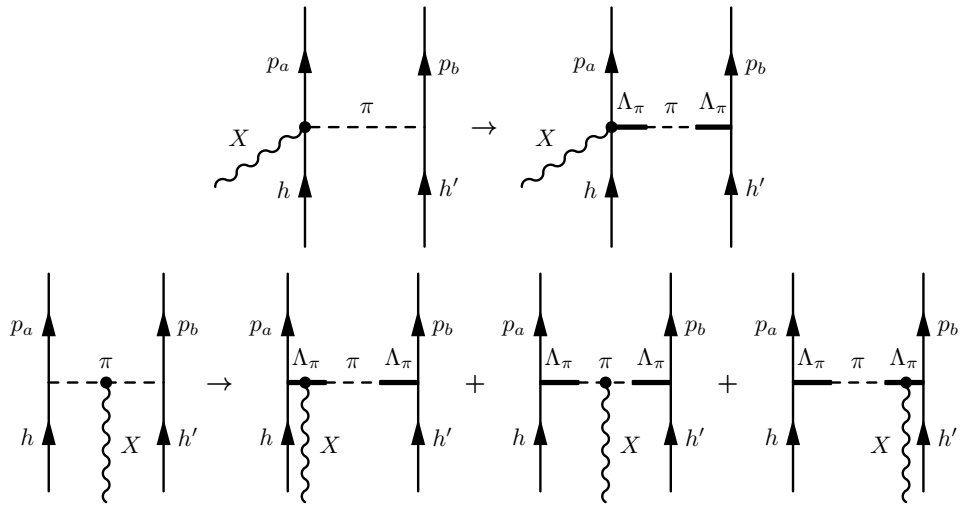

Figure 6.3: Interpretation of the pion vertex form factor as the conversion of the pion into a *heavy pion* with mass Λ_π.

$$\widehat{\boldsymbol{J}}_V^{[2],\mathrm{pif}}(\boldsymbol{q}) = i\left(\frac{f_{\pi NN}}{m_\pi}\right)^2 (\boldsymbol{I}_V)_3\, F_1^V(Q^2) F(\boldsymbol{q}_1^2, \boldsymbol{q}_2^2) \frac{(\boldsymbol{\sigma}_1 \cdot \boldsymbol{q}_1)\,(\boldsymbol{\sigma}_2 \cdot \boldsymbol{q}_2)}{(\boldsymbol{q}_1^2 + m_\pi^2)\,(\boldsymbol{q}_2^2 + m_\pi^2)} (\boldsymbol{q}_1 - \boldsymbol{q}_2), \tag{6.9}$$

At the πNN vertices, the seagull currents were regularized by introducing a monopole form factor as is commonly done,

$$\Gamma_\pi(\boldsymbol{q}^2) = \frac{\Lambda_\pi^2 - m_\pi^2}{\boldsymbol{q}^2 + \Lambda_\pi^2}, \tag{6.10}$$

with cutoff mass $\Lambda_\pi = 1250$ MeV. We follow the procedure introduced in [29] to ensure CVC. The first term in the seagull current is multiplied by $\Gamma_\pi^2(\boldsymbol{q}_2^2)$ and the second exchange term with $\Gamma_\pi^2(\boldsymbol{q}_1^2)$. Multiplying the pion-in-flight current by $\Gamma_\pi(\boldsymbol{q}_1^2)\Gamma_\pi(\boldsymbol{q}_2^2)$ would lead to a current which no longer respects CVC. Therefore we multiply the pion-in-flight current by

$$F(\boldsymbol{q}_1^2, \boldsymbol{q}_2^2) = \Gamma_\pi(\boldsymbol{q}_1^2)\Gamma_\pi(\boldsymbol{q}_2^2)\left(1 + \frac{\boldsymbol{q}_1^2 + m_\pi^2}{\boldsymbol{q}_2^2 + \Lambda_\pi^2} + \frac{\boldsymbol{q}_2^2 + m_\pi^2}{\boldsymbol{q}_1^2 + \Lambda_\pi^2}\right). \tag{6.11}$$

The introduction of the form factors at the πNN vertices can be understood if one imagines the nucleon emitting a *heavy pion* of mass Λ_π which is subsequently *converted* into a pion [29]. This way, the boson cannot only couple to the pion but also to the heavy boson, which results in three diagrams for the pion-in-flight current as shown in Fig. 6.3.

The choice of the form factor at the electroweak vertex is not trivial. In principle, the seagull current has to be multiplied by a form factor e.g. $F_{\mathrm{sea}}(Q^2)$, to regularize the coupling at the $X\pi NN$ vertex. The pion-in-flight current should be multiplied by a different form factor e.g. $F_{\mathrm{pif}}\,(Q^2)$, since no nucleons are present at the $X\pi\pi$ vertex. In [29], it is argued that these form factors should be equal, and from current conservation arguments, it is determined that the correct form factor one should use at the electroweak vertices, is the isovector nucleon form factor $F_1^V(Q^2)$.

6.2 Axial currents

For the construction of the axial currents we rely on the method using an effective Lagrangian [4,30]. Considering MECs with a pion exchange, only the seagull current has an axial counterpart. In the low-energy limit its expression is

$$\widehat{\rho}_A^{[2],\mathrm{sea}}(\boldsymbol{q}) = \frac{i}{g_A}\left(\frac{f_{\pi NN}}{m_\pi}\right)^2 (\boldsymbol{I}_V)\left(\frac{\boldsymbol{\sigma}_2\cdot\boldsymbol{q}_2}{\boldsymbol{q}_2^2+m_\pi^2} - \frac{\boldsymbol{\sigma}_1\cdot\boldsymbol{q}_1}{\boldsymbol{q}_1^2+m_\pi^2}\right), \tag{6.12}$$

with $g_A = 1.26$. In contrast to the vector currents, this current is purely timelike, which means that only the Coulomb response is affected by the axial MEC. The relativistic version also contain a spacelike component, which is negligible in the low-energy limit.

The πNN vertex is regularized by introducing monopole factors in a similar way as was done for the vector seagull current. At the electroweak vertices one relies on the partially conserved axial current (PCAC) hypothesis to constrain the currents. Unfortunately, in the low-energy limit, this procedure is not unambiguous. Several different results are found in literature, depending on the approximations that are used. An in-depth discussion of these differences can be found e.g. in [1,30]. In this work, we consider the following three axial currents: the first two are different parameterizations for the axial seagull current and the third expression is an extension containing more diagrams

$$\widehat{\rho}_A^{[2],\mathrm{sea},1}(\boldsymbol{q}) = \frac{i}{g_A}\left(\frac{f_{\pi NN}}{m_\pi}\right)^2 (\boldsymbol{I}_V)\, G_A(Q^2)\left(\Gamma_\pi^2(\boldsymbol{q}_2^2)\frac{\boldsymbol{\sigma}_2\cdot\boldsymbol{q}_2}{\boldsymbol{q}_2^2+m_\pi^2} - \Gamma_\pi^2(\boldsymbol{q}_1^2)\frac{\boldsymbol{\sigma}_1\cdot\boldsymbol{q}_1}{\boldsymbol{q}_1^2+m_\pi^2}\right), \tag{6.13}$$

$$\widehat{\rho}_A^{[2],\mathrm{sea},2}(\boldsymbol{q}) = \frac{i}{g_A}\left(\frac{f_{\pi NN}}{m_\pi}\right)^2 (\boldsymbol{I}_V)\left(F_\pi(\boldsymbol{q}_1^2)\,\Gamma_\pi^2(\boldsymbol{q}_2^2)\frac{\boldsymbol{\sigma}_2\cdot\boldsymbol{q}_2}{\boldsymbol{q}_2^2+m_\pi^2} - F_\pi(\boldsymbol{q}_2^2)\,\Gamma_\pi^2(\boldsymbol{q}_1^2)\frac{\boldsymbol{\sigma}_1\cdot\boldsymbol{q}_1}{\boldsymbol{q}_1^2+m_\pi^2}\right), \tag{6.14}$$

$$\widehat{\rho}_A^{[2],\mathrm{axi}}(\boldsymbol{q}) = \frac{i}{g_A}\left(\frac{f_{\pi NN}}{m_\pi}\right)^2 (\boldsymbol{I}_V)\left(F_\pi(\boldsymbol{q}_2^2)\,\Gamma_\pi^2(\boldsymbol{q}_2^2)\frac{\boldsymbol{\sigma}_2\cdot\boldsymbol{q}_2}{\boldsymbol{q}_2^2+m_\pi^2} - F_\pi(\boldsymbol{q}_1^2)\,\Gamma_\pi^2(\boldsymbol{q}_1^2)\frac{\boldsymbol{\sigma}_1\cdot\boldsymbol{q}_1}{\boldsymbol{q}_1^2+m_\pi^2}\right). \tag{6.15}$$

Pion form factors are introduced to comply with the PCAC hypothesis

$$F_\pi(\boldsymbol{q}^2) = \frac{m_\rho^2}{\boldsymbol{q}^2+m_\rho^2}. \tag{6.16}$$

Expression sea,1 The first current, labeled with the superscript 'sea,1', is the axial version of the seagull current, derived using the soft-pion approximation [4,30]. It can be constructed from Eq. (6.12) by introducing the monopole form factors $\Gamma_\pi(\boldsymbol{q}_i^2)$ at the πNN vertices and multiplying it by the axial form factor $G_A(Q^2)$, for which we assume the standard dipole parameterization. The expression (6.13) was used in the neutrino-deuteron scattering studies of Refs. [31] and [32]. This version of the axial seagull current does not consider the PCAC hypothesis in its construction.

Expression sea,2 For the construction of the axial current with superscript 'sea,2', a non-relativistic reduction of the axial seagull current used in the calculations by Ruiz Simo *et al.* [22] was performed. In that work, the MECs were constructed by appending the pion

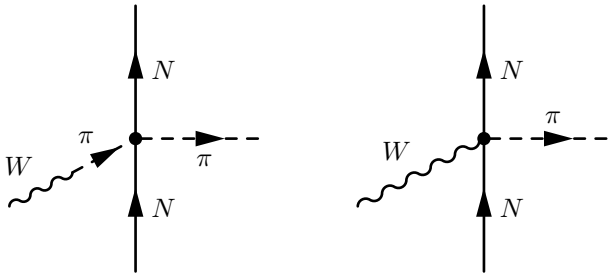

(a) π-pole **(b)** Contact

Figure 6.4: Diagrammatic representation of the axial pion production amplitudes with π-pole and contact interaction.

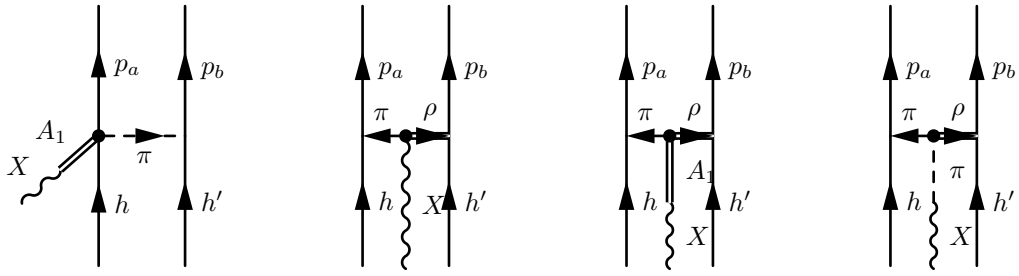

Figure 6.5: Diagrams considered in the axial charge density $\widehat{\rho}_A^{[2],\mathrm{axi}}$ derived in [30].

production diagrams of [33] with an extra nucleon that reabsorbs the pion. So in order to understand the form factors in the axial seagull current, we must revert to the weak pion production amplitudes.

The pion form factor was introduced to account for the ρ-meson dominance of the $\pi\pi NN$ vertex, and to preserve the *one-body version* of PCAC, the same form factor was used to regularize the axial $W\pi NN$ vertex. In a diagrammatic way this is explained as follows: the πNN vertex in diagram (a) of Fig. 6.4 should be multiplied by F_π and to comply with PCAC, the vertex in (b) is multiplied by the same form factor. This axial contact interaction is then appended with a second nucleon line to construct the axial seagull current.

The πNN vertices are then multiplied by the $\Gamma_\pi(\boldsymbol{q}_i^2)$ form factors to constrain these vertices in the same way as was done for the vector currents in our model. We note that in [22] a pion-pole current is also considered next to the axial seagull current. This current is not considered separately in this work, as its contribution is negligible in the low-energy limit [34]. The vector currents in this work correspond to the nonrelativistic limits of the vector seagull and pion-in-flight currents of [22], except for the fact that the Γ_π vertices were not included in that work.

Expression axi The axial current, labeled 'axi', was derived in [30]. The four diagrams displayed in Fig. 6.5 are included. The first one is the axial version of the seagull current (a), which has an exchange term as well. The other three diagrams have a pion-in-flight-like structure, but one of the two pions is replaced with a ρ-meson, and the coupling of the

W-boson at the $\pi\rho$ vertex is a contact coupling (b), an A_1-pole (c) or π-pole coupling (d). The three diagrams with a $\pi - \rho$ exchange (b-d) have no vector counterpart and since one of the two mesons is a pion, they can be considered to have the same range as the vector diagrams. The pion-in-flight diagram shown in Fig. 6.2 has no axial counterpart.

The divergence of the combination of these four currents obeys the *two-nucleon version* of the PCAC relation. In a diagrammatic sense: the divergence of the diagrams (a-d) is related to the two-nucleon pion absorption diagram, which is equal to diagram (d) stripped of the boson. The nonrelativistic limit of these currents is purely time-like. The vertices are multiplied by the appropriate $\Gamma_\pi(\boldsymbol{q}_i^2)$ hadronic form factors to regularize the coupling at the πNN vertices. This current has the same operator structure as the two axial seagull currents, though, by construction, it contains more diagrams. We argue that this axial current is the optimal choice for our model, as it uses the two-nucleon version of the PCAC relation to constrain the currents, and further.

The remainder of this chapter is dedicated to the impact these MECs have on electron and neutrino interactions. First the influence is studied for $1N$ knockout reactions $^{12}\mathrm{C}(e,e')$ and $^{12}\mathrm{C}(\nu_\mu,\mu^-)$. For electron scattering calculations our results are compared with data and other predictions found in literature.

The $2N$ knockout results are presented for exclusive, semi-exclusive and inclusive interactions. The strength of the different MECs are studied separately. For inclusive $2p2h$ interactions, electron scattering calculations are compared with data and other numerical predictions. For neutrino interactions, we pay special attention to the axial two-body currents. The validity of the axial currents is checked by comparing our results with [35].

6.3 Influence of MECs on inclusive $1N$ knockout

In Figs. 6.6 and 6.7 the difference between the $1p1h$ responses for $^{12}\mathrm{C}(e,e')$ and $^{12}\mathrm{C}(\nu_\mu,\mu^-)$ interactions, calculated with and without MECs, is shown

$$\Delta W_i = W_i^{\mathrm{IA+MEC}} - W_i^{\mathrm{IA}}. \tag{6.17}$$

In Fig. 6.6a, the Coulomb and transverse $1p1h$ response functions for $^{12}\mathrm{C}(e,e')$ are shown and compared with data. Corresponding calculations of Amaro *et al.* [36], obtained in a MF calculation using a Woods-Saxon potential, are displayed as well. The agreement between both $1p1h$ calculations is remarkable. Since the vector seagull and pion-in-flight currents are purely space-like, only the transverse response is affected when including the MECs. This results in a small increase of the W_T response for all displayed values of the momentum transfer. The relative increase of the response is of the order $\approx 5\%$.

The relative influence of the two different MECs, ΔW_i, is displayed in Fig. 6.6b. The seagull currents increase the transverse response. The pion-in-flight currents have a smaller effect and tend to decrease the response for small ω but increase it for larger energy transfers.

The differences with the numerical results of [36], obtained in a Fermi gas model[1], are relatively large, even though similar expressions for the two-body currents were used. It

[1]Other predictions in [36] suggest that the MF results of that work are equal in size to the Fermi gas results, but have a larger tail at high ω.

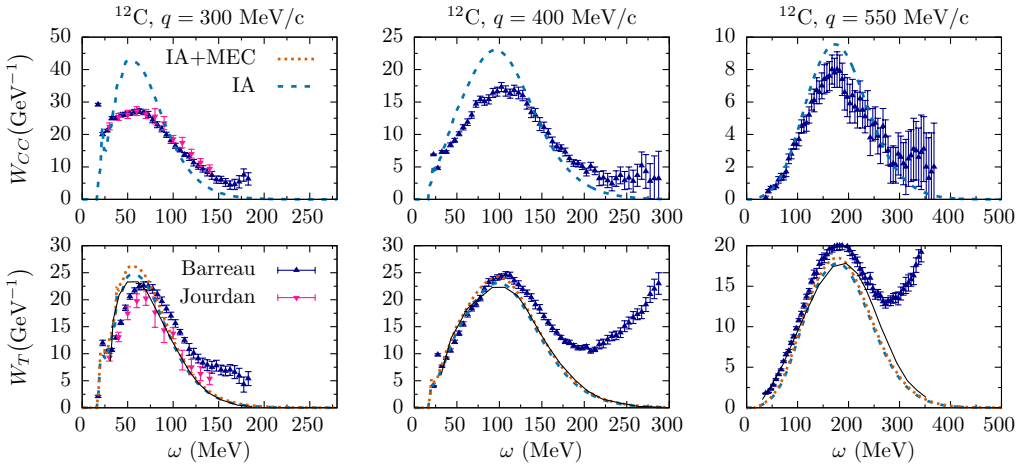

(a) The $1p1h$ response, MEC=sea+pif for W_T. The solid black lines are the $1p1h$ MF results of [36].

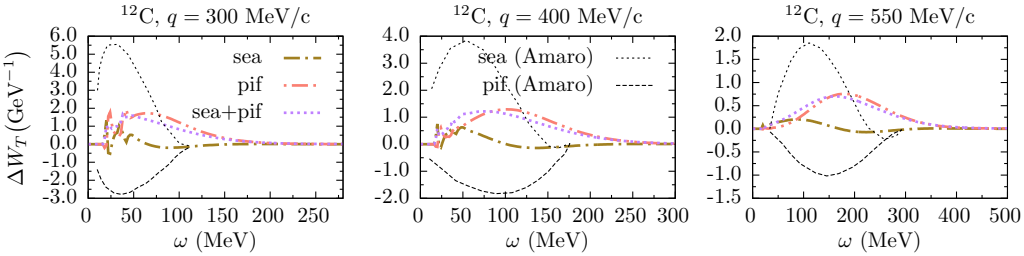

(b) The correction of the MECs to the $1p1h$ responses. The black lines are Fermi gas results of Amaro *et al.* [36].

Figure 6.6: The computed ω dependence of the ^{12}C(e,e') responses W_{CC} and W_T for three different momentum transfers. Data is taken from Refs. [37,38].

appears that the 'sea+pif' combination of both calculations is comparable in size, however, we have not found sea+pif results including interference.

One difference between this model, and the one used in [36], is that seagull and pion-in-flight currents were multiplied by different form factors at the electroweak vertices in [36]. The pion-in-flight current was multiplied by $F_\pi(Q^2)$ compared to $F_1^V(Q^2)$ in this work. This way, the seagull and pion-in-flight currents cannot comply with CVC. Another difference is that a value of $\Lambda_\pi = 1000$ MeV was adopted in the monopole form factor in those calculations.

Many other calculations also studied the effect of MECs to $1p1h$ responses for electron scattering, using different approaches [7,39–41], however not all obtained the same conclusions. In all cases, the effects were relatively small.

The $1p1h$ responses for neutrino interactions, with and without MECs, are shown in Fig. 6.7a. Fig. 6.7b shows that the three axial currents considered here interfere constructively with the nuclear current in the IA, resulting in an increase of the Coulomb response. The

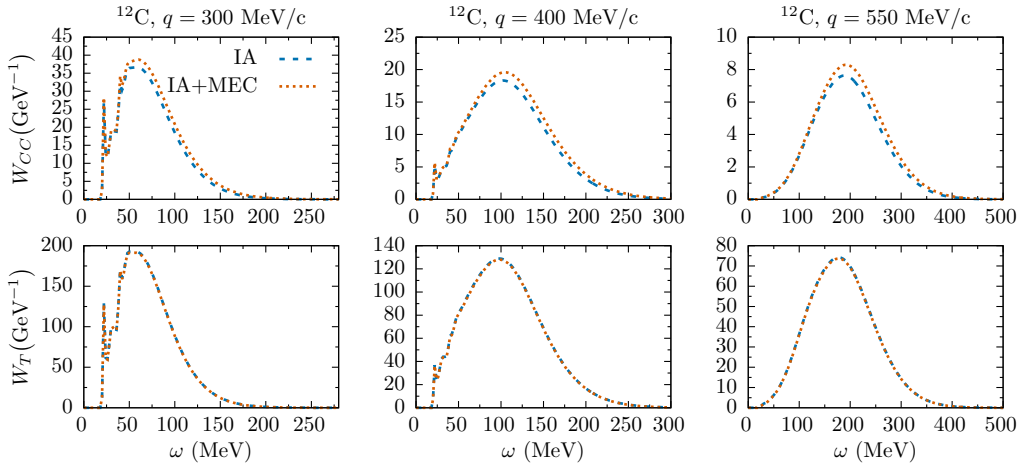

(a) The $1p1h$ responses. MEC=axi for W_{CC} and MEC=sea+pif for W_T.

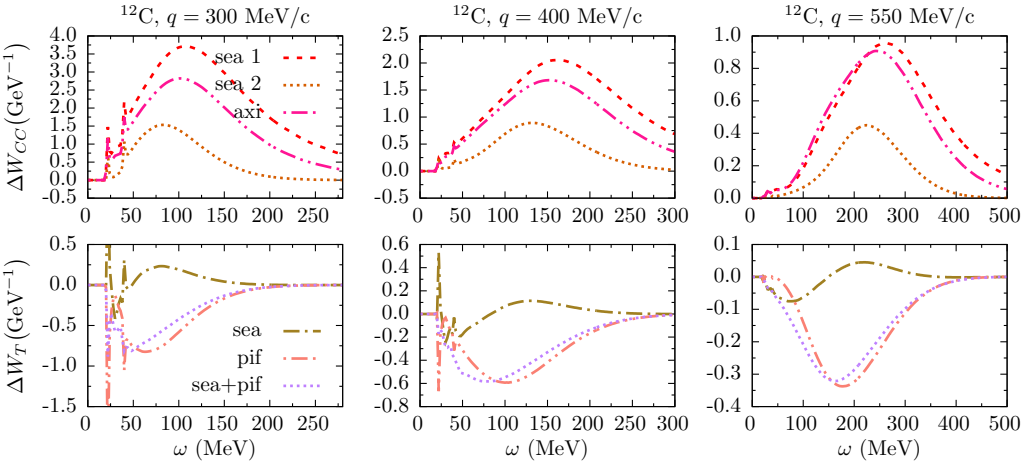

(b) The correction of the MECs to the $1p1h$ responses.

Figure 6.7: The computed ω dependence of the ^{12}C(ν_μ, μ^-) responses W_{CC} and W_T for three different momentum transfers.

effect of the expression labeled 'sea,2' is smallest. The current 'axi' yields an increase of $\approx 10\%$ of the $1p1h$ response in the IA. The combined effect of the seagull and pion-in-flight currents on the transverse response function results in a negligible decrease of the $1p1h$ response, the total decrease is less than 1% compared to the $1p1h$ response in the IA. In fact it is smaller than the variation from alternate parameterizations of the nucleon form factor. The small impact is partly due to the fact that a large part of the transverse strength comes from the axial part of the current, see Fig. 3.9, which is unaffected by the MECs in the low-energy limit. We note that the effect of the MECs on the $1N$ knockout channel of the double differential cross sections will be negligible since the cross section is dominated by the transverse channel, see Fig. 3.8. When comparing Figs. 6.6b and 6.7b, we note that

the effect for neutrino scattering has an opposite sign and is a factor 2 smaller. These differences are linked to the isospin operators.

6.4 Exclusive knockout of MEC pairs

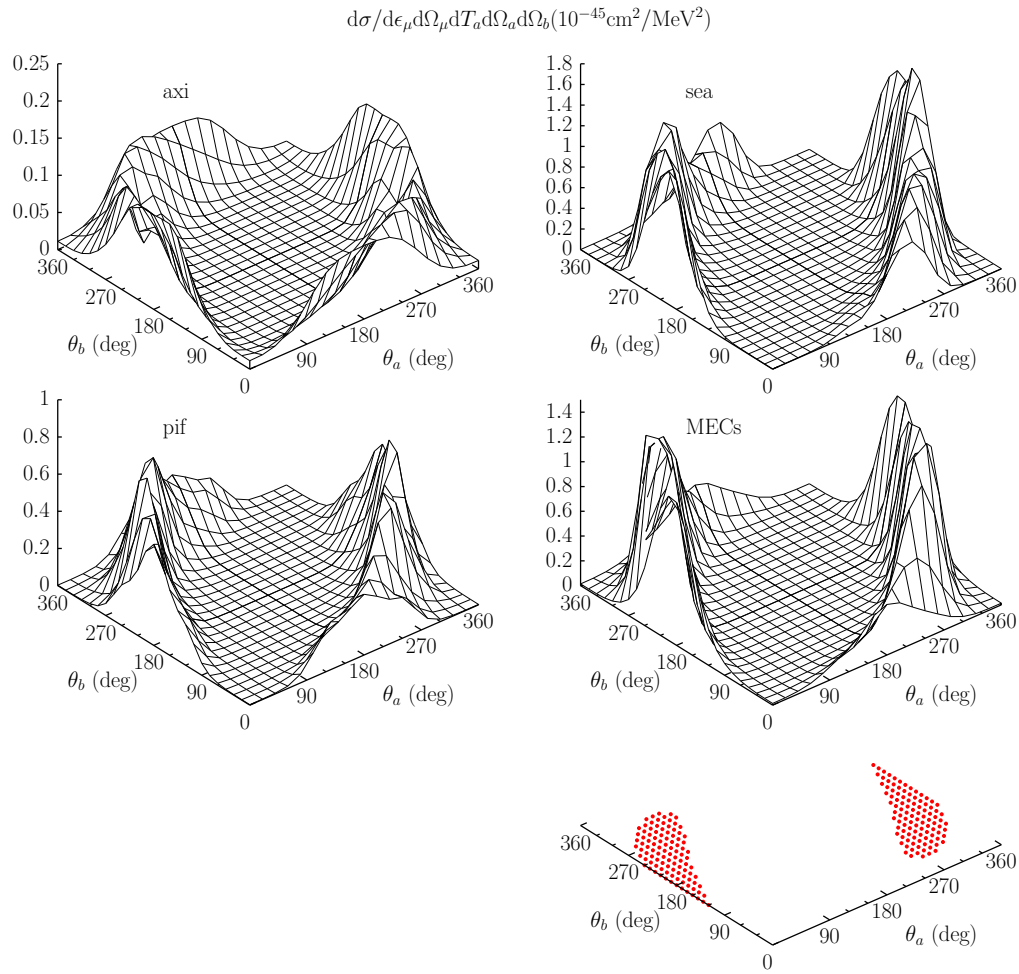

Figure 6.8: The $^{12}\mathrm{C}(\nu_\mu, \mu^- N_a N_b)$ cross section (N_a = p, N_b = p′, n) at $\epsilon_{\nu_\mu} = 750$ MeV, $\epsilon_\mu = 550$ MeV, $\theta_\mu = 15°$ and $T_\mathrm{p} = 50$ MeV for in-plane kinematics ($x_B = 0.08$). The three contributions to the MECs are shown, and the bottom plot shows the (θ_a, θ_b) regions with $P_{12} < 300$ MeV/c.

In [42] the knockout of seagull and pion-in-flight pairs for $^{16}\mathrm{O}(\gamma, \mathrm{pn})$ interactions were studied, where the residual nucleus is left in a specific final state. In this work, we extended those calculations to neutrino interactions. Compared to the photo-induced interactions, neutrino-induced $2N$ knockout has an effect on the nn pairs as well. A real or virtual photon can only couple to a pn pair when seagull and pion-in-flight currents are considered. Further, the residual nucleus was not studied so a summation over all possible final states was performed.

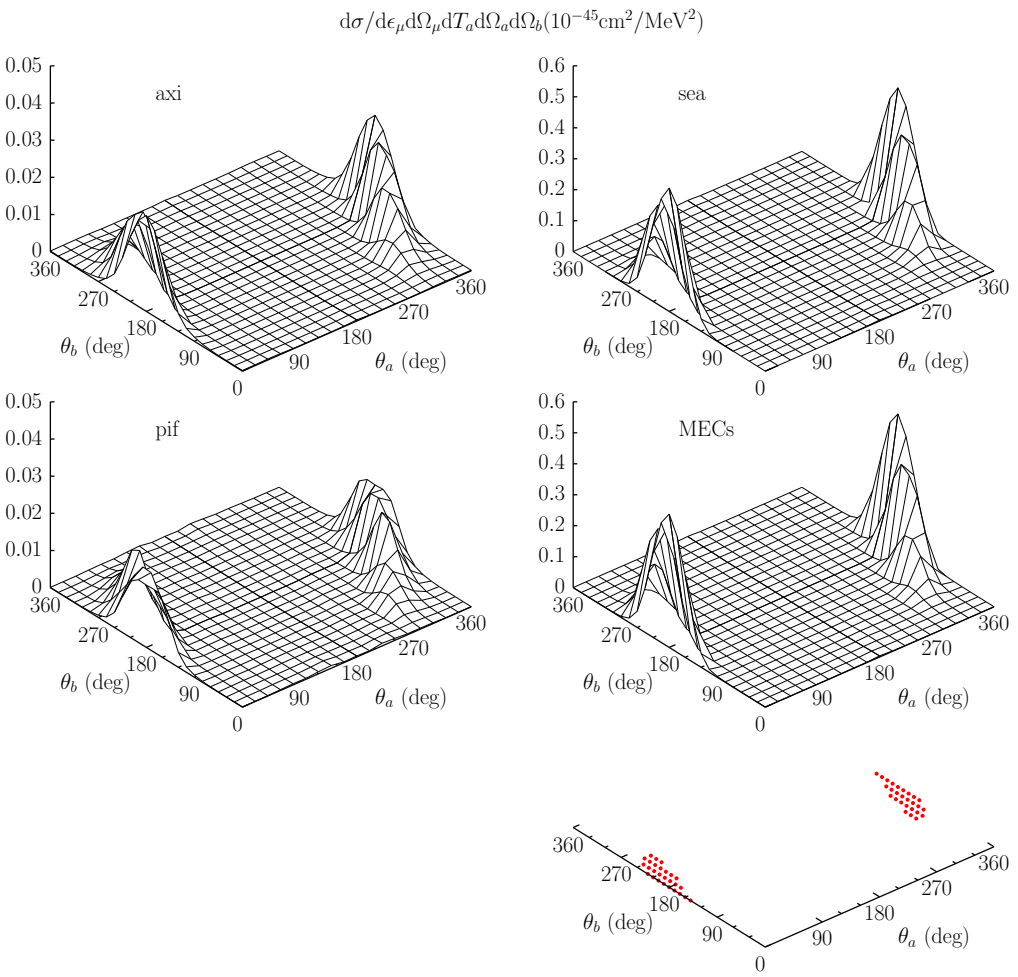

Figure 6.9: Similar as Fig. 6.8 but scattering on ^{16}O with $\epsilon_\mu = 250$ MeV ($x_B = 0.04$).

The result of such an exclusive $^{12}\mathrm{C}(\nu_\mu, \mu^- N_a N_b)$ cross section calculation (N_a = p, N_b = p′, n) is shown in Fig. 6.8 for the knockout of seagull and pion-in-flight pairs. The result is an incoherent sum of pn and nn pair knockout. In Fig. 6.9 a similar calculation is shown but with ^{16}O as target nucleus and different kinematics.

As expected, the cross sections show the back-to-back knockout behavior, as observed for the knockout of SRC pairs, where the same kinematics were studied in Fig. 5.12, and the cross section strength resides in the (θ_a, θ_b) area where $P_{12} < 300$ MeV/c. Comparing with [42], the overall shape of the $2N$ knockout cross section is independent of the incoming boson (γ or $W^\pm$) and the specific nuclear final state, the strength varies but the shape remains similar. Comparing results for ^{12}C and ^{16}O, the characteristics of the cross section are similar. This is not surprising given that we assumed a direct knockout mechanism.

In Fig. 6.8, the majority of the strength for the seagull current comes from the axial part of the current and hence from the *CC* channel. If one only considers the vector part of the currents, the seagull and pion-in-flight currents interfere destructively, as already seen in

[42] for photo-induced interactions.

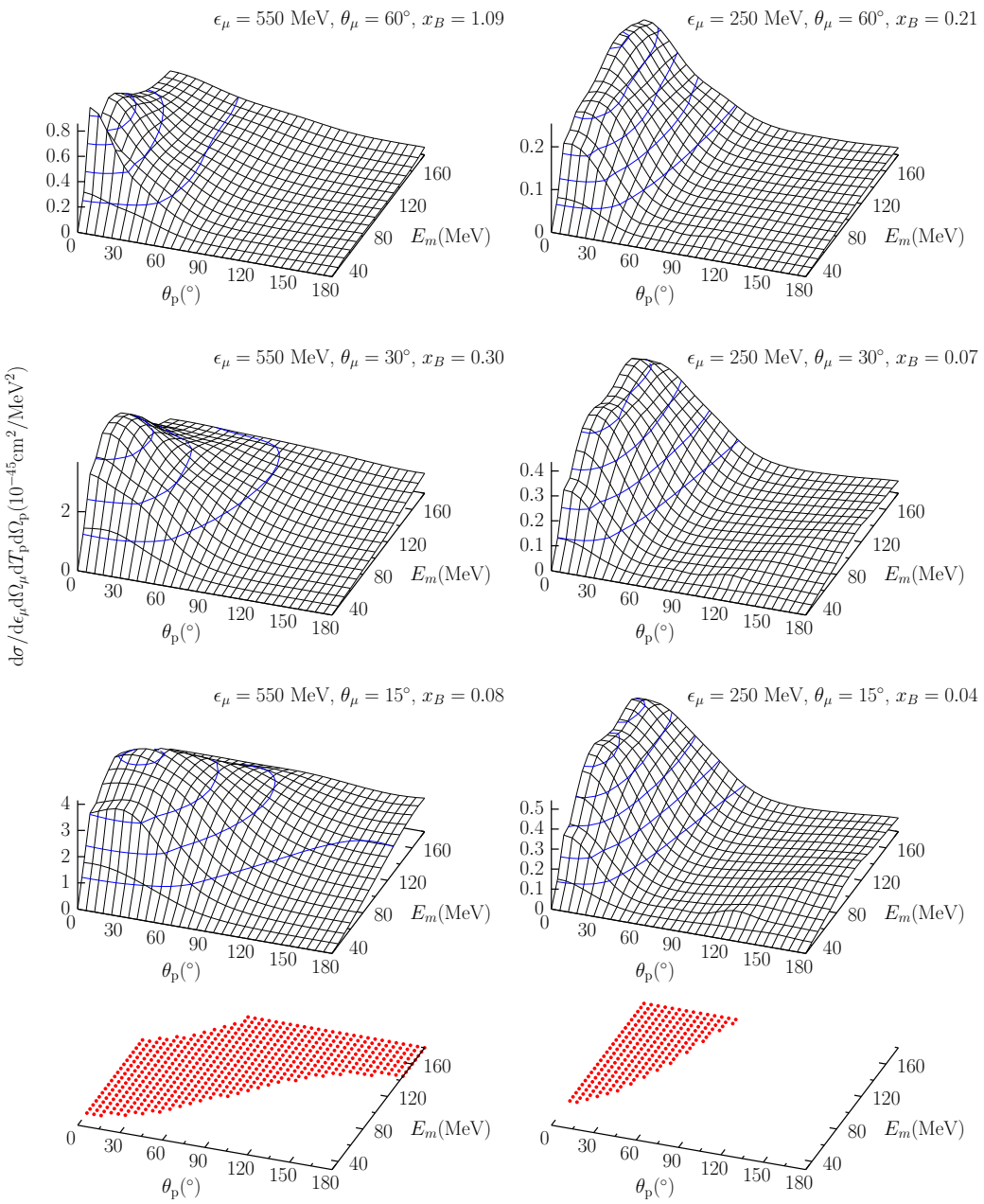

Figure 6.10: Semi-exclusive $^{12}C(\nu_\mu, \mu^- p)$ cross section for $\epsilon_{\nu_\mu} = 750$ MeV, for six different muon kinematics and in-plane nucleon kinematics ($\varphi_p = 0°$). The bottom panels shows the (θ_p, E_m) area with $P_{12} < 300$ MeV/c for the two situations with $\theta_\mu = 15°$.

6.5 Semi-exclusive knockout of MEC pairs

Integrating the exclusive $2N$ knockout cross section over the angle of one of the emitted nucleons, the semi-exclusive $2N$ knockout cross section is obtained, Eq. (4.25), where the residual $A-1$ is excited above the two nucleon emission threshold. For fixed lepton kinematics, the semi-exclusive cross section depends on three independent variables T_p, θ_p and φ_p. In Fig. 6.10, the results of such a calculation are shown for six different lepton kinematics, the same kinematic situations as in Fig. 5.14 where SRCs were studied.

Comparing the results for MECs and SRCs, we observe that the MECs generate strength in roughly the same (θ_p, E_m) regions as the SRCs do, restricted by $P_{12} < 300$ MeV/c. The majority of the MEC strength appears to be situated at lower E_m and θ_p compared to the SRC strength. The short-range character of the correlations allows them to probe high relative momenta k_{12} and consequently higher missing energy.

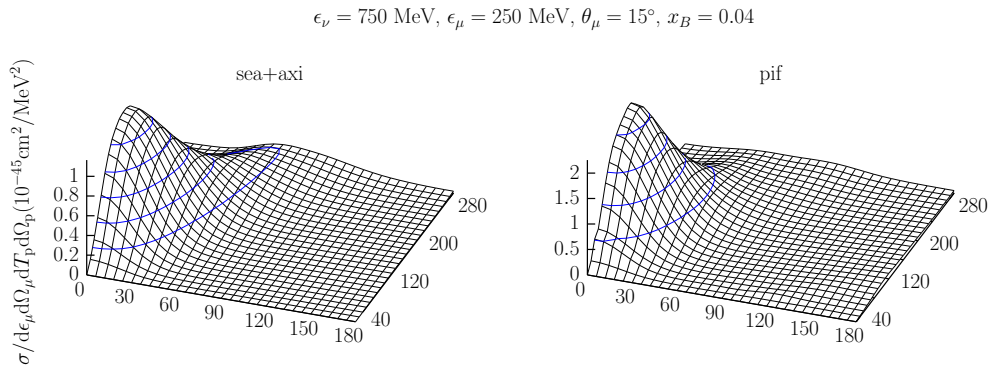

Figure 6.11: Semi-exclusive $^{12}\mathrm{C}(\nu_\mu, \mu^- \mathrm{p})$ cross section for $\epsilon_{\nu_\mu} = 750$ MeV, $\epsilon_\mu = 250$ MeV and $\theta_\mu = 15°$ for in-plane nucleon kinematics ($\varphi_\mathrm{p} = 0°$). The three contributions to the MECs are shown separately.

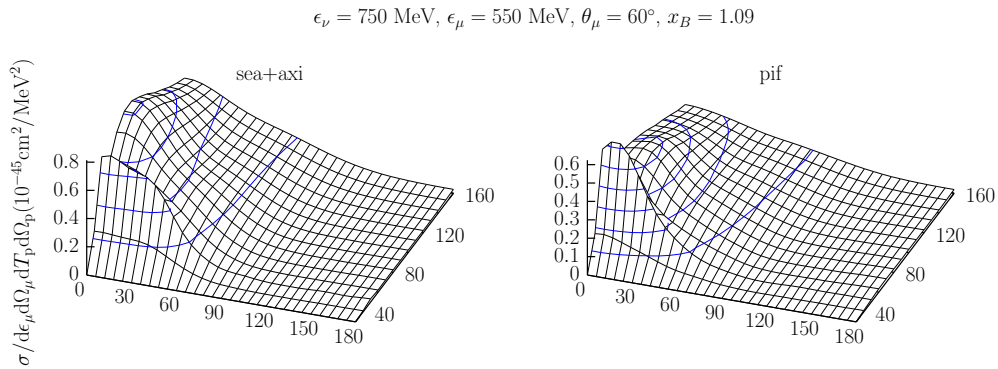

Figure 6.12: Same as Fig. 6.11 but for $\epsilon_{\nu_\mu} = 750$ MeV, $\epsilon_\mu = 550$ MeV and $\theta_\mu = 60°$.

Another observation is that the strength stemming from the MECs is slightly smaller than

the strength from the SRCs, which appears to contradict the results found in literature, e.g. [43]. We stress that the reason for this discrepancy, is that we only include seagull and pion-in-flight currents and that Δ-currents are expected to dominate the cross sections in the kinematic situations examined here.

In Figs. 6.11 and 6.12, the seagull+axial and pion-in-flight contributions are separated for two kinematic situations. For $x_B = 0.04$, the contribution of the axial current is relatively small, and the seagull current is of comparable size as the pion-in-flight current. For increasing x_B the relative strength of the axial current increases. At $x_B = 1.09$ the contribution of the three currents are comparable in size. The seagull and pion-in-flight currents interfere destructively for semi-exclusive reactions, in a similar way as was seen for the exclusive cross sections.

6.6 Influence of MECs on inclusive cross sections

Before we consider inclusive $2N$ knockout responses for neutrino interactions, we confront our results for electron scattering with data and models found in literature. In Fig. 6.13a the $1p1h$ and $2p2h$ response functions W_{CC} and W_T are shown and compared with Rosenbluth separated cross section data. The seagull and pion-in-flight currents have no effect on the Coulomb response, as the vector currents have no time-like component in the low-energy limit. In the $1p1h$ responses, the MECs result in a small increase of the responses, as discussed earlier. The $2p2h$ responses appear as a broad background to the $1p1h$ ones. Fig. 6.13b shows the results of the inclusive transverse $2p2h$ responses, where the knockout of seagull and pion-in-flight currents was studied separately. We observe that the strength from both types of two-body currents is of similar size. The pion-in-flight current is slightly more important at large ω for the three momentum transfers studied. More interesting is that the currents interfere destructively. In [44] e.g, the same destructive interference was observed between the seagull and pion-in-flight currents in a RFG model for scattering on ^{56}Fe, however, in that calculation, the seagull contribution is roughly three times larger than the pion-in-flight contribution. Further, we compared our calculations with MF results from Amaro *et al.* [36], where a similar model was used. The results of both calculations are very similar.

In Figs. 6.14 and 6.15, inclusive $^{12}\mathrm{C}(e, e')$ and $^{12}\mathrm{C}(\nu_\mu, \mu^-)$ responses are studied at $q = 500$ MeV/c. Only the vector seagull current and the three axial currents are accounted for in the $2N$ knockout calculations. For simplicity, the results of the $1N$ knockout calculations in the IA are displayed. For the electron-scattering calculations, the dipole parameterization of the nucleon form factors was used [45], while for neutrino interactions, we adopted the BBBA05 parameterization for the Q^2 dependence of the form factors [46]. For the axial form factor G_A, we used the dipole form factor with $m_A = 1.03$ GeV. Our results are compared with the corresponding numerical results of Ruiz Simo *et al.* [35], where a RFG was used for the calculation of the responses. The $1p1h$ responses calculated in the RFG are displayed for reference. The shift of the peak of the $1p1h$ responses between both calculations is related to the different treatment of the binding energy of the nucleons.

For electron scattering, the $2N$ knockout strength attributed to the seagull current is roughly a factor 2 smaller compared to the RFG calculations. The $2N$ knockout strength to the transverse response for neutrino interactions appears very similar in both calculations. In

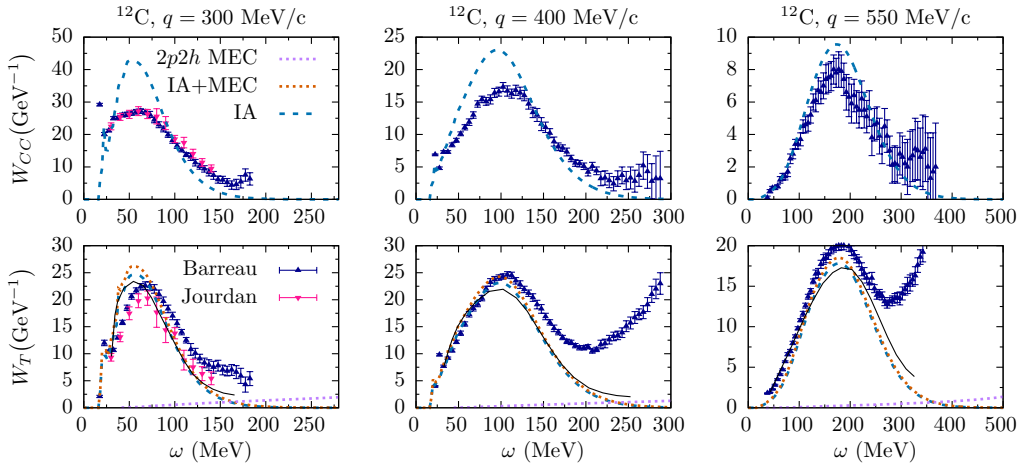

(a) The 1p1h and 2p2h responses, MEC=sea+pif for W_T. The solid black lines are the 1p1h+2p2h MF results of [36].

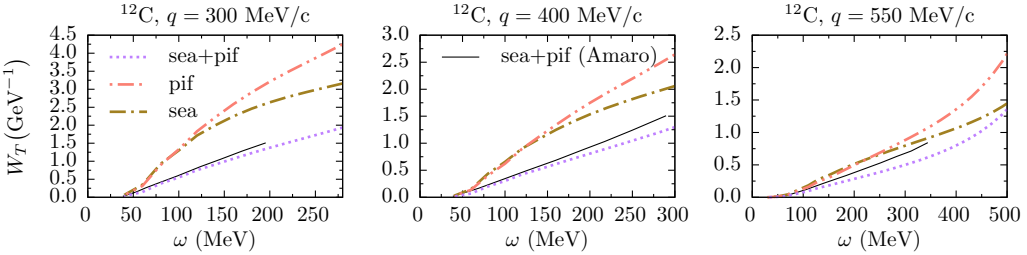

(b) The 2p2h responses. The solid black lines are the sea+pif results from [36].

Figure 6.13: The 1p1h and 2p2h MEC response functions W_{CC} and W_T for ^{12}C(e, e') for three values of q. Data is taken from Refs. [37,38].

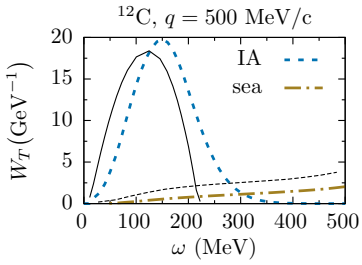

Figure 6.14: The transverse 1p1h and 2p2h responses for ^{12}C(e, e') at $q = 500$ MeV/c with MEC. The solid (dashed) black lines are the 1p1h (2p2h) RFG results from Ref. [35].

the Coulomb channel, the results for the three different axial currents are compared. The currents labeled 'sea,1' and 'axi' yield a strength which is of similar size as the strength of

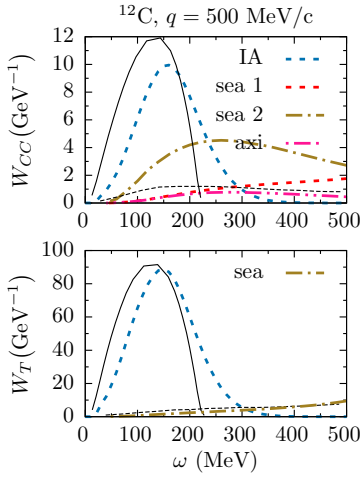

Figure 6.15: The Coulomb and transverse $1p1h$ and $2p2h$ responses for $^{12}\mathrm{C}(\nu_\mu, \mu^-)$ at $q = 500$ MeV/c with MEC. The solid (dashed) black lines are the $1p1h$ ($2p2h$) RFG results from Ref. [35].

the RFG calculations. For low ω, the results of the currents '1' and '3' are very similar, however for increasing energy transfers, the former keeps increasing while the latter decreases slightly for $\omega \gtrsim 250$ MeV. The strength of the current 'sea,2', which was obtained after a nonrelativistic reduction of the axial seagull current in [35], is roughly five times larger and seems unrealistically large compared to the $1p1h$ response. This suggests that this current is not well constrained.

The results for the responses W_{CC} and W_T for an inclusive $^{12}\mathrm{C}(\nu_\mu, \mu^-)$ calculation, including seagull and pion-in-flight currents in the $1p1h$ and $2p2h$ channels, are presented in Fig. 6.16a. In the $1p1h$ channel, we only show the results using the expression 'axi' for the axial current, the results using the other two expressions can be inferred from Fig. 6.7b.

In Fig. 6.16b, the $2p2h$ responses are shown in detail, showing the separate strengths of the seagull and pion-in-flight currents, and the three different axial currents. Comparing the $2p2h$ results in the transverse channel for electron and neutrino scattering, we observe that the contributions of the seagull and pion-in-flight currents behave in a similar way as a function of ω. The currents interfere destructively in both cases. The $2p2h$ responses for neutrino scattering are roughly a factor 4 larger than in electron interactions. The relative effect of the $2p2h$ responses with respect to the $1p1h$ responses shows an identical behavior for electron and neutrino interactions. The $2p2h$ responses calculated using expressions 'sea,1' and 'axi' for the axial current are smaller then the transverse $2p2h$ responses, however their effect relative to the corresponding $1p1h$ Coulomb response is larger.

Summarizing, in Fig. 6.17, the results of a $^{12}\mathrm{C}(\nu_\mu, \mu^-)$ cross section calculation are shown, for a fixed incoming neutrino energy $\epsilon_{\nu_\mu} = 750$ MeV and three different scattering angles. In these calculations, the axial current 'axi', the seagull current and the pion-in-flight current are accounted for. The effect of the MECs on the $1p1h$ channel is rather small, because the two-body effects tend to cancel each other. The double differential cross sections are dominated by the transverse channel, see Fig. 3.8, and the effect of the MECs on the transverse responses is very small, as shown in Fig. 6.7. Even though the currents are

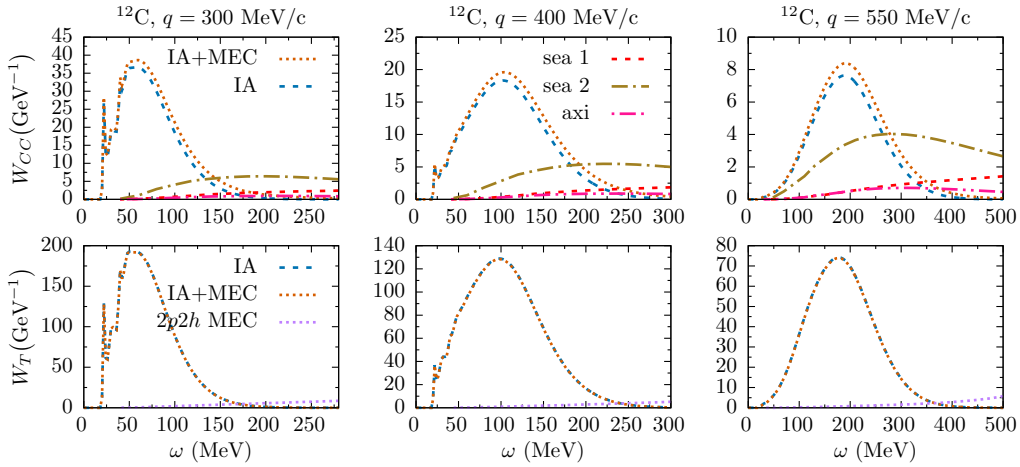

(a) The $1p1h$ and $2p2h$ responses. The three expressions of the axial current are compared in the CC response. The seagull and pion-in-flight contribution are included in the T response.

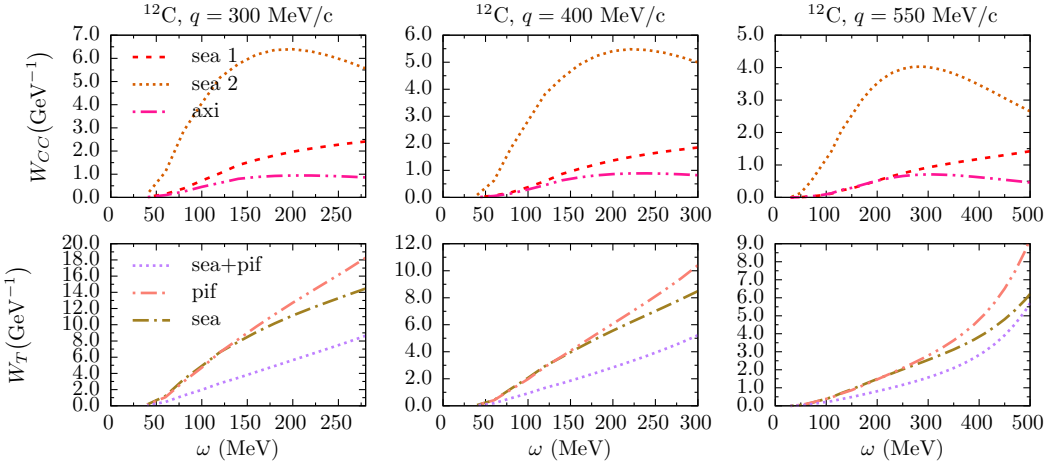

(b) The different contributions to the $2p2h$ responses.

Figure 6.16: The $1p1h$ and $2p2h$ MEC response functions W_{CC} and W_T for $^{12}\mathrm{C}(\nu_\mu, \mu^-)$ for three values of q.

dominated by the transverse part, the absolute effect of the axial current on the cross section is largest.

The contribution of the MECs to the $2p2h$ channel yields a small contribution to the inclusive cross section, appearing as a broad background to the $1p1h$ channel. This small effect is partly due to the destructive interference between the vector currents. Comparing with the SRC induced channel, Fig. 5.25, the MEC $2N$ knockout contribution is roughly a factor 3 smaller for $\theta_\mu = 15°$ to a factor 5 for $\theta_\mu = 60°$.

We conclude this chapter with Fig. 6.18, where the $2N$ knockout of MEC pairs from ^{12}C

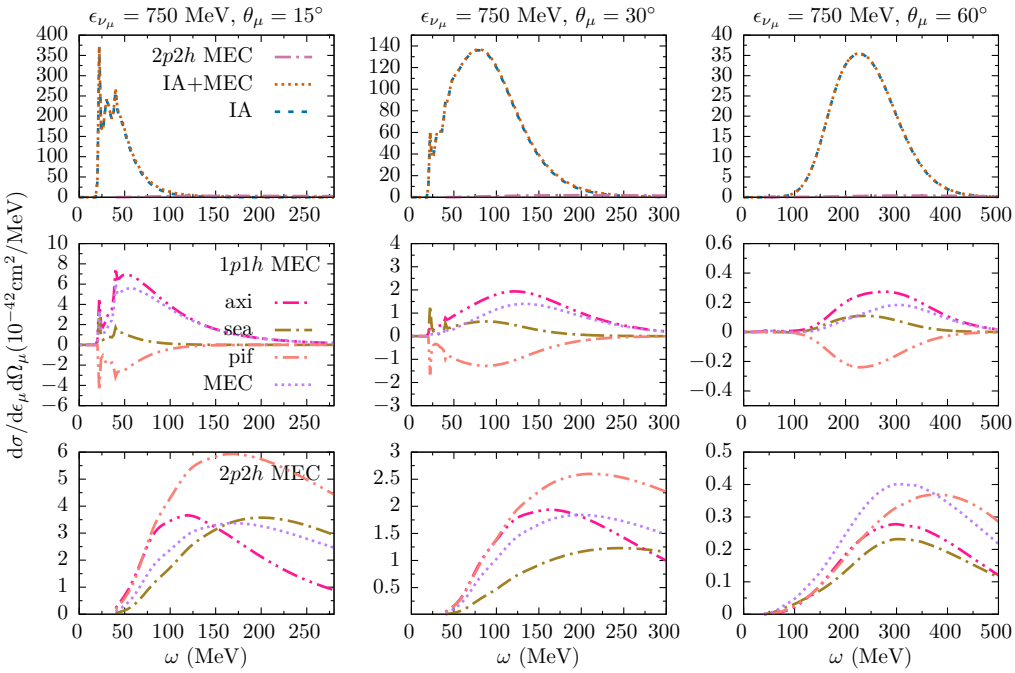

Figure 6.17: The ω dependence of the $^{12}C(\nu_\mu, \mu^-)$ cross section for ϵ_{ν_μ} = 750 MeV and three different values of the lepton scattering angle θ_μ. The top panels show the combined $1p1h$ and $2p2h$ cross sections. The middle panels show the correction of the MECs on the $1p1h$ cross section and the bottom panels show the $2p2h$ MEC part of the cross section.

and ^{16}O are compared. In the top panels, the absolute $2N$ knockout strengths are shown, and the pp and pn pair emission are separated. The full lines are the results for ^{16}O and the dashed lines the corresponding results for ^{12}C. The ratios are displayed in the bottom panels, together with the ratios of the number of pairs in the nucleus.

In Fig. 5.27, the same ratio was studied for SRC pairs. For SRC pairs, a scaling relation $A^{1.44}$ was proposed in [47] for the number of SRC-prone pairs in the nucleus. The cross sections ratios were found to roughly follow this scaling law.

The labels in Fig. 6.18 correspond with the particles in the continuum. This means that for the emission of pp pairs, one could naively expect that the cross section would scale with the number of pn pairs in the target nucleus, i.e. $N \cdot Z$. Similarly, knockout of pn pairs could be expected to scale like $N(N-1)/2$. These naive assumptions are based only on the long range of the MECs in the sense that they have a range spanning the whole size of the nucleus. We find that cross section ratios do not follow these basic assumptions.

The emission of pp pairs appears to follow the $A^{1.44}$ scaling relation, while the emission of pn pairs doesn't. This seems to imply that the pn pairs in the nucleus, stemming from MECs, are dominated by close-proximity pairs as well. The fact that the emission of pn pairs does not follow any of these scaling relations, suggests this reaction channel has different combinatorial behavior, which might be related to the spin and isospin dependence of the two-body currents.

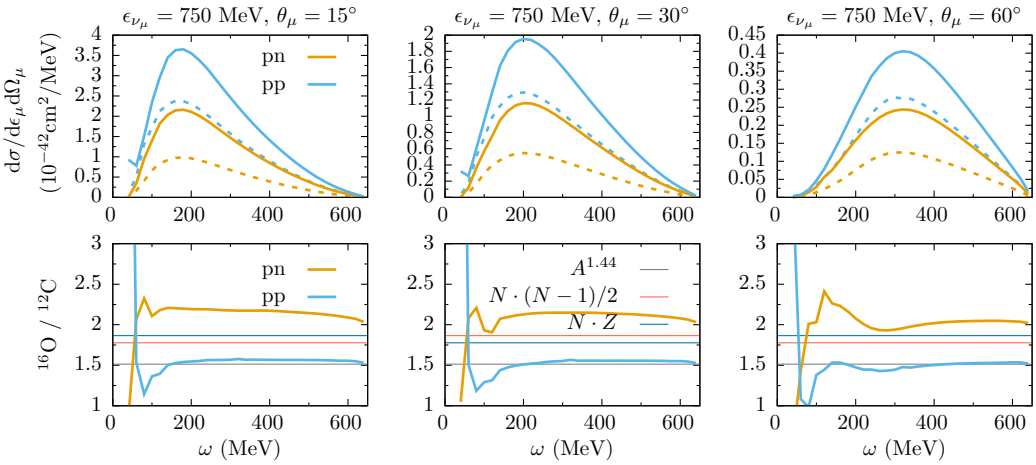

Figure 6.18: (top) The contribution of MEC pn- and pp-pair emission to the inclusive $A(\nu_\mu, \mu^-)$ cross section for ^{16}O (full line) and ^{12}C (dashed line). (bottom) The ratio of the cross sections ^{16}O/^{12}C.

6.7 Summary

The nuclear force, which binds the nucleons, is understood via the exchange of virtual mesons. In the IA, these residual interactions are neglected when an electroweak boson interacts with a nucleus. This shortcomming is met by extending the model with MECs. The vector currents included here, the seagull and pion-in-flight currents, are well-known from electron-scattering [1,28–30].

For the inclusion of the axial current, we opted for the approach of [30]. This currents fits most naturally in the presented model. This axial two-body current is constrained by the two-nucleon version of the PCAC relation, in a similar way as the vector two-body currents fulfill the two-body CVC relation. Two other axial two-body currents were compared as well.

In general, the inclusion of MECs in double differential cross section calculations of electron and neutrino scattering interactions yields relatively small effects, because a lot of the effects tend to cancel each other. The inclusion of seagull and pion-in-flight currents in electron scattering interactions results in a small increase of the $1p1h$ channel and the $2p2h$ channel shows up as a broad background. For neutrino scattering calculations, the combined effect of the MECs on the $1p1h$ channel is negligible. In the $2N$ knockout channel, a small background is visible, extending into the dip region. In this dip region, the experimental data is underpredicted by the IA, and the small contribution of the MECs partly accounts for the missing strength.

The challenges related to the construction of the axial currents studied here will provide useful information for further development of the model, e.g. in the construction of the Δ-currents.

References

[1] I. Towner, Phys. Rept. **155**, 263 (1987).

[2] M. Chemtob and M. Rho, Nucl. Phys. **A163**, 1 (1971).

[3] D. Riska and G. Brown, Phys. Lett. **B38**, 193 (1972).

[4] K. Kubodera, J. Delorme, and M. Rho, Phys. Rev. Lett. **40**, 755 (1978).

[5] E. Ivanov and E. Truhlik, Nucl. Phys. **A316**, 437 (1979).

[6] J. Van Orden and T. Donnelly, Ann. Phys. **131**, 451 (1981).

[7] M. Kohno and N. Ohtsuka, Phys. Lett. **B98**, 335 (1981).

[8] W. Alberico, M. Ericson, and A. Molinari, Ann. Phys. **154**, 356 (1984).

[9] M. Dekker, P. Brussaard, and J. Tjon, Phys. Lett. **B266**, 249 (1991).

[10] A. De Pace, M. Nardi, W. Alberico, *et al.* Nucl. Phys. **A726**, 303 (2003).

[11] C. Giusti and F. D. Pacati, Phys. Rev. **C67**, 044601 (2003).

[12] M. Anguiano, G. Co', A. Lallena, *et al.* Ann. Phys. **296**, 235 (2002).

[13] M. Anguiano, G. Co', and A. M. Lallena, J. Phys. **G29**, 1119 (2003).

[14] O. Benhar, A. Lovato, and N. Rocco, Phys. Rev. **C92**, 024602 (2015).

[15] N. Rocco, A. Lovato, and O. Benhar, Phys. Rev. Lett. **116**, 192501 (2016).

[16] Y. Umino and J. Udias, Phys. Rev. **C52**, 3399 (1995).

[17] M. Martini, M. Ericson, G. Chanfray, *et al.* Phys. Rev. **C80**, 065501 (2009).

[18] J. Nieves, I. Ruiz Simo, and M. Vicente Vacas, Phys. Rev. **C83**, 045501 (2011).

[19] J. Amaro, M. Barbaro, J. Caballero, *et al.* Phys. Lett. **B696**, 151 (2011).

[20] I. Ruiz Simo, C. Albertus, J. Amaro, *et al.* Phys. Rev. **D90**, 033012 (2014).

[21] I. Ruiz Simo, C. Albertus, J. Amaro, *et al.* Phys. Rev. **D90**, 053010 (2014).

[22] I. Ruiz Simo, J. Amaro, M. Barbaro, *et al.* (2016), arXiv:1604.08426.

[23] I. Ruiz Simo, J. Amaro, M. Barbaro, *et al.* Phys. Lett. **B762**, 124 (2016).

[24] G. Megias, T. Donnelly, O. Moreno, *et al.* Phys. Rev. **D91**, 073004 (2015).

[25] G. D. Megias, J. E. Amaro, M. B. Barbaro, *et al.* Phys. Rev. **D94**, 093004 (2016).

[26] A. Lovato, S. Gandolfi, R. Butler, *et al.* Phys. Rev. Lett. **111**, 092501 (2013).

[27] A. Lovato, S. Gandolfi, J. Carlson, *et al.* Phys. Rev. **C91**, 062501 (2015).

[28] D. Riska, Phys. Rept. **181**, 207 (1989).

[29] J. Mathiot, Phys. Rept. **173**, 63 (1989).

[30] I. Towner, Nucl. Phys. **A542**, 631 (1992).

[31] S. Nakamura, T. Sato, S. Ando, *et al.* Nucl. Phys. **A707**, 561 (2002).

[32] G. Shen, L. Marcucci, J. Carlson, *et al.* Phys. Rev. **C86**, 035503 (2012).

[33] E. Hernandez, J. Nieves, and M. Valverde, Phys. Rev. **D76**, 033005 (2007).

[34] T. Ericson and W. Weise, *Pions and nuclei* (1988).

[35] I. Ruiz Simo, C. Albertus, J. Amaro, *et al.* (2014), arXiv:1405.4280v1.

[36] J. Amaro, A. Lallena, and G. Co, Nucl. Phys. **A578**, 365 (1994).

[37] P. Barreau, M. Bernheim, J. Duclos, *et al.* Nucl. Phys. **A402**, 515 (1983).

[38] J. Jourdan, Nucl. Phys. **A603**, 117 (1996).
[39] W. Alberico, T. Donnelly, and A. Molinari, Nucl. Phys. **A512**, 541 (1990).
[40] Y. Umino, J. Udias, and P. Mulders, Phys. Rev. Lett. **74**, 4993 (1995).
[41] J. Amaro, M. Barbaro, J. Caballero, *et al.* Phys. Rept. **368**, 317 (2002).
[42] J. Ryckebusch, M. Vanderhaeghen, L. Machenil, *et al.* Nucl. Phys. **A568**, 828 (1994).
[43] S. Janssen, J. Ryckebusch, W. Van Nespen, *et al.* Nucl. Phys. **A672**, 285 (2000).
[44] J. Amaro, C. Maieron, M. Barbaro, *et al.* Phys. Rev. **C82**, 044601 (2010).
[45] S. Galster, H. Klein, J. Moritz, *et al.* Nucl. Phys. **B32**, 221 (1971).
[46] R. Bradford, A. Bodek, H. Budd, *et al.* Nucl. Phys. Proc. Suppl. **159**, 127 (2006).
[47] M. Vanhalst, W. Cosyn, and J. Ryckebusch, Phys. Rev. **C84**, 031302 (2011).

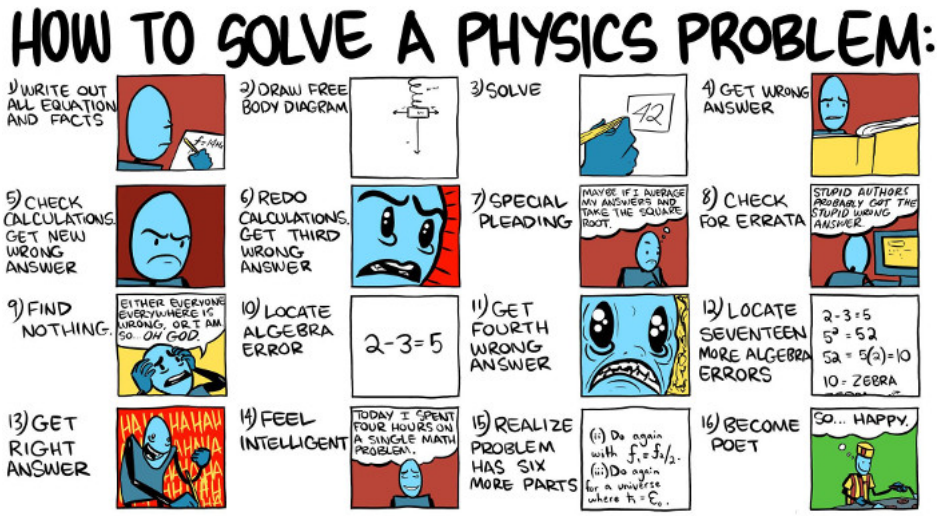

Chapter 7

Summary and outlook

The confirmation of neutrino-oscillations around the year 2000 initiated a whole range of experiments aiming at the precise determination of the neutrino-oscillation parameters. One of the major sources of systematic uncertainty in these studies is related to the neutrino scattering cross section. A precise neutrino-nucleus scattering model is necessary for an accurate interpretation of the data and hence for the extraction of neutrino-oscillation parameters.

From a theoretical point of view, accelerator-based neutrino experiments offer an interesting opportunity to study properties of the nucleus related to the axial structure. The low interaction probability of neutrinos, compared to that of electrons or hadrons, necessitates a high luminosity neutrino beam and large detectors. Furthermore, the latest technological developments in detector technology make the detection of nucleons in the final state possible, with a 4π coverage.

In this thesis, we present a model that meets the questions posed by these experiments. The model describes $1N$ and $2N$ knockout reactions, induced by a CC neutrino-scattering interaction. To assess the reliability of the model, we presented several electron-nucleus scattering calculations, for which a lot of exclusive and inclusive data is available.

The starting point of the development was an existing model for photo- and electron-induced interactions, accounting for two-body currents in $1N$ and $2N$ knockout reactions [1–3]. This model was extended to the weak sector, accounting for CC neutrino-scattering interactions. Nuclear targets are described using an IPM picture, the bound-state wave functions are

obtained via a HF calculation using an effective Skyrme-type nucleon-nucleon interaction. These wave-functions are used to generate the MF potential of the nucleus, and the same potential is used for the calculation of the nucleons in the continuum. This way distortion effects of the residual nucleus on the emitted nucleons are accounted for, and the nucleons are represented by realistic wave functions instead of plane waves. The inherently nonrelativistic nature of the nuclear dynamics is accounted for in an effective way, significantly improving the description of electron-scattering data at larger momentum transfers.

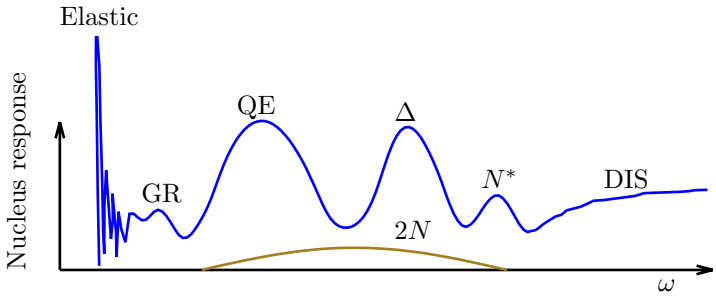

Figure 7.1: Schematic response of the nucleus to a leptonic probe.

In Fig. 7.1, the response of the nucleus to a leptonic probe is presented schematically. It demonstrates that several interaction mechanisms play a role in cross section calculations. Only the QE and $2N$ knockout channel were the topic of this work. The predictions presented below can be compared with this graphical representation.

In an IPM picture, the nucleons move independently of each other in the potential well generated by the nucleons themselves, and the probability of finding two nucleons at the same location is finite. Due to the short-range repulsive part of the nuclear force, this probability should equal zero. To tackle this limitation, SRCs are introduced as effective two-body currents. These correlations induce a high-momentum tail in the single-nucleon momentum distribution, and they affect $1N$ and $2N$ knockout cross sections.

The simplest way to describe the coupling between a boson and the nuclear current is the IA: the A-body nuclear current is approximated as a sum of A one-body currents. The IA is then extended with actual two-body MECs to account for the coupling of the boson to a pair of nucleons exchanging a pion, the carrier of the nuclear force. Only seagull and pion-in-flight currents, and the corresponding axial currents, are taken into account.

The exclusive $2N$ knockout calculations shown in this work display some interesting properties. In Fig. 7.2, exclusive $2N$ knockout results are presented, accounting for SRCs and MECs. The behavior is very similar for both types of two-body currents and can be related to the initial c.o.m. momentum P_{12} of the pair in the nucleus, as displayed by the red dots. The exclusive $2N$ knockout cross section is dominated by pairs with low c.o.m. momentum. For the displayed kinematics, the strength of the SRCs is roughly a factor 4 larger than the MEC contribution, however, the relative strength of the knockout of SRC pairs to MEC pairs depends a lot on the kinematics of the interaction. The kinematic situation shown here displays a clear back-to-back $2N$ emission signature, which is reminiscent of the 'hammer events' seen by the ArgoNeuT collaboration [4].

Fig. 7.3 shows the prediction of an inclusive double differential $^{12}\mathrm{C}(\nu_\mu, \mu^-)$ cross section.

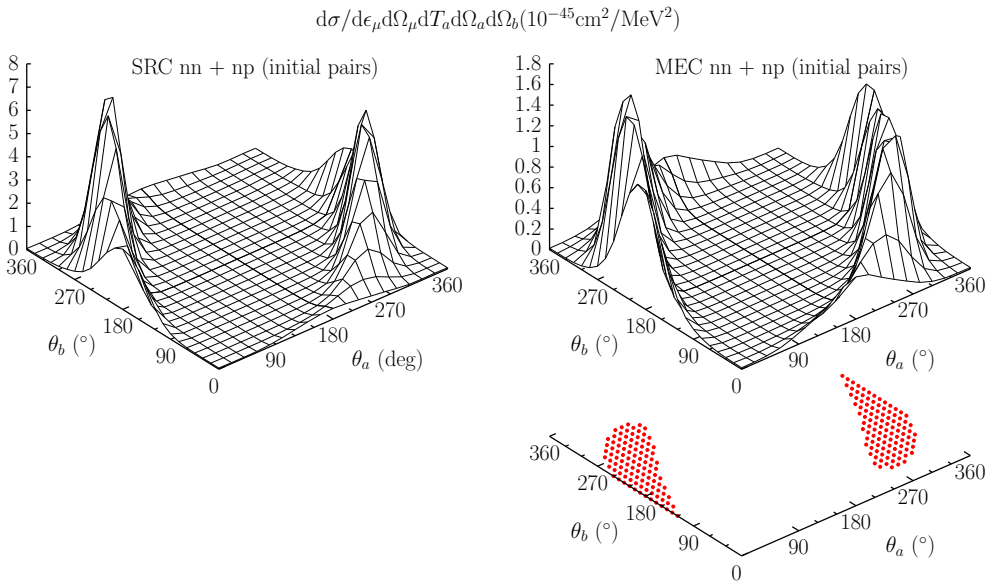

Figure 7.2: The $^{12}\mathrm{C}(\nu_\mu, \mu^- N_a N_b)$ cross section (N_a = p, N_b = p′, n) at $\epsilon_{\nu_\mu} = 750$ MeV, $\epsilon_\mu = 550$ MeV, $\theta_\mu = 15^\circ$ and $T_\mathrm{p} = 50$ MeV for in-plane kinematics ($q = 268$ MeV/c, $x_B = 0.08$). θ_a and θ_b are the nucleon emission angles in the lepton scattering plane. The bottom panel shows the (θ_a, θ_b) region of the nucleon pair with initial c.o.m. momentum $P_{12} < 300$ MeV/c.

The incoming energy was chosen to be 750 MeV, roughly equal to the peak of the MiniBooNE and T2K flux, and results three different scattering angles are shown. The results displayed in the panels row should be compared with the schematic representation of the response shown above, Fig. 7.1. The $2p2h$ contribution to the inclusive cross section (or QE-like cross section) appears as a broad background, ranging from the $2N$ knockout threshold into the dip region. The difference between the full $1p1h$ calculations (IA+SRC+MEC) and the IA results is very small.

The middle panels of Fig. 7.3 show the details of the influence of the two-body currents on the $1p1h$ results. It is interesting to see that MECs have the biggest effect at small scattering angles, increasing the cross section, while the influence of the SRCs is largest for $\theta_\mu = 60^\circ$, where it results in a decrease. The overall effect on the inclusive cross section, however, is very small, which is partly because the effects tend to cancel out each other.

The $2p2h$ contribution to the inclusive double differential cross section is shown in the bottom panels of Fig. 7.3, including interference between the SRC and MEC contributions. The contribution of the SRC channel is a factor 3 to 5 bigger than the contribution of the MECs. Remind that the Δ currents are not included. The figure suggests that the total $2p2h$ strength equals the sum of the SRC and MEC contributions, however a small destructive interference is present between both types of two-body currents. In the dip region, experimental data is underpredicted by calculations in the IA, and the $2N$ knockout contribution of SRC and MEC pairs partially accounts for the missing strength in this region.

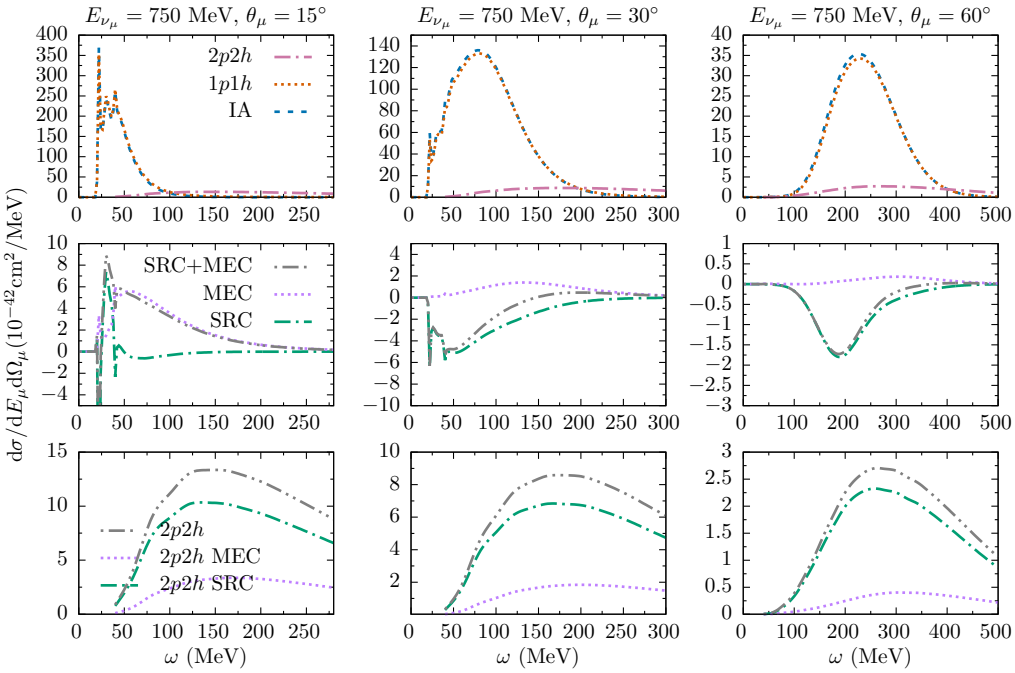

Figure 7.3: The computed ω dependence of the $^{12}\mathrm{C}(\nu_\mu, \mu^-)$ cross section for $\epsilon_{\nu_\mu} = 750$ MeV and three different values for the lepton scattering angle θ_μ. The top panels show the combined $1p1h$ and $2p2h$ cross sections. The middle panels show the correction of the two-body currents to the $1p1h$ cross section and the bottom panels show the $2p2h$ part of the cross section.

Conclusions SRCs The influence of SRCs on neutrino-induced $1N$ and $2N$ differential cross sections was studied, using the central correlation function by Gearhart and Dickhoff and the tensor and spin-isospin correlation functions of S. Pieper *et al.* SRCs reduce inclusive $1N$ knockout cross sections slightly, and the inclusive $2N$ knockout strength appears as a broad background to the QE peak. This is reminiscent of the schematic representation of the nuclear response to a leptonic probe in Fig. 7.1.

The relative strengths of the three components of the SRCs, i.e. the central, tensor and spin-isospin correlations, were systematically compared. Many of the features can be explained with the properties of the correlation functions in momentum space and kinematic arguments. As the tensor correlation function in momentum space dominates for intermediate momenta, the tensor contribution to the $2N$ knockout cross section is strongest when nucleon pairs with intermediate relative momenta are probed. When nucleon pairs with large relative momenta are probed, e.g. at large energy transfers, the central correlations start to dominate.

Another interesting property is that the ratio of the inclusive $2N$ knockout cross section of SRC pairs from $^{16}\mathrm{O}$ to $^{12}\mathrm{C}$ seems to be following the scaling relation $A^{1.44}$ proposed in [5]. The scaling relation was obtained by counting the number of pairs in a relative $l = 0$ state. This shows that the $2N$ knockout of SRC pairs is dominated by close-proximity pairs and allows one to extrapolate the $2N$ knockout contribution of SRCs pairs to other nuclei.

Conclusions MECs To account for MECs, two types of vector two-body currents were included: the seagull and the pion-in-flight currents. Both types consider a single pion-exchange. In the vector channel, these currents are well-determined and they satisfy the CVC relation. Even after the introduction of form factors, the vector currents can be considered model independent to some extent, because they involve no parameters not already present in the model, or in the pion-exchange potential that was used to determine the currents.

The inclusion of the axial counterparts of these seagull and pion-in-flight currents is less straightforward. We opted for the approach outlined in [6]. This way, diagrams where a ρ and a π are exchanged are included as well, and the currents satisfy the two-nucleon version of the PCAC relation.

The predictions were compared with other axial currents found in literature. The substantial differences in the predictions between the different expressions show that the way the currents are constrained are not unambiguous. This information will guide future implementations of other two-body currents, such as the Δ-currents discussed below.

Comparison with neutrino data In this work, we have shown results at several kinematic settings which are relevant for experimental studies, by using the neutrino energy at the peak of the neutrino flux. However, we never made the comparison with neutrino data so far. As explained in the introduction, the neutrinos produced by accelerator-based experiments are not mono-energetic, they come in a wide range of energies, see Fig. 1.9. To compare with data, the differential cross sections have to be integrated over the neutrino flux, i.e.

$$\left\langle \frac{\mathrm{d}\sigma}{\mathrm{d}\epsilon_\mu \mathrm{d}\cos\Omega_\mu} \right\rangle = \frac{1}{\int \mathrm{d}\epsilon_{\nu_\mu} \Phi(\epsilon_{\nu_\mu})} \int \mathrm{d}\epsilon_{\nu_\mu} \Phi(\epsilon_{\nu_\mu}) \left[\frac{\mathrm{d}\sigma}{\mathrm{d}\epsilon_\mu \mathrm{d}\cos\Omega_\mu} \right]_{\epsilon_{\nu_\mu}} . \tag{7.1}$$

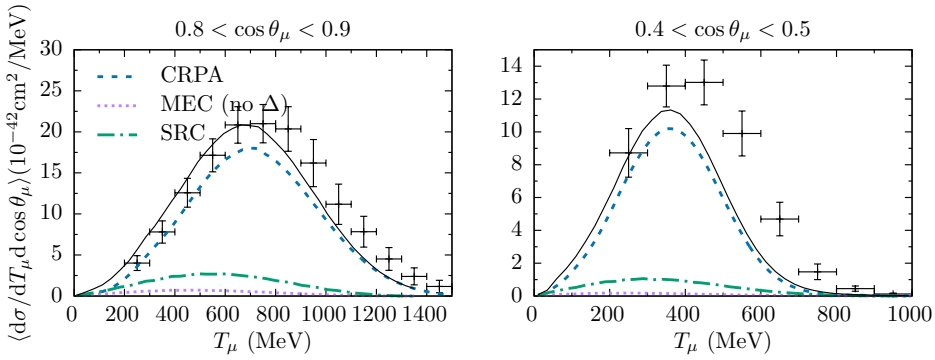

Figure 7.4: MiniBooNE CCQE-like flux-folded double differential cross sections per target neutron for $^{12}\mathrm{C}(\nu_\mu, \mu^-)$. The solid line is the sum of the three contributions. Data is from Ref. [7], the experimental error bars represent the shape uncertainties, flux uncertainties are not included.

In Fig. 7.4, a prediction for the strength of the MiniBooNE flux-folded differential CCQE-like cross section is shown as a function of the muon kinetic energy T_μ, and compared with data. We have chosen to use the CRPA results to account for $1N$ knockout. They are taken from Refs. [8,9] and account for long-range correlations, in the same HF framework as presented in this work.

For forward scattering, the double differential CRPA cross section is slightly larger than the corresponding IA strength, while for $\cos\theta_\mu < 0.9$ the CRPA predictions are smaller compared to the IA. The CRPA results were shown to reproduce the MiniBooNE data well in the most forward angular bin $0.9 < \cos\theta_\mu < 1.0$. For more backward scattering, the CRPA results underestimated the data, as multinucleon emission is not included.

The SRC and MEC results account for the $2N$ knockout contribution to the inclusive cross section, and are expected to partially account for the missing strength of the CRPA prediction. The solid black line is the sum of the contributions. Interference between the SRC and MEC contribution is not included in the black line, but this effect is small, as can be inferred from Fig. 7.3.

Due to the heavy computational cost, the flux-folding was done in steps of 100 MeV, while the integration over the bin in $\cos\theta_\mu$ was done in three steps. Although this integration was done with a rather crude mesh, we do not expect major differences when using a more detailed calculation.

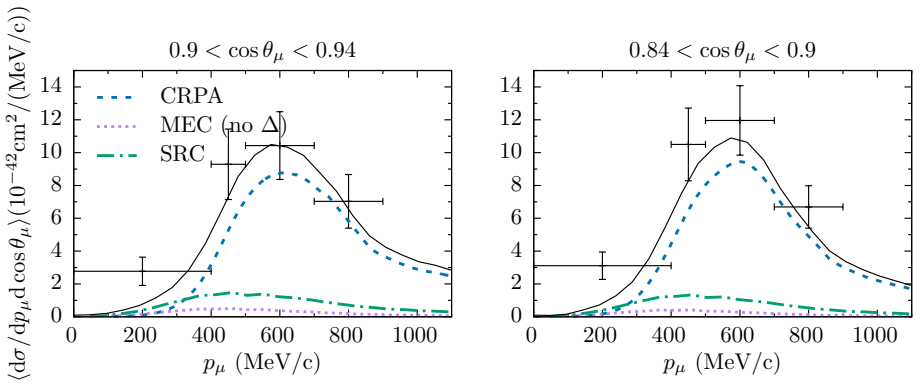

(a) Inclusive T2K data from Ref. [10].

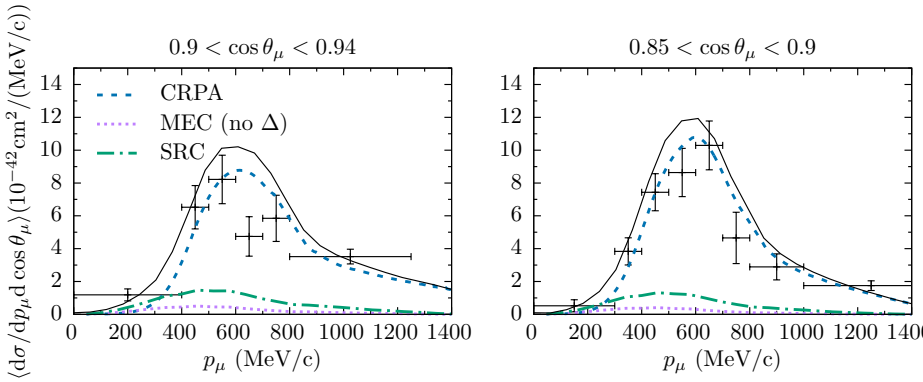

(b) CC0π T2K data from Ref. [11].

Figure 7.5: T2K flux-folded double differential cross sections per target nucleon for $^{12}C(\nu_\mu, \mu^-)$. The solid line is the sum of the three contributions. The experimental error bars represent the shape uncertainties, flux uncertainties are not included.

The MiniBooNE CCQE-like data set is defined as the processes where one muon and no pions are observed in the final state. Yet, in the analysis, the CCQE-like data has partly

been corrected for Δ-currents by subtracting pion-less Δ decays from the data [12].

The CRPA approach combined with $2N$ knockout of MEC and SRC pairs reproduces the strength and shape of the forward bin in Fig. 7.4 very well, however, the predictions and data appear to be shifted over 50 MeV. The agreement in the bin with more backward lepton scattering is less satisfactory, it appears that a large fraction of the measured strength is not accounted for by the calculations.

In Fig. 7.5, the corresponding double differential results for two T2K angular bins are shown as a function of the muon momentum p_μ. In contrast with the MiniBooNE results, only two steps were used for the averaging over the $\cos\theta_\mu$ bins, the limiting values. Again, we expect that no major differences will be obtained when using a more precise integration mesh. In the top panels, the results are compared with the inclusive data, i.e. processes with pions in the final state are included. In the bottom panels, the results are compared with T2K CC0π data, defined as the processes where no pions are observed in the final state. This data was not corrected for the Δ-current contribution, and they should be included in the $2N$ knockout channel for a complete description of the data.

The theoretical predictions already reproduce the inclusive data in Fig. 7.5a rather well, while extra strength from Δ-currents and pion production still has to be included for a complete description of the data. If the Δ-current and pion production contributions would be of the same size as those of Martini *et al.* [13], Megias *et al.* [14] or GiBUU [15], some overestimation is expected.

The prediction of the CC0π data in Fig. 7.5b, already appears to be on the high side, and the Δ-current contribution has not yet been included. The $1p1h$ calculations in the CRPA approach already overestimate part of the data, hence little room is left to add the necessary $2p2h$ channel without overpredicting the data. A satisfactory description of the data is not strictly ruled out since all possible interference effects between the contributions should be included, and the flux normalization error of the data should be accounted for. However, the prediction will undoubtedly be on the high side.

The results of the flux-folded double differential cross sections are in line with the unfolded cross sections displayed in Fig. 7.3. The strength of the SRCs is a factor 3 to 5 larger compared to the MECs.

What about double counting? The SRCs are constructed in a way that the operator structure of the correlations mimics the behavior of the nucleon-nucleon potential. The one-pion exchange potential for example, contains a central and a tensor component. The seagull and pion-in-flight MEC currents, on the other hand, are actual implementations of two nucleons exchanging a single pion. How can we be sure that we didn't include contributions twice?

MECs correct the way the bosons couple to the nuclear current, hence they can be considered as a correction to the IA. SRCs were included to correct the IPM behavior of the nuclear system. The coupling strength between bosons and SRC pairs is the same as the coupling to a single nucleon.

The SRCs are a manifestation of the short- and intermediate-range properties of the nucleon-nucleon force. The MECs, on the contrary, consider diagrams of pion-range, which is associated with the long-range attractive part of the nucleon-nucleon force. The currents with a ρ and a π exchange, diagrams (b-d) in Fig. 6.5, seem to violate this distinction, however,

the pion propagator in these axial currents suggests they are of pion-range as well. With these arguments, we feel confident that our model is free of sizeable double-counting issues.

How to include delta currents? The major missing ingredient in this model are Δ-currents or isobar currents. These are two-body currents that belong to the group of MECs where the nucleon that interacts with the incoming boson is excited to a virtual Δ before it exchanges a meson with a second nucleon. The Δ-currents, where the exchanged meson is a π, have been shown to provide a large contribution of the $2N$ knockout strength for electron scattering interactions [1–3].

Extending these calculations to neutrino-scattering interactions is not a trivial task. Our study of the axial MEC currents has shown that the introduction of form factors and the way the current is constrained via PCAC leads to different results. A promising way to continue this work is to start from the axial-vector isobar current derived in [16]. The current derived in [16] fulfills the two-nucleon version of the PCAC relation, with isobar intermediate states. This current fits consistently in the scheme used for the determination of the axial current 'axi' used in our calculations. Other approaches to include Δ-currents, however, should also be explored.

And exclusive data? In the near future, more exclusive cross section data of neutrino scattering will become available. One of the main assets of the model presented in this work is that it can calculate exclusive and inclusive cross sections in a consistent framework. However, to make comparison with exclusive data, where nucleons in the final state are detected, one needs a more detailed model for FSIs.

The distortion effects on the nuclear wave functions in the continuum fall short for these exclusive predictions. An advanced FSI model should account for rescattering processes between the emitted nucleon and the individual nucleons in the residual nucleus, reabsorption effects etc. One could account for these effects via a Glauber multiple scattering calculation or by using an optical potential. However, it could also be interesting to interface the model presented here with a semi-classical cascade model as used in neutrino event generators such as NuWro [17].

Mono-energetic neutrinos? Considering experimental measurements, we mention the proposal to use kaon decay-at-rest neutrinos for the construction of a mono-energetic neutrino beam [18] These 236 MeV neutrinos would offer a unique opportunity to measure cross sections at low energies, where the model presented here excels. The combination of this mono-energetic beam with the latest detectors that are capable of detecting nucleons in the final state would provide an opportunity to study exclusive cross sections. The knowledge of the initial neutrino energy significantly decreases the modeling efforts. Further, nuclear effects are not *averaged out* by the neutrino flux, presenting interesting information from a theoretical point of view.

References

[1] J. Ryckebusch, M. Vanderhaeghen, L. Machenil, *et al.* Nucl. Phys. **A568**, 828 (1994).

[2] J. Ryckebusch, V. Van der Sluys, K. Heyde, *et al.* Nucl. Phys. **A624**, 581 (1997).

[3] S. Janssen, J. Ryckebusch, W. Van Nespen, *et al.* Nucl. Phys. **A672**, 285 (2000).

[4] ArgoNeuT collaboration, R. Acciarri *et al.* Phys. Rev. **D90**, 012008 (2014).

[5] M. Vanhalst, W. Cosyn, and J. Ryckebusch, Phys. Rev. **C84**, 031302 (2011).

[6] I. Towner, Nucl. Phys. **A542**, 631 (1992).

[7] MiniBooNE collaboration, A. Aguilar-Arevalo *et al.* Phys. Rev. **D81**, 092005 (2010).

[8] V. Pandey, N. Jachowicz, M. Martini, *et al.* Phys. Rev. **C94**, 054609 (2016).

[9] V. Pandey, *Quasielastic electroweak scattering cross sections in kinematics relevant for accelerator-based neutrino-oscillation experiments*, PhD thesis (Ghent University, 2016).

[10] T2K collaboration, K. Abe *et al.* Phys. Rev. **D87**, 092003 (2013).

[11] T2K collaboration, K. Abe *et al.* Phys. Rev. **D93**, 112012 (2016).

[12] T. Katori, private communication, 2017.

[13] M. Martini and M. Ericson, Phys. Rev. **C90**, 025501 (2014).

[14] G. D. Megias, J. E. Amaro, M. B. Barbaro, *et al.* Phys. Rev. **D94**, 093004 (2016).

[15] K. Gallmeister, U. Mosel, and J. Weil, Phys. Rev. **C94**, 035502 (2016).

[16] I. Towner, Phys. Rept. **155**, 263 (1987).

[17] J. Sobczyk, Phys. Rev. **C86**, 015504 (2012).

[18] J. Spitz, Phys. Rev. **D85**, 093020 (2012).

II Supplementary material

Appendix A

Notations and conventions

A.1 Conventions

Throughout this work, following conventions are used:

- The four-momenta of leptons are denoted by k and the four-momenta of hadrons by P. Energy and three-momentum are denoted as

$$k = (\epsilon, \boldsymbol{k}), \qquad P = (E, \boldsymbol{p}). \tag{A.1}$$

- Protons and neutrons are written in plain roman (p and n) and particles in italic (p), to be able to distinguish protons and particles $\mathrm{p} \leftrightarrow p$
- We work with natural units

$$\hbar = 1, \qquad c = 1, \tag{A.2}$$

  further, e is the absolute value of the electric charge $|e|$.

- $\epsilon_{\alpha\beta\gamma\delta}$ is the completely antisymmetrized tensor, $+1$ for even permutations and -1 for odd permutations of $(0, 1, 2, 3)$ and 0 when two or more indices are equal and

$$\epsilon_{\alpha\beta\gamma\delta} = -\epsilon^{\alpha\beta\gamma\delta}. \tag{A.3}$$

- The spherical basis vectors are defined through

$$\boldsymbol{e}_{\pm 1} = \mp \frac{1}{\sqrt{2}} \left(\boldsymbol{e}_x \pm i \boldsymbol{e}_y \right), \qquad \boldsymbol{e}_0 = \boldsymbol{e}_z. \tag{A.4}$$

- All coupling of angular momenta happens with the conventions of De-Shalit and Talmi [1]. For all properties and useful formula concerning Racah algebra and tensor operators we refer to some standard works in nuclear physics [1–5]. For coupling of two angular momenta, Clebsch-Gordon coefficients and Wigner three-j symbols in the Condon-Shortley phase convention are used. They are related via ($\widehat{J} \equiv \sqrt{2J+1}$)

$$\langle j_1 \;\; m_1 \;\; j_2 \;\; m_2 \,|\, J \;\; M \rangle = (-1)^{-j_1+j_2-M} \widehat{J} \begin{pmatrix} j_1 & j_2 & J \\ m_1 & m_2 & -M \end{pmatrix} \tag{A.5}$$

$$\begin{pmatrix} j_1 & j_2 & J \\ m_1 & m_2 & M \end{pmatrix} = \frac{(-1)^{j_1-j_2-M}}{\widehat{J}} \langle j_1 \;\; m_1 \;\; j_2 \;\; m_2 \,|\, J \;\; -M \rangle. \tag{A.6}$$

Six-j symbols are used for coupling of three angular momenta

$$\begin{Bmatrix} j_1 & j_2 & j_3 \\ j_4 & j_5 & j_6 \end{Bmatrix}. \tag{A.7}$$

Nine-j symbols are used for coupling of four angular momenta

$$\begin{Bmatrix} j_1 & j_2 & j_3 \\ j_4 & j_5 & j_6 \\ j_7 & j_8 & j_9 \end{Bmatrix}. \tag{A.8}$$

- For the spherical harmonics, the Condon-Shortley phase convention is used

$$Y^*_{LM_L}(\Omega) = (-1)^{M_L} Y_{L-M_L}(\Omega). \tag{A.9}$$

Coupling of a spherical harmonic and the spherical basis vector is defined as a vector spherical harmonic (coupling with spin 1)

$$\boldsymbol{\mathcal{Y}}^M_{J(L,1)}(\Omega) = \sum_{M_L,\lambda} \langle L \;\; M_L \;\; 1 \;\; \lambda \,|\, J \;\; M \rangle Y_{LM_L}(\Omega) \boldsymbol{e}_\lambda, \tag{A.10}$$

and coupling of a spherical harmonic with a spin state is called a spin spherical harmonic (coupling with spin 1/2)

$$\mathcal{Y}^m_{j(l,1/2)}(\Omega) = \sum_{m_l,m_s} \langle l \;\; m_l \;\; 1/2 \;\; m_s \,|\, j \;\; m \rangle Y_{lm_l}(\Omega) \chi_{m_s}. \tag{A.11}$$

- ls coupling is adopted in this work

$$|\, ljm \,\rangle = \sum_{m_l,m_s} \langle l \;\; m_l \;\; 1/2 \;\; m_s \,|\, j \;\; m \rangle Y_{lm_l}(\Omega) \chi_{m_s} \tag{A.12}$$

- The Rayleigh formula allows the expansion of the plane wave in a series of spherical harmonics, which is the basis ingredient of the partial wave expansion

$$e^{i\boldsymbol{r}\cdot\boldsymbol{q}} = \sqrt{4\pi} \sum_{J=0}^{\infty} i^J \widehat{J} j_J(qr) Y_{J0}(\Omega_r), \tag{A.13}$$

or in another form

$$e^{i\boldsymbol{r}\cdot\boldsymbol{q}} = 4\pi \sum_{JM} i^J j_J(qr) Y^*_{JM}(\Omega_r) Y_{JM}(\Omega_q). \tag{A.14}$$

- A property of Bessel functions and spherical harmonics which will be useful in this work [6]

$$\begin{aligned} \boldsymbol{\nabla}_{M_2} \left[j_{J_1}(qr) Y_{J_1 M_1}(\Omega) \right] = q \sum_{M_3,\eta=\pm1} & j_{J_1+\eta}(qr) Y_{J_1+\eta M_3}(\Omega) \frac{1}{\widehat{J_1+\eta}} \\ & \times \langle J_1 \;\; M_1 \;\; 1 \;\; M_2 \,|\, J_1+\eta \;\; M_3 \rangle \sqrt{J_1+\delta_{\eta,+1}}. \end{aligned} \tag{A.15}$$

- The product of spherical tensors is defined as

$$[T_{J_1} \otimes U_{J_2}]_{JM} = \sum_{M_1,M_2} \langle J_1 \;\; M_1 \;\; J_2 \;\; M_2 \,|\, J \;\; M \rangle \, T_{J_1,M_1} U_{J_2,M_2}, \tag{A.16}$$

  with the following useful property

$$T_J \cdot U_J = (-1)^J \, [T_J \otimes U_J]_{00} \, . \tag{A.17}$$

- The Wigner-Eckart theorem states that for each tensor operator $\widehat{\mathcal{O}}_{JM}$

$$\langle \, j_p m_p \,|\, \widehat{\mathcal{O}}_{JM} \,|\, j_h m_h \, \rangle = (-1)^{j_p - m_p} \begin{pmatrix} j_p & J & j_h \\ -m_p & M & m_h \end{pmatrix} \langle \, j_p \parallel \widehat{\mathcal{O}}_J \parallel j_h \, \rangle. \tag{A.18}$$

A.2 Gamma matrices and Dirac spinors

The Bjorken and Drell convention [7] was used throughout this work for the gamma matrices and Dirac spinors. The metric tensor used in this work reads

$$g_{\mu\nu} = g^{\mu\nu} = \begin{pmatrix} 1 & 0 & 0 & 0 \\ 0 & -1 & 0 & 0 \\ 0 & 0 & -1 & 0 \\ 0 & 0 & 0 & -1 \end{pmatrix}, \tag{A.19}$$

which commonly goes under the name of the time-like convention. The Pauli matrices are defined as

$$\sigma_x = \begin{pmatrix} 0 & 1 \\ 1 & 0 \end{pmatrix}, \qquad \sigma_y = \begin{pmatrix} 0 & -i \\ i & 0 \end{pmatrix}, \qquad \sigma_z = \begin{pmatrix} 1 & 0 \\ 0 & -1 \end{pmatrix}, \tag{A.20}$$

and the gamma matrices as follows

$$\gamma^0 = \begin{pmatrix} \mathbb{1} & 0 \\ 0 & -\mathbb{1} \end{pmatrix}, \qquad \gamma^i = \begin{pmatrix} 0 & \boldsymbol{\sigma}_i \\ -\boldsymbol{\sigma}_i & 0 \end{pmatrix}, \qquad \gamma^5 = \begin{pmatrix} 0 & \mathbb{1} \\ \mathbb{1} & 0 \end{pmatrix}. \tag{A.21}$$

Furthermore the gamma matrices satisfy

$$g^{\mu\nu} = \frac{1}{2}\{\gamma^\mu, \gamma^\nu\}, \qquad \sigma^{\mu\nu} = \frac{i}{2} \, [\gamma^\mu, \gamma^\nu] \, , \qquad \{\gamma^\mu, \gamma^5\} = 0, \tag{A.22}$$

where $\{\,,\}$ and $[\,,]$ refer to the anticommutator and commutator respectively. The Hermitian conjugates of the gamma matrices are fixed by these commutation relations

$$(\gamma^\mu)^\dagger = \gamma^0 \gamma^\mu \gamma^0, \qquad (\gamma^5)^\dagger = \gamma^5, \tag{A.23}$$

and they obey the following trace identities, which are useful in this work

$$\mathrm{Tr}\,(\gamma^\mu \gamma^\nu) = 4 g^{\mu\nu} \tag{A.24}$$

$$\mathrm{Tr}\,(\gamma^\mu \gamma^\nu \gamma^\rho \gamma^\sigma) = 4\,(g^{\mu\nu} g^{\rho\sigma} - g^{\mu\rho} g^{\nu\sigma} + g^{\mu\sigma} g^{\nu\rho}) \tag{A.25}$$

$$\mathrm{Tr}\left(\gamma^\mu \gamma^\nu \gamma^\rho \gamma^\sigma \gamma^5\right) = 4 i \epsilon^{\mu\nu\rho\sigma}. \tag{A.26}$$

The wave function of a free spin 1/2 particle is a solution of the Dirac equation

$$\left(\not{p} - m\right)\psi = \left(i\not{\partial} - m\right)\psi = 0, \tag{A.27}$$

where the shorthand notation $\not{p} = \gamma_\mu p^\mu$ has been introduced. The solution of this equation can be written as a product of a Dirac spinor and a plane wave

$$\psi(r,p) = \mathcal{A}\, u(p,s) \exp\left(-ir\cdot p\right), \tag{A.28}$$

with $\mathcal{A}$ a normalization constant. The Dirac spinors are defined as solutions of the Dirac equation ($\overline{u} = u^\dagger\gamma^0$)

$$\left(\not{p} - m\right) u(p,s) = 0, \tag{A.29}$$

$$\overline{u}(p,s)\left(\not{p} - m\right) = 0, \tag{A.30}$$

and given by

$$u(p,s) = \sqrt{\frac{E+m}{2m}} \begin{pmatrix} 1 \\ \frac{\boldsymbol{\sigma}\cdot\boldsymbol{p}}{E+m} \end{pmatrix} \chi_s, \tag{A.31}$$

where $E = \sqrt{p^2+m^2}$ and χ_s denotes the two-component spin state,

$$\chi_{+1/2} = \begin{pmatrix} 1 \\ 0 \end{pmatrix}, \qquad \chi_{-1/2} = \begin{pmatrix} 0 \\ 1 \end{pmatrix}. \tag{A.32}$$

For nucleons, we introduce ζ_t, the two-component isospin state

$$\zeta_{+1/2} = \begin{pmatrix} 1 \\ 0 \end{pmatrix}, \qquad \zeta_{-1/2} = \begin{pmatrix} 0 \\ 1 \end{pmatrix}. \tag{A.33}$$

This allows us to write the Dirac equation for a nucleon doublet as

$$\left(\not{p} - m_N\right)\Psi = \left(i\not{\partial} - m_N\right)\Psi = 0, \tag{A.34}$$

where the nucleon doublet is written as

$$\Psi = \begin{pmatrix} \psi_{\mathrm{p}} \\ \psi_{\mathrm{n}} \end{pmatrix}, \tag{A.35}$$

with

$$\psi_{\mathrm{p}}(r,p) = \sqrt{\frac{E_N+m_N}{2m_N}} \begin{pmatrix} 1 \\ \frac{\boldsymbol{\sigma}\cdot\boldsymbol{p}_N}{E_N+m_N} \end{pmatrix} \exp\left(-ip\cdot x\right) \chi_s\zeta_{+1/2}, \tag{A.36}$$

$$\psi_{\mathrm{n}}(r,p) = \sqrt{\frac{E_N+m_N}{2m_N}} \begin{pmatrix} 1 \\ \frac{\boldsymbol{\sigma}\cdot\boldsymbol{p}_N}{E_N+m_N} \end{pmatrix} \exp\left(-ip\cdot x\right) \chi_s\zeta_{-1/2}. \tag{A.37}$$

The Dirac adjoint of field operator Ψ is defined as

$$\overline{\Psi} = \Psi^\dagger\gamma^0, \tag{A.38}$$

where $\Psi^\dagger$ is the Hermitian adjoint, and analog for $\overline{\psi}$ etc. The spin states up and down, can also be written using the $|\, s, m_s \,\rangle$ notation, or denoted with arrows

$$|\uparrow\rangle = \chi_{+1/2} = |\, 1/2, +1/2 \,\rangle = \begin{pmatrix} 1 \\ 0 \end{pmatrix}, \tag{A.39}$$

$$|\downarrow\rangle = \chi_{-1/2} = |\,1/2,-1/2\,\rangle = \begin{pmatrix}0\\1\end{pmatrix}. \tag{A.40}$$

The Dirac spinors are normalized as

$$\overline{u}(p,s)u(p,s) = 1, \tag{A.41}$$

or

$$u^{\dagger}(p,s)u(p,s) = \frac{E}{m}, \tag{A.42}$$

and the energy projection operators are given by

$$\sum_{s} u(p,s)\overline{u}(p,s) = \frac{\not{p}+m}{2m}. \tag{A.43}$$

Using these conventions, a wave function normalized to unit in a box of volume V is written as

$$\psi(r,p) = \sqrt{\frac{m}{EV}}u(p,s)\exp\left(-ip\cdot x\right) \tag{A.44}$$

The differential cross section for scattering of two, on-shell, massive, Dirac particles is given by

$$\mathrm{d}\sigma = \frac{m_1}{E_1}\frac{m_2}{E_2}\left(\prod_f \frac{m_f}{E_f}\frac{\mathrm{d}\boldsymbol{k}_f}{(2\pi)^3}\right)(2\pi)^4\delta^{(4)}\left(k_1+k_2-\sum_f k_f\right)\overline{\sum_{if}}\left|\mathcal{M}_{fi}\right|^2, \tag{A.45}$$

where particles 1 and 2 are initial state particles and f refers to all particles in the final state. For spinless particles and photons, the factors m/E should be replaced with $1/2E$. The summation sign $\overline{\sum}_{if}$ stands for a correct averaging and summation over initial and final states.

A.3 Second quantization

In second quantization, particle states with quantum numbers j_p and m_p are defined as

$$|\,p(j_p m_p)\,\rangle = \widehat{c}^{\dagger}_{j_p,m_p}\,|\,0\,\rangle, \tag{A.46}$$

where $|\,0\,\rangle$ denotes the vacuum. Hole states are defined as

$$|\,h^{-1}(j_h m_h)\,\rangle = \widetilde{c}^{\dagger}_{j_h,m_h}\,|\,0\,\rangle = (-1)^{j_h+m_h}\widehat{c}_{j_h,-m_h}\,|\,0\,\rangle, \tag{A.47}$$

denoting the fact that taking away a nucleon from a shell $|\,j_h,-m_h\,\rangle$, leaves the nucleus in a state with quantum numbers (j_h,m_h). A general particle-hole state is written as

$$|\,ph^{-1}\,\rangle = |\,j_p m_p, j_h^{-1} m_h\,\rangle = \widetilde{c}_{j_h,m_h}\widehat{c}^{\dagger}_{j_p,m_p}\,|\,0\,\rangle, \tag{A.48}$$

in an uncoupled state, or

$$|\,ph^{-1};JM\,\rangle = \sum_{m_p,m_h}\langle j_p\ \ m_p\ \ j_h\ \ m_h\,|\,J\ \ M\rangle\widetilde{c}_{j_h,m_h}\widehat{c}^{\dagger}_{j_p,m_p}\,|\,0\,\rangle, \tag{A.49}$$

with coupled angular momenta.

A.4 Isospin operators

The numerous appearances of isospin operators necessitates a succinct discussion of the isospin notation. The books with the most clear description on this topic are [8–10]. We follow the conventions given in the appendix of Ericson and Weise [9]. The proton and neutron are defined as two particle states of an isospin doublet in $SU(2)$

$$|\,\mathrm{p}\,\rangle = \zeta_{+1/2} = |\,1/2, +1/2\,\rangle = \begin{pmatrix} 1 \\ 0 \end{pmatrix}, \tag{A.50}$$

$$|\,\mathrm{n}\,\rangle = \zeta_{-1/2} = |\,1/2, -1/2\,\rangle = \begin{pmatrix} 0 \\ 1 \end{pmatrix}, \tag{A.51}$$

where the $|\,t, m_t\,\rangle$ notation has been introduced. The isospin matrices are defined as (note that these are exactly the same as the Pauli matrices)

$$\tau_x = \begin{pmatrix} 0 & 1 \\ 1 & 0 \end{pmatrix}, \qquad \tau_y = \begin{pmatrix} 0 & -i \\ i & 0 \end{pmatrix}, \qquad \tau_z = \begin{pmatrix} 1 & 0 \\ 0 & -1 \end{pmatrix}, \tag{A.52}$$

and form the isospin vector $\boldsymbol{\tau}$. The isospin raising and lowering operators are defined as

$$\tau_+ = \frac{1}{2}\left(\tau_x + i\tau_y\right) = \begin{pmatrix} 0 & 1 \\ 0 & 0 \end{pmatrix}, \qquad \tau_- = \frac{1}{2}\left(\tau_x - i\tau_y\right) = \begin{pmatrix} 0 & 0 \\ 1 & 0 \end{pmatrix}, \qquad \tau_3 = \tau_z \tag{A.53}$$

They have the following properties

$$\tau_3\,|\,\mathrm{p}\,\rangle = +\,|\,\mathrm{p}\,\rangle \qquad \tau_3\,|\,\mathrm{n}\,\rangle = -\,|\,\mathrm{n}\,\rangle \tag{A.54}$$

$$\tau_+\,|\,\mathrm{p}\,\rangle = 0 \qquad \tau_+\,|\,\mathrm{n}\,\rangle = +\,|\,\mathrm{p}\,\rangle \tag{A.55}$$

$$\tau_-\,|\,\mathrm{p}\,\rangle = +\,|\,\mathrm{n}\,\rangle \qquad \tau_-\,|\,\mathrm{n}\,\rangle = 0. \tag{A.56}$$

The inverse relations are given by

$$\tau_x = \left(\tau_+ + \tau_-\right), \qquad \tau_y = -i\left(\tau_+ - \tau_-\right), \qquad \tau_z = \tau_3. \tag{A.57}$$

In addition, isospin-projection operators are defined as

$$\tau_\mathrm{p} = \frac{1}{2}\left(1 + \tau_3\right), \qquad \tau_\mathrm{n} = \frac{1}{2}\left(1 - \tau_3\right) \tag{A.58}$$

such that

$$\tau_\mathrm{p}\,|\,\mathrm{p}\,\rangle = |\,\mathrm{p}\,\rangle \qquad \tau_\mathrm{p}\,|\,\mathrm{n}\,\rangle = 0 \tag{A.59}$$

$$\tau_\mathrm{n}\,|\,\mathrm{p}\,\rangle = 0 \qquad \tau_\mathrm{n}\,|\,\mathrm{n}\,\rangle = |\,\mathrm{n}\,\rangle. \tag{A.60}$$

Note that $\tau_\pm$ are not the spherical components of $\boldsymbol{\tau}$, these are defined as

$$\tau_{\pm 1} = \mp\frac{1}{\sqrt{2}}\left(\tau_x \pm i\tau_y\right), \tag{A.61}$$

but have no intuitive physical meaning.

In the expressions for the MECs, the following isospin operator is encountered

$$\boldsymbol{I}_V = \left(\boldsymbol{\tau}_1 \times \boldsymbol{\tau}_2\right) \tag{A.62}$$

The components corresponding with γ^* and $W^{\pm}$ interactions can be written as a function of isospin raising and lowering operators

$$(\boldsymbol{I}_V)_+ = i\,(\tau_3(1)\tau_+(2) - \tau_+(1)\tau_3(2)) \tag{A.63}$$
$$(\boldsymbol{I}_V)_3 = 2i\,(\tau_+(1)\tau_-(2) - \tau_-(1)\tau_+(2)) \tag{A.64}$$
$$(\boldsymbol{I}_V)_- = i\,(\tau_-(1)\tau_3(2) - \tau_3(1)\tau_-(2))\,, \tag{A.65}$$

where the $+$ and $-$ components are defined as

$$(\boldsymbol{I}_V)_\pm = \frac{1}{2}\left((\boldsymbol{I}_V)_x \pm i(\boldsymbol{I}_V)_y\right). \tag{A.66}$$

The single-particle isospin operator $\boldsymbol{t}$ is defined via its components ($k \in \{1,2,3\}$)

$$t_k = \frac{1}{2}\tau_k \qquad\qquad t_\pm = \pm\frac{1}{2}\tau_\pm, \tag{A.67}$$

and have the same commutation properties of ordinary angular momentum operators so that

$$t^2\,|\,t, m_t\,\rangle = t(t+1)\,|\,t, m_t\,\rangle \tag{A.68}$$
$$t_3\,|\,t, m_t\,\rangle = m_t\,|\,t, m_t\,\rangle. \tag{A.69}$$

In other words, the isospin state $|\,t, m_t\,\rangle$ is an eigenstate of the operators t^2 and t_3. This translates into

$$t^2\,|\,\mathrm{p}\,\rangle = +\frac{3}{4}\,|\,\mathrm{p}\,\rangle \qquad\qquad t^2\,|\,\mathrm{n}\,\rangle = +\frac{3}{4}\,|\,\mathrm{n}\,\rangle \tag{A.70}$$
$$t_3\,|\,\mathrm{p}\,\rangle = +\frac{1}{2}\,|\,\mathrm{p}\,\rangle \qquad\qquad t_3\,|\,\mathrm{n}\,\rangle = -\frac{1}{2}\,|\,\mathrm{n}\,\rangle \tag{A.71}$$
$$t_+\,|\,\mathrm{p}\,\rangle = 0 \qquad\qquad t_+\,|\,\mathrm{n}\,\rangle = +\frac{1}{2}\,|\,\mathrm{p}\,\rangle \tag{A.72}$$
$$t_-\,|\,\mathrm{p}\,\rangle = -\frac{1}{2}\,|\,\mathrm{n}\,\rangle \qquad\qquad t_-\,|\,\mathrm{n}\,\rangle = 0. \tag{A.73}$$

The total isospin operator of a coupled system is

$$\boldsymbol{T} = \sum_{i=1}^{A} \boldsymbol{t}(i), \tag{A.74}$$

just as the total angular momentum $\boldsymbol{J}$ is the sum of all individual angular momenta $\boldsymbol{j}$, we have here

$$T^2\,|\,T, M_T\,\rangle = T(T+1)\,|\,T, M_T\,\rangle \tag{A.75}$$
$$T_3\,|\,T, M_T\,\rangle = M_T\,|\,T, M_T\,\rangle. \tag{A.76}$$

The last useful relation with respect to the isospin relates to the Wigner-Eckart theorem, which states

$$\langle\,t, m_t\,|\,\tau_k\,|\,t', m_t'\,\rangle = (-1)^{t-m_t}\begin{pmatrix} t & 1 & t' \\ -m_t & k & m_t' \end{pmatrix}\langle\,t\,\|\,\boldsymbol{\tau}\,\|\,t'\,\rangle, \tag{A.77}$$

so that $\langle\,N\,\|\,\boldsymbol{\tau}\,\|\,N\,\rangle \equiv \langle\,N\,\|\,\boldsymbol{\sigma}\,\|\,N\,\rangle = \sqrt{6}$ where N can be either a proton or a neutron.

References

[1] A. de-Shalit, I. Talmi, and H. Massey, *Nuclear shell theory* (2013).

[2] A. de-Shalit and H. Feshbach, *Theoretical nuclear physics: nuclear physics* (1974).

[3] I. Talmi, *Simple models of complex nuclei* (1993).

[4] P. Brussaard and P. Glaudemans, *Shell-model applications in nuclear spectroscopy* (1977).

[5] K. Heyde, *The nuclear shell model: study edition* (2013).

[6] A. Edmonds, *Angular momentum in quantum mechanics* (1996).

[7] J. Bjorken and S. Drell, *Relativistic quantum fields* (1965).

[8] R. Lawson, *Theory of the nuclear shell model* (1980).

[9] T. Ericson and W. Weise, *Pions and nuclei* (1988).

[10] J. Suhonen, *From nucleons to nucleus: microscopic nuclear theory* (2007).

Appendix B

Form factors

In Chapter 2, the nuclear current operator in the IA was discussed. In this appendix, we discuss the form factors that appear in these currents. An excellent overview of this can be found as a review article by I. Towner in [1]. In the IA, the nuclear many-body current operator is replaced by a sum of one-body current operators $\widehat{J}_\mu^{[1]}$, each of which yields the same contribution to the nuclear current

$$\widehat{J}_\mu^{\text{nuc}} = \sum_{i=1}^{A} \widehat{J}_\mu^{[1]}(i). \tag{B.1}$$

The general procedure to obtain an expression for the one-body current operator, is to construct an operator using all possible four-vectors that describe the nucleon, and that transforms like a four-vector and obeys the physical symmetry principles. The most general expression contains six different terms, three of which are of vector nature and three of axial-vector nature [2]. Each of these terms is multiplied by a form factor, which is a Lorentz-scalar function of Q^2, to account for the finite extension of the nucleons. Enforcing conservation of the vector current (CVC) and removing the term which is odd under a time-reversal transformation, four terms remain and one arrives at the following expression for the one-nucleon current operator in momentum space[1]

$$\widehat{J}_\mu^{[1]}(q) = F_1(Q^2)\gamma_\mu + \frac{i}{2m_N}F_2(Q^2)\sigma_{\mu\nu}q^\nu + G_A(Q^2)\gamma_\mu\gamma^5 + G_P(Q^2)q_\mu\gamma^5. \tag{B.2}$$

In the numerical calculations presented in this work, we will not consider the pseudoscalar term, as its contribution to the cross section is considered to be small compared to the other terms in the low-energy limit [3]. Further, calculations which included the pseudoscalar term have shown that its contribution is negligible, e.g. [4].

In general, the nucleon current is written as

$$\langle J_\mu^{[1]}(q)\rangle = \Psi(p_f)\left[F_1(Q^2)\gamma_\mu + \frac{i}{2m_N}F_2(Q^2)\sigma_{\mu\nu}q^\nu + G_A(Q^2)\gamma_\mu\gamma^5\right]\Psi(p_i), \tag{B.3}$$

where the Ψ are the wave functions describing the initial and final state nucleons. This expression for the nuclear current operator is a relativistic expression. Since our model is a nonrelativistic one, we need to obtain an expression for the operator in the low-energy

[1] This is the so-called *cc2* form of the current.

limit. We follow the so-called Foldy-Wouthuysen procedure to perform this nonrelativistic reduction. For a broad explanation we refer to [5,6]. Using the low-energy limits of the spinors, the following expressions are found for the time and space component of the current

$$\widehat{\rho}_V^{[1]}(\boldsymbol{q}) = F_1(Q^2), \tag{B.4}$$

$$\widehat{\rho}_A^{[1]}(\boldsymbol{q}) = \frac{G_A(Q^2)}{2m_N}\boldsymbol{\sigma}\cdot\left(\boldsymbol{p}_i+\boldsymbol{p}_f\right), \tag{B.5}$$

$$\begin{aligned}\widehat{\boldsymbol{J}}_V^{[1]}(\boldsymbol{q}) &= \widehat{\boldsymbol{J}}_{\rm con}^{[1]}(\boldsymbol{q}) + \widehat{\boldsymbol{J}}_{\rm mag}^{[1]}(\boldsymbol{q}) \\ &= \frac{F_1(Q^2)}{2m_N}\left(\boldsymbol{p}_i+\boldsymbol{p}_f\right) + i\frac{F_1(Q^2)+F_2(Q^2)}{2m_N}\left(\boldsymbol{\sigma}\times\boldsymbol{q}\right),\end{aligned} \tag{B.6}$$

$$\widehat{\boldsymbol{J}}_A^{[1]}(\boldsymbol{q}) = G_A(Q^2)\boldsymbol{\sigma}. \tag{B.7}$$

The expressions in coordinate space are obtained by replacing the momenta with the momentum operators. The operators $\boldsymbol{p}_i$ work on the initial state wave functions, to the right ($\boldsymbol{p}_i = -i\overrightarrow{\boldsymbol{\nabla}}$) while the $\boldsymbol{p}_f$ work on the final states, to the left ($\boldsymbol{p}_f = -i\overleftarrow{\boldsymbol{\nabla}}$). Introducing the sum over all nucleons, the expressions for the nuclear current operators in coordinate space, Eqs. (2.89)-(2.93) are obtained.

From a theoretical point of view, the Pauli and Dirac form factors $F_1(Q^2)$ and $F_2(Q^2)$ are the elementary form factors, they are a natural extension of the nuclear current in the IA, Eq. (B.2). From a historical point of view, the electric and magnetic Sachs form factors $G_E(Q^2)$ and $G_M(Q^2)$ appear as a convenient parameterization of the experimental cross section. They are related through[2]

$$G_E(Q^2) = F_1(Q^2) - \tau F_2(Q^2), \tag{B.8}$$

$$G_M(Q^2) = F_1(Q^2) + F_2(Q^2). \tag{B.9}$$

with $\tau = Q^2/4m_N^2$. The inverse relations are

$$F_1(Q^2) = \frac{1}{1+\tau}\left(G_E(Q^2)+\tau G_M(Q^2)\right), \tag{B.10}$$

$$F_2(Q^2) = \frac{1}{1+\tau}\left(G_M(Q^2)-G_E(Q^2)\right). \tag{B.11}$$

Using these expressions, the form factor combination in the magnetization current can be replaced with the magnetic form factor. Usually, the form factor F_1 for electron scattering is replaced with the electric form factor G_E, this is a valid approximation in the low-energy limit.

The asymptotic values of these form factors, are given by

$$F_{1,\rm p}(0) = 1 \qquad F_{1,\rm n}(0) = 0 \tag{B.12}$$

$$F_{2,\rm p}(0) = \kappa_{\rm p} \qquad F_{2,\rm n}(0) = \lambda_{\rm n}, \tag{B.13}$$

or equivalently

$$G_{E,\rm p}(0) = 1 \qquad G_{E,\rm n}(0) = 0 \tag{B.14}$$

$$G_{M,\rm p}(0) = \lambda_{\rm p} \qquad G_{M,\rm n}(0) = \lambda_{\rm n}, \tag{B.15}$$

[2]We use a different convention compared to [3].

where $\lambda_\mathrm{p} = 2.793$ and $\lambda_\mathrm{n} = -1.913$ are the proton and neutron magnetic moment, and $\kappa_\mathrm{p} = \lambda_\mathrm{p} - 1 = 1.793$ is the proton anomalous magnetic moment. The negative sign of λ_n incorporates $\tau_3 \,|\, \mathrm{n} \,\rangle = - \,|\, \mathrm{n} \,\rangle$.

Historically, the electric and magnetic form factors are defined as a function of the dipole form factor

$$G_D(Q^2) = \frac{1}{\left(1 + \frac{Q^2}{M_V^2}\right)^2}, \qquad M_V = 843 \text{ MeV}. \tag{B.16}$$

In units of the electric charge e, the form factors can then be written as

$$G_{E,\mathrm{p}}(Q^2) = G_D(Q^2), \quad G_{M,\mathrm{p}}(Q^2) = \lambda_\mathrm{p} G_D(Q^2), \quad G_{M,\mathrm{n}}(Q^2) = \lambda_\mathrm{n} G_D(Q^2). \tag{B.17}$$

The neutron electric form factor is usually written as

$$G_{E,\mathrm{n}}(Q^2) = -\frac{\tau}{1 + 5.6\tau} \lambda_\mathrm{n} G_D(Q^2), \tag{B.18}$$

with $\tau = Q^4/4m_N^2$. The axial form factor is written as

$$G_A(Q^2) = -\frac{1.262}{\left(1 + \frac{Q^2}{M_A^2}\right)^2} \tau_\pm, \qquad M_A = 1.03 \text{ GeV}. \tag{B.19}$$

The dipole structure of these form factors was historically explained in the vector-meson dominance (VMD) model, where the electron couples to the nucleons via the exchange of a virtual meson. The dipole form factors correspond with the propagators of these virtual mesons. At higher energies, the dipole form factors were shown to be unable to predict the interactions, thereby disproving the VMD hypothesis. Throughout this work, the dipole form factors will be used in the calculations for electron scattering, as no noticeable deviation from the dipole structure is observed for the energy and momentum transfers considered in this work.

Another parameterization of the form factors is the BBBA05 parameterization [7]. They were obtained from a fit to the world neutrino data. The dipoles form factors G_D in each of the form factors above should be replaced with a better fit to the experimental data. They are parameterized as follows

$$G_{BBBA05}(Q^2) = \frac{\sum_{k=0}^{2} a_k \tau^k}{1 + \sum_{k=0}^{4} b_k \tau^k}, \tag{B.20}$$

with parameters given in Table B.1. In this work, this parameterization for the form factors

Table B.1: Fit parameters for the BBBA05 parameterization of Eq. (B.20), as taken from [7]. The a_0 impose correct low Q^2 behavior and were not adjusted during the fitting.

	a_0	a_1	a_2	b_1	b_2	b_3	b_4
$G_{E,\mathrm{p}}$	1	-0.0578	0.00	11.1	13.6	33.0	0.00
$G_{E,\mathrm{n}}$	0	1.25	1.30	-9.86	305	-758	802
$G_{M,\mathrm{p}}$	1	0.15	0.00	11.1	19.6	7.54	0.00
$G_{M,\mathrm{n}}$	1	1.81	0.00	14.1	20.7	68.7	0.00

was used for all neutrino scattering processes.

To relate the form factors for neutrino interactions to those for electron interactions, we introduce the isoscalar and isovector form factors. For electron scattering, the *cc2* expression for the electromagnetic current can be written as

$$\widehat{J}_\mu^{[1],em}(q) = F_1(Q^2)\gamma_\mu + \frac{i}{2m_N}F_2(Q^2)\sigma_{\mu\nu}q^\nu \tag{B.21}$$

$$= \left(F_1^S(Q^2)\gamma_\mu + \frac{i}{2m_N}F_2^S(Q^2)\sigma_{\mu\nu}q^\nu\right)\frac{1}{2} + \left(F_1^V(Q^2)\gamma_\mu + \frac{i}{2m_N}F_2^V(Q^2)\sigma_{\mu\nu}q^\nu\right)\frac{\tau_3}{2}, \tag{B.22}$$

where we have split up the current in an isoscalar (S) and an isovector (V) part. The corresponding form factors are given by

$$F_i^S(Q^2) = F_{i,\mathrm{p}}(Q^2) + F_{i,\mathrm{n}}(Q^2), \tag{B.23}$$

$$F_i^V(Q^2) = F_{i,\mathrm{p}}(Q^2) - F_{i,\mathrm{n}}(Q^2). \tag{B.24}$$

On the other hand, the nuclear current for CC neutrino interactions, can be split up in a vector and an axial-vector part

$$\widehat{J}_\mu^{[1],CC}(q) = \widehat{J}_\mu^{[1],V}(q) + \widehat{J}_\mu^{[1],A}(q) \tag{B.25}$$

$$= \left(G_1(Q^2)\gamma_\mu + \frac{i}{2m_N}G_2(Q^2)\sigma_{\mu\nu}q^\nu\right)\tau_\pm + \left(G_A(Q^2)\gamma_\mu\gamma^5 + G_P(Q^2)q_\mu\gamma^5\right)\tau_\pm, \tag{B.26}$$

where we have written the form factors with a different notation on purpose. We note that the isovector part electromagnetic current and the vector part of the weak current are of identical structure, with $\tau_3/2$ replaced by $\tau_\pm$ in the latter[3]. Feynman and Gell-Mann postulated that they are members of an isotriplet of vector current operators. A consequence of this hypotheses is that the weak vector current is also a conserved current, this is the conserved vector current (CVC) relation, from which it follows that

$$G_1(Q^2) = F_1^V(Q^2), \qquad G_2(Q^2) = F_2^V(Q^2). \tag{B.27}$$

References

[1] W. Haxton and E. Henley, *Symmetries and fundamental interactions in nuclei* (1995).

[2] M. Nowakowski, E. A. Paschos, and J. M. Rodriguez, Eur. J. Phys. **26**, 545 (2005).

[3] J. Walecka, *Theoretical nuclear and subnuclear physics* (2004).

[4] C. Praet, *Modeling quasi-free neutrino-nucleus reactions for accelerator-based experiments*, PhD thesis (Ghent University, 2009).

[3] Note that our definition of $\tau_\pm$ differs a factor 2 compared to [1].

[5] N. Jachowicz, *Many-body description of neutrino-nucleus interactions*, PhD thesis (Ghent University, 2000).

[6] A. Botrugno, *Interazione neutrino-nucleo*, PhD thesis (Universita Degli Studi Di Lecce, 2004).

[7] R. Bradford, A. Bodek, H. Budd, *et al.* Nucl. Phys. Proc. Suppl. **159**, 127 (2006).

Appendix C

CVC and PCAC

In this appendix, we include a short discussion of CVC and the PCAC relation, to show how these two relations can help constraining the currents. An excellent review on these two relations can be found in [1]. The difference between the one-body and two-body versions of these relations is explained and it is explicitly shown that the vector currents used in Chapter 6 fulfill the two-nucleon CVC relation. For proof that the axial current 'axi' complies with the two-nucleon version of the PCAC relation, we refer to [2].

C.1 Conservation of vector current

The CVC relation is a conservation law that states that the vector part nuclear current is a conserved quantity

$$\partial_\mu J_V^\mu = 0. \tag{C.1}$$

The vector part of the relativistic one-nucleon current, Eq. (B.2)

$$J_\mu^{[1],V}(q) = \overline{u}(p') \left(F_1(Q^2)\gamma_\mu + \frac{i}{2m_N} F_2(Q^2)\sigma_{\mu\nu}q^\nu \right) u(p)\, \frac{\tau_\pm}{2}, \tag{C.2}$$

is trivially shown to satisfy the equation.

As we work in a nonrelativistic model, we will show that the currents in the low-energy limit also satisfy this continuity equation. First, the continuity equation is written as a function of the charge density and the current density

$$\boldsymbol{\nabla} \cdot \widehat{\boldsymbol{J}}_V + i \left[\widehat{H}, \widehat{\rho}_V \right] = 0. \tag{C.3}$$

The Hamiltonian contains a kinetic energy (one-body) and a potential energy (two-body) term

$$\widehat{H} = \sum_{i=1}^{A} \widehat{T}(\boldsymbol{r}_i) + \frac{1}{2} \sum_{i<j}^{A} \widehat{V}(\boldsymbol{r}_i, \boldsymbol{r}_j) \tag{C.4}$$

$$= \sum_{i=1}^{A} \widehat{T}(\boldsymbol{r}_i) + \frac{1}{2} \sum_{i<j}^{A} V_T(\boldsymbol{r}_i - \boldsymbol{r}_j)(\boldsymbol{\tau}_i \cdot \boldsymbol{\tau}_j), \tag{C.5}$$

with $V_T(\boldsymbol{r})$ the spatial component of the pion-exchange potential. In momentum space, this potential is given by[3,4]

$$V_\pi(\boldsymbol{q}) = -\frac{g^2_{\pi NN}}{4m_N^2}\frac{(\boldsymbol{\sigma}_1\cdot\boldsymbol{q})\,(\boldsymbol{\sigma}_2\cdot\boldsymbol{q})}{m_\pi^2+\boldsymbol{q}^2}\,(\boldsymbol{\tau}_1\cdot\boldsymbol{\tau}_2)\,. \tag{C.6}$$

The potential in coordinate space is defined as its Fourier transform, see Eq. (2.70). Separating one- and two-body currents in Eq. (C.3), we obtain

$$\boldsymbol{\nabla}\cdot\widehat{\boldsymbol{J}}_V^{[1]} + i\left[\widehat{T},\widehat{\rho}_V^{[1]}\right] = 0, \tag{C.7}$$

$$\boldsymbol{\nabla}\cdot\widehat{\boldsymbol{J}}_V^{[2]} + i\left[\widehat{V},\widehat{\rho}_V^{[1]}\right] + i\left[\widehat{T},\widehat{\rho}_V^{[2]}\right] = 0, \tag{C.8}$$

or written per nucleon

$$\boldsymbol{\nabla}\cdot\widehat{\boldsymbol{J}}_V^{[1]}(i) + i\left[\widehat{T}(i),\widehat{\rho}_V^{[1]}(i)\right] = 0, \tag{C.9}$$

$$\boldsymbol{\nabla}\cdot\widehat{\boldsymbol{J}}_V^{[2]}(i,j) + i\left[\widehat{V}(i,j),\widehat{\rho}_V^{[1]}(i)+\widehat{\rho}_V^{[1]}(j)\right] = 0, \tag{C.10}$$

where we left out the commutator $\left[\widehat{T},\widehat{\rho}_V^{[2]}\right]$ because our model does not include a time-like component of the vector two-body current. In the nonrelativistic reduction, the one-body operators $\widehat{\rho}_V^{[1]}$ and $\widehat{\boldsymbol{J}}_V^{[1]}$ are given by Eqs. (2.89) and (2.93) respectively and the kinetic energy operator is defined as

$$\widehat{T}(\boldsymbol{r}) = -\sum_{i=1}^{A}\frac{\boldsymbol{\nabla}_i^2}{2m_N}\delta^{(3)}(\boldsymbol{r}-\boldsymbol{r}_i). \tag{C.11}$$

Using these expressions it is easily proven that the vector one-body nuclear current operators $\widehat{\rho}_V^{[1]}$ and $\widehat{\boldsymbol{J}}_V^{[1]}$ satisfy the *one-body* continuity equation Eq. (C.7).

Now we examine whether the seagull and pion-in-flight currents, defined in Eqs. (6.1) and (6.2) fulfill the two-body continuity relation Eq. (C.8). The continuity equation i[1]

$$\boldsymbol{\nabla}\cdot\widehat{\boldsymbol{J}}_V^{[2]}(\boldsymbol{r}_1,\boldsymbol{r}_2) = \left[V(\boldsymbol{r}_1,\boldsymbol{r}_2),\widehat{\rho}_V^{[1]}(\boldsymbol{r}_1)+\widehat{\rho}_V^{[1]}(\boldsymbol{r}_2)\right] \tag{C.12}$$

$$= (\boldsymbol{\tau}_1\times\boldsymbol{\tau}_2)_3\,V_T(\boldsymbol{r}_1-\boldsymbol{r}_2)\left[\delta^{(3)}(\boldsymbol{r}-\boldsymbol{r}_1)-\delta^{(3)}(\boldsymbol{r}-\boldsymbol{r}_2)\right]. \tag{C.13}$$

In momentum space this is written as

$$-i\boldsymbol{q}\cdot\widehat{\boldsymbol{J}}_V^{[2]}(\boldsymbol{q}_1,\boldsymbol{q}_2) = (\boldsymbol{\tau}_1\times\boldsymbol{\tau}_2)_3\left[V_T(\boldsymbol{q}_1)-V_T(\boldsymbol{q}_2)\right]. \tag{C.14}$$

Filling in the expressions for the two-body currents and the potential, it is proven that the seagull and pion-in-flight currents satisfy the *two-body* continuity equation Eq. (C.8).

C.2 Partial conservation of the axial current

The PCAC hypothesis states that the axial current is conserved in limit in which the pion mass tends to zero [1]. We will use this hypothesis to constrain the axial currents. The

[1] We made use of the following relation $[\boldsymbol{\tau}_1\cdot\boldsymbol{\tau}_2,\tau_3(i)] = 2i\,(\boldsymbol{\tau}_1\times\boldsymbol{\tau}_2)_3\,(\delta_{i1}-\delta_{i2})$.

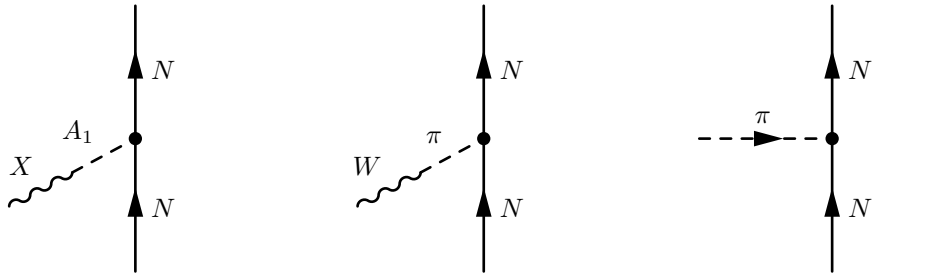

(a) A_1-pole **(b)** π-pole **(c)** π absorption

Figure C.1: Diagrammatic representation of the axial one-body currents mediated by the A_1 and π meson and the π absorption amplitude.

PCAC relation can be formulated as follows [2,3,5]

$$\partial_\mu J_A^\mu = -f_\pi \frac{m_\pi^2}{Q^2+m_\pi^2}\, M(\pi^\pm), \tag{C.15}$$

which states that the divergence of the axial current is related to the pion absorption amplitude $M(\pi^\pm)$. In the chiral limit, current conservation is obtained.

We first turn our attention to the axial part of the relativistic single-nucleon current, Eq. (B.2)

$$J_\mu^{[1],A}(q) = \overline{u}(p')\left(G_A(Q^2)\gamma_\mu\gamma^5 + G_P(Q^2)q_\mu\gamma^5\right)u(p)\,\frac{\tau_\pm}{2} \tag{C.16}$$

$$= \overline{u}(p')\left(G_A(Q^2)\gamma_\mu\gamma^5 + G_A(Q^2)\frac{2m_N}{Q^2+m_\pi^2}\,q_\mu\gamma^5\right)u(p)\,\frac{\tau_\pm}{2}. \tag{C.17}$$

This current was derived from symmetry principles, and phenomenological form factors were introduced to account for the finite extension of the hadrons. In Eq. (C.17), we already used the result from the PCAC hypothesis to relate the pseudoscalar form factor to the axial form factor. This current does not fulfill Eq. (C.15).

A second way to obtain the axial current is to describe the current as being mediated by mesons, as shown in Fig. C.1. Two mesons are responsible for the axial current, the A_1 meson (a), a pseudovector particle and the π (b), a pseudoscalar. The current obtained following this approach is given by [2]

$$J_\mu^{[1],A}(q) = \overline{u}(p')\left(g_A\frac{m_A^2}{Q^2+m_A^2}\gamma_\mu\gamma^5 + g_A\frac{m_A^2-m_\pi^2}{(Q^2+m_A^2)(Q^2+m_\pi^2)}q_\mu\not{q}\gamma^5\right)u(p)\,\frac{\tau_\pm}{2}, \tag{C.18}$$

$$= \overline{u}(p')\left(g_A(Q^2)\gamma_\mu\gamma^5 + g_A(Q^2)\left(1-\frac{m_\pi^2}{m_A^2}\right)\frac{2m_N}{Q^2+m_\pi^2}\,q_\mu\gamma^5\right)u(p)\,\frac{\tau_\pm}{2}, \tag{C.19}$$

with $g_A(Q^2) = g_A m_A^2/(Q^2+m_A^2)$. This current can be compared with the phenomenological expressions above. For vanishing pion mass and $Q^2 \to 0$, both currents are identical. It was derived using meson-pole graphs, so the deduced form factor $g_A(Q^2)$ is a monopole with range $m_A = 1086$ MeV. Experimentally, the form factor $G_A(Q^2)$ has a dipole structure, with $m_A \approx 1000$ MeV. This value corresponds with the theoretically obtained value, however suggests that another monopole form factor of similar range should be introduced at the

ANN vertex, to obtain the experimental form factor. Calculating the divergence of the current, Eq. (C.18), we obtain

$$q^\mu J^{[1],A}_\mu(q) = g_A \frac{m_\pi^2}{Q^2+m_\pi^2}\,\overline{u}(p')\not{q}\gamma^5 u(p)\,\frac{\tau_\pm}{2}, \tag{C.20}$$

$$= i f_\pi \frac{m_\pi^2}{Q^2+m_\pi^2} M(\pi^\pm), \tag{C.21}$$

with

$$M(\pi^\pm) = -i\frac{f_{\pi NN}}{m_\pi}\,\overline{u}(p')\not{q}\gamma^5 u(p)\,\tau_\pm, \tag{C.22}$$

the pion absorption amplitude on a single nucleon with a pseudovector coupling. For an intuitive interpretation of these results, we refer to Fig. C.1. The derivative of the currents (a) and (b) is related to the pion absorption amplitude (c).

In the low-energy limit, the same strategy can be followed. The PCAC relation is written as

$$\boldsymbol{\nabla}\cdot\widehat{\boldsymbol{J}}_A + i\left[\widehat{H},\boldsymbol{\rho}_A\right] = -f_\pi\frac{m_\pi^2}{\boldsymbol{q}^2+m_\pi^2}\,M(\pi^\pm), \tag{C.23}$$

in which $M(\pi^\pm)$ is the pion absorption amplitude in the low-energy limit. Separating the one- and two-body terms, we obtain

$$\boldsymbol{\nabla}\cdot\widehat{\boldsymbol{J}}^{[1]}_A + i\left[\widehat{T},\widehat{\rho}^{[1]}_A\right] = -f_\pi\frac{m_\pi^2}{\boldsymbol{k}_\pi^2+m_\pi^2}\,M^{[1]}(\pi^\pm), \tag{C.24}$$

$$\boldsymbol{\nabla}\cdot\widehat{\boldsymbol{J}}^{[2]}_A + i\left[\widehat{V},\widehat{\rho}^{[1]}_A\right] + i\left[\widehat{T},\widehat{\rho}^{[2]}_A\right] = -f_\pi\frac{m_\pi^2}{\boldsymbol{k}_\pi^2+m_\pi^2}\,M^{[2]}(\pi^\pm), \tag{C.25}$$

where $M^{[1]}$ and $M^{[2]}$ are the pion absorption amplitudes on a single nucleon and on a nucleon pair respectively. In the low-energy limit, one-body currents associated with the diagrams shown in Fig. C.1 are given by [5]

$$\widehat{\rho}^{[1]}_A(\boldsymbol{x}) = \frac{G_A(Q^2)}{2m_N i}\sum_{i=1}^{A}\boldsymbol{\sigma}_i\cdot\left[\delta^{(3)}(\boldsymbol{x}-\boldsymbol{x}_i)\overrightarrow{\boldsymbol{\nabla}}_i - \overleftarrow{\boldsymbol{\nabla}}_i\delta^{(3)}(\boldsymbol{x}-\boldsymbol{x}_i)\right]\tau_\pm(i), \tag{C.26}$$

$$\widehat{\boldsymbol{J}}^{[1]}_A(\boldsymbol{x}) = G_A(Q^2)\sum_{i=1}^{A}\boldsymbol{\sigma}_i\,\delta^{(3)}(\boldsymbol{x}-\boldsymbol{x}_i)\tau_\pm(i) - G_A(Q^2)\sum_{i=1}^{A}\overrightarrow{\boldsymbol{\nabla}}\left(\frac{\boldsymbol{\sigma}_i\cdot\overrightarrow{\boldsymbol{\nabla}}}{\overrightarrow{\boldsymbol{\nabla}}^2-m_\pi^2}\right)\delta^{(3)}(\boldsymbol{x}-\boldsymbol{x}_i)\tau_\pm(i). \tag{C.27}$$

The second term in the current density was neglected in Eq. (2.93). This term is related to the pion-pole term and is usually left out in cross section calculations since it is expected to be small compared to the first term in the low-energy limit [6]. Relativistic calculations which included the pseudoscalar term for QE $1N$ knockout calculations, e.g. [7], have explicitly shown this. For the discussion of the PCAC relation, however, it should be included.

To show that the PCAC hypothesis is valid for one-body currents, we note that the commutator $[\widehat{T},\widehat{\rho}^{[1]}_A]=0$, as the kinetic energy only depends on the momentum operator, which

commutes with the axial density. Due to the appearance of the derivatives, we will benefit from working in momentum space. The current density in momentum space is given by

$$\widehat{\boldsymbol{J}}_A^{[1]}(\boldsymbol{q}) = G_A(Q^2) \sum_{i=1}^{A} \left[\boldsymbol{\sigma}_i - \boldsymbol{q} \left(\frac{\boldsymbol{\sigma}_i \cdot \boldsymbol{q}}{\boldsymbol{q}^2 + m_\pi^2} \right) \right] \tau_\pm(i). \tag{C.28}$$

It is then easily shown that the *one-body* PCAC relation, Eq. (C.24), is fulfilled, with

$$M(\pi^\pm(i)) = \frac{f_{\pi NN}}{m_\pi} \left(\boldsymbol{\sigma}_i \cdot \boldsymbol{q} \right) \tau_\pm(i), \tag{C.29}$$

the nonrelativistic pion-absorption amplitude on a single nucleon i.

References

[1] W. Haxton and E. Henley, *Symmetries and fundamental interactions in nuclei* (1995).

[2] I. Towner, Nucl. Phys. **A542**, 631 (1992).

[3] J. Mathiot, Phys. Rept. **173**, 63 (1989).

[4] D. Riska, Phys. Rept. **181**, 207 (1989).

[5] V. Dmitrasinovic and T. Sato, Phys. Rev. **C58**, 1937 (1998).

[6] J. Walecka, *Theoretical nuclear and subnuclear physics* (2004).

[7] C. Praet, *Modeling quasi-free neutrino-nucleus reactions for accelerator-based experiments*, PhD thesis (Ghent University, 2009).

Appendix D

Reduced matrix elements

In this appendix, we define five *basic reduced matrix elements*. These basic reduced matrix elements are expectation values of combinations of the spherical harmonics Y_{LM}, the derivatives $\boldsymbol{\nabla}$ and the spin operator $\boldsymbol{\sigma}$. They are the backbone of the code, all the $1p1h$ and $2p2h$ matrix elements in subsequent appendices have been written in a way that they are the product of a prefactor, an isospin factor and one or two basic reduced matrix elements. In Appendix E, the five $1p1h$ matrix elements in the IA are reduced to the computation of four types of reduced matrix elements. Further, in Appendix F and G, all the $2p2h$ matrix elements are reduced to products of five types of basic matrix elements. This chapter summarizes these matrix elements. The results for some of these matrix elements can be found e.g. in Refs. [1–3]. The different matrix elements are defined as

$$\texttt{reej} = \langle\, a \parallel Y_L(\Omega) \parallel b \,\rangle_r, \tag{D.1}$$

$$\texttt{reed} = \langle\, a \parallel [Y_L(\Omega) \otimes \boldsymbol{\sigma}]_J \parallel b \,\rangle_r, \tag{D.2}$$

$$\texttt{reeh} = \langle\, a \parallel \left[Y_L(\Omega) \otimes \left(\overrightarrow{\boldsymbol{\nabla}} - \overleftarrow{\boldsymbol{\nabla}} \right) \right]_J \parallel b \,\rangle_r, \tag{D.3}$$

$$\texttt{reep} = \langle\, a \parallel Y_L(\Omega)\boldsymbol{\sigma} \cdot \left(\overrightarrow{\boldsymbol{\nabla}} - \overleftarrow{\boldsymbol{\nabla}} \right) \parallel b \,\rangle_r, \tag{D.4}$$

$$\texttt{reek} = \langle\, a \parallel \left[Y_L(\Omega)\boldsymbol{\sigma} \cdot \left(\overrightarrow{\boldsymbol{\nabla}} - \overleftarrow{\boldsymbol{\nabla}} \right) \otimes \boldsymbol{\sigma} \right]_J \parallel b \,\rangle_r, \tag{D.5}$$

$$\texttt{reehx} = \langle\, l_a \parallel \left[Y_L(\Omega) \otimes \left(\overrightarrow{\boldsymbol{\nabla}} - \overleftarrow{\boldsymbol{\nabla}} \right) \right]_J \parallel l_b \,\rangle_r, \tag{D.6}$$

where the nicknames which are used in the code have been given as well for convenience. The sixth matrix element is an intermediate result encountered during the calculations. In all but the last expression, the bras and kets are defined as $|\, a \,\rangle \equiv |\, l_a, 1/2, j_a \,\rangle$. The first four matrix elements appear in the IA calculations. When calculating correlations only one extra matrix element shows up. The radial transition density $\langle\, a \parallel \widehat{\mathcal{O}} \parallel b \,\rangle_r$ is defined such that it is related to the full matrix element through

$$\langle\, a \parallel \widehat{\mathcal{O}} \parallel b \,\rangle \equiv \int \mathrm{d}r \, \langle\, a \parallel \widehat{\mathcal{O}} \parallel b \,\rangle_r. \tag{D.7}$$

First we show how to calculate the matrix element `reej`. This is the easiest one and is calculated as follows

$$\langle\, a \parallel Y_L(\Omega) \parallel b \,\rangle_r = \langle\, l_a, 1/2, j_a \parallel Y_L(\Omega) \parallel l_b, 1/2, j_b \,\rangle_r \tag{D.8}$$

$$= (-1)^{l_a+1/2+j_b+L}\widehat{j_a}\widehat{j_b}\begin{Bmatrix} l_a & j_a & 1/2 \\ j_b & l_b & L \end{Bmatrix}\langle\, l_a \parallel Y_L(\Omega) \parallel l_b \,\rangle r^2\varphi_a^*(r)\varphi_b(r) \tag{D.9}$$

$$= (-1)^{l_a+1/2+j_b+L}\widehat{j_a}\widehat{j_b}\begin{Bmatrix} l_a & j_a & 1/2 \\ j_b & l_b & L \end{Bmatrix}(-1)^{l_a}\frac{\widehat{l_a}\widehat{l_b}\widehat{L}}{\sqrt{4\pi}}\begin{pmatrix} l_a & L & l_b \\ 0 & 0 & 0 \end{pmatrix} r^2\varphi_a^*(r)\varphi_b(r) \tag{D.10}$$

$$= (-1)^{j_b-1/2+L}\frac{\widehat{j_a}\widehat{j_b}\widehat{L}}{\sqrt{4\pi}}\begin{pmatrix} j_b & j_a & L \\ 1/2 & -1/2 & 0 \end{pmatrix}\frac{1}{2}\left(1+(-1)^{l_a+l_b+L}\right) r^2\varphi_a^*(r)\varphi_b(r). \tag{D.11}$$

In this derivation, we used a general property of reduced matrix elements in the first step. In the second step, $\langle\, l_a \parallel Y_L(\Omega) \parallel l_b \,\rangle$ was calculated, an expression easily found in literature, e.g. [4]. In the last step we used one of the many properties of Wigner 3j and 6j-symbols to simplify the expression.

The calculation of `reed` is not much more complicated and can be done in a few steps. The operator $Y_L(\Omega)$ works in configuration space, while the operator $\boldsymbol{\sigma}$ works in spin space. Using this information the expectation of the tensor product can be written as a product of a matrix element in configuration space and a matrix element in spin space, multiplied by a prefactor

$$\begin{aligned}&\langle\, a \parallel [Y_L(\Omega)\otimes\boldsymbol{\sigma}]_J \parallel b \,\rangle_r \\ &\quad= \widehat{j_a}\widehat{j_b}\widehat{J}\begin{Bmatrix} l_a & 1/2 & j_a \\ l_b & 1/2 & j_b \\ L & 1 & J \end{Bmatrix}\langle\, l_a \parallel Y_L(\Omega) \parallel l_b \,\rangle\langle\, 1/2 \parallel \boldsymbol{\sigma} \parallel 1/2 \,\rangle r^2\varphi_a^*(r)\varphi_b(r).\end{aligned} \tag{D.12}$$

The final result is obtained by substituting the expectation value of the spherical harmonic and using $\langle\, 1/2 \parallel \boldsymbol{\sigma} \parallel 1/2 \,\rangle = \sqrt{6}$ (see Section A.4). The final result is written below.

For the calculation of `reeh`, we note that both $Y_L(\Omega)$ and $\boldsymbol{\nabla}$ operate in configuration space. Using this information, the matrix element is written as

$$\begin{aligned}&\langle\, a \parallel \left[Y_L(\Omega)\otimes\left(\overrightarrow{\boldsymbol{\nabla}}-\overleftarrow{\boldsymbol{\nabla}}\right)\right]_J \parallel b \,\rangle \\ &\quad= (-1)^{l_a+1/2+j_b+J}\widehat{j_a}\widehat{j_b}\begin{Bmatrix} l_a & j_a & 1/2 \\ j_b & l_b & J \end{Bmatrix}\underline{\langle\, l_a \parallel \left[Y_L(\Omega)\otimes\left(\overrightarrow{\boldsymbol{\nabla}}-\overleftarrow{\boldsymbol{\nabla}}\right)\right]_J \parallel l_b \,\rangle}.\end{aligned} \tag{D.13}$$

The result is reduced to the calculation of a certain matrix element, underlined in red, which is nicknamed `reehx`. This matrix element can be calculated using the expectation values of the $\boldsymbol{\nabla}$ found in [4]. The final results for both `reeh` and `reehx` are given below.

The operator in `reep` is a complicated one. We show an efficient way of calculating its expectation value, reusing parts of already calculated matrix elements. As a first step, we write the operator it as a tensor product

$$Y_L(\Omega)\boldsymbol{\sigma}\cdot(\overrightarrow{\boldsymbol{\nabla}}-\overleftarrow{\boldsymbol{\nabla}}) = -\sqrt{3}\Big[Y_L(\Omega)\otimes\big[(\overrightarrow{\boldsymbol{\nabla}}-\overleftarrow{\boldsymbol{\nabla}})\otimes\boldsymbol{\sigma}\big]_0\Big]_L. \tag{D.14}$$

Unfortunately, this operator structure is not useful to work with, therefore we recouple the operator. This recoupling is done by expanding the tensor expression, and recombining the terms efficiently by introducing couplings in completeness relations. We obtain

$$Y_L(\Omega)\boldsymbol{\sigma}\cdot(\overrightarrow{\boldsymbol{\nabla}}-\overleftarrow{\boldsymbol{\nabla}}) = -\sum_J \widehat{J}\frac{(-1)^{L+1+J}}{\widehat{L}}\Big[\big[Y_L(\Omega)\otimes(\overrightarrow{\boldsymbol{\nabla}}-\overleftarrow{\boldsymbol{\nabla}})\big]_J\otimes\boldsymbol{\sigma}\Big]_L. \tag{D.15}$$

Looking at the expression, J can only have three values $L-1, L, L+1$. The matrix elements of this operator can be calculated as follows

$$\begin{aligned}
&\langle\, a \,\|\Big[\big[Y_L(\Omega)\otimes(\overrightarrow{\boldsymbol{\nabla}}-\overleftarrow{\boldsymbol{\nabla}})\big]_J\otimes\boldsymbol{\sigma}\Big]_L\|\, b\,\rangle \\
&\quad=\langle\, l_a,1/2,j_a\,\|\,\Big[\big[Y_L(\Omega)\otimes(\overrightarrow{\boldsymbol{\nabla}}-\overleftarrow{\boldsymbol{\nabla}})\big]_J\otimes\boldsymbol{\sigma}\Big]_L\|\, l_b,1/2,j_b\,\rangle \qquad \text{(D.16)}\\
&\quad=\widehat{j_a}\widehat{j_b}\widehat{L}\begin{Bmatrix} l_a & 1/2 & j_a\\ l_b & 1/2 & j_b\\ J & 1 & L\end{Bmatrix}\langle\, l_a\,\|\,\big[Y_L(\Omega)\otimes(\overrightarrow{\boldsymbol{\nabla}}-\overleftarrow{\boldsymbol{\nabla}})\big]_J\|\, l_b\,\rangle\langle\, 1/2\,\|\,\boldsymbol{\sigma}\,\|\,1/2\,\rangle \qquad \text{(D.17)}\\
&\quad=\sqrt{6}\widehat{j_a}\widehat{j_b}\widehat{L}\begin{Bmatrix} l_a & 1/2 & j_a\\ l_b & 1/2 & j_b\\ J & 1 & L\end{Bmatrix}\langle\, l_a\,\|\,\big[Y_L(\Omega)\otimes(\overrightarrow{\boldsymbol{\nabla}}-\overleftarrow{\boldsymbol{\nabla}})\big]_J\|\, l_b\,\rangle. \qquad \text{(D.18)}
\end{aligned}$$

The expression for the matrix element `reep` can now be written as a function of the matrix element `reehx`

$$\begin{aligned}
&\underline{\langle\, a\,\|\, Y_L(\Omega)\boldsymbol{\sigma}\cdot(\overrightarrow{\boldsymbol{\nabla}}-\overleftarrow{\boldsymbol{\nabla}})\,\|\, b\,\rangle}\\
&=-\sum_J(-1)^{L+1+J}\sqrt{6}\widehat{j_a}\widehat{j_b}\widehat{J}\begin{Bmatrix} l_a & 1/2 & j_a\\ l_b & 1/2 & j_b\\ J & 1 & L\end{Bmatrix}\underline{\langle\, l_a\,\|\,\big[Y_L(\Omega)\otimes(\overrightarrow{\boldsymbol{\nabla}}-\overleftarrow{\boldsymbol{\nabla}})\big]_J\|\, l_b\,\rangle}. \qquad \text{(D.19)}
\end{aligned}$$

The final results follows by substituting the result for `reehx`, underlined in red, and is given below.

The last reduced matrix element, `reek`, is necessary when calculating tensor correlations. It can be written as a sum of other matrix elements, which are already calculated before. It is calculated as follows

$$\begin{aligned}
&\langle\, a\,\|\Big[Y_L(\Omega)\boldsymbol{\sigma}\cdot(\overrightarrow{\boldsymbol{\nabla}}-\overleftarrow{\boldsymbol{\nabla}})\otimes\boldsymbol{\sigma}\Big]_J\|\, b\,\rangle\\
&\quad=\langle\, l_a,1/2,j_a\,\|\,\Big[Y_L(\Omega)\boldsymbol{\sigma}\cdot(\overrightarrow{\boldsymbol{\nabla}}-\overleftarrow{\boldsymbol{\nabla}})\otimes\boldsymbol{\sigma}\Big]_J\|\, l_b,1/2,j_b\,\rangle \qquad \text{(D.20)}\\
&\quad=(-1)^{j_a+J+j_b}\widehat{J}\sum_{l'j'}\begin{Bmatrix} L & 1 & J\\ j_b & j_a & j'\end{Bmatrix}\langle\, l_a,1/2,j_a\,\|\, Y_L(\Omega)\boldsymbol{\sigma}\cdot(\overrightarrow{\boldsymbol{\nabla}}-\overleftarrow{\boldsymbol{\nabla}})\,\|\, l',1/2,j'\,\rangle\\
&\qquad\qquad\times\langle\, l',1/2,j'\,\|\,\boldsymbol{\sigma}\,\|\, l_b,1/2,j_b\,\rangle. \qquad \text{(D.21)}
\end{aligned}$$

The expectation value of the $\boldsymbol{\sigma}$ is easily calculated

$$\langle\, l',1/2,j'\,\|\,\boldsymbol{\sigma}\,\|\, l_b,1/2,j_b\,\rangle=(-1)^{l'+1/2+j'+1}\widehat{j'}\widehat{j_b}\sqrt{6}\delta_{l',l_b}\begin{Bmatrix} 1/2 & j' & l'\\ j_b & 1/2 & 1\end{Bmatrix}. \qquad \text{(D.22)}$$

Combining this with the previous expression, the final result for `reek` can be written as a function of the matrix element `reep`, underlined in blue

$$\begin{aligned}
&\langle\, a\,\|\Big[Y_L(\Omega)\boldsymbol{\sigma}\cdot(\overrightarrow{\boldsymbol{\nabla}}-\overleftarrow{\boldsymbol{\nabla}})\otimes\boldsymbol{\sigma}\Big]_J\|\, b\,\rangle\\
&\quad=(-1)^{j_a+J+j_b+l_b+3/2}\sqrt{6}\widehat{J}\sum_{j'}(-1)^{j'}\widehat{j'}\widehat{j_b}\begin{Bmatrix} L & 1 & J\\ j_b & j_a & j'\end{Bmatrix}\begin{Bmatrix} 1/2 & j' & l_b\\ j_b & 1/2 & 1\end{Bmatrix}\\
&\quad\times\underline{\langle\, a\,\|\, Y_L(\Omega)\boldsymbol{\sigma}\cdot(\overrightarrow{\boldsymbol{\nabla}}-\overleftarrow{\boldsymbol{\nabla}})\,\|\, l_b,1/2,j'\,\rangle}. \qquad \text{(D.23)}
\end{aligned}$$

$$\langle\, a \parallel Y_L(\Omega) \parallel b \,\rangle_r = (-1)^{j_b-1/2+L}\frac{\widehat{j_a}\widehat{j_b}\widehat{L}}{\sqrt{4\pi}}\begin{pmatrix} j_b & j_a & L \\ 1/2 & -1/2 & 0\end{pmatrix}\frac{1}{2}\left(1+(-1)^{l_a+l_b+L}\right) r^2\varphi_a^*(r)\varphi_b(r) \tag{D.24}$$

$$\langle\, a \parallel [Y_L(\Omega)\otimes\boldsymbol{\sigma}]_J \parallel b \,\rangle_r = \sqrt{\frac{3}{2\pi}}\widehat{j_a}\widehat{j_b}\widehat{L}\widehat{J}\widehat{l_a}(-1)^L\langle l_a\ 0\ L\ 0\,|\,l_b\ 0\rangle\begin{Bmatrix} l_a & 1/2 & j_a \\ l_b & 1/2 & j_b \\ L & 1 & J\end{Bmatrix} r^2\varphi_a^*(r)\varphi_b(r) \tag{D.25}$$

$$\begin{aligned}\langle\, a \parallel \left[Y_L(\Omega)\otimes\left(\overrightarrow{\boldsymbol{\nabla}}-\overleftarrow{\boldsymbol{\nabla}}\right)\right]_J \parallel b \,\rangle_r &= \sqrt{\frac{1}{4\pi}}\widehat{j_a}\widehat{j_b}\widehat{J}(-1)^{l_a+1/2+j_b+J}\begin{Bmatrix} l_a & j_a & 1/2 \\ j_b & l_b & J\end{Bmatrix}\\
&\times(-1)^{J+l_b}\widehat{l_a}\Bigg(\langle l_a\ 0\ l_b+1\ 0\,|\,L\ 0\rangle\begin{Bmatrix} L & 1 & J \\ l_b & l_a & l_b+1\end{Bmatrix}\sqrt{2l_b+3}\sqrt{l_b+1}r^2\varphi_a^*(r)\left(\frac{\partial}{\partial r}-\frac{l_b}{r}\right)\varphi_b(r)\\
&\quad-\langle l_a\ 0\ l_b-1\ 0\,|\,L\ 0\rangle\begin{Bmatrix} L & 1 & J \\ l_b & l_a & l_b-1\end{Bmatrix}\sqrt{2l_b-1}\sqrt{l_b}r^2\varphi_a^*(r)\left(\frac{\partial}{\partial r}+\frac{l_b+1}{r}\right)\varphi_b(r)\Bigg)\\
&-(-1)^{l_a}\widehat{l_b}\Bigg(\langle l_a+1\ 0\ l_b\ 0\,|\,L\ 0\rangle\begin{Bmatrix} L & 1 & J \\ l_a & l_b & l_a+1\end{Bmatrix}\sqrt{2l_a+3}\sqrt{l_a+1}r^2\varphi_b^*(r)\left(\frac{\partial}{\partial r}-\frac{l_a}{r}\right)\varphi_a(r)\\
&\quad-\langle l_a-1\ 0\ l_b\ 0\,|\,L\ 0\rangle\begin{Bmatrix} L & 1 & J \\ l_a & l_b & l_a-1\end{Bmatrix}\sqrt{2l_a-1}\sqrt{l_a}r^2\varphi_b^*(r)\left(\frac{\partial}{\partial r}+\frac{l_a+1}{r}\right)\varphi_a(r)\Bigg)\end{aligned} \tag{D.26}$$

$$\langle\, l_a \parallel \Big[Y_L(\Omega) \otimes \Big(\overrightarrow{\boldsymbol{\nabla}} - \overleftarrow{\boldsymbol{\nabla}} \Big) \Big]_J \parallel l_b \,\rangle_r = \frac{1}{\sqrt{4\pi}} \widehat{J}$$

$$\times (-1)^{J+l_b} \widehat{l_a} \Bigg(\langle l_a \;\; 0 \;\; l_b+1 \;\; 0 \,|\, L \;\; 0 \rangle \begin{Bmatrix} L & 1 & J \\ l_b & l_a & l_b+1 \end{Bmatrix} \sqrt{2l_b+3} \sqrt{l_b+1} r^2 \varphi_a^*(r) \left(\frac{\partial}{\partial r} - \frac{l_b}{r} \right) \varphi_b(r)$$

$$- \langle l_a \;\; 0 \;\; l_b-1 \;\; 0 \,|\, L \;\; 0 \rangle \begin{Bmatrix} L & 1 & J \\ l_b & l_a & l_b-1 \end{Bmatrix} \sqrt{2l_b-1} \sqrt{l_b} r^2 \varphi_a^*(r) \left(\frac{\partial}{\partial r} + \frac{l_b+1}{r} \right) \varphi_b(r) \Bigg)$$

$$- (-1)^{l_a} \widehat{l_b} \Bigg(\langle l_a+1 \;\; 0 \;\; l_b \;\; 0 \,|\, L \;\; 0 \rangle \begin{Bmatrix} L & 1 & J \\ l_a & l_b & l_a+1 \end{Bmatrix} \sqrt{2l_a+3} \sqrt{l_a+1} r^2 \varphi_b^*(r) \left(\frac{\partial}{\partial r} - \frac{l_a}{r} \right) \varphi_a(r)$$

$$- \langle l_a-1 \;\; 0 \;\; l_b \;\; 0 \,|\, L \;\; 0 \rangle \begin{Bmatrix} L & 1 & J \\ l_a & l_b & l_a-1 \end{Bmatrix} \sqrt{2l_a-1} \sqrt{l_a} r^2 \varphi_b^*(r) \left(\frac{\partial}{\partial r} + \frac{l_a+1}{r} \right) \varphi_a(r) \Bigg) \tag{D.27}$$

$$\langle\, a \parallel Y_L(\Omega) \boldsymbol{\sigma} \cdot (\overrightarrow{\boldsymbol{\nabla}} - \overleftarrow{\boldsymbol{\nabla}}) \parallel b \,\rangle_r = - \frac{\sqrt{6}}{\sqrt{4\pi}} \sum_J (-1)^{L+1+J} \widehat{j_a} \widehat{j_b} \widehat{J} \widehat{J} \begin{Bmatrix} l_a & 1/2 & j_a \\ l_b & 1/2 & j_b \\ J & 1 & L \end{Bmatrix}$$

$$\times (-1)^{J+l_a} \widehat{l_a} \Bigg(\langle l_a \;\; 0 \;\; l_b+1 \;\; 0 \,|\, L \;\; 0 \rangle \begin{Bmatrix} L & 1 & J \\ l_b & l_a & l_b+1 \end{Bmatrix} \sqrt{2l_b+3} \sqrt{l_b+1} r^2 \varphi_a^*(r) \left(\frac{\partial}{\partial r} - \frac{l_b}{r} \right) \varphi_b(r)$$

$$- \langle l_a \;\; 0 \;\; l_b-1 \;\; 0 \,|\, L \;\; 0 \rangle \begin{Bmatrix} L & 1 & J \\ l_b & l_a & l_b-1 \end{Bmatrix} \sqrt{2l_b-1} \sqrt{l_b} r^2 \varphi_a^*(r) \left(\frac{\partial}{\partial r} + \frac{l_b+1}{r} \right) \varphi_b(r) \Bigg)$$

$$- (-1)^{l_b} \widehat{l_b} \Bigg(\langle l_a+1 \;\; 0 \;\; l_b \;\; 0 \,|\, L \;\; 0 \rangle \begin{Bmatrix} L & 1 & J \\ l_a & l_b & l_a+1 \end{Bmatrix} \sqrt{2l_a+3} \sqrt{l_a+1} r^2 \varphi_b^*(r) \left(\frac{\partial}{\partial r} - \frac{l_a}{r} \right) \varphi_a(r)$$

$$- \langle l_a-1 \;\; 0 \;\; l_b \;\; 0 \,|\, L \;\; 0 \rangle \begin{Bmatrix} L & 1 & J \\ l_a & l_b & l_a-1 \end{Bmatrix} \sqrt{2l_a-1} \sqrt{l_a} r^2 \varphi_b^*(r) \left(\frac{\partial}{\partial r} + \frac{l_a+1}{r} \right) \varphi_a(r) \Bigg) \tag{D.28}$$

References

[1] J. Ryckebusch, *Photon and electron-induced one-nucleon emission within a selfconsistent* HF-RPA *model*, PhD thesis (Ghent University, 1988).

[2] N. Jachowicz, *Many-body description of neutrino-nucleus interactions*, PhD thesis (Ghent University, 2000).

[3] J. Ryckebusch, V. Van der Sluys, K. Heyde, *et al.* Nucl. Phys. **A624**, 581 (1997).

[4] A. Edmonds, *Angular momentum in quantum mechanics* (1996).

Appendix E

IA $1p1h$ reduced matrix elements

Here, we summarize the $1p1h$ reduced matrix elements necessary for the calculation of the inclusive $1N$ knockout response functions in the IA. As explained in Chapter 2, the four multipole operators can be reduced to two operators $\widehat{M}$ and $\widehat{O}$, Eqs. (2.74) and (2.78).

$$\widehat{M}^{\text{Coul}}_{JM}(q) = \int \mathrm{d}\boldsymbol{r}\,[j_J(qr)Y_{JM}(\Omega_r)]\,\widehat{\rho}(\boldsymbol{r}) \tag{E.1}$$

$$\widehat{O}^{\kappa}_{JM}(q) = \int \mathrm{d}\boldsymbol{r}\left[j_{J+\kappa}(qr)\boldsymbol{\mathcal{Y}}^{M}_{J(J+\kappa,1)}(\Omega_r)\right]\cdot\widehat{\boldsymbol{J}}(\boldsymbol{r}). \tag{E.2}$$

The nuclear current in the IA is a sum of one-body currents

$$\widehat{J}^{\text{IA}}_{\lambda}(\boldsymbol{r}) = \sum_{i=1}^{A}\widehat{J}^{[1]}_{\lambda}(\boldsymbol{r}_i) = \sum_{i=1}^{A}\widehat{J}^{[1]}_{\lambda}(\boldsymbol{r})\delta^{(3)}(\boldsymbol{r}-\boldsymbol{r}_i). \tag{E.3}$$

In the low-energy limit, the one-body currents consist of five separate contributions, Eqs. (2.89)-(2.93). The time-like component of the one-body current $\widehat{\rho}^{[1]}$ consists of a vector $\widehat{\rho}^{[1]}_V$ and an axial $\widehat{\rho}^{[1]}_A$ part. The spacial part of the current, $\widehat{\boldsymbol{J}}^{[1]}$, is composed of a convection, magnetization and axial current, denoted as $\widehat{\boldsymbol{J}}^{[1]}_{\text{con}}$, $\widehat{\boldsymbol{J}}^{[1]}_{\text{mag}}$ and $\widehat{\boldsymbol{J}}^{[1]}_{A}$ respectively. This means we need to calculate five expectation values.

We will reduce the five matrix elements to products of a prefactor, an isospin factor and a *basic reduced matrix element*. These basic reduced matrix elements are expectation values of combinations of the spherical harmonics Y_{LM}, the derivatives $\boldsymbol{\nabla}$ and the spin operator. They were defined and calculated in Appendix D.

The results presented below are given for particle 1 in the sum $\sum_{i=1}^{A}$ and are valid for CC neutrino scattering and can be compared with the expressions in [1]. The corresponding expressions for electron scattering interactions can be obtained after a rotation in isospin space and using the corresponding form factors.

References

[1] N. Jachowicz, *Many-body description of neutrino-nucleus interactions*, PhD thesis (Ghent University, 2000).

$$\langle\, a \parallel \widehat{M}_J^{\mathrm{Coul}} \left[\widehat{\rho}_V^{[1]}(\boldsymbol{r}_1)\right] \parallel b \,\rangle = G_E(Q^2) \int \mathrm{d}r_1 \,\langle\, a \,|\, \tau_\pm \,|\, b \,\rangle \,\langle\, a \parallel j_J(qr_1) Y_J(\Omega_1) \parallel b \,\rangle_{r_1} \tag{E.4}$$

$$\langle\, a \parallel \widehat{M}_J^{\mathrm{Coul}} \left[\widehat{\rho}_A^{[1]}(\boldsymbol{r}_1)\right] \parallel b \,\rangle = \frac{G_A(Q^2)}{2m_N i} \int \mathrm{d}r_1 \,\langle\, a \,|\, \tau_\pm \,|\, b \,\rangle \,\langle\, a \parallel j_J(qr_1) Y_J(\Omega_1)\, \boldsymbol{\sigma}_1 \cdot \left(\overrightarrow{\boldsymbol{\nabla}}_1 - \overleftarrow{\boldsymbol{\nabla}}_1\right) \parallel b \,\rangle_{r_1} \tag{E.5}$$

$$\langle\, a \parallel \widehat{O}_J^\kappa \left[\widehat{\boldsymbol{J}}_{\mathrm{con}}^{[1]}(\boldsymbol{r}_1)\right] \parallel b \,\rangle = \frac{G_E(Q^2)}{2m_N i} \int \mathrm{d}r_1 \,\langle\, a \,|\, \tau_\pm \,|\, b \,\rangle \,\langle\, a \parallel j_{J+\kappa}(qr_1) \left[Y_{J+\kappa}(\Omega_1) \otimes \left(\overrightarrow{\boldsymbol{\nabla}}_1 - \overleftarrow{\boldsymbol{\nabla}}_1\right)\right]_J \parallel b \,\rangle_{r_1} \tag{E.6}$$

$$\begin{aligned}\langle\, a \parallel \widehat{O}_J^\kappa \left[\widehat{\boldsymbol{J}}_{\mathrm{mag}}^{[1]}(\boldsymbol{r}_1)\right] \parallel b \,\rangle = i\sqrt{6} q \frac{G_M(Q^2)}{2m_N} \int \mathrm{d}r_1 \,\langle\, a \,|\, \tau_\pm \,|\, b \,\rangle \sum_{\eta=\pm 1} \sqrt{J+\kappa+\delta_{\eta,+1}} \begin{Bmatrix} J & J+\kappa & 1 \\ 1 & 1 & J+\kappa+\eta \end{Bmatrix} \\ \times \,\langle\, a \parallel j_{J+\kappa+\eta}(qr_1) \left[Y_{J+\kappa+\eta}(\Omega_1) \otimes \boldsymbol{\sigma}_1\right]_J \parallel b \,\rangle_{r_1}\end{aligned} \tag{E.7}$$

$$\langle\, a \parallel \widehat{O}_J^\kappa \left[\widehat{\boldsymbol{J}}_A^{[1]}(\boldsymbol{r}_1)\right] \parallel b \,\rangle = G_A(Q^2) \int \mathrm{d}r_1 \,\langle\, a \,|\, \tau_\pm \,|\, b \,\rangle \,\langle\, a \parallel j_{J+\kappa}(qr_1) \left[Y_{J+\kappa}(\Omega_1) \otimes \boldsymbol{\sigma}_1\right]_J \parallel b \,\rangle_{r_1} \tag{E.8}$$

Appendix F

SRC $2p2h$ reduced matrix elements

In this appendix, we summarize the results of the SRC $2p2h$ matrix elements. These were obtained after some *lengthy but straightforward* calculations. The $2p2h$ matrix elements will be expressed as a function of the *basic reduced matrix elements*, which have been defined in Appendix D.

The $2p2h$ reduced matrix elements for central correlations in electron scattering cross sections can be found in [1] and those for spin-dependent correlations in [2]. The results for the axial matrix elements have been published in [3]. Recapitulating Chapter 5: to account for SRCs in the calculation of a transition matrix element, the operator is replaced with an effective operator which accounts for the SRCs. In the case of the nuclear current operator in the IA, the one-body current is extended with two-body current terms to account for SRCs

$$\widehat{J}^{\text{eff}}_{\lambda}(\boldsymbol{r}) \approx \widehat{J}^{\text{IA}}_{\lambda}(\boldsymbol{r}) + \widehat{J}^{[1],c}_{\lambda}(\boldsymbol{r}) + \widehat{J}^{[1],t\tau}_{\lambda}(\boldsymbol{r}) + \widehat{J}^{[1],\sigma\tau}_{\lambda}(\boldsymbol{r}), \tag{F.1}$$

where the superscripts IA, c, $t\tau$ and $\sigma\tau$ stand for the impulse approximation and central, tensor and spin-isospin correlations. The components λ refer to the time-like and three spherical components. The current in the IA is a sum of one-body currents

$$\widehat{J}^{\text{IA}}_{\lambda}(\boldsymbol{r}) = \sum_{i=1}^{A} \widehat{J}^{[1]}_{\lambda}(\boldsymbol{r}_i), \tag{F.2}$$

where the superscript [1] points to the fact that the current is a one-body current. The two-body terms, corresponding with the central correlations have the following structure

$$\widehat{J}^{[1],c}_{\lambda}(\boldsymbol{r}) = \sum_{i<j}^{A} \widehat{J}^{[1],c}_{\lambda}(\boldsymbol{r}_i, \boldsymbol{r}_j) + \left[\sum_{i<j}^{A} \widehat{J}^{[1],c}_{\lambda}(\boldsymbol{r}_i, \boldsymbol{r}_j) \right]^{\dagger} \tag{F.3}$$

with

$$\widehat{J}^{[1],c}_{\lambda}(\boldsymbol{r}_i, \boldsymbol{r}_j) = -\left[\widehat{J}^{[1]}_{\lambda}(\boldsymbol{r}_i) + \widehat{J}^{[1]}_{\lambda}(\boldsymbol{r}_j) \right] \widehat{g}(i,j). \tag{F.4}$$

The two-body currents are thus a product of a one-body current and a two-body correlation function. We have chosen to denote this with the superscript [1],c to distinguish from the genuine two-body currents encountered throughout this work. The structure of the tensor and spin-isospin terms follows automatically.

F.1 Central correlations

In this section, we only consider central correlations. We demonstrate how to calculate the $2p2h$ reduced matrix elements for SRCs. In a case with only central correlations, the vector part of the time-like component of the effective current is given by

$$\widehat{\rho}_V^{\text{eff}}(\boldsymbol{r}) = \widehat{\rho}_V^{\text{IA}}(\boldsymbol{r}) + \widehat{\rho}_V^{[1],c}(\boldsymbol{r}). \tag{F.5}$$

The first term is simply the time-like part of the current in the IA, Eq. (2.89). The second term is the correlated operator and has the following structure

$$\widehat{\rho}_V^{[1],c}(\boldsymbol{r}) = -\sum_{i<j}^{A} \widehat{\rho}_V(\boldsymbol{r}_i)\widehat{g}(i,j) - \sum_{i<j}^{A} \widehat{\rho}_V(\boldsymbol{r}_j)\widehat{g}(i,j) \tag{F.6}$$

$$= -G_E(Q^2) \sum_{i<j}^{A} \tau_{\pm}(i)\delta^{(3)}(\boldsymbol{r}-\boldsymbol{r}_i) f_c(r_{ij}) \quad + \quad (i \leftrightarrow j), \tag{F.7}$$

with $f_c(r_{ij})$ the central correlation function. For simplicity, we will not write down the symmetric term $(i \leftrightarrow j)$ each time. The correlation function can be expanded as

$$f_c(r_{ij}) = \sum_{lm} \frac{4\pi}{2l+1} \chi^c(l, r_i, r_j) Y_{l-m}(\Omega_i) Y_{lm}(\Omega_j)(-1)^m, \tag{F.8}$$

where the partial wave components $\chi^c(l, r_i, r_j)$ are obtained via

$$\chi^c(l, r_i, r_j) = \frac{2l+1}{2} \int_{-1}^{+1} \mathrm{d}\cos\theta P_l(\cos\theta) f_c\left(\sqrt{r_i^2 + r_j^2 - 2r_i r_j \cos\theta}\right). \tag{F.9}$$

Substituting this in the expression for Coulomb multipole operator $\widehat{M}_{JM}^{\text{Coul}}$, Eq. (2.74), we obtain

$$\widehat{M}_{JM}^{\text{Coul}}\left[\widehat{\rho}_V^{[1],c}(\boldsymbol{r})\right] = -G_E(Q^2) \sum_{i<j}^{A} \tau_{\pm}(i) \int \mathrm{d}\boldsymbol{r}\, [j_J(qr) Y_{JM}(\Omega_x)]\, \delta^{(3)}(\boldsymbol{r}-\boldsymbol{r}_i)$$
$$\times \sum_{lm} \frac{4\pi}{2l+1} \chi^c(l, r_i, r_j) Y_{l-m}(\Omega_i) Y_{lm}(\Omega_j)(-1)^m \tag{F.10}$$

$$= -G_E(Q^2) \sum_{i<j}^{A} \sum_{lL} \sqrt{4\pi}\frac{\widehat{L}}{\widehat{l}\widehat{J}} \langle L\ 0\ l\ 0 \,|\, J\ 0\rangle \tau_{\pm}(i) j_J(qr_i) \chi^c(l, r_i, r_j)$$
$$\times [Y_L(\Omega_i) \otimes Y_l(\Omega_j)]_{JM} \tag{F.11}$$

Using this expression and the properties of the 9j-symbol, the $2p2h$ reduced matrix element can be calculated. In Eq. (F.15), the result is shown for particles 1 and 2 in the sum $\sum_{i<j}^{A}$, with the inclusion of the $(i \leftrightarrow j)$ term. The radial transition density $\langle a \parallel \widehat{\mathcal{O}} \parallel b\rangle$ in the result is defined such that it is related to the full matrix element through

$$\langle a \parallel \widehat{\mathcal{O}} \parallel b\rangle \equiv \int \mathrm{d}r \langle a \parallel \widehat{\mathcal{O}} \parallel b\rangle_r. \tag{F.12}$$

The results for the other components of the nuclear current can be obtained by following the same approach. For the vector part of the current, the results can be found in [1], the axial part is published in [3]. All results are listed below. When deriving the matrix elements for the axial-vector current, we can make efficient use of the similarities with the convection current

$$\widehat{\boldsymbol{J}}_{\mathrm{con}}(\boldsymbol{r}) = \frac{G_E(Q^2)}{2m_N i}\sum_{i=1}^{A}\tau_{\pm}(i)\left[\delta^{(3)}(\boldsymbol{r}-\boldsymbol{r}_i)\overrightarrow{\boldsymbol{\nabla}}_i - \overleftarrow{\boldsymbol{\nabla}}_i\delta^{(3)}(\boldsymbol{r}-\boldsymbol{r}_i)\right] \tag{F.13}$$

$$= \frac{G_E(Q^2)}{2m_N i}\sum_{i=1}^{A}\tau_{\pm}(i)\left(\overrightarrow{\boldsymbol{\nabla}}_i - \overleftarrow{\boldsymbol{\nabla}}_i\right)\delta^{(3)}(\boldsymbol{r}-\boldsymbol{r}_i)$$

$$\widehat{\boldsymbol{J}}_{\mathrm{A}}(\boldsymbol{r}) = G_A(Q^2)\sum_{i=1}^{A}\tau_{\pm}(i)\boldsymbol{\sigma}_i\delta^{(3)}(\boldsymbol{r}-\boldsymbol{r}_i). \tag{F.14}$$

In the second the operators $\overrightarrow{\boldsymbol{\nabla}}$ and $\overleftarrow{\boldsymbol{\nabla}}$ do not act on the delta-function. Comparing both expressions, the only difference is the operator, both are vector operators, and the prefactor. Since these operators are still standing in the $2p2h$ matrix element of the convection current, which is a sum of $1p1h$ reduced matrix elements, we can simply replace them. Note that in the calculations, both operators have a different parity hence only one of them will differ from zero for a specific quantum state. All results are listed below for particles 1 and 2 in the sum $\sum_{i<j}^{A}$.

$$\langle ab; J_1 \parallel \widehat{M}_J^{\mathrm{Coul}} \left[\widehat{\rho}_V^{[1],c}(\boldsymbol{r}_1, \boldsymbol{r}_2)\right] \parallel cd; J_2\rangle = -G_E(Q^2)\sqrt{4\pi}\sum_{lL}\int \mathrm{d}r_1 \int \mathrm{d}r_2 \frac{\widehat{J_1}\widehat{J_2}\widehat{L}}{\widehat{l}} \langle L\ 0\ l\ 0 \,|\, J\ 0\rangle\ \chi^c(l, r_1, r_2)$$
$$\times \Bigg(\langle a \,|\, \tau_\pm \,|\, c\rangle\ \langle a \parallel j_J(qr_1) Y_L(\Omega_1) \parallel c\rangle_{r_1} \langle b \parallel Y_l(\Omega_2) \parallel d\rangle_{r_2} \begin{Bmatrix} j_a & j_b & J_1 \\ j_c & j_d & J_2 \\ L & l & J \end{Bmatrix}$$
$$+ \langle b \,|\, \tau_\pm \,|\, d\rangle\ \langle a \parallel Y_l(\Omega_1) \parallel c\rangle_{r_1} \langle b \parallel j_J(qr_2) Y_L(\Omega_2) \parallel d\rangle_{r_2} \begin{Bmatrix} j_a & j_b & J_1 \\ j_c & j_d & J_2 \\ l & L & J \end{Bmatrix} \Bigg) \tag{F.15}$$

$$\langle ab; J_1 \parallel \widehat{M}_J^{\mathrm{Coul}} \left[\widehat{\rho}_A^{[1],c}(\boldsymbol{r}_1, \boldsymbol{r}_2)\right] \parallel cd; J_2\rangle = -\frac{G_A(Q^2)}{m_N i}\sqrt{\pi}\sum_{lL}\int \mathrm{d}r_1 \int \mathrm{d}r_2 \frac{\widehat{J_1}\widehat{J_2}\widehat{L}}{\widehat{l}} \langle L\ 0\ l\ 0 \,|\, J\ 0\rangle\ \chi^c(l, r_1, r_2)$$
$$\times \Bigg(\langle a \,|\, \tau_\pm \,|\, c\rangle\ \langle a \parallel j_J(qr_1) Y_L(\Omega_1) \left[\boldsymbol{\sigma}_1 \cdot (\overrightarrow{\boldsymbol{\nabla}}_1 - \overleftarrow{\boldsymbol{\nabla}}_1)\right] \parallel c\rangle_{r_1} \langle b \parallel Y_l(\Omega_2) \parallel d\rangle_{r_2} \begin{Bmatrix} j_a & j_b & J_1 \\ j_c & j_d & J_2 \\ L & l & J \end{Bmatrix}$$
$$+ \langle b \,|\, \tau_\pm \,|\, d\rangle\ \langle a \parallel Y_l(\Omega_1) \parallel c\rangle_{r_1} \langle b \parallel j_J(qr_2) Y_L(\Omega_2) \left[\boldsymbol{\sigma}_2 \cdot (\overrightarrow{\boldsymbol{\nabla}}_2 - \overleftarrow{\boldsymbol{\nabla}}_2)\right] \parallel d\rangle_{r_2} \begin{Bmatrix} j_a & j_b & J_1 \\ j_c & j_d & J_2 \\ l & L & J \end{Bmatrix} \Bigg) \tag{F.16}$$

$$\langle ab;J_1 \parallel \widehat{O}^{\kappa}_{J}\left[\widehat{\boldsymbol{J}}^{[1],c}_{\rm con}(\boldsymbol{r}_1,\boldsymbol{r}_2)\right] \parallel cd;J_2\rangle = \frac{G_E(Q^2)}{m_N i}\sqrt{\pi}\sum_{lL}\sum_{J_x}\int \mathrm{d}r_1 \int \mathrm{d}r_2 \frac{\widehat{L}\widehat{J_x}\widehat{J_1}\widehat{J_2}\widehat{J}}{\widehat{l}}$$
$$\times \langle L\ 0\ l\ 0 \,|\, J+\kappa\ 0\rangle \begin{Bmatrix} L & l & J+\kappa \\ J & 1 & J_x \end{Bmatrix}\ \chi^c(l,r_1,r_2)$$
$$\times\Bigg(\langle\, a \,|\, \tau_\pm \,|\, c\,\rangle\langle\, a \parallel j_{J+\kappa}(qr_1)\left[Y_L(\Omega_1)\otimes\left(\overrightarrow{\boldsymbol{\nabla}}_1-\overleftarrow{\boldsymbol{\nabla}}_1\right)\right]_{J_x} \parallel c\,\rangle_{r_1}\langle\, b \parallel Y_l(\Omega_2)\parallel d\,\rangle_{r_2}\begin{Bmatrix} j_a & j_b & J_1 \\ j_c & j_d & J_2 \\ J_x & l & J \end{Bmatrix}(-1)^{(J_x+L)}$$
$$+\langle\, b \,|\, \tau_\pm \,|\, d\,\rangle\ \langle\, a \parallel Y_l(\Omega_1)\parallel c\,\rangle_{r_1}\langle\, b \parallel j_{J+\kappa}(qr_2)\left[Y_L(\Omega_2)\otimes\left(\overrightarrow{\boldsymbol{\nabla}}_2-\overleftarrow{\boldsymbol{\nabla}}_2\right)\right]_{J_x} \parallel d\,\rangle_{r_2}\begin{Bmatrix} j_a & j_b & J_1 \\ j_c & j_d & J_2 \\ l & J_x & J \end{Bmatrix}(-1)^{(L+l+J)}\Bigg) \tag{F.17}$$

$$\langle ab;J_1 \parallel \widehat{O}^{\kappa}_{J}\left[\widehat{\boldsymbol{J}}^{[1],c}_{\rm mag}(\boldsymbol{r}_1,\boldsymbol{r}_2)\right] \parallel cd;J_2\rangle = \frac{G_M(Q^2)}{m_N}\sqrt{6\pi}iq\sum_{lL}\sum_{J_x}\sum_{\eta=\pm1}\int \mathrm{d}r_1 \int \mathrm{d}r_2 \frac{\widehat{L}\widehat{J_x}\widehat{J_1}\widehat{J_2}\widehat{J}}{\widehat{l}}\sqrt{J+\kappa+\delta_{\eta,+1}}$$
$$\times \langle L\ 0\ l\ 0 \,|\, J+\kappa+\eta\ 0\rangle \begin{Bmatrix} J+\kappa & J+\kappa+\eta & 1 \\ 1 & 1 & J \end{Bmatrix}\begin{Bmatrix} J & 1 & J+\kappa+\eta \\ L & l & J_x \end{Bmatrix}\ \chi^c(l,r_1,r_2)$$
$$\times\Bigg(\langle\, a \,|\, \tau_\pm \,|\, c\,\rangle\ \langle\, a \parallel j_{J+\kappa+\eta}(qr_1)\left[Y_L(\Omega_1)\otimes\boldsymbol{\sigma}_1\right]_{J_x} \parallel c\,\rangle_{r_1}\langle\, b \parallel Y_l(\Omega_2)\parallel d\,\rangle_{r_2}\begin{Bmatrix} j_a & j_b & J_1 \\ j_c & j_d & J_2 \\ J_x & l & J \end{Bmatrix}(-1)^{(J_x+L)}$$
$$+\langle\, b \,|\, \tau_\pm \,|\, d\,\rangle\ \langle\, a \parallel Y_l(\Omega_1)\parallel c\,\rangle_{r_1}\langle\, b \parallel j_{J+\kappa+\eta}(qr_2)\left[Y_L(\Omega_2)\otimes\boldsymbol{\sigma}_2\right]_{J_x} \parallel d\,\rangle_{r_2}\begin{Bmatrix} j_a & j_b & J_1 \\ j_c & j_d & J_2 \\ l & J_x & J \end{Bmatrix}(-1)^{(L+l+J)}\Bigg) \tag{F.18}$$

$$\langle ab; J_1 \parallel \widehat{O}^{\kappa}_{J} \left[\widehat{\boldsymbol{J}}^{[1],c}_{A}(\boldsymbol{r}_1, \boldsymbol{r}_2) \right] \parallel cd; J_2 \rangle = G_A(Q^2)\sqrt{4\pi} \sum_{lL} \sum_{J_x} \int \mathrm{d}r_1 \int \mathrm{d}r_2 \frac{\widehat{L}\widehat{J_x}\widehat{J_1}\widehat{J_2}\widehat{J}}{\widehat{l}}$$

$$\times \langle L\ 0\ l\ 0 \,|\, J+\kappa\ 0 \rangle \begin{Bmatrix} L & l & J+\kappa \\ J & 1 & J_x \end{Bmatrix} \chi^c(l, r_1, r_2)$$

$$\times \Bigg(\langle\, a \,|\, \tau_{\pm} \,|\, c \,\rangle \, \langle\, a \parallel j_{J+\kappa}(qr_1) \left[Y_L(\Omega_1) \otimes \boldsymbol{\sigma}_1 \right]_{J_x} \parallel c \,\rangle_{r_1} \langle\, b \parallel Y_l(\Omega_2) \parallel d \,\rangle_{r_2} \begin{Bmatrix} j_a & j_b & J_1 \\ j_c & j_d & J_2 \\ J_x & l & J \end{Bmatrix} (-1)^{(J_x+L)}$$

$$+ \langle\, b \,|\, \tau_{\pm} \,|\, d \,\rangle \, \langle\, a \parallel Y_l(\Omega_1) \parallel c \,\rangle_{r_1} \langle\, b \parallel j_{J+\kappa}(qr_2) \left[Y_L(\Omega_2) \otimes \boldsymbol{\sigma}_2 \right]_{J_x} \parallel d \,\rangle_{r_2} \begin{Bmatrix} j_a & j_b & J_1 \\ j_c & j_d & J_2 \\ l & J_x & J \end{Bmatrix} (-1)^{(L+l+J)} \Bigg) \tag{F.19}$$

F.2 Tensor correlations

Compared to the tensor correlations, calculating the central correlation matrix elements is like a walk in the park. Introducing the tensor part in the effective operator, the vector part of the time-like component of the effective operator reads

$$\widehat{\rho}_V^{\text{eff}}(\boldsymbol{r}) = \widehat{\rho}_V^{\text{IA}}(\boldsymbol{r}) + \widehat{\rho}^{[1],c}(\boldsymbol{r}) + \widehat{\rho}_V^{[1],t\tau}(\boldsymbol{r}), \tag{F.20}$$

where the tensor part of the operator is given by

$$\widehat{\rho}_V^{[1],t\tau}(\boldsymbol{r}) = \sum_{i<j}^{A} \widehat{\rho}_V(\boldsymbol{r}_i)\widehat{t}(i,j) + \sum_{i<j}^{A} \widehat{\rho}_V(\boldsymbol{r}_j)\widehat{t}(i,j) \tag{F.21}$$

$$= G_E(Q^2) \sum_{i<j}^{A} \tau_{\pm}(i)\delta^{(3)}(\boldsymbol{r}-\boldsymbol{r}_i) f_{t\tau}(r_{ij}) \widehat{S}_{ij}\left(\boldsymbol{\tau}_i \cdot \boldsymbol{\tau}_j\right) \quad + \quad (i \leftrightarrow j). \tag{F.22}$$

The operator $\widehat{S}_{ij}$ is defined as

$$\widehat{S}_{ij} = \frac{3}{r_{ij}^2}\left(\boldsymbol{\sigma}_i \cdot \boldsymbol{r}_{ij}\right)\left(\boldsymbol{\sigma}_j \cdot \boldsymbol{r}_{ij}\right) - \left(\boldsymbol{\sigma}_i \cdot \boldsymbol{\sigma}_j\right), \tag{F.23}$$

and $f_{t\tau}(r_{ij})$ is the tensor correlation function. Note the sign difference between the central and tensor part. For tensor correlations, a simple partial wave expansion of the correlation function is not useful due to the structure of the tensor operator. To separate the time-like and spin operators, we use the following expression

$$f_{t\tau}(r_{ij})\Big(3\left(\boldsymbol{\sigma}_i \cdot \boldsymbol{r}_{ij}\right)\left(\boldsymbol{\sigma}_j \cdot \boldsymbol{r}_{ij}\right) - \left(\boldsymbol{\sigma}_i \cdot \boldsymbol{\sigma}_j\right)\Big) = \frac{8\sqrt{6}}{5} \sum_{l_1 l_2} \chi^{t\tau}(l_1, l_2, r_i, r_j)\widehat{l}_1\widehat{l}_2$$
$$\times\, i^{l_1-l_2+2}\langle l_1\ 0\ l_2\ 0\,|\,2\ 0\rangle\Big(\left[Y_{l_1}(\Omega_i) \otimes Y_{l_2}(\Omega_j)\right]_2 \cdot \left[\boldsymbol{\sigma}_1 \otimes \boldsymbol{\sigma}_2\right]_2\Big), \tag{F.24}$$

with

$$\chi^{t\tau}\left(l_1, l_2, r_i, r_j\right) = \int \mathrm{d}q \int \mathrm{d}r\ q^2 r^2 j_2(qr)\, f_{t\tau}(r)\, j_{l_1}(qr_i)\, j_{l_2}(qr_j) \tag{F.25}$$

Plugging these expressions in the Coulomb operator, Eq. (2.74), the following expression can be found

$$\widehat{M}_{JM}^{\text{Coul}}\left[\widehat{\rho}_V^{[1],t\tau}(\boldsymbol{r})\right] = G_E(Q^2)\frac{4\sqrt{6}}{\sqrt{\pi}} \sum_{i<j}^{A} \sum_{l_1 l_2} \sum_{L} \sum_{J_3 J_4} \widehat{l}_1\widehat{l}_2\widehat{L}\widehat{J}_3\widehat{J}_4 \chi^{t\tau}(l_1, l_2, r_i, r_j)$$
$$\times \langle l_1\ 0\ l_2\ 0\,|\,2\ 0\rangle \begin{Bmatrix} 1 & 1 & 2 \\ l_1 & l_2 & J_3 \end{Bmatrix} i^{l_1+l_2}\left(\boldsymbol{\tau}_i \cdot \boldsymbol{\tau}_j\right)$$
$$\times \Bigg(\tau_{\pm}(i)\,\widehat{l}_1 \begin{pmatrix} L & J & l_1 \\ 0 & 0 & 0 \end{pmatrix} \begin{Bmatrix} L & J & l_1 \\ J_3 & 1 & J_4 \end{Bmatrix} (-1)^{J+1}\, j_J\left(qr_i\right)$$
$$\times \Big[\left[Y_L\left(\Omega_i\right) \otimes \boldsymbol{\sigma}_i\right]_{J_4} \otimes \left[Y_{l_2}\left(\Omega_j\right) \otimes \boldsymbol{\sigma}_j\right]_{J_3}\Big]_{JM}$$

$$+\tau_{\pm}(j)\,\widehat{l}_2 \begin{pmatrix} L & J & l_2 \\ 0 & 0 & 0 \end{pmatrix} \begin{Bmatrix} L & J & l_2 \\ J_3 & 1 & J_4 \end{Bmatrix} (-1)^{J_3+J_4+1}\, j_J\left(qr_j\right) \times \left[\left[Y_{l_1}\left(\Omega_i\right)\otimes\boldsymbol{\sigma}_i\right]_{J_3}\otimes\left[Y_L\left(\Omega_j\right)\otimes\boldsymbol{\sigma}_j\right]_{J_4}\right]_{JM}\Bigg). \quad \text{(F.26)}$$

It is now a simple step of using the properties of Wigner 9j-symbols and reduced matrix elements to obtain the $2p2h$ reduced matrix element. The result for particles 1 and 2 is shown below. For the other four matrix elements, analogous but slightly longer calculations are to be done. Similarities between vector and axial currents again allow us to onsight[1] the calculation of the axial matrix elements. For the vector part of the current, the results can be found in [2], the axial part is published in [3]. All results are listed below.

[1] Onsight: A clean ascent, with no prior practice or beta.

$$\langle ab;J_1 \parallel \widehat{M}_J^{\mathrm{Coul}}\left[\widehat{\rho}_V^{[1],t\tau}(\boldsymbol{r}_1,\boldsymbol{r}_2)\right] \parallel cd;J_2\rangle = G_E(Q^2)\frac{4\sqrt{6}}{\sqrt{\pi}}\sum_{l_1l_2}\sum_{L}\sum_{J_3J_4}\int \mathrm{d}r_1\int \mathrm{d}r_2\widehat{l_1}\widehat{l_2}\widehat{L}\widehat{J_3}\widehat{J_4}\widehat{J_1}\widehat{J_2}\widehat{J}$$

$$\times\langle l_1\ 0\ l_2\ 0\,|\,2\ 0\rangle\begin{Bmatrix}1 & 1 & 2\\ l_1 & l_2 & J_3\end{Bmatrix} i^{l_1+l_2}\ \chi^{t\tau}\left(l_1,l_2,r_1,r_2\right)$$

$$\times\Bigg(\langle ab\,|\,\tau_{\pm}(1)\left(\boldsymbol{\tau}_1\cdot\boldsymbol{\tau}_2\right)\,|\,cd\rangle\begin{pmatrix}L & J & l_1\\ 0 & 0 & 0\end{pmatrix}\begin{Bmatrix}L & J & l_1\\ J_3 & 1 & J_4\end{Bmatrix}\begin{Bmatrix}j_a & j_b & J_1\\ j_c & j_d & J_2\\ J_4 & J_3 & J\end{Bmatrix}\widehat{l_1}\left(-1\right)^{J+1}$$

$$\times\langle a \parallel j_J\left(qr_1\right)\left[Y_L\left(\Omega_1\right)\otimes\boldsymbol{\sigma}_1\right]_{J_4} \parallel c\rangle_{r_1}\langle b \parallel \left[Y_{l_2}\left(\Omega_2\right)\otimes\boldsymbol{\sigma}_2\right]_{J_3} \parallel d\rangle_{r_2}$$

$$+\langle ab\,|\,\tau_{\pm}(2)\left(\boldsymbol{\tau}_1\cdot\boldsymbol{\tau}_2\right)\,|\,cd\rangle\begin{pmatrix}L & J & l_2\\ 0 & 0 & 0\end{pmatrix}\begin{Bmatrix}L & J & l_2\\ J_3 & 1 & J_4\end{Bmatrix}\begin{Bmatrix}j_a & j_b & J_1\\ j_c & j_b & J_2\\ J_3 & J_4 & J\end{Bmatrix}\widehat{l_2}\left(-1\right)^{J_3+J_4+1}$$

$$\times\langle a \parallel \left[Y_{l_1}\left(\Omega_1\right)\otimes\boldsymbol{\sigma}_1\right]_{J_3} \parallel c\rangle_{r_1}\langle b \parallel j_J\left(qr_2\right)\left[Y_L\left(\Omega_2\right)\otimes\boldsymbol{\sigma}_2\right]_{J_4} \parallel d\rangle_{r_2}\Bigg) \tag{F.27}$$

$$\langle ab;J_1 \parallel \widehat{M}_J^{\mathrm{Coul}}\left[\widehat{\rho}_A^{[1],t\tau}(\boldsymbol{r}_1,\boldsymbol{r}_2)\right] \parallel cd;J_2\rangle = \frac{G_A(Q^2)}{m_N i}\frac{2\sqrt{6}}{\sqrt{\pi}}\sum_{l_1 l_2}\sum_{L}\sum_{J_3 J_4}\int \mathrm{d}r_1 \int \mathrm{d}r_2 \widehat{l_1}\widehat{l_2}\widehat{L}\widehat{J_3}\widehat{J_4}\widehat{J_1}\widehat{J_2}\widehat{J}$$

$$\times \langle l_1\ 0\ l_2\ 0\,|\,2\ 0\rangle \begin{Bmatrix} 1 & 1 & 2 \\ l_1 & l_2 & J_3 \end{Bmatrix} i^{l_1+l_2}\ \chi^{t\tau}\left(l_1,l_2,r_1,r_2\right)$$

$$\times\Bigg(\langle\, ab\,|\,\tau_{\pm}(1)\left(\boldsymbol{\tau}_1\cdot\boldsymbol{\tau}_2\right)\,|\,cd\,\rangle \begin{pmatrix} L & J & l_1 \\ 0 & 0 & 0 \end{pmatrix} \begin{Bmatrix} L & J & l_1 \\ J_3 & 1 & J_4 \end{Bmatrix} \begin{Bmatrix} j_a & j_b & J_1 \\ j_c & j_d & J_2 \\ J_4 & J_3 & J \end{Bmatrix} \widehat{l_1}\,(-1)^{J+1}$$

$$\times \langle\, a \parallel j_J\left(qr_1\right)\left[Y_L\left(\Omega_1\right)\boldsymbol{\sigma}_1\cdot\left(\overrightarrow{\boldsymbol{\nabla}}_1-\overleftarrow{\boldsymbol{\nabla}}_1\right)\otimes\boldsymbol{\sigma}_1\right]_{J_4} \parallel c\,\rangle_{r_1}\langle\, b \parallel \left[Y_{l_2}\left(\Omega_2\right)\otimes\boldsymbol{\sigma}_2\right]_{J_3} \parallel d\,\rangle_{r_2}$$

$$+\langle\, ab\,|\,\tau_{\pm}(2)\left(\boldsymbol{\tau}_1\cdot\boldsymbol{\tau}_2\right)\,|\,cd\,\rangle \begin{pmatrix} L & J & l_2 \\ 0 & 0 & 0 \end{pmatrix} \begin{Bmatrix} L & J & l_2 \\ J_3 & 1 & J_4 \end{Bmatrix} \begin{Bmatrix} j_a & j_b & J_1 \\ j_c & j_b & J_2 \\ J_3 & J_4 & J \end{Bmatrix} \widehat{l_2}\,(-1)^{J_3+J_4+1}$$

$$\times \langle\, a \parallel \left[Y_{l_1}\left(\Omega_1\right)\otimes\boldsymbol{\sigma}_1\right]_{J_3} \parallel c\,\rangle_{r_1}\langle\, b \parallel j_J\left(qr_2\right)\left[Y_L\left(\Omega_2\right)\boldsymbol{\sigma}_2\cdot\left(\overrightarrow{\boldsymbol{\nabla}}_2-\overleftarrow{\boldsymbol{\nabla}}_2\right)\otimes\boldsymbol{\sigma}_2\right]_{J_4} \parallel d\,\rangle_{r_2}\Bigg) \tag{F.28}$$

$$\langle ab;J_1 \parallel \widehat{O}^{\kappa}_{J}\left[\widehat{\boldsymbol{J}}^{[1],t\tau}_{\rm con}(\boldsymbol{r}_1,\boldsymbol{r}_2)\right] \parallel cd;J_2\rangle = \frac{G_E(Q^2)}{m_N i}\frac{12}{\sqrt{\pi}}\sum_{l_1l_2}\sum_{J_3J_4}\sum_{J_5L}\int \mathrm{d}r_1\int \mathrm{d}r_2 \widehat{l_1}\widehat{l_2}\widehat{J_1}\widehat{J_2}\widehat{J_3}\widehat{J_4}\left(\widehat{J_5}\right)^2 \widehat{L}\widehat{J+\kappa}\widehat{J}$$

$$\times \langle l_1\ 0\ l_2\ 0\,|\,2\ 0\rangle \begin{Bmatrix} 1 & 1 & 2 \\ l_2 & l_1 & J_3 \end{Bmatrix} i^{l_1+l_2}\ \chi^{t\tau}(l_1,l_2,r_1,r_2)$$

$$\times\Bigg(\langle\, ab\,|\,\tau_{\pm}(1)\,(\boldsymbol{\tau}_1\cdot\boldsymbol{\tau}_2)\ |\,cd\,\rangle \begin{pmatrix} L & l_1 & J+\kappa \\ 0 & 0 & 0 \end{pmatrix} \begin{Bmatrix} 1 & J & J+\kappa \\ l_1 & L & J_4 \end{Bmatrix} \begin{Bmatrix} 1 & J_3 & l_1 \\ J & J_4 & J_5 \end{Bmatrix}$$

$$\times \begin{Bmatrix} j_a & j_b & J_1 \\ j_c & j_d & J_2 \\ J_5 & J_3 & J \end{Bmatrix} \begin{Bmatrix} l_a & 1/2 & j_a \\ l_c & 1/2 & j_c \\ J_4 & 1 & J_5 \end{Bmatrix} \widehat{l_1}\widehat{j_a}\widehat{j_c}\,(-1)^J$$

$$\times \langle\ n_a l_a \parallel j_{J+\kappa}(qr_1)\left[Y_L(\Omega_1)\otimes\left(\overrightarrow{\boldsymbol{\nabla}}_1-\overleftarrow{\boldsymbol{\nabla}}_1\right)\right]_{J_4} \parallel n_c l_c\rangle_{r_1}\langle\, b \parallel [Y_{l_2}(\Omega_2)\otimes\boldsymbol{\sigma}_2]_{J_3} \parallel d\,\rangle_{r_2}$$

$$+\langle\, ab\,|\,\tau_{\pm}(2)\,(\boldsymbol{\tau}_1\cdot\boldsymbol{\tau}_2)\ |\,cd\,\rangle \begin{pmatrix} L & l_2 & J+\kappa \\ 0 & 0 & 0 \end{pmatrix} \begin{Bmatrix} 1 & J & J+\kappa \\ l_2 & L & J_4 \end{Bmatrix} \begin{Bmatrix} 1 & J_3 & l_2 \\ J & J_4 & J_5 \end{Bmatrix}$$

$$\times \begin{Bmatrix} j_a & j_b & J_1 \\ j_c & j_d & J_2 \\ J_3 & J_5 & J \end{Bmatrix} \begin{Bmatrix} l_b & 1/2 & j_b \\ l_d & 1/2 & j_d \\ J_4 & 1 & J_5 \end{Bmatrix} \widehat{l_2}\widehat{j_b}\widehat{j_d}\,(-1)^{J_3+J_5}$$

$$\times \langle\, a \parallel [Y_{l_1}(\Omega_1)\otimes\boldsymbol{\sigma}_1]_{J_3} \parallel c\,\rangle_{r_1}\langle\ n_b l_b \parallel j_{J+\kappa}(qr_2)\left[Y_L(\Omega_2)\otimes\left(\overrightarrow{\boldsymbol{\nabla}}_2-\overleftarrow{\boldsymbol{\nabla}}_2\right)\right]_{J_4} \parallel n_d l_d\ \rangle_{r_2}\Bigg) \tag{F.29}$$

$$
\begin{aligned}
\langle ab;J_1 \parallel \widehat{O}^{\kappa}_{J}\left[\widehat{\boldsymbol{J}}^{[1],t\tau}_{\rm mag}(\boldsymbol{r}_1,\boldsymbol{r}_2)\right] \parallel cd;J_2\rangle &= \frac{G_M(Q^2)}{m_N}\frac{12\sqrt{6}q}{\sqrt{\pi}}\sum_{l_1l_2}\sum_{J_3J_4}\sum_{LL_3}\sum_{\eta=\pm1}\sum_{j}\int \mathrm{d}r_1\int \mathrm{d}r_2\ \widehat{l_1}\widehat{l_2}\widehat{J_3}\widehat{J_4}\widehat{L}\left(\widehat{L_3}\right)^2\widehat{J+\kappa+\eta}\widehat{J_1}\widehat{J_2}\widehat{j} \\
&\times\sqrt{J+\kappa+\delta_{\eta,+1}}\,\langle l_1\ 0\ l_2\ 0\,|\,2\ 0\rangle \\
&\times\begin{Bmatrix}1 & 1 & 2\\ l_2 & l_1 & J_3\end{Bmatrix}\begin{Bmatrix}1 & J & J+\kappa\\ J+\kappa+\eta & 1 & 1\end{Bmatrix}\begin{Bmatrix}J & 1 & J+\kappa+\eta\\ J_4 & J_3 & L_3\end{Bmatrix} i^{l_1+l_2+1}\ \chi^{t\tau}(l_1,l_2,r_1,r_2) \\
\times\Bigg(&\langle\, ab\,|\,\tau_{\pm}(1)\,(\boldsymbol{\tau}_1\cdot\boldsymbol{\tau}_2)\,|\,cd\,\rangle\begin{pmatrix}L & l_1 & J+\kappa+\eta\\ 0 & 0 & 0\end{pmatrix}\begin{Bmatrix}L & J+\kappa+\eta & l_1\\ J_3 & 1 & J_4\end{Bmatrix} \\
&\times\begin{Bmatrix}J_4 & 1 & L_3\\ j_c & j_a & j\end{Bmatrix}\begin{Bmatrix}l_c & 1/2 & j\\ 1 & j_c & 1/2\end{Bmatrix}\begin{Bmatrix}j_a & j_b & J_1\\ j_c & j_d & J_2\\ L_3 & J_3 & J\end{Bmatrix}\widehat{l_1}\widehat{j_c}\,(-1)^{j_a+j_c+l_c+j-J_3+\kappa+3/2} \\
&\times\langle\, a\parallel j_{J+\kappa+\eta}(qr_1)\,[Y_L(\Omega_1)\otimes\boldsymbol{\sigma}_1]_{J_4}\parallel n_cl_c\tfrac{1}{2}j\,\rangle_{r_1}\langle\, b\parallel[Y_{l_2}(\Omega_2)\otimes\boldsymbol{\sigma}_2]_{J_3}\parallel d\,\rangle_{r_2} \\
+\langle\, ab\,|\,&\tau_{\pm}(2)\,(\boldsymbol{\tau}_1\cdot\boldsymbol{\tau}_2)\,|\,cd\,\rangle\begin{pmatrix}L & l_2 & J+\kappa+\eta\\ 0 & 0 & 0\end{pmatrix}\begin{Bmatrix}L & J+\kappa+\eta & l_2\\ J_3 & 1 & J_4\end{Bmatrix} \\
&\times\begin{Bmatrix}J_4 & 1 & L_3\\ j_d & j_b & j\end{Bmatrix}\begin{Bmatrix}l_d & 1/2 & j\\ 1 & j_d & 1/2\end{Bmatrix}\begin{Bmatrix}j_a & j_b & J_1\\ j_c & j_d & J_2\\ J_3 & L_3 & J\end{Bmatrix}\widehat{l_2}\widehat{j_d}\,(-1)^{j_b+j_d+l_d+j+L_3+J+\kappa+3/2} \\
&\times\langle\, a\parallel[Y_{l_1}(\Omega_1)\otimes\boldsymbol{\sigma}_1]_{J_3}\parallel c\,\rangle_{r_1}\langle\, b\parallel j_{J+\kappa+\eta}(qr_2)\,[Y_L(\Omega_2)\otimes\boldsymbol{\sigma}_2]_{J_4}\parallel n_dl_d\tfrac{1}{2}j\,\rangle_{r_2}\Bigg)
\end{aligned}
\tag{F.30}
$$

$$\langle ab;J_1 \parallel \widehat{O}^{\kappa}_{J}\left[\widehat{\boldsymbol{J}}^{[1],t\tau}_{A}(\boldsymbol{r}_1,\boldsymbol{r}_2)\right] \parallel cd;J_2\rangle = G_A(Q^2)\frac{24}{\sqrt{\pi}}\sum_{l_1l_2}\sum_{J_3J_4}\sum_{J_5L}\sum_{j}\int \mathrm{d}r_1\int \mathrm{d}r_2 \widehat{l_1}\widehat{l_2}\widehat{J_1}\widehat{J_2}\widehat{J_3}\widehat{J_4}\widehat{J_5}\widehat{L}\widehat{J+\kappa}\widehat{J}$$

$$\times \langle l_1\ 0\ l_2\ 0\,|\,2\ 0\rangle \begin{Bmatrix} 1 & 1 & 2 \\ l_2 & l_1 & J_3 \end{Bmatrix} i^{l_1+l_2}\ \chi^{t\tau}(l_1,l_2,r_1,r_2)$$

$$\times\Bigg(\langle\, ab\,|\,\tau_{\pm}(1)\,(\boldsymbol{\tau}_1\cdot\boldsymbol{\tau}_2)\,|\,cd\,\rangle \begin{pmatrix} L & l_1 & J+\kappa \\ 0 & 0 & 0 \end{pmatrix} \begin{Bmatrix} 1 & J & J+\kappa \\ l_1 & L & J_4 \end{Bmatrix} \begin{Bmatrix} 1 & J_3 & l_1 \\ J & J_4 & J_5 \end{Bmatrix} \begin{Bmatrix} j_a & j_b & J_1 \\ j_c & j_d & J_2 \\ J_5 & J_3 & J \end{Bmatrix}$$

$$\times \begin{Bmatrix} J_4 & 1 & J_5 \\ j_c & j_a & j \end{Bmatrix} \begin{Bmatrix} 1/2 & j & l_c \\ j_c & 1/2 & 1 \end{Bmatrix} \widehat{l_1}\widehat{j}\widehat{j_c}\,(-1)^{J+J_5+j_a+j_c+j+l_c+3/2}$$

$$\times \langle\, a \parallel j_{J+\kappa}(qr_1)\,[Y_L(\Omega_1)\otimes\boldsymbol{\sigma}_1]_{J_4} \parallel n_c j\tfrac{1}{2} l_c\rangle_{r_1}\langle\, b \parallel [Y_{l_2}(\Omega_2)\otimes\boldsymbol{\sigma}_2]_{J_3} \parallel d\,\rangle_{r_2}$$

$$+\langle\, ab\,|\,\tau_{\pm}(2)\,(\boldsymbol{\tau}_1\cdot\boldsymbol{\tau}_2)\,|\,cd\,\rangle \begin{pmatrix} L & l_2 & J+\kappa \\ 0 & 0 & 0 \end{pmatrix} \begin{Bmatrix} 1 & J & J+\kappa \\ l_2 & L & J_4 \end{Bmatrix} \begin{Bmatrix} 1 & J_3 & l_2 \\ J & J_4 & J_5 \end{Bmatrix} \begin{Bmatrix} j_a & j_b & J_1 \\ j_c & j_d & J_2 \\ J_3 & J_5 & J \end{Bmatrix}$$

$$\times \begin{Bmatrix} J_4 & 1 & J_5 \\ j_d & j_b & j \end{Bmatrix} \begin{Bmatrix} 1/2 & j & l_d \\ j_d & 1/2 & 1 \end{Bmatrix} \widehat{l_2}\widehat{j}\widehat{j_d}\,(-1)^{J_3+j_b+j_d+j+l+d+3/2}$$

$$\times \langle\, a \parallel [Y_{l_1}(\Omega_1)\otimes\boldsymbol{\sigma}_1]_{J_3} \parallel c\,\rangle_{r_1}\langle\, b \parallel j_{J+\kappa}(qr_2)\,[Y_L(\Omega_2)\otimes\boldsymbol{\sigma}_2]_{J_4} \parallel n_d j\tfrac{1}{2} l_d\,\rangle_{r_2}\Bigg) \tag{F.31}$$

F.3 Spin-isospin correlations

Last, but not least, are the spin-isospin correlations. Introducing the spin-isospin part, the vector part of the time-like component of the effective operator reads

$$\widehat{\rho}_V^{\text{eff}}(\boldsymbol{r}) = \widehat{\rho}_V^{\text{IA}}(\boldsymbol{r}) + \widehat{\rho}_V^{[1],c}(\boldsymbol{r}) + \widehat{\rho}_V^{[1],t\tau}(\boldsymbol{r}) + \widehat{\rho}_V^{[1],\sigma\tau}(\boldsymbol{r}), \tag{F.32}$$

where the spin-isospin part of the operator is given by

$$\widehat{\rho}_V^{[1],\sigma\tau}(\boldsymbol{r}) = \sum_{i<j}^{A} \widehat{\rho}_V(\boldsymbol{r}_i)\widehat{s}(i,j) + \sum_{i<j}^{A} \widehat{\rho}_V(\boldsymbol{r}_j)\widehat{s}(i,j) \tag{F.33}$$

$$= G_E(Q^2) \sum_{i<j}^{A} \tau_{\pm}(i)\delta^{(3)}(\boldsymbol{r}-\boldsymbol{r}_i) f_{\sigma\tau}(r_{ij}) \left(\boldsymbol{\sigma}_i \cdot \boldsymbol{\sigma}_j\right)\left(\boldsymbol{\tau}_i \cdot \boldsymbol{\tau}_j\right) \quad + \quad (i \leftrightarrow j), \tag{F.34}$$

with $f_{\sigma\tau}(r_{ij})$ the spin-isospin correlation function. We define the partial wave components of the spin-isospin correlation function

$$\chi^{\sigma\tau}(l, r_i, r_j) = \frac{2l+1}{2} \int_{-1}^{+1} \mathrm{d}\cos\theta P_l(\cos\theta) f_{\sigma\tau}\left(\sqrt{r_i^2 + r_j^2 - 2r_i r_j \cos\theta}\right), \tag{F.35}$$

which can be used in the calculations via

$$f_{\sigma\tau}(r_{ij}) = \sum_{lm} \frac{4\pi}{2l+1} \chi^{\sigma\tau}(l, r_i, r_j) Y_{l-m}(\Omega_i) Y_{lm}(\Omega_j)(-1)^m. \tag{F.36}$$

Furthermore, in the calculations we will use the following equivalence

$$\left(\boldsymbol{\sigma}_i \cdot \boldsymbol{\sigma}_j\right) = -\sqrt{3}\left[\boldsymbol{\sigma}_i \otimes \boldsymbol{\sigma}_j\right]_{00}, \tag{F.37}$$

to couple the operators to an operator with a convenient tensor structure. Substituting this effective current in Eq. (2.74) results in

$$\begin{aligned} M_{JM}^{\text{Coul}}\left[\widehat{\rho}_V^{[1],\sigma\tau}(\boldsymbol{r})\right] = G_E(Q^2)\sqrt{4\pi} \sum_{i<j}^{A} \sum_{lL} \sum_{J_3 J_4} \frac{\widehat{L}\widehat{J_3}\widehat{J_4}}{\widehat{l}} \\ \times \begin{pmatrix} J & L & l \\ 0 & 0 & 0 \end{pmatrix} \begin{Bmatrix} J_3 & L & 1 \\ l & J_4 & J \end{Bmatrix} \left(\boldsymbol{\tau}_i \cdot \boldsymbol{\tau}_i\right) \chi^{\sigma\tau}(l, r_i, r_j) \\ \times \Bigg(j_J(qr_i)\, \tau_{\pm}(i) \left[\left[Y_L(\Omega_i) \otimes \boldsymbol{\sigma}_i\right]_{J_3} \otimes \left[Y_l(\Omega_j) \otimes \boldsymbol{\sigma}_j\right]_{J_4}\right]_{JM} (-1)^{J_4+L} \\ j_J(qr_j)\, \tau_{\pm}(j) \left[\left[Y_l(\Omega_i) \otimes \boldsymbol{\sigma}_i\right]_{J_4} \otimes \left[Y_L(\Omega_j) \otimes \boldsymbol{\sigma}_j\right]_{J_3}\right]_{JM} (-1)^{J+J_3+L} \Bigg). \end{aligned} \tag{F.38}$$

The $2p2h$ reduced matrix elements follow easily, using the properties of the Wigner 9j-symbols. For the vector part of the current, the results can be found in [2], the axial part is published in [3]. All results are listed below.

$$\langle ab;J_1 \parallel \widehat{M}_J^{\mathrm{Coul}}\left[\widehat{\rho}_V^{[1],\sigma\tau}(\boldsymbol{r}_1,\boldsymbol{r}_2)\right] \parallel cd;J_2\rangle = G_E(Q^2)\sqrt{4\pi}\sum_{lL}\sum_{J_3J_4}\int \mathrm{d}r_1 \int \mathrm{d}r_2 \frac{\widehat{L}\widehat{J_1}\widehat{J_2}\widehat{J_3}\widehat{J_4}}{\widehat{l}}$$

$$\times \langle l\ 0\ L\ 0 \,|\, J\ 0\rangle \begin{Bmatrix} J_3 & L & 1 \\ l & J_4 & J \end{Bmatrix} \chi^{\sigma\tau}(l,r_1,r_2)$$

$$\times \Bigg(\langle\, ab \,|\, \tau_{\pm}(1)\,(\boldsymbol{\tau}_1\cdot\boldsymbol{\tau}_2) \,|\, cd\,\rangle \begin{Bmatrix} j_a & j_b & J_1 \\ j_c & j_d & J_2 \\ J_3 & J_4 & J \end{Bmatrix} (-1)^{l+J_4}$$

$$\times \langle\, a \parallel j_J\,(qr_1)\,[Y_L\,(\Omega_1)\otimes\boldsymbol{\sigma}_1]_{J_3} \parallel c\,\rangle_{r_1} \langle\, b \parallel [Y_l\,(\Omega_2)\otimes\boldsymbol{\sigma}_2]_{J_4} \parallel d\,\rangle_{r_2}$$

$$+\langle\, ab \,|\, \tau_{\pm}(2)\,(\boldsymbol{\tau}_1\cdot\boldsymbol{\tau}_2) \,|\, cd\,\rangle \begin{Bmatrix} j_a & j_b & J_1 \\ j_c & j_b & J_2 \\ J_4 & J_3 & J \end{Bmatrix} (-1)^{l+J+J_3}$$

$$\times \langle\, a \parallel [Y_l\,(\Omega_1)\otimes\boldsymbol{\sigma}_1]_{J_4} \parallel c\,\rangle_{r_1} \langle\, b \parallel j_J\,(qr_2)\,[Y_L\,(\Omega_2)\otimes\boldsymbol{\sigma}_2]_{J_3} \parallel d\,\rangle_{r_2} \Bigg) \tag{F.39}$$

$$\langle ab;J_1 \parallel \widehat{M}_J^{\mathrm{Coul}}\left[\widehat{\rho}_A^{[1],\sigma\tau}(\boldsymbol{r}_1,\boldsymbol{r}_2)\right] \parallel cd;J_2\rangle = \frac{G_A(Q^2)}{m_N i}\sqrt{\pi}\sum_{lL}\sum_{J_3J_4}\int \mathrm{d}r_1 \int \mathrm{d}r_2 \frac{\widehat{L}\widehat{J_1}\widehat{J_2}\widehat{J_3}\widehat{J_4}}{\widehat{l}}$$

$$\times \langle l\ 0\ L\ 0 \,|\, J\ 0\rangle \begin{Bmatrix} J_3 & L & 1 \\ l & J_4 & J \end{Bmatrix} \chi^{\sigma\tau}(l,r_1,r_2)$$

$$\times \Bigg(\langle\, ab \,|\, \tau_{\pm}(1)\,(\boldsymbol{\tau}_1\cdot\boldsymbol{\tau}_2) \,|\, cd\,\rangle \begin{Bmatrix} j_a & j_b & J_1 \\ j_c & j_d & J_2 \\ J_3 & J_4 & J \end{Bmatrix} (-1)^{l+J_4}$$

$$\times \langle\, a \parallel j_J(qr_1)\left[Y_L(\Omega_1)\,\boldsymbol{\sigma}_1\cdot\left(\overrightarrow{\boldsymbol{\nabla}}_1 - \overleftarrow{\boldsymbol{\nabla}}_1\right)\otimes\boldsymbol{\sigma}_1\right]_{J_3} \parallel c\,\rangle_{r_1}\langle\, b \parallel \left[Y_l(\Omega_2)\otimes\boldsymbol{\sigma}_2\right]_{J_4} \parallel d\,\rangle_{r_2}$$

$$+\langle\, ab \,|\, \tau_{\pm}(2)\,(\boldsymbol{\tau}_1\cdot\boldsymbol{\tau}_2) \,|\, cd\,\rangle \begin{Bmatrix} j_a & j_b & J_1 \\ j_c & j_b & J_2 \\ J_4 & J_3 & J \end{Bmatrix} (-1)^{l+J+J_3}$$

$$\times \langle\, a \parallel \left[Y_l(\Omega_1)\otimes\boldsymbol{\sigma}_1\right]_{J_4} \parallel c\,\rangle_{r_1}\langle\, b \parallel j_J(qr_2)\left[Y_L(\Omega_2)\,\boldsymbol{\sigma}_2\cdot\left(\overrightarrow{\boldsymbol{\nabla}}_2 - \overleftarrow{\boldsymbol{\nabla}}_2\right)\otimes\boldsymbol{\sigma}_2\right]_{J_3} \parallel d\,\rangle_{r_2} \Bigg) \tag{F.40}$$

$$\langle ab;J_1 \parallel \widehat{O}^{\kappa}_{J}\left[\widehat{\boldsymbol{J}}^{[1],\sigma\tau}_{\rm con}(\boldsymbol{r}_1,\boldsymbol{r}_2)\right] \parallel cd;J_1\rangle = \frac{G_E(Q^2)}{m_N i}\sqrt{6\pi}\sum_{lL}\sum_{J_4J_5}\sum_{J_6}\sum_{j}\int \mathrm{d}r_1\int \mathrm{d}r_2 \frac{\widehat{L}\widehat{J}\widehat{J+\kappa}\widehat{J_1}\widehat{J_2}\left(\widehat{J_4}\right)^2\widehat{J_5}\widehat{J_6}}{\widehat{l}}$$
$$\times \begin{pmatrix} J+\kappa & L & l \\ 0 & 0 & 0\end{pmatrix}\begin{Bmatrix} J & 1 & J+\kappa \\ L & l & J_6\end{Bmatrix}\begin{Bmatrix} J_6 & l & J \\ J_5 & J_4 & 1\end{Bmatrix}\chi^{\sigma\tau}(l,r_1,r_2)$$
$$\times\Bigg(\langle\, ab\,|\,\tau_{\pm}(1)\,(\boldsymbol{\tau}_1\cdot\boldsymbol{\tau}_2)\,|\,cd\,\rangle\begin{Bmatrix} J_6 & 1 & J_4 \\ j_c & j_a & j\end{Bmatrix}\begin{Bmatrix} 1/2 & j & l_c \\ j_c & 1/2 & 1\end{Bmatrix}\begin{Bmatrix} j_a & j_b & J_1 \\ j_c & j_d & J_2 \\ J_4 & J_5 & J\end{Bmatrix}\widehat{j}\widehat{j_c}(-1)^{L+J_4+J_5+j_a+j_c+j+l_c+3/2}$$
$$\times\langle\, a \parallel j_{J+\kappa}(qr_1)\left[Y_L(\Omega_1)\otimes\left(\overrightarrow{\boldsymbol{\nabla}}_1-\overleftarrow{\boldsymbol{\nabla}}_1\right)\right]_{J_6}\parallel n_c l_c \tfrac{1}{2} j\rangle\,\langle\, b \parallel [Y_l(\Omega_2)\otimes\boldsymbol{\sigma}_2]_{J_5}\parallel d\,\rangle$$
$$\times\langle\, ab\,|\,\tau_{\pm}(2)\,(\boldsymbol{\tau}_1\cdot\boldsymbol{\tau}_2)\,|\,cd\,\rangle\begin{Bmatrix} J_6 & 1 & J_4 \\ j_d & j_b & j\end{Bmatrix}\begin{Bmatrix} 1/2 & j & l_d \\ j_d & 1/2 & 1\end{Bmatrix}\begin{Bmatrix} j_a & j_b & J_1 \\ j_c & j_d & J_2 \\ J_5 & J_4 & J\end{Bmatrix}\widehat{j}\widehat{j_d}(-1)^{L+J+j_b+j_d+j+l_d+3/2}$$
$$\times\langle\, a \parallel [Y_l(\Omega_1)\otimes\boldsymbol{\sigma}_1]_{J_5}\parallel c\,\rangle\,\langle\, b \parallel j_{J+\kappa}(qr_2)\left[Y_L(\Omega_2)\otimes\left(\overrightarrow{\boldsymbol{\nabla}}_1-\overleftarrow{\boldsymbol{\nabla}}_1\right)\right]_{J_6}\parallel n_d l_d \tfrac{1}{2} j\rangle\Bigg) \tag{F.41}$$

$$\langle ab;J_1 \parallel \widehat{O}^{\kappa}_{J}\left[\widehat{\boldsymbol{J}}^{[1],\sigma\tau}_{\rm mag}(\boldsymbol{r}_1,\boldsymbol{r}_2)\right] \parallel cd;J_2\rangle = \frac{G_M(Q^2)}{m_N} 6\sqrt{\pi} iq \sum_{lL}\sum_{J_3J_4}\sum_{J_5J_6}\sum_{j}\sum_{\eta=\pm1}\int \mathrm{d}r_1 \int \mathrm{d}r_2 \frac{\widehat{L}\widehat{J_1}\widehat{J_2}\widehat{J_3}\widehat{J_4}\left(\widehat{J_5}\right)^2\left(\widehat{J_6}\right)^2\widehat{J}}{\widehat{l}}$$
$$\times \sqrt{J+\kappa+\delta_{\eta,+1}}\langle l\ 0\ L\ 0\,|\,J+\kappa+\eta\ 0\rangle\ \chi^{\sigma\tau}(l,r_1,r_2)$$
$$\times \begin{Bmatrix} 1 & 1 & 1 \\ J+\kappa & J+\kappa+\eta & J \end{Bmatrix} \begin{Bmatrix} l & L & J+\kappa+\eta \\ 1 & J & J_5 \end{Bmatrix} \begin{Bmatrix} J_5 & 1 & L \\ J_3 & 1 & J_6 \end{Bmatrix} \begin{Bmatrix} J_6 & J_5 & 1 \\ l & J_4 & J \end{Bmatrix}$$
$$\times \Bigg(\langle\, ab\,|\,\tau_{\pm}(1)\,(\boldsymbol{\tau}_1\cdot\boldsymbol{\tau}_2)\,|\,cd\,\rangle \begin{Bmatrix} J_3 & 1 & J_6 \\ j_c & j_a & j \end{Bmatrix} \begin{Bmatrix} l_c & 1/2 & j \\ 1 & j_c & 1/2 \end{Bmatrix} \begin{Bmatrix} j_a & j_b & J_1 \\ j_c & j_d & J_2 \\ J_6 & J_4 & J \end{Bmatrix} \widehat{j}\widehat{j_c}(-1)^{L+J_3+J_4+J_5+J_6+J+\kappa+j+j_a+j_c+l_c+1/2}$$
$$\times \langle\, a \parallel j_{J+\kappa+\eta}(qr_1)\left[Y_L(\Omega_1)\otimes\boldsymbol{\sigma}_1\right]_{J_3} \parallel n_c l_c \tfrac{1}{2} j\rangle_{r_1} \langle\, b \parallel \left[Y_l(\Omega_2)\otimes\boldsymbol{\sigma}_2\right]_{J_4} \parallel d\,\rangle_{r_2}$$
$$+\langle\, ab\,|\,\tau_{\pm}(2)\,(\boldsymbol{\tau}_1\cdot\boldsymbol{\tau}_2)\,|\,cd\,\rangle \begin{Bmatrix} J_3 & 1 & J_6 \\ j_d & j_b & j \end{Bmatrix} \begin{Bmatrix} l_d & 1/2 & j \\ 1 & j_d & 1/2 \end{Bmatrix} \begin{Bmatrix} j_a & j_b & J_1 \\ j_c & j_d & J_2 \\ J_4 & J_6 & J \end{Bmatrix} \widehat{j}\widehat{j_d}(-1)^{L+J_3+J_5+\kappa+j+j_b+j_d+l_d+1/2}$$
$$\times \langle\, a \parallel \left[Y_l(\Omega_1)\otimes\boldsymbol{\sigma}_1\right]_{J_4} \parallel c\,\rangle_{r_1} \langle\, b \parallel j_{J+\kappa+\eta}(qr_2)\left[Y_L(\Omega_2)\otimes\boldsymbol{\sigma}_2\right]_{J_3} \parallel n_d l_d \tfrac{1}{2} j\rangle_{r_2} \Bigg) \tag{F.42}$$

$$\langle ab;J_1 \parallel \widehat{O}^{\kappa}_{J}\left[\widehat{\boldsymbol{J}}^{[1],\sigma\tau}_{A}(\boldsymbol{r}_1,\boldsymbol{r}_2)\right] \parallel cd;J_1\rangle = G_A(Q^2)\sqrt{24\pi}\sum_{lL}\sum_{J_4J_5}\sum_{J_6}\sum_{j}\int \mathrm{d}r_1\int \mathrm{d}r_2 \frac{\widehat{L}\widehat{J}\widehat{J+\kappa}\widehat{J}_1\widehat{J}_2\left(\widehat{J_4}\right)^2\widehat{J_5}\widehat{J_6}}{\widehat{l}}$$

$$\times\begin{pmatrix} J+\kappa & L & l \\ 0 & 0 & 0\end{pmatrix}\begin{Bmatrix} J & 1 & J+\kappa \\ L & l & J_6\end{Bmatrix}\begin{Bmatrix} J_6 & l & J \\ J_5 & J_4 & 1\end{Bmatrix}\chi^{\sigma\tau}(l,r_1,r_2)$$

$$\times\Bigg(\langle ab\,|\,\tau_{\pm}(1)\,(\boldsymbol{\tau}_1\cdot\boldsymbol{\tau}_2)\,|\,cd\rangle\begin{Bmatrix} J_6 & 1 & J_4 \\ j_c & j_a & j\end{Bmatrix}\begin{Bmatrix} 1/2 & j & l_c \\ j_c & 1/2 & 1\end{Bmatrix}\begin{Bmatrix} j_a & j_b & J_1 \\ j_c & j_d & J_2 \\ J_4 & J_5 & J\end{Bmatrix}\widehat{j}\widehat{j_c}(-1)^{L+J_4+J_5+j_a+j_c+j+l_c+3/2}$$

$$\times\langle a \parallel j_{J+\kappa}(qr_1)\left[Y_L(\Omega_1)\otimes\boldsymbol{\sigma}_1\right]_{J_6}\parallel n_c l_c \tfrac{1}{2} j\rangle\,\langle b \parallel \left[Y_l(\Omega_2)\otimes\boldsymbol{\sigma}_2\right]_{J_5}\parallel d\rangle$$

$$\times\langle ab\,|\,\tau_{\pm}(2)\,(\boldsymbol{\tau}_1\cdot\boldsymbol{\tau}_2)\,|\,cd\rangle\begin{Bmatrix} J_6 & 1 & J_4 \\ j_d & j_b & j\end{Bmatrix}\begin{Bmatrix} 1/2 & j & l_d \\ j_d & 1/2 & 1\end{Bmatrix}\begin{Bmatrix} j_a & j_b & J_1 \\ j_c & j_d & J_2 \\ J_5 & J_4 & J\end{Bmatrix}\widehat{j}\widehat{j_d}(-1)^{L+J+j_b+j_d+j+l_d+3/2}$$

$$\times\langle a \parallel \left[Y_l(\Omega_1)\otimes\boldsymbol{\sigma}_1\right]_{J_5}\parallel c\rangle\,\langle b \parallel j_{J+\kappa}(qr_2)\left[Y_L(\Omega_2)\otimes\boldsymbol{\sigma}_2\right]_{J_6}\parallel n_d l_d \tfrac{1}{2} j\rangle\Bigg) \tag{F.43}$$

References

[1] J. Ryckebusch, V. Van der Sluys, K. Heyde, *et al.* Nucl. Phys. **A624**, 581 (1997).

[2] S. Janssen, J. Ryckebusch, W. Van Nespen, *et al.* Nucl. Phys. **A672**, 285 (2000).

[3] T. Van Cuyck, N. Jachowicz, R. González–Jiménez, *et al.* Phys. Rev. **C94**, 024611 (2016).

Appendix G

MEC $2p2h$ reduced matrix elements

In this appendix, we explain how the MEC $2p2h$ matrix elements are calculated. These calculations involve some *lengthy but straightforward manipulations*. The MEC $2p2h$ reduced matrix elements for electron scattering cross sections can be found in [1]. The MEC $2p2h$ reduced matrix element for three different expressions of the axial seagull current in [2]. The expressions for the MECs used in the calculations are given in Chapter 6.

We follow the same approach as used in the calculation of the SRC matrix elements and express the MEC $2p2h$ matrix element as a function of the five *basic reduced matrix elements* defined in Appendix D.

G.1 MEC in coordinate space

The expressions for the seagull, pion-in-flight and three different axial currents discussed in Chapter 6 are written in momentum space. For the derivation of the matrix elements associated with the MECs, we want expressions for the currents in coordinate space, in correspondence with the nuclear current in the IA. These currents in coordinate space can then be substituted in the two multipole operators $\widehat{M}$ and $\widehat{O}$, Eqs. (2.74) and (2.78) to calculate the matrix elements.

In general, the currents in coordinate space are given by the Fourier transforms of the currents in momentum space, see e.g. Eq. (2.70)

$$J^{\mu}(\boldsymbol{r},\boldsymbol{r}_1,\boldsymbol{r}_2) = \int \frac{\mathrm{d}^3\boldsymbol{q}}{(2\pi)^3} e^{-i\boldsymbol{q}\cdot\boldsymbol{r}} \int \frac{\mathrm{d}^3\boldsymbol{q}_1}{(2\pi)^3} e^{i\boldsymbol{q}_1\cdot\boldsymbol{r}_1} \int \frac{\mathrm{d}^3\boldsymbol{q}_2}{(2\pi)^3} e^{i\boldsymbol{q}_2\cdot\boldsymbol{r}_2} \times (2\pi)^3\delta^{(3)}(\boldsymbol{q}-\boldsymbol{q}_1-\boldsymbol{q}_2) J^{\mu}(\boldsymbol{q},\boldsymbol{q}_1,\boldsymbol{q}_2). \tag{G.1}$$

We start by calculating the MECs in coordinate space *without inclusion of form factors*. In this case, the three different expressions for the axial current are equivalent, Eq. (6.12), and it is denoted by 'sea'. Using the definition of the Dirac delta distribution

$$\int \frac{\mathrm{d}^3\boldsymbol{q}}{(2\pi)^3} e^{i\boldsymbol{q}\cdot(\boldsymbol{r}_1-\boldsymbol{r}_2)} = \delta^{(3)}(\boldsymbol{r}_1-\boldsymbol{r}_2), \tag{G.2}$$

the expression

$$\int \frac{\mathrm{d}^3\boldsymbol{q}}{(2\pi)^3}\frac{e^{i\boldsymbol{q}\cdot(\boldsymbol{r}_1-\boldsymbol{r}_2)}}{\boldsymbol{q}^2+m_\pi^2}=\frac{e^{-m_\pi|\boldsymbol{r}_1-\boldsymbol{r}_2|}}{4\pi\,|\boldsymbol{r}_1-\boldsymbol{r}_2|}, \tag{G.3}$$

and doing the replacement $\boldsymbol{q}\to-i\boldsymbol{\nabla}$ in the numerator, the axial and vector part of the seagull current, Eqs. (6.12) and (6.8), without inclusion of form factors, can be written as[1]

$$\begin{aligned}\widehat{\rho}_A^{[2],\mathrm{sea}}(\boldsymbol{r}) &= \frac{1}{g_A}\left(\frac{f_{\pi NN}}{m_\pi}\right)^2(\boldsymbol{I}_V)\\ &\quad\times\Big(\delta^{(3)}(\boldsymbol{r}-\boldsymbol{r}_1)\,(\boldsymbol{\sigma}_2\cdot\boldsymbol{\nabla}_2)-\delta^{(3)}(\boldsymbol{r}-\boldsymbol{r}_2)\,(\boldsymbol{\sigma}_1\cdot\boldsymbol{\nabla}_1)\Big)\frac{e^{-m_\pi|\boldsymbol{r}_1-\boldsymbol{r}_2|}}{4\pi\,|\boldsymbol{r}_1-\boldsymbol{r}_2|},\end{aligned} \tag{G.4}$$

$$\begin{aligned}\widehat{\boldsymbol{J}}_V^{[2],\mathrm{sea}}(\boldsymbol{r}) &= -\left(\frac{f_{\pi NN}}{m_\pi}\right)^2(\boldsymbol{I}_V)\\ &\quad\times\Big(\delta^{(3)}(\boldsymbol{r}-\boldsymbol{r}_1)\boldsymbol{\sigma}_1\,(\boldsymbol{\sigma}_2\cdot\boldsymbol{\nabla}_2)-\delta^{(3)}(\boldsymbol{r}-\boldsymbol{r}_2)\boldsymbol{\sigma}_2\,(\boldsymbol{\sigma}_1\cdot\boldsymbol{\nabla}_1)\Big)\frac{e^{-m_\pi|\boldsymbol{r}_1-\boldsymbol{r}_2|}}{4\pi\,|\boldsymbol{r}_1-\boldsymbol{r}_2|}.\end{aligned} \tag{G.5}$$

Similarly, the pion-in-flight current without form factors can be written as

$$\begin{aligned}\widehat{\boldsymbol{J}}_V^{[2],\mathrm{pif}}(\boldsymbol{r}) &= \left(\frac{f_{\pi NN}}{m_\pi}\right)^2(\boldsymbol{I}_V)\Big((\boldsymbol{\sigma}_1\cdot\boldsymbol{\nabla}_1)\,(\boldsymbol{\sigma}_2\cdot\boldsymbol{\nabla}_2)\,\boldsymbol{\nabla}_2-(\boldsymbol{\sigma}_2\cdot\boldsymbol{\nabla}_{\boldsymbol{2}})\,(\boldsymbol{\sigma}_1\cdot\boldsymbol{\nabla}_1)\,\boldsymbol{\nabla}_1\Big)\\ &\quad\times\frac{e^{-m_\pi|\boldsymbol{r}-\boldsymbol{r}_1|}}{4\pi\,|\boldsymbol{r}-\boldsymbol{r}_1|}\frac{e^{-m_\pi|\boldsymbol{r}-\boldsymbol{r}_2|}}{4\pi\,|\boldsymbol{r}-\boldsymbol{r}_2|}.\end{aligned} \tag{G.6}$$

G.2 Introduction of partial wave expansion

We now have currents in coordinate space, unfortunately, they are of no use yet. To calculate the matrix elements, we introduce a multipole expansion. Therefore we use the following expressions

$$\frac{e^{-m_\pi|\boldsymbol{r}_1-\boldsymbol{r}_2|}}{4\pi\,|\boldsymbol{r}_1-\boldsymbol{r}_2|}=\left(\frac{2}{\pi}\right)\sum_{lm}\int\mathrm{d}p\frac{p^2}{p^2+m_\pi^2}j_l(pr_1)j_l(pr_2)Y_{lm}(\Omega_1)Y_{lm}^*(\Omega_2), \tag{G.7}$$

and

$$\begin{aligned}(\boldsymbol{\sigma}_1\cdot\boldsymbol{\nabla}_1)\frac{e^{-m_\pi|\boldsymbol{r}_1-\boldsymbol{r}_2|}}{4\pi\,|\boldsymbol{r}_1-\boldsymbol{r}_2|} &= \left(\frac{2}{\pi}\right)\sum_l(-1)^l\int\mathrm{d}p\frac{p^3}{p^2+m_\pi^2}\sum_{\eta=\pm1}\sqrt{l+\delta_{\eta,+1}}j_{l+\eta}(pr_1)j_l(pr_2)\\ &\quad\times\left[[Y_{l+\eta}(\Omega_1)\otimes\boldsymbol{\sigma}_1]_l\otimes Y_l(\Omega_2)\right]_{00}.\end{aligned} \tag{G.8}$$

Using this, the seagull currents, Eqs. (G.4) and (G.5), can be written as

$$\widehat{\rho}_A^{[2],\mathrm{sea}}(\boldsymbol{r})=\frac{1}{g_A}\left(\frac{f_{\pi NN}}{m_\pi}\right)^2(\boldsymbol{I}_V)\left(\frac{2}{\pi}\right)\sum_l(-1)^l\int\mathrm{d}p\frac{p^3}{p^2+m_\pi^2}\delta^{(3)}(\boldsymbol{r}-\boldsymbol{r}_1)$$

[1] From here on, we will write $J^\mu(\boldsymbol{r})$ and $J^\mu(\boldsymbol{q})$ instead of $J^\mu(\boldsymbol{r},\boldsymbol{r}_1,\boldsymbol{r}_2)$ and $J^\mu(\boldsymbol{q},\boldsymbol{q}_1,\boldsymbol{q}_2)$ to keep the notation concise.

$$\times \sum_{\eta=\pm1} \sqrt{l+\delta_{\eta,+1}}\, j_l(pr_1) j_{l+\eta}(pr_2) \left[\left[Y_{l+\eta}(\Omega_2)\otimes\boldsymbol{\sigma}_2\right]_l \otimes Y_l(\Omega_1)\right]_{00} - (1\leftrightarrow 2), \quad \text{(G.9)}$$

$$\widehat{\boldsymbol{J}}_V^{[2],\text{sea}}(\boldsymbol{r}) = -\left(\frac{f_{\pi NN}}{m_\pi}\right)^2 (\boldsymbol{I}_V)\left(\frac{2}{\pi}\right)\sum_l (-1)^l \int \mathrm{d}p \frac{p^3}{p^2+m_\pi^2}\delta^{(3)}(\boldsymbol{r}-\boldsymbol{r}_1)\boldsymbol{\sigma}_1$$
$$\times \sum_{\eta=\pm1} \sqrt{l+\delta_{\eta,+1}}\, j_l(pr_1) j_{l+\eta}(pr_2) \left[\left[Y_{l+\eta}(\Omega_2)\otimes\boldsymbol{\sigma}_2\right]_l \otimes Y_l(\Omega_1)\right]_{00} - (1\leftrightarrow 2). \quad \text{(G.10)}$$

The only difference between both expressions, except for the prefactor, is the extra $\boldsymbol{\sigma}$ in the vector current. The pion-in-flight current, Eq. (G.6), results in

$$\widehat{\boldsymbol{J}}_V^{[2],\text{pif}}(\boldsymbol{r}) = \left(\frac{f_{\pi NN}}{m_\pi}\right)^2 (\boldsymbol{I}_V)\left(\frac{2}{\pi}\right)^2$$
$$\times \sum_{ll'}\sum_{\eta=\pm1}\sum_{\eta'=\pm1} (-1)^{l+l'} \int \mathrm{d}p_1 \frac{p_1^3}{p_1^2+m_\pi^2} \int \mathrm{d}p_2 \frac{p_2^3}{p_2^2+m_\pi^2} (\boldsymbol{\nabla}_2-\boldsymbol{\nabla}_1)$$
$$\times \sqrt{l+\delta_{\eta,+1}}\sqrt{l'+\delta_{\eta',+1}}\, j_l(p_1r) j_{l'}(p_2r)\, j_{l+\eta}(p_1r_1) j_{l'+\eta'}(p_2r_2)$$
$$\times \left[\left[Y_{l+\eta}(\Omega_1)\otimes\boldsymbol{\sigma}_1\right]_l \otimes Y_l(\Omega)\right]_{00} \left[\left[Y_{l'+\eta'}(\Omega_2)\otimes\boldsymbol{\sigma}_2\right]_{l'} \otimes Y_{l'}(\Omega)\right]_{00}. \quad \text{(G.11)}$$

Electroweak form factors The axial form factor $G_A(Q^2)$, for expression 1 of the axial seagull current, and the isovector form factor $F_1^V(Q^2)$, for the vector currents can be placed in front of the expressions derived above. For the second expression of the axial seagull current, 'sea,2', the pion form factors F_π depend on $\boldsymbol{q}_1$ and $\boldsymbol{q}_2$ and can't be placed in front of the expression. This means that we first have to rewrite Eq. (G.4), accounting for the pion form factor. This is done by the following replacement

$$\delta^{(3)}(\boldsymbol{r}-\boldsymbol{r}_1)\frac{e^{-m_\pi|\boldsymbol{r}_1-\boldsymbol{r}_2|}}{4\pi|\boldsymbol{r}_1-\boldsymbol{r}_2|} \to m_\rho^2 \frac{e^{-m_\rho|\boldsymbol{r}-\boldsymbol{r}_1|}}{4\pi|\boldsymbol{r}-\boldsymbol{r}_1|}\frac{e^{-m_\pi|\boldsymbol{r}-\boldsymbol{r}_2|}}{4\pi|\boldsymbol{r}-\boldsymbol{r}_2|}, \quad \text{(G.12)}$$

in the first term of Eq. (G.4) and $(1\leftrightarrow 2)$ in the second. The resulting axial seagull current is given by

$$\widehat{\rho}_A^{[2],\text{sea},2}(\boldsymbol{r}) = \frac{1}{g_A}\left(\frac{f_{\pi NN}}{m_\pi}\right)^2 (\boldsymbol{I}_V)\, m_\rho^2$$
$$\times \left((\boldsymbol{\sigma}_2\cdot\boldsymbol{\nabla}_2)\frac{e^{-m_\rho|\boldsymbol{r}-\boldsymbol{r}_1|}}{4\pi|\boldsymbol{r}-\boldsymbol{r}_1|}\frac{e^{-m_\pi|\boldsymbol{r}-\boldsymbol{r}_2|}}{4\pi|\boldsymbol{r}-\boldsymbol{r}_2|} - (\boldsymbol{\sigma}_1\cdot\boldsymbol{\nabla}_1)\frac{e^{-m_\pi|\boldsymbol{r}-\boldsymbol{r}_1|}}{4\pi|\boldsymbol{r}-\boldsymbol{r}_1|}\frac{e^{-m_\rho|\boldsymbol{r}-\boldsymbol{r}_2|}}{4\pi|\boldsymbol{r}-\boldsymbol{r}_2|}\right). \quad \text{(G.13)}$$

Introducing the partial wave expansions we obtain

$$\widehat{\rho}_A^{[2],\text{sea},2}(\boldsymbol{r}) = \frac{1}{g_A}\left(\frac{f_{\pi NN}}{m_\pi}\right)^2 (\boldsymbol{I}_V)\left(\frac{2}{\pi}\right)^2 m_\rho^2 \quad \text{(G.14)}$$
$$\times \sum_{lm}\sum_{l'}\sum_{\eta=\pm1} (-1)^{l'} \int \mathrm{d}p_1 \frac{p_1^2}{p_1^2+m_\rho^2} \int \mathrm{d}p_2 \frac{p_2^3}{p_2^2+m_\pi^2}$$
$$\times \sqrt{l'+\delta_{\eta,+1}}\, j_l(p_1r) j_{l'}(p_2r)\, j_l(p_1r_1) j_{l'+\eta}(p_2r_2)$$
$$\times Y_{lm}(\Omega_1) Y_{lm}^*(\Omega) \left[\left[Y_{l'+\eta}(\Omega_2)\otimes\boldsymbol{\sigma}_2\right]_{l'} \otimes Y_{l'}(\Omega)\right]_{00} - (1\leftrightarrow 2). \quad \text{(G.15)}$$

The introduction of the pion form factor F_π in the third seagull current is explained below.

Hadron form factors As a next step, we introduce the Γ_π form factors at the πNN vertices in these expressions. We note that Eq. (G.3), used to obtain expressions for the currents in coordinate space, and Eq. (G.7), used afterwards to introduce a partial wave expansion, are related

$$\frac{e^{-m_\pi|\boldsymbol{r}_1-\boldsymbol{r}_2|}}{4\pi\,|\boldsymbol{r}_1-\boldsymbol{r}_2|} = \int \frac{\mathrm{d}^3\boldsymbol{q}}{(2\pi)^3}\frac{e^{i\boldsymbol{q}\cdot(\boldsymbol{r}_1-\boldsymbol{r}_2)}}{\boldsymbol{q}^2+m_\pi^2} \tag{G.16}$$

$$= \frac{2}{\pi}\sum_{lm}\int \mathrm{d}q \frac{q^2}{q^2+m_\pi^2} j_l(qr_1)j_l(qr_2)Y_{lm}(\Omega_1)Y^*_{lm}(\Omega_2). \tag{G.17}$$

Exploiting this, we can easily introduce the monopole form factors in the momentum integrals as follows

$$\int \frac{\mathrm{d}^3\boldsymbol{q}}{(2\pi)^3}\frac{(\Lambda_\pi^2-m_\pi^2)e^{i\boldsymbol{q}\cdot(\boldsymbol{r}_1-\boldsymbol{r}_2)}}{(\boldsymbol{q}^2+m_\pi^2)\,(\boldsymbol{q}^2+\Lambda_\pi^2)} \tag{G.18}$$

$$= \frac{2}{\pi}\sum_{lm}\int \mathrm{d}q \frac{q^2}{q^2+m_\pi^2}\left(\frac{\Lambda_\pi^2-m_\pi^2}{q^2+\Lambda_\pi^2}\right) j_l(qr_1)j_l(qr_2)Y_{lm}(\Omega_1)Y^*_{lm}(\Omega_2). \tag{G.19}$$

In the first line, the monopole form factor is included in the Fourier transform. The second line shows how this translates to the partial wave expansion. An analogous procedure is applied to the other terms. The inclusion of the pion form factor F_π in the expression labeled 'axi' can also be introduced this way.

G.3 Multipole operators

With the expressions for the MECs in coordinate space, accounting for form factors at the electroweak and the hadron vertices, all the ingredients are present for the determination of the matrix elements. Since the charge density is purely axial and the current is purely vector, only three matrix elements have to be calculated. We substitute the expressions obtained above in the multipole operators, Eqs. (2.74) and (2.78)

$$\widehat{M}^{\mathrm{Coul}}_{JM}(q) = \int \mathrm{d}\boldsymbol{r}\,[j_J(qr)Y_{JM}(\Omega_r)]\,\widehat{\rho}(\boldsymbol{r}) \tag{G.20}$$

$$\widehat{O}^{\kappa}_{JM}(q) = \int \mathrm{d}\boldsymbol{r}\left[j_{J+\kappa}(qr)\boldsymbol{\mathcal{Y}}^M_{J(J+\kappa,1)}(\Omega_r)\right]\cdot\widehat{\boldsymbol{J}}(\boldsymbol{r}) \tag{G.21}$$

$$= \int \mathrm{d}\boldsymbol{r}\sum_{M_1M_2}\langle J+\kappa\;\; M_2\;\; 1\;\; M_1\,|\,J\;\; M\rangle\,[j_{J+\kappa}(qr)Y_{J+\kappa,M_2}(\Omega_r)]\,\widehat{J}_{M_1}(\boldsymbol{r}). \tag{G.22}$$

The results are given below, for a current consisting of particle 1 and 2. For the axial seagull current, the results for the expressions 'sea,1' and 'sea,2' are given. The result for the third expression of the axial current, 'axi', is obtained after a simple substitution as explained below. For the pion-in-flight current, we neglected the contribution of the two terms in $F(\boldsymbol{q}_1,\boldsymbol{q}_2)$ with a Λ_π propagator. This is a valid approximation since the heavy-boson mass is much larger than the pion mass: $\Lambda_\pi^2 \gg m_\pi^2$. As these two extra terms have a very short range, their contributions will be negligible.

$$\langle ab;J_1 \parallel \widehat{M}_J^{\rm Coul}\left[\widehat{\rho}_A^{[2],{\rm sea},1}(1,2)\right] \parallel cd;J_2\rangle = \frac{1}{g_A}\left(\frac{f_{\pi NN}}{m_\pi}\right)^2 \frac{1}{\sqrt{4\pi}}\frac{2}{\pi} G_A(Q^2) \sum_l \sum_{J_3} \sum_{\eta=\pm 1} \widehat{J}\widehat{J_1}\widehat{J_2}\widehat{J_3}(-1)^{J_3+l}$$
$$\times \langle\, ab \,|\, \boldsymbol{I}_V \,|\, cd \,\rangle \sqrt{l+\delta_{\eta,+1}} \begin{pmatrix} J & l & J_3 \\ 0 & 0 & 0 \end{pmatrix} \int {\rm d}p \frac{p^3}{p^2+m_\pi^2} \Gamma_\pi^2(p^2) \int {\rm d}r_1 \int {\rm d}r_2$$
$$\times \Bigg(\langle j_a \parallel j_J(qr_1) j_l(pr_1) Y_{J_3}(\Omega_1) \parallel j_c\rangle_{r_1} \langle j_b \parallel j_{l+\eta}(pr_2) \left[Y_{l+\eta}(\Omega_2)\otimes \boldsymbol{\sigma}_2\right]_l \parallel j_d\rangle_{r_2} \begin{Bmatrix} j_a & j_b & J_1 \\ j_c & j_d & J_2 \\ J_3 & l & J \end{Bmatrix}$$
$$-(-1)^{l+J_3+J} \langle j_a \parallel j_{l+\eta}(pr_1) \left[Y_{l+\eta}(\Omega_1)\otimes \boldsymbol{\sigma}_1\right]_l \parallel j_c\rangle_{r_1} \langle j_b \parallel j_J(qr_2) j_l(pr_2) Y_{J_3}(\Omega_2) \parallel j_d\rangle_{r_2} \begin{Bmatrix} j_a & j_b & J_1 \\ j_c & j_d & J_2 \\ l & J_3 & J \end{Bmatrix} \Bigg) \tag{G.23}$$

The matrix element for the third expression of the axial current, $\widehat{\rho}_A^{[2],{\rm axi}}$, is obtained by removing the $G_A(Q^2)$ form factor in Eq. (G.23) and introducing the p-dependent form factor $F_\pi(p^2)$ in the integral.

$$\langle ab;J_1 \parallel \widehat{M}_J^{\rm Coul}\left[\widehat{\rho}_A^{[2],{\rm sea},2}(1,2)\right] \parallel cd;J_2\rangle = \frac{1}{g_A}\left(\frac{f_{\pi NN}}{m_\pi}\right)^2 \frac{1}{\sqrt{4\pi}}\left(\frac{2}{\pi}\right)^2 \sum_{ll'} \sum_{\eta=\pm 1} \widehat{J}\widehat{J_1}\widehat{J_2}\widehat{l}(-1)^{l-l'}$$
$$\times \langle\, ab \,|\, \boldsymbol{I}_V \,|\, cd \,\rangle \sqrt{l'+\delta_{\eta,+1}} \begin{pmatrix} l & l' & J \\ 0 & 0 & 0 \end{pmatrix}$$
$$\times \int {\rm d}p_1 p_1^2 F_\pi(p_1^2) \int {\rm d}p_2 \frac{p_2^3}{p_2^2+m_\pi^2} \Gamma_\pi^2(p_2^2) \int {\rm d}r_1 \int {\rm d}r_2 \int {\rm d}r r^2 j_l(p_1 r) j_{l'}(p_2 r) j_J(qr)$$
$$\times \Bigg(\langle j_a \parallel j_l(p_1 r_1) Y_l(\Omega_1) \parallel j_c\rangle_{r_1} \langle j_b \parallel j_{l'+\eta}(p_2 r_2) \left[Y_{l'+\eta}(\Omega_2)\otimes \boldsymbol{\sigma}_2\right]_{l'} \parallel j_d\rangle_{r_2} \begin{Bmatrix} j_a & j_b & J_1 \\ j_c & j_d & J_2 \\ l & l' & J \end{Bmatrix}$$
$$-(-1)^{l+l'+J} \langle j_a \parallel j_{l'+\eta}(p_2 r_1) \left[Y_{l'+\eta}(\Omega_1)\otimes \boldsymbol{\sigma}_1\right]_{l'} \parallel j_c\rangle_{r_1} \langle j_b \parallel j_l(p_1 r_2) Y_l(\Omega_2) \parallel j_d\rangle_{r_2} \begin{Bmatrix} j_a & j_b & J_1 \\ j_c & j_d & J_2 \\ l' & l & J \end{Bmatrix} \Bigg) \tag{G.24}$$

$$\langle ab;J_1 \parallel \widehat{O}^{\kappa}_{J}\left[\widehat{\boldsymbol{J}}^{[2],\mathrm{sea}}_{V}(1,2)\right] \parallel cd;J_2\rangle = \left(\frac{f_{\pi NN}}{m_\pi}\right)^2 \frac{1}{\sqrt{4\pi}}\frac{2}{\pi}\sum_{l}\sum_{J_3J_4}\sum_{\eta=\pm1}\widehat{J}\widehat{J_1}\widehat{J_2}\widehat{J_3}\widehat{J_4}\widehat{J+\kappa}(-1)^{J_3+l+1}$$
$$\times \langle\, ab \,|\, \boldsymbol{I}_V \,|\, cd \,\rangle \sqrt{l+\delta_{\eta,+1}} \begin{pmatrix} l & J_3 & J+\kappa \\ 0 & 0 & 0 \end{pmatrix} \begin{Bmatrix} l & J_3 & J+\kappa \\ 1 & J & J_4 \end{Bmatrix}$$
$$\times \int \mathrm{d}p \frac{p^3}{p^2+m_\pi^2}\Gamma^2_\pi(p^2) \int \mathrm{d}r_1 \int \mathrm{d}r_2$$
$$\times \Bigg(\langle j_a \parallel j_{l+\eta}(pr_1)\left[Y_{l+\eta}(\Omega_1)\otimes\boldsymbol{\sigma}_1\right]_l \parallel j_c\rangle_{r_1} \langle j_b \parallel j_{J+\kappa}(qr_2) j_l(pr_2)\left[Y_{J_3}(\Omega_2)\otimes\boldsymbol{\sigma}_2\right]_{J_4} \parallel j_d\rangle_{r_2} \begin{Bmatrix} j_a & j_b & J_1 \\ j_c & j_d & J_2 \\ l & J_4 & J \end{Bmatrix}$$
$$-(-1)^{l+J_4+J}\langle j_a \parallel j_{J+\kappa}(pr_1) j_l(pr_1)\left[Y_{J_3}(\Omega_1)\otimes\boldsymbol{\sigma}_1\right]_{J_4} \parallel j_c\rangle_{r_1} \langle j_b \parallel j_{l+\eta}(qr_2)\left[Y_{l+\eta}(\Omega_2)\otimes\boldsymbol{\sigma}_2\right]_l \parallel j_d\rangle_{r_2} \begin{Bmatrix} j_a & j_b & J_1 \\ j_c & j_d & J_2 \\ J_4 & l & J \end{Bmatrix} \Bigg) \tag{G.25}$$

$$
\begin{aligned}
\langle ab;J_1 \parallel \widehat{O}^{\kappa}_{J}\left[\widehat{\boldsymbol{J}}^{[2],\mathrm{pif}}_{V}\right] \parallel cd;J_2\rangle &= \left(\frac{f_{\pi NN}}{m_\pi}\right)^2 \frac{1}{\sqrt{4\pi}}\left(\frac{2}{\pi}\right)^2 \sum_{ll'}\sum_{J_3}\sum_{\eta=\pm1}\sum_{\eta'=\pm1}\sum_{\epsilon=\pm1} \widehat{l'}\,\widehat{J}\widehat{J_1}\widehat{J_2}\widehat{J_3}\widehat{J+\kappa}(-1)^{J+\kappa} \\
&\times \langle\, ab \,|\, \boldsymbol{I}_V \,|\, cd \,\rangle \sqrt{l+\delta_{\eta,+1}}\sqrt{l'+\delta_{\eta',+1}} + \sqrt{l'+\eta'+\delta_{\epsilon,+1}} \\
&\times \begin{pmatrix} l & J+\kappa & l' \\ 0 & 0 & 0 \end{pmatrix} \begin{Bmatrix} J+\kappa & l & l' \\ J_3 & 1 & J \end{Bmatrix} \begin{Bmatrix} 1 & l' & l'+\eta' \\ 1 & l'+\eta'+\epsilon & J_3 \end{Bmatrix} \\
&\times \int \mathrm{d}p_1 \frac{p_1^3}{p_1^2+m_\pi^2}\Gamma_\pi(p_1^2) \int \mathrm{d}p_2 \frac{p_2^4}{p_2^2+m_\pi^2}\Gamma_\pi(p_2^2) \int \mathrm{d}r_1 \int \mathrm{d}r_2 \int \mathrm{d}r r^2 j_l(p_1 r) j_{l'}(p_2 r) j_{J+\kappa}(qr) \\
\times \Bigg(&\langle j_a \parallel j_{l+\eta}(p_1 r_1)\left[Y_{l+\eta}(\Omega_1)\otimes\boldsymbol{\sigma}_1\right]_l \parallel j_c\rangle_{r_1} \langle j_b \parallel j_{l'+\eta'+\epsilon}(p_2 r_2)\left[Y_{l'+\eta'+\epsilon}(\Omega_2)\otimes\boldsymbol{\sigma}_2\right]_{J_3} \parallel j_d\rangle_{r_2} \begin{Bmatrix} j_a & j_b & J_1 \\ j_c & j_d & J_2 \\ l & J_3 & J \end{Bmatrix} \\
-(-1)^{l+J_3+J} &\langle j_a \parallel j_{l'+\eta'+\epsilon}(p_2 r_1)\left[Y_{l'+\eta'+\epsilon}(\Omega_1)\otimes\boldsymbol{\sigma}_1\right]_{J_3} \parallel j_c\rangle_{r_1} \langle j_b \parallel j_{l+\eta}(p_1 r_2)\left[Y_{l+\eta}(\Omega_2)\otimes\boldsymbol{\sigma}_2\right]_l \parallel j_d\rangle_{r_2} \begin{Bmatrix} j_a & j_b & J_1 \\ j_c & j_d & J_2 \\ J_3 & l & J \end{Bmatrix} \Bigg)
\end{aligned}
\tag{G.26}
$$

References

[1] J. Ryckebusch, M. Vanderhaeghen, L. Machenil, *et al.* Nucl. Phys. **A568**, 828 (1994).

[2] T. Van Cuyck, N. Jachowicz, R. González–Jiménez, *et al.* (2017), arXiv:1702.06402.

List of abbreviations

CC . . . . . Charged Current
CCQE . . . . . Charged Current Quasielastic
CRPA . . . . . Continuum Random Phase Approximation
CVC . . . . . Conserved Vector Current
em . . . . . electromagnetic
ew . . . . . electroweak
FSI . . . . . Final-State Interaction
GR . . . . . Giant Resonance
HF . . . . . Hartree-Fock
IA . . . . . Impulse Approximation
IPM . . . . . Independent Particle Model
LCA . . . . . Lowest order Correlation operator expansion Approximation
MC . . . . . Monte Carlo
MEC . . . . . Meson-Exchange Current
MF . . . . . Mean Field
NC . . . . . Neutral Current
PCAC . . . . . Partially Conserved Axial Current
pif . . . . . pion-in-flight
RFG . . . . . Relativistic Fermi Gas
RPA . . . . . Random Phase Approximation
SA . . . . . Spectator Approach
sea . . . . . seagull
SuSA . . . . . Superscaling Approximation
QE . . . . . Quasielastic
SRC . . . . . Short-Range Correlation
WNC . . . . . Weak Neutral Current

List of publications

First author

[1] T. Van Cuyck, N. Jachowicz, R. González–Jiménez, *et al.* Phys. Rev. **C94**, 024611 (2016).

[2] T. Van Cuyck, N. Jachowicz, R. González–Jiménez, *et al.* (2017), arXiv:1702.06402.

Co-author

[1] T. Vrancx, J. Ryckebusch, T. Van Cuyck, *et al.* Phys. Rev. **C87**, 055205 (2013).

[2] V. Pandey, N. Jachowicz, J. Ryckebusch, *et al.* Phys. Rev. **C89**, 024601 (2014).

[3] V. Pandey, N. Jachowicz, T. Van Cuyck, *et al.* Phys. Rev. **C92**, 024606 (2015).

[4] M. Martini, N. Jachowicz, M. Ericson, *et al.* Phys. Rev. **C94**, 015501 (2016).

[5] V. Pandey, N. Jachowicz, M. Martini, *et al.* Phys. Rev. **C94**, 054609 (2016).

[6] R. González-Jiménez, N. Jachowicz, J. Nys, *et al.* (2016), arXiv:1612.05511.

Conference proceedings

[1] V. Pandey, N. Jachowicz, T. Van Cuyck, *et al.* PoS **NUFACT2014**, 055 (2015), arXiv:1501.04018.

[2] T. Van Cuyck, V. Pandey, N. Jachowicz, *et al.* (2016), arXiv:1606.08636.

[3] R. González-Jiménez, T. Van Cuyck, N. Van Dessel, *et al.* JPS Conf. Proc. **12**, 010047 (2016).

[4] N. Jachowicz, V. Pandey, M. Martini, *et al.* JPS Conf. Proc. **12**, 010018 (2016).

Samenvatting

In de voorbije twee decennia kwam het onderzoek naar neutrino's in een stroomversnelling terecht. Rond de millenniumwissel werden neutrino oscillaties, een fenomeen dat bijna 50 jaar eerder werd voorgesteld, experimenteel bevestigd door twee verschillende onderzoeksgroepen. Deze ontdekking, die zegt dat een neutrino van één smaak kan veranderen in een neutrino van een andere smaak, had verregaande gevolgen. Dit impliceerde dat neutrino's een massa hebben en verlegde daarmee de grenzen van de neutrinofysica voorbij deze van het standaardmodel. Voor deze ontdekking werd de Nobelprijs voor natuurkunde in 2015 uitgereikt aan deze onderzoeksgroepen.

Verschillende experimenten werden opgestart om de parameters die deze neutrino oscillaties beschrijven: de verschillen tussen de gekwadrateerde massa's en de menghoeken, met hogere precisie te bepalen. De meeste van deze experimenten gebruiken een deeltjesversneller om neutrino's te produceren, op deze manier kan een zeer hoge intensiteit aan neutrino's geproduceerd worden, wat tegemoetkomt aan de zeer lage interactiewaarschijnlijkheid van de neutrino's. Door neutrino's van een welbepaalde smaak te produceren op één plaats, en te tellen hoeveel van deze neutrino's aankomen op een andere plaats, verschillende honderden kilometers verderop, kunnen de oscillatieparameters bepaald worden. Experimenten gebaseerd op een deeltjesversneller hebben ook het voordeel dat de parameters die invloed hebben op de oscillaties, zoals de energie van het neutrino en de afstand tussen productie en detectie, gekozen kunnen worden om zo de oscillatiewaarschijnlijkheid te maximaliseren.

Neutrino's kunnen gedetecteerd, en dus ook geteld, worden door te kijken naar de deeltjes die geproduceerd worden bij de interactie van een neutrino met een atoomkern in het detectormateriaal. Voor een correcte interpretatie van deze data moet de interactiewaarschijnlijkheid van neutrino's met atoomkernen gekend zijn: de werkzame doorsnede. De onzekerheid op deze werkzame doorsnede is een van de grootste systematische onzekerheden in de studie van de oscillatieparameters.

Voor de deeltjesfysica zijn neutrino-atoomkern werkzame doorsneden onmisbare informatie voor de interpretatie van de data en de bepaling van de neutrino-oscillatie parameters. Door de opkomst van neutrino experimenten met een hoge intensiteit, werd het echter mogelijk om ook neutrino's te gebruiken om axiale respons van atoomkernen te bestuderen. Tot heden is de meeste informatie over de respons van atoomkernen afkomstig van verstrooiingsexperimenten met protonen of elektronen, maar de intrinsieke polarisatie van de neutrino's laat toe op een unieke wijze de zwakke response en axiale structuur van atoomkernen te onderzoeken. Deze informatie was eerder niet of moeilijk toegankelijk was.

In dit werk wordt de werkzame doorsnede bepaald voor verstrooiing van neutrino's aan atoomkernen via een geladen-stroom interactie. De meeste moeilijkheden in de berekening van deze werkzame doorsneden zijn gerelateerd aan de beschrijving van de atoomkernen, dit zijn namelijk gecompliceerde veeldeeltjessystemen. Als uitgangspunt voor de beschrijv-

ing van de atoomkernen wordt een onafhankelijk-deeltjes model (IPM) gebruikt: de kern wordt beschreven als protonen en neutronen die onafhankelijk van elkaar bewegen in een gemiddelde potentiaal die gegenereerd wordt door de deeltjes zelf. De potentiaal wordt bepaald door de Hartree-Fock vergelijkingen op te lossen met een effectieve nucleon-nucleon interactie. Dit onafhankelijk-deeltjes model kan verschillende kerneigenschappen verklaren, zoals de bindingsenergieën van de nucleonen en de extra stabiliteit van kernen met volledig gevulde kernorbitalen, maar het heeft echter nog enkele tekortkomingen. Twee van deze tekortkomingen, die beide te maken hebben met tweedeeltjeseffecten, worden uitgebreid bestudeerd in deze thesis.

Wanneer de protonen en neutronen in een kern beschreven worden in een onafhankelijk-deeltjes model, dan kunnen deze nucleonen elkaar willekeurig dicht benaderen. Dit zou onmogelijk moeten zijn, door de afstotende eigenschappen van de nucleon-nucleon kracht op korte afstand. Daarom worden korteafstandscorrelaties (SRCs) geïntroduceerd in het onafhankelijk-deeltjes model [1–3]. Naast de centrale afstotende eigenschappen van de nucleon-nucleon kracht worden ook de tensor- en de spin-isospin component in rekening gebracht.

Een tweede tekortkoming van het basismodel is gerelateerd aan de manier waarop een neutrino inwerkt op een atoomkern. In de impuls benadering (IA) worden de residuele interacties tussen de nucleonen genegeerd tijdens de neutrino-atoomkern interacties, de atoomkern wordt omschreven als een som van protonen en neutronen. Deze bindingskrachten worden in rekening gebracht door de toevoeging van mesonuitwisselingsstromen (MECs) [4,5]. Enkel de mesonuitwisselingsstromen met de langste dracht worden in rekening gebracht, dit zijn stromen waar een pion uitgewisseld wordt tussen twee nucleonen.

Beide tweedeeltjeseffecten zorgen ervoor dat de nucleonen in paren kunnen voorkomen in de atoomkern, en wanneer een neutrino interageert met een nucleonpaar, kunnen beide nucleonen uit de atoomkern gestoten worden. Dit in tegenstelling tot het basismodel, waarbij het neutrino bij constructie interageert met één enkel nucleon, dat hierdoor uit de atoomkern geslagen wordt. Het kan echter ook gebeuren dat een neutrino interageert met een nucleonpaar, maar slechts één van de deeltjes uit de kern gestoten wordt. Al deze processen worden uitvoerig bestudeerd in dit werk. Bij de tweedeeltjesemissie processen wordt onderscheid gemaakt tussen reacties waarbij beide uitgestoten nucleonen gedetecteerd worden, reacties waarbij slechts één van de twee nucleonen gedetecteerd worden, en reacties waarbij helemaal geen nucleon gedetecteerd wordt.

Door de gelijkenissen tussen elektronen en neutrino's, worden de resultaten van het model vergeleken met elektronverstrooiingsdata. Bij deze resultaten voor elektron-interacties is de energie van het elektron nauwkeurig bepaald en het reactiemechanisme gekend. Een goede overeenstemming met deze data is een grondige test voor het model. Resultaten voor neutrinoverstrooiing worden dan getoond voor gelijkaardige kinematische situaties, die relevant zijn voor actuele neutrino-oscillatie experimenten. Om te vergelijken met neutrinoverstrooiingsdata wordt geïntegreerd over de energiedistributie van de neutrino's.

Interacties waarbij een neutrino interageert met een nucleonpaar, en waarbij beide uitgestoten nucleonen experimenteel geobserveerd worden, vertonen een kenmerkend gedrag. De sterkte van de tweedeeltjesemissie kan gerelateerd worden aan de massamiddelpuntsimpulsdistributie van het paar in de atoomkern. Voornamelijk nucleonparen met een lage massamiddelpuntsimpuls dragen bij tot de sterkte.

Dit kenmerkend gedrag wordt gebruikt om neutrino-atoomkern werkzame doorsneden te

bepalen voor inclusieve reacties. Dit zijn interacties waarbij geen uitgestoten nucleonen gedetecteerd worden, en betekent dat één- en tweedeeltjesemissie processen opgeteld moeten worden. Door voornamelijk nucleonparen met een lage massamiddelpuntsimpuls in rekening te brengen kan de tweedeeltjessterkte tot de inclusieve reactie efficiënt berekend worden.

Bij deze inclusieve interacties, produceren de tweedeeltjeseffecten een extra bijdrage tot het inclusieve signaal, met een sterkte van zo'n 5% van de ééndeeltjessterkte. Ze verklaren dus deels de ontbrekende sterkte in de vergelijking tussen theorie en data, die het basismodel niet kon verklaren.

De relatieve sterkte van de drie componenten van de kortedrachtscorrelaties worden systematisch vergeleken voor één- en tweedeeltjesemissie processen. Veel kenmerken hiervan kunnen verklaard worden via de eigenschappen van de correlatiefuncties in de impulsruimte en kinematische argumenten. Als de faseruimte van de interactie vooral nucleonparen met een gemiddelde relatieve impuls bevat, zal de tensorcontributie tot de tweedeeltjesemissiesterkte het grootst zijn, omdat de tensorcorrelatiefunctie domineert voor gemiddelde impulswaarden. Als daarentegen voornamelijk nucleonparen met een hoge relatieve impuls voorkomen in de faseruimte, zullen de centrale correlaties de meeste sterkte leveren.

Bij het onderzoek naar mesonuitwisselingsstromen worden twee vectorstromen in rekening gebracht: de zeemeeuw- en pion-in-vlucht-stroom. Beide stromen zijn welbekend door elektronverstrooiingsonderzoek. Voor de overeenkomstige axiaalvector-mesonuitwisselingsstroom, wordt de benadering van [6] gevolgd. Verder wordt nog vergeleken met twee andere mogelijkheden om de beschrijving van de stroom te begrenzen aan de hand van symmetrieoverwegingen. De verschillen tussen deze mogelijkheden tonen aan dat de axiaalvectorstroom niet eenduidig bepaald is.

Finaal worden de theoretische voorspellingen vergeleken met experimentele neutrinoverstrooiingsdata. Als vergeleken wordt met MiniBooNE data, waarbij het muon dat gecreëerd wordt in de geladen stroom interactie, voorwaarts verstrooid wordt, komen de numerieke voorspellingen goed overeen met de data. Bij grotere leptonverstrooiingshoeken wordt de data echter nog onderschat. Ook de overeenkomst tussen de voorspellingen en de data van het T2K experiment is bevredigend. Hierbij moeten we echter opmerken dat deze data nog reactiekanalen bevat, die niet inbegrepen zijn in het model dat hier beschreven wordt.

Bibliografie

[1] J. Ryckebusch, V. Van der Sluys, K. Heyde, *et al.* Nucl. Phys. **A624**, 581 (1997).

[2] S. Janssen, J. Ryckebusch, W. Van Nespen, *et al.* Nucl. Phys. **A672**, 285 (2000).

[3] T. Van Cuyck, N. Jachowicz, R. González–Jiménez, *et al.* Phys. Rev. **C94**, 024611 (2016).

[4] J. Ryckebusch, M. Vanderhaeghen, L. Machenil, *et al.* Nucl. Phys. **A568**, 828 (1994).

[5] T. Van Cuyck, N. Jachowicz, R. González–Jiménez, *et al.* (2017), arXiv:1702.06402.

[6] I. Towner, Nucl. Phys. **A542**, 631 (1992).